ORNL/TM-12398

ornl

OAK RIDGE NATIONAL LABORATORY

MARTIN MARIETTA

Steady-State Thermal-Hydraulic Design Analysis of the Advanced Neutron Source Reactor

Advanced Neutron Source

MANAGED BY
MARTIN MARIETTA ENERGY SYSTEMS, INC.
FOR THE UNITED STATES
DEPARTMENT OF ENERGY

ORNL/TM-12398

STEADY-STATE THERMAL-HYDRAULIC DESIGN ANALYSIS OF THE ADVANCED NEUTRON SOURCE REACTOR

Compiled by

G. L. Yoder, Jr.

Contributing Authors

J. R. Dixon
Y. Elkassabgi
D. K. Felde
G. E. Giles
R. M. Harrington
D. G. Morris
W. R. Nelson
A. E. Ruggles
M. Siman-Tov
T. K. Stovall
G. L. Yoder, Jr.

May 1994

Prepared by
OAK RIDGE NATIONAL LABORATORY
managed by
MARTIN MARIETTA ENERGY SYSTEMS, INC.
for the
U.S. DEPARTMENT OF ENERGY
under contract DE-AC05-84OR21400

CONTENTS

CONTENTS (continued)

CONTENTS (continued)

LIST OF FIGURES

LIST OF FIGURES (continued)

LIST OF FIGURES (continued)

LIST OF TABLES

ACRONYMS

1-D	one-dimensional
2-D	two-dimensional
3-D	three-dimensional
ACSL	Advanced Continuous Simulation Language
ANS	Advanced Neutron Source
ANSR	Advanced Neutron Source reactor
BOC	beginning-of-cycle
B-R	Bergles–Rohsenow
B&W	Babcock and Wilcox
CDF	cumulative distribution function
CHF	critical heat flux
CPBT	core pressure boundary tube
CSAR	conceptual safety analysis report
CSAU	code sealing, applicability, and uncertainty
CTL	corrosion test loop
DNB	departure from nucleate boiling
EOC	end-of-cycle
FCFF	forced convection friction factor
FCHTC	forced convection heat transfer coefficient
FE	flow excursion
FEHF	flow excursion heat flux
FF	friction factor
FPI	fast probability integration
FSAR	final safety analysis report
HFIR	High Flux Isotope Reactor
HTC	heat transfer coefficient
IB	incipient boiling
IBHF	incipient boiling heat flux
ID	identification
INEL	Idaho National Engineering Laboratory
L/D	length over diameter
LHS	latin hypercube sampling
LSSS	limiting safety system set points
MC	Monte Carlo
NA	not applicable
OFI	onset of flow instability
ONVG	onset of net vapor generation
ORNL	Oak Ridge National Laboratory
OSV	onset of significant void
PC	personal computer
PDF	probability distribution function
PIRT	Phenomena Identification and Ranking Table
PRA	probabilistic risk assessment
PSAR	preliminary safety analysis report
S&Z	Saha & Zuber

SNL	Sandia National Laboratories
SRL	Savannah River Laboratory
SRSS	square root of the sum of the squares
T/H	thermal-hydraulic
TASHA	Thermal Analysis of Steady-State Heat Transfer for ANS
THTL	thermal-hydraulic test loop
U	uncertainty (factor)

NOMENCLATURE

q''	local heat flux (kW/m^2)
T_{sat}	saturation temperature (K)
T_b	bulk coolant temperature (K)
V	coolant velocity (m/s)
$T_{sat,ex}$	saturated exit temperature (K)
x_t	oxide thickness at time t (μm)
$U9$	uncertainty factor for the oxide correlation (unitless)
t	time (h)
$T_{x/c}$	oxide coolant interface temperature (K)
x_o	oxide thickness at $t = 0$ (μm)
k_i	rate constant (μm^{n+1}/h)
T_c	bulk coolant temperature (K)
ϕ	local heat flux (MW/m^2)
f	friction factor
F	constant
Re	Reynolds number
f_d	friction factor (Darcy formulation)
b	gap of a rectangular channel or annulus (m)
s	span of a rectangular channel (m)
μ_b	bulk dynamic viscosity (Pa • s)
μ_w	wall dynamic viscosity (Pa • s)
Re_b	bulk coolant Reynolds number
Nu	Nusselt number (unitless) [hD/k]
X^*	nondimensional length [z/Re/Pr/D]
f_f	Fanning friction factor
T	temperature (K)
q'''	volumetric heat generation rate (kW/m^3)
r	radius (m)
C_1	integration constant
C_2	integration constant
T_o	outside temperature (K)
T_i	inside temperature (K); inlet temperature (K)
k	thermal conductivity (kW/m • K)
r_i	inside radius (m)
r_o	outside radius (m)
r_m	maximum radius (m)
q	surface heat flux (kW/m^2)
A	area (m^2)
Q_i	inside heat flow (kW); inlet heat flow (kW)
A_i	inside area (m^2)
Q_o	outside heat flow (kW)
A_o	outside area (m^2)
Q	heat flow (kW)
h_{FC}	forced convection heat transfer coefficient (kW/m^2• K)

T_W	wall temperature (K)
$T_{b,o}$	outside bulk coolant temperature (K)
$h_{FC,o}$	forced convection heat transfer coefficient, outside (kW/m^2 • K)
$h_{FC,i}$	forced convection heat transfer coefficient, inside (kW/m^2 • K)
$T_{b,i}$	inside bulk coolant temperature (K)
Q_{tot}	total heat flow (kW)
ρ	coolant density (kg/m^3)
C_p	mean coolant specific heat (kJ/kg • K)
T_{ex}	exit temperature (K)
Q_{sp}	side plate heat flow (kW)
x	oxide thickness (μm)
e	2.71828
T_{ba}	average bulk coolant temperature (K)
T_{alx}	inside surface temperature of the oxide layer (K)
q_{CHF}	critical heat flux (kW/m^2)
$q_{pool,sub}$	subcooled pool boiling heat flux (kW/m^2)
$q_{conv,sub}$	subcooled convective heat flux (kW/m^2)
h_{lv}	latent heat of vaporization (kJ/kg)
ρ_v	vapor coolant density (kg/m^3)
σ	surface tension (N/m)
g	acceleration due to gravity (9.81 m/s^2)
$\Delta\rho$	liquid to vapor density difference (kg/m^3)
F_{sub}	subcooling factor
ρ_1	density of pure U_3Si_2 (12.2 mg/mm^3)
ΔT_{sub}	subcooling temperature difference (K)
q_{IB}	local incipient boiling heat flux (kW/m^2)
F_{D_2O}	correction factor for applying B-R correlation for heavy water
P	pressure (Pa)
K_b	bulk coolant thermal productivity (kW/m • K)
D_e	equivalent channel diameter (m)
Pr_b	bulk coolant Prandtl number
s	span of a rectangular channel (m)
K_H	correction factor for heated liquids
n	constant (mechanism number)
σ_{streak}	standard deviation for a continuous hot streak
σ_{seg}	standard deviation of the hot streak distribution
N_{seg}	number of stacked segments
P_{nr}^T	probability plate not rejected because of a heat transfer area defect
P_{nr}^s	probability plate not rejected because of a "span defect"
P_{nr}^l	probability plate not rejected because of a "length defect"
P_{rej}	probability of rejection because of the length of the defect
σ_l^{ANS}	ANS standard deviation for length variance
σ_l^{HFIR}	HFIR standard deviation for length variance
Z	HFIR P_{rej} value
f_{hs}^{CHF}	hot spot factor for CHF
f_{hs}^{FE}	hot spot factor for FE

U_{sm}	combined effect of local fuel segregation plus nonbond
F_{hc}	hot channel factor
U_{pd}	streak-average power distribution
MP_d	maximum relative power density (unitless)
ϕ_a	average local heat flux (MW/m^2)
t_m	meat thickness (m)
R_s	ratio of heat generated in segregated fuel to that of normal fuel (unitless)
p	volume fraction of U_3Si_2 (0.50)
ρ_s	^{235}U density in segregated fuel (mg/mm^3)
ρ_n	^{235}U density in normal fuel (^{235}U mg/mm^3)
d_s	diameter of segregation spot $\left(\sqrt{0.84A_i}/3.682\pi = 0.471 \; mm \; for \; 50\% \; U_3Si_2 \right)$
p_d	local relative power density (unitless)
q'''_{sat}	volumetric heat generation (MW/m^3)
F_d	fission density (fissions/mm^3)
S_d	initial surface density (g ^{235}U/mm^2)
B_u	burnup (P_{uf}/P_{ua})
ρ_{uf}	density of fissioned ^{235}U
ρ_{ua}	maximum density of ^{235}U atoms that can fission
V_f	volume fraction of fuel
A_v	Avogadro's number (6.023 × 10^{23} molecules/g • mole)
M_w	molecular weight (^{235}U g/g • mole)
T_{cl}	temperature at centerline
ΔP_{ext}	external supply pressure drop (Pa)
ΔP_{ts}	test section pressure drop (Pa)
Q''_{loc}	local heat flux
$T_{w,in}$	local inside surface temperature (K)
Q''_{loc}	local heat flux on the flats
Q''_{av}	average heat flux on the flats
Q_{loss}	heat loss (kW)
th_{Al}	aluminum thickness (m)
L	heated length (m)
A_{Al}	aluminum cross-sectional area (m^2)
E	voltage (V)
I	current (A)
A_{cs}	cross-sectional flow area (m^2)
$T_{w,ex}$	temperature on the ceramic insulator (K)
th_{ox}	oxide thickness (m)
k_{Al}	aluminum thermal conductivity (W/m/°C)
k_{ox}	oxide thermal conductivity (W/m/°C)

ABSTRACT

The Advanced Neutron Source (ANS) is a research reactor that is planned for construction at Oak Ridge National Laboratory. This reactor will be a user facility with the major objective of providing the highest continuous neutron beam intensities of any reactor in the world. Additional objectives for the facility include providing materials irradiation facilities and isotope production facilities as good as, or better than, those in the High Flux Isotope Reactor.

To achieve these objectives, the reactor design uses highly subcooled heavy water as both coolant and moderator. Two separate core halves of 67.6-L total volume operate at an average power density of 4.5 MW(t)/L, and the coolant flows upward through the core at 25 m/s. Operating pressure is 3.1 MPa at the core inlet with a 1.4-MPa pressure drop through the core region. Finally, in order to make the resources available for experimentation, the fuel is designed to provide a 17-d fuel cycle with an additional 4 d planned in each cycle for the refueling process.

This report examines the codes and models used to develop the thermal-hydraulic design for ANS, as well as the correlations and physical data; evaluates thermal-hydraulic uncertainties; reports on thermal-hydraulic design and safety analysis; describes experimentation in support of the ANS reactor design and safety analysis; and provides an overview of the experimental plan.

1. INTRODUCTION

The Advanced Neutron Source (ANS) is a research reactor planned to be built at the Oak Ridge National Laboratory (ORNL). It will be a user facility with the major objective of providing the highest continuous neutron beam intensities of any reactor in the world. Other design objectives include: (1) providing materials irradiation facilities as good as, or better than, those existing in the High Flux Isotope Reactor (HFIR) and (2) providing isotope production facilities as good as, or better than, those in HFIR. An array of user experimental equipment is incorporated in the design to provide experimental capability in a wide range of areas, including chemistry, biology, fundamental physics, high temperature superconductivity, solid state physics, weak interaction physics, and many others.

To achieve those objectives, the reactor design uses highly subcooled heavy water as both coolant and moderator. Two separate core halves of 67.6 L total volume operate at an average power density of 4.5 MW(t)/L. The coolant flows upward through the core at 25 m/s velocity. Operating pressure is 3.1 MPa at the core inlet with a 1.4-MPa pressure drop through the core region. In order to provide a high reactor availability for these experiments, the fuel is designed to provide a 17-d fuel cycle with an additional 4 d planned in each cycle for the refueling process. A comparison of ANS thermal-hydraulic (T/H) parameters to those of other reactor systems is provided in Table 1.1.

1.1 SYSTEM DESIGN

Each element of the core (see Fig. 1.1) is constructed with a series of involute fuel plates arranged in an annular array. The involute design provides uniform coolant gaps at all spanwise positions. The fuel plate is 1.27-mm thick and consists of 0.254-mm thick 6061 aluminum cladding material sandwiching a 0.762-mm mixture of uranium silicide fuel (U_3Si_2) and aluminum. Each coolant gap is also 1.27 mm in width and has a span of 70.29 or 87.35 mm (upper or lower core, respectively). Fuel plates are welded to inner and outer cylindrical side plates with each element having 507 mm of fueled length. Unheated 10-mm leading and trailing edges complete the fuel plate design.

The core is surrounded by a double walled core pressure boundary tube (CPBT), which serves as the primary system pressure boundary in the core region. The double wall design of the CPBT ensures that a break in the outer wall will not lead to core damage. The outer diameter of the aluminum CPBT is 519 mm with a 3-mm coolant gap between the inner and outer CPBT walls. Coolant flows at 7 m/s through this gap to ensure adequate cooling.

Three control and shutdown rods are located in the central hole region of the core (see Fig. 1.1). Insertion of any one of these rods is sufficient to ensure shutdown of the reactor. The control function of the rods is performed mechanically through a series of electric motors. The scram function of these rods is activated through a ball latch mechanism, while fast rod insertion is ensured using scram springs incorporated in the rod design. The rods are 71-mm diam and are designed to provide coolant paths internal to the rods to ensure coolability of both the hafnium absorber material and the aluminum carrier (see Fig. 1.2). Heavy water coolant flowing at 6 m/s over the rod surface as well as in the internal coolant channels is provided to cool these rods.

Thirty transuranic production rods, each 9.5-mm diam with a 508-mm active length, are located immediately upstream of the upper fuel element. Additional experimental positions are also located in the flow stream above the lower fuel element.

Table 1.1. Comparison of Advanced Neutron Source thermal-hydraulic parameters to other reactor designs

	ANS[a]	HFIR[b]	SM-2	ILL[c]	Sequoyah NPP[d]
Coolant	D_2O	H_2O	H_2O	D_2O	H_2O
Core volume (L)	67.6	50.6	48	46.3	35,000
Peak thermal neutron flux ($m^{-2} \cdot s^{-1}$)	7.4×10^{19}	1.6×10^{19}	3×10^{19}[e]	1.5×10^{19}	8.0×10^{17}
Thermal power (MW)	303	97.5[f]	75	57	3,500
Average power density (MW/L)	4.5	1.9	1.6	1.2	0.1
Peak heat flux (MW/m^2)	12	4.0	7	4	1.8
Coolant inlet velocity (m/s)	25	15	13.5	15.5	5
Core inlet pressure (MPa)	3.2	3.3	1.0	1.5	15.9
Core pressure drop (MPa)	1.5	0.7		1.0	0.15
Inlet coolant temperature (°C)	45	49	50	30	285
Exit coolant temperature (°C)	85	70	80	50	320
Exit subcooling level (°C)	110	155		50	27
Core exit Reynolds number	2×10^5	1×10^5		1×10^5	5×10^5
Fuel	Silicide	Oxide	Oxide	Alloy	Oxide
Cladding	Al	Al	Ni	Al	Zr

[a]ANS = Advanced Neutron Source.
[b]HFIR = High Flux Isotope Reactor.
[c]ILL = Institute Laue Langevin.
[d]NPP = Nuclear Power Plant.
[e]Flux in the trap.
[f]The HFIR power level has recently been reduced by 15% because of pressure vessel embrittlement. However, HFIR operated for more than 20 years at the 97.5 MW(t) level.

The CPBT is surrounded by a 3.4-m diam, 3.6-m high cylindrical reflector tank also containing heavy water. This tank operates at a normal pressure of 0.3 MPa and contains thermal beam tubes, the two cold sources, the hot source, and many other pieces of experimental equipment. Flow in the reflector tank is dictated by cooling requirements of the various components within this region and is supplied by independent cooling loops. A schematic of the reflector tank region is shown in Fig. 1.3.

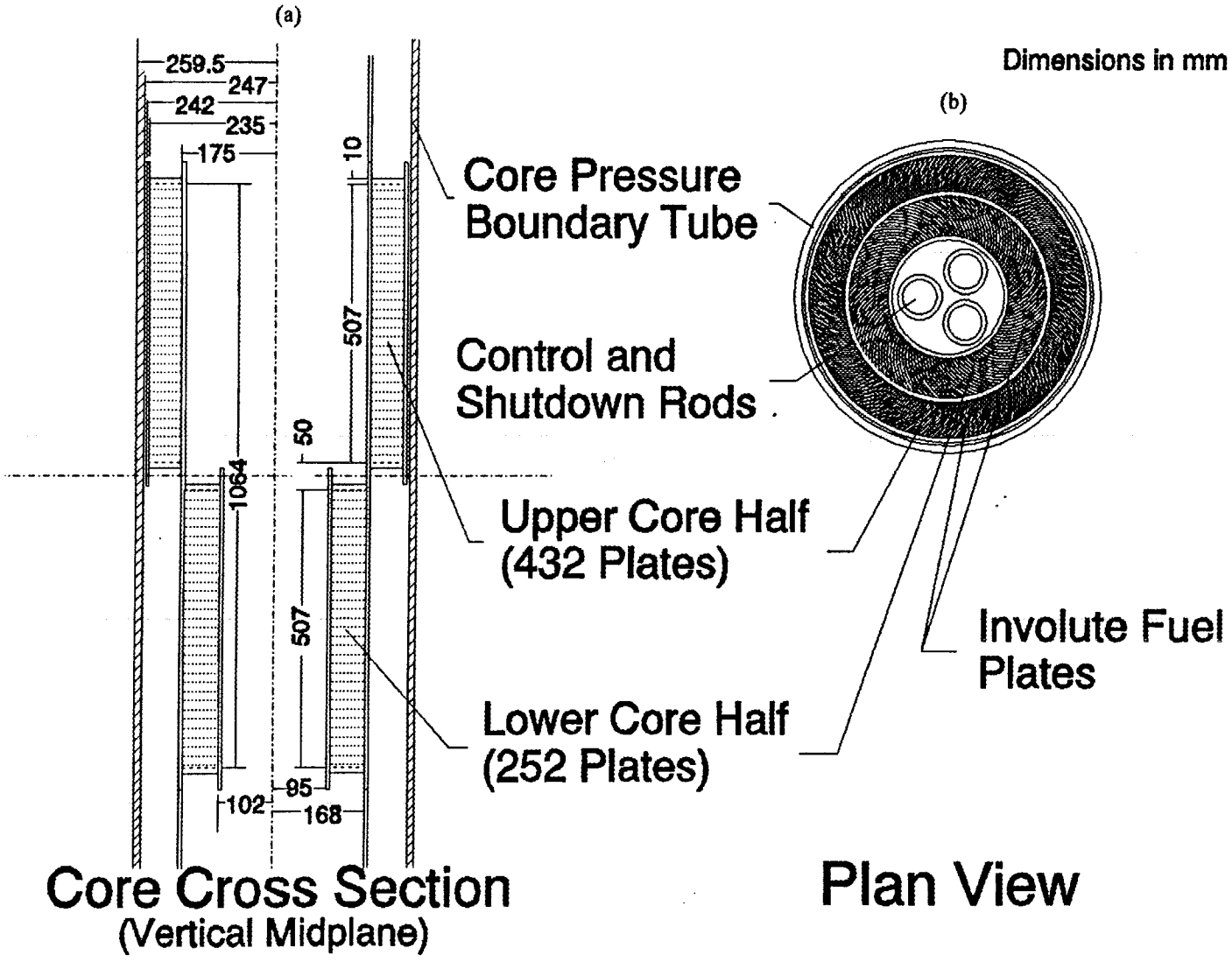

Fig. 1.1. Fuel elements: (a) vertical midplane cross-section and (b) plan view.

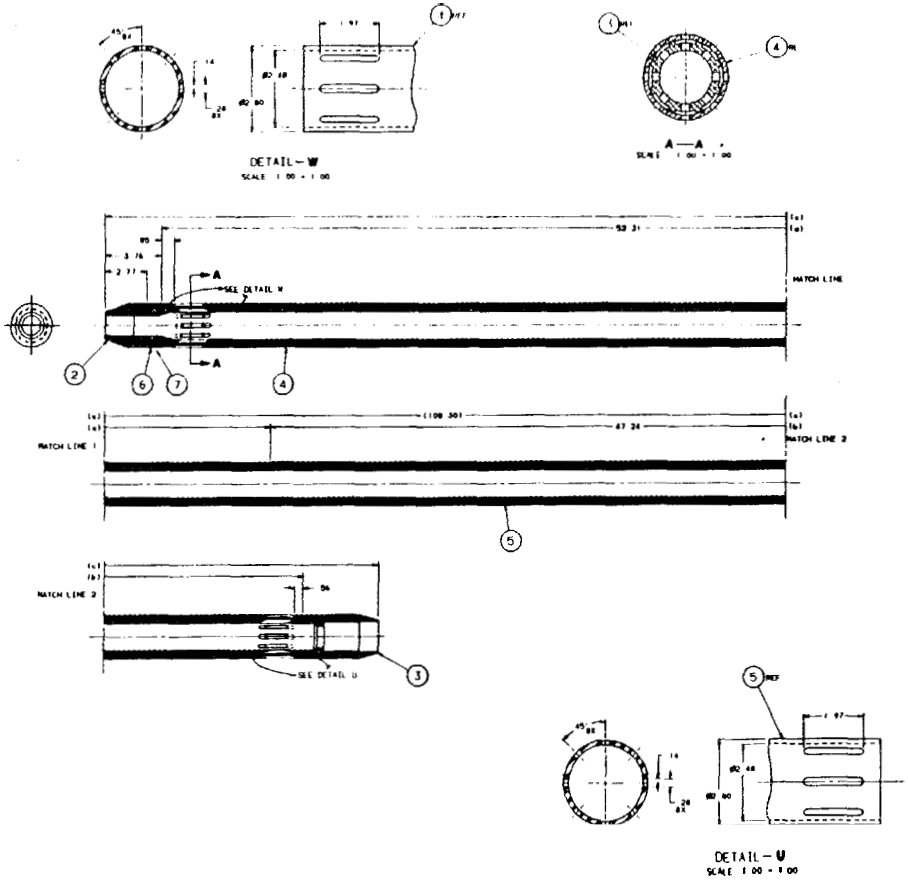

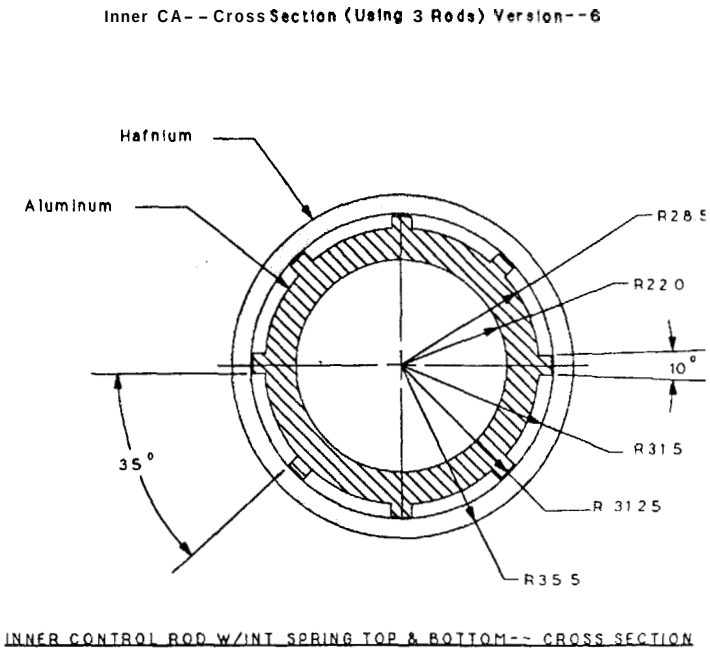

Fig. 12. Central control rod geometry.

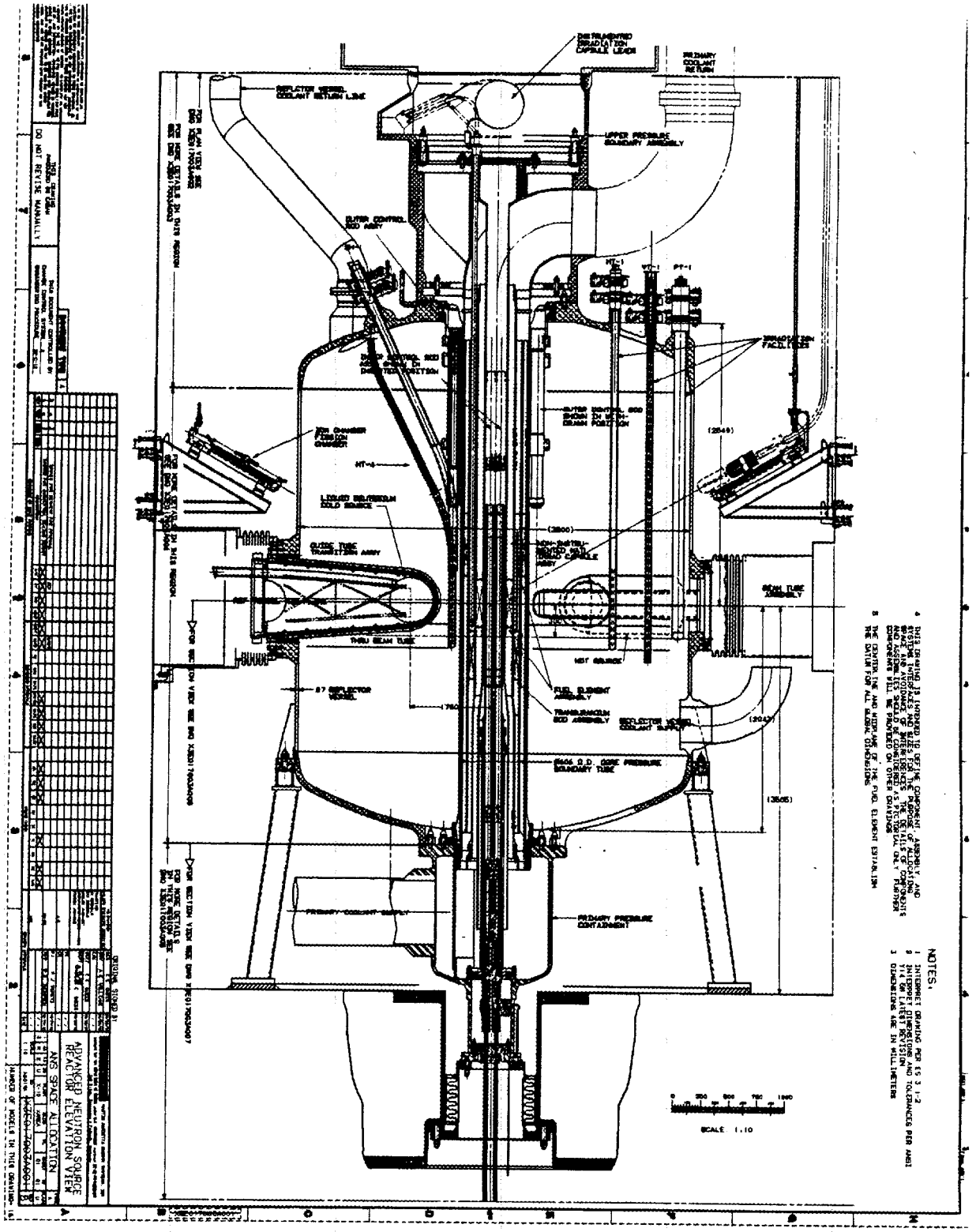

Fig. 1.3. Reflector tank components.

Eight hydraulically actuated safety rods are situated external to the CPBT and located within the reflector tank. These rods are incorporated as a redundant means of shutting down the reactor with insertion of seven of these rods being sufficient to shut down the reactor even if the inner control rods are totally lost. If the inner rods remain stuck in their critical position, insertion of only one of the outer rods would be required to shut down the reactor. The outer rods are withdrawn by hydraulic pressure applied to the internal regions of each rod, which acts against scram springs. A scram signal releases the hydraulic pressure and the spring scrams the rod. A diagram of the safety rods is shown in Fig. 1.4.

The cooling system design uses four independent coolant loops (three active during normal operation), each equipped with two heat exchanger systems (both of which are submerged in the light water pool). The main heat exchanger in each loop has primary reactor coolant flowing on the shell side, with cooling tower water flowing on the tube side to improve the ability to maintain the heat exchanger. The emergency heat exchanger, located in series with the main heat exchanger, also has primary reactor coolant on the shell side, but is cooled under emergency conditions by natural circulation of the pool water on the tube side. The piping design is optimized for natural convection cooling after shutdown. In addition, the cooling tower design is such that natural circulation cooling between the main heat exchanger and cooling tower can also be used if necessary.

A main circulation pump, a check valve, and a flow diode (a preferred direction flow device) complete each reactor coolant loop. Each pump is equipped with a battery powered pony motor that can maintain 10% of full flow for 30 min if the main motors lose power. Pump coastdown requires 2 s to reach one half of the original speed. Each loop also contains a gas pressurized accumulator that slows system depressurization during some accident scenarios. Each accumulator has a liquid volume of 7.5 m^3 and a gas volume (nitrogen or argon) of 0.52 m^3. A cooling system schematic diagram, which shows one loop of this four-loop system, is shown in Fig. 1.5, while Fig. 1.6 indicates relative piping elevations in the design.

The requirement that the reactor piping must either be submerged in one of the light water pools or located in one of several limited volume cells is also included in the design. These cells are used to isolate instrumentation and components requiring access for routine maintenance on inspection and those that are not designed to operate under water. The cells are designed to occupy only limited floor area and are watertight in order to ensure that, in the event of a piping break in one of these cells, the accumulators will supply enough coolant to submerge the piping.

Each loop also contains a pressurizing and letdown system that is used to maintain primary system pressure and also provide a means of water cleanup. The pressurizing system consists of a makeup tank at atmospheric pressure and a pressurizing pump that is used to supply heavy water to the primary system continuously at a rate of ~5 kg/s. In parallel to the main pressurizing pump is a standby pump that is started only if the letdown valve closes on a low pressure signal. System pressure is maintained by modulating the letdown valves located near the inlet of the main heat exchanger in each loop. The low pressure heavy water from the letdown valves is then passed through a D_2O cleanup system and returned to the makeup tank.

1.2 HYDRAULIC DESIGN AND HEAT LOADS

During normal operation [at 303 MW(t)], ~80% of the system pressure drop is taken through the core region. Total primary heavy water coolant flow through all three active loops is 1994 kg/s, while the nominal core inlet temperature is 45°C with a temperature rise through the core of 37°C. Figure 1.7 shows loop conditions under steady-state operation. Flow splits and pressures in the core

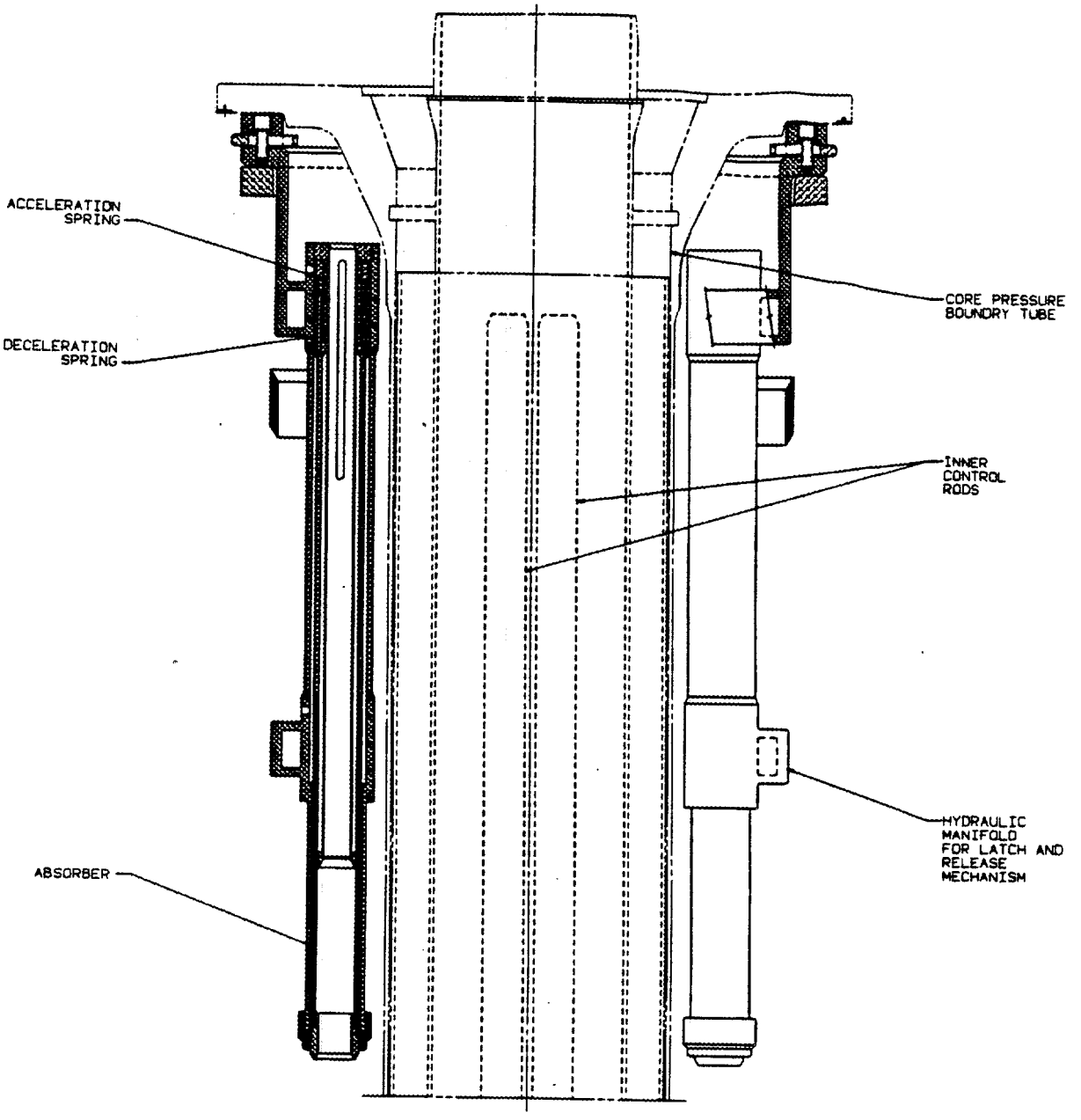

Fig. 1.4. Outer shutdown rod assembly.

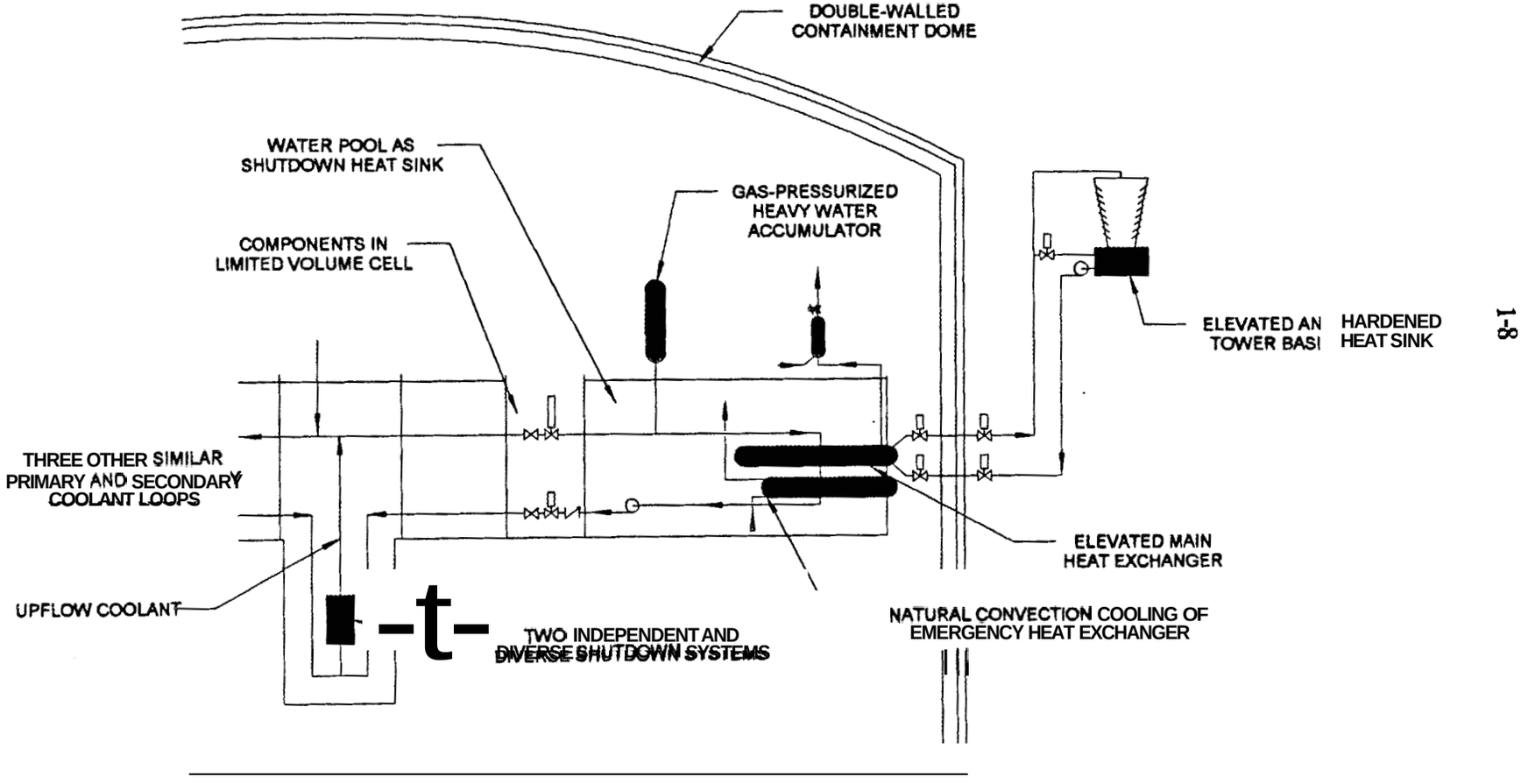

Fig. 15. Cooling system schematic of one loop.

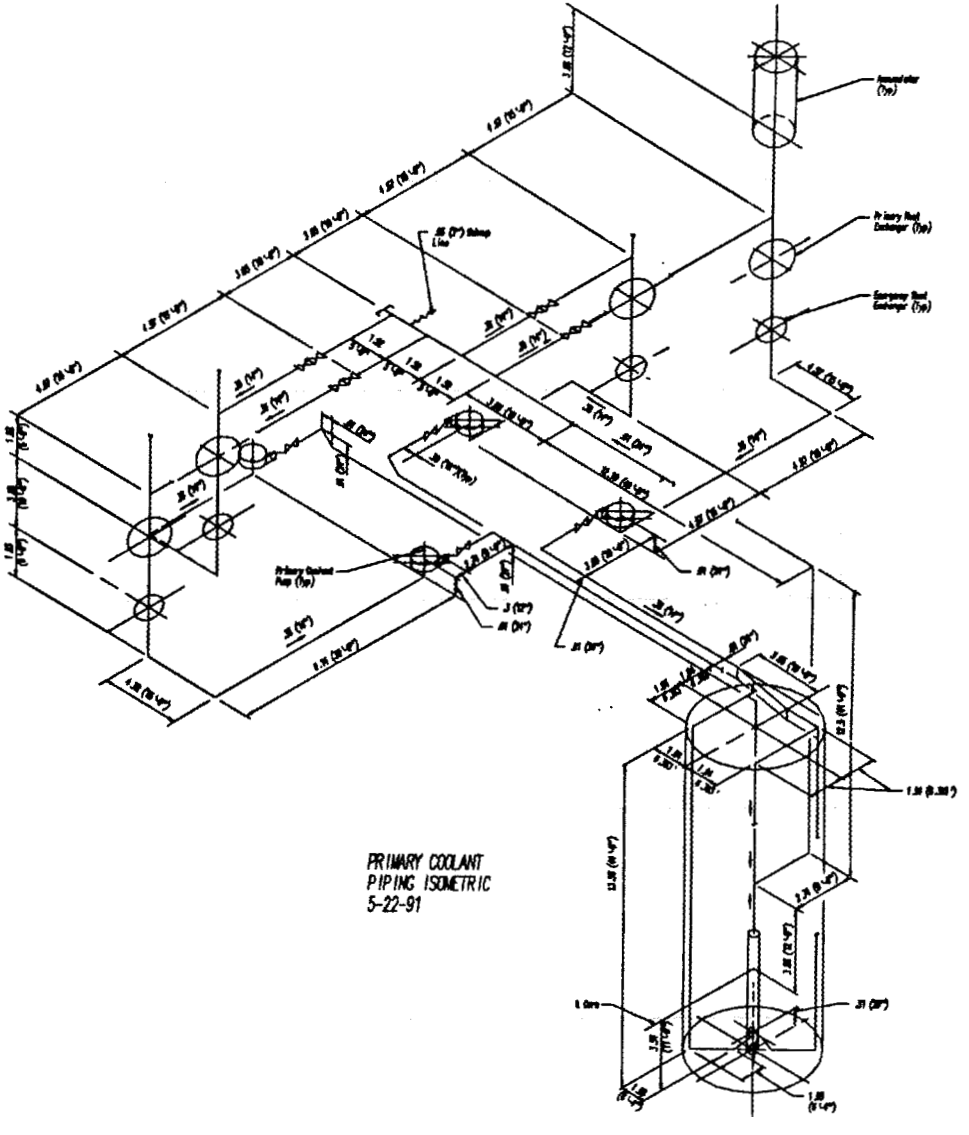

Fig. 1.6. Primary coolant piping isometric.

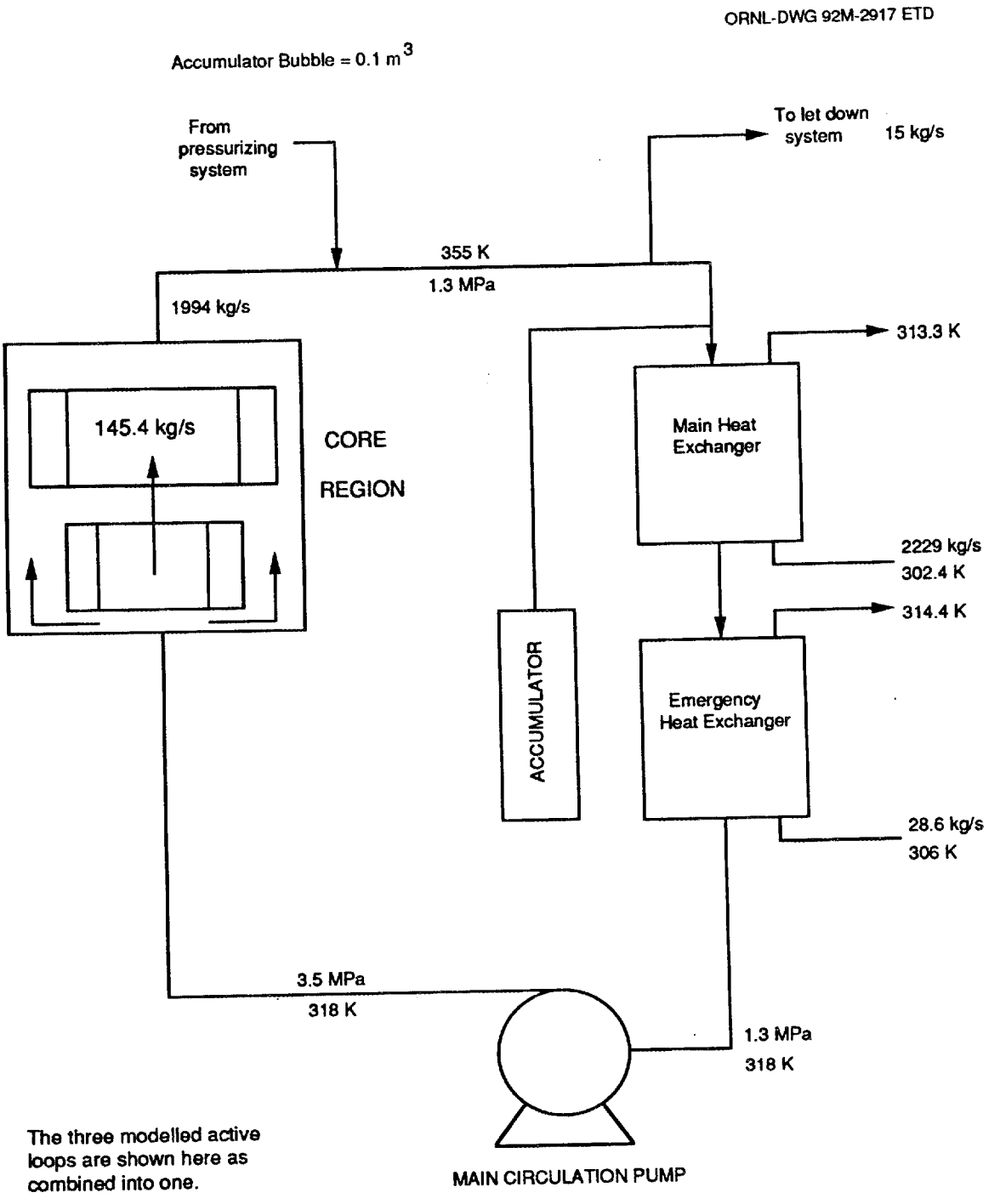

Fig. 1.7. Loop conditions under steady-state operation.

region under isothermal conditions are shown in Fig. 1.8. Ten separate orifices are located within the core region in order to ensure correct flow rates and pressure loadings on various components. Peak heat fluxes in components external to the fueled region under normal operating conditions are shown in Fig. 1.9. After shutdown, core power drops significantly (see Fig. 1.10), while heat loads in other components drop less rapidly as a result of aluminum-29 decay and fission product gamma heating from the core. An example of the heating after shutdown in the CPBT is shown in Fig. 1.11, where ~40% of the nominal heat load remains immediately after shutdown (as compared to 7% in the core).

The ANS reactor (ANSR) fuel design uses fuel graded in both the radial and axial directions. Because of fuel burnup and control rod movement during the core lifetime, the power distribution within the core varies during the fuel cycle. This variation is presented in Fig. 1.12, which shows the calculated relative power density (defined as the local power density at each location divided by the average power density for the core) as a function of position in the fuel for each fuel element at three times within the cycle. For these calculations, the grid size over which the fuel is graded is coarser than that used in the neutronics calculations, which results in the "steps" noted in the relative power density profiles. The highest relative power densities and the highest hot streak ratio (defined as the ratio of bulk coolant temperature rise along the hottest axial streak divided by the average bulk temperature rise in the core) for each core half are presented in Table 1.2.

Table 1.2. Peak power densities and hot streak ratios for the L7 core design

	Time in cycle (d)	Peak relative power density	Hot streak ratio
Upper core	0	2.20	1.32
	4.25	2.12	1.23
	8.50	2.05	1.12
	12.75	1.90	1.21
	17	1.78	1.57
Lower core	0	2.31	1.76
	4.25	2.29	1.49
	8.50	2.08	1.20
	12.75	1.53	0.96
	17	0.98	0.74

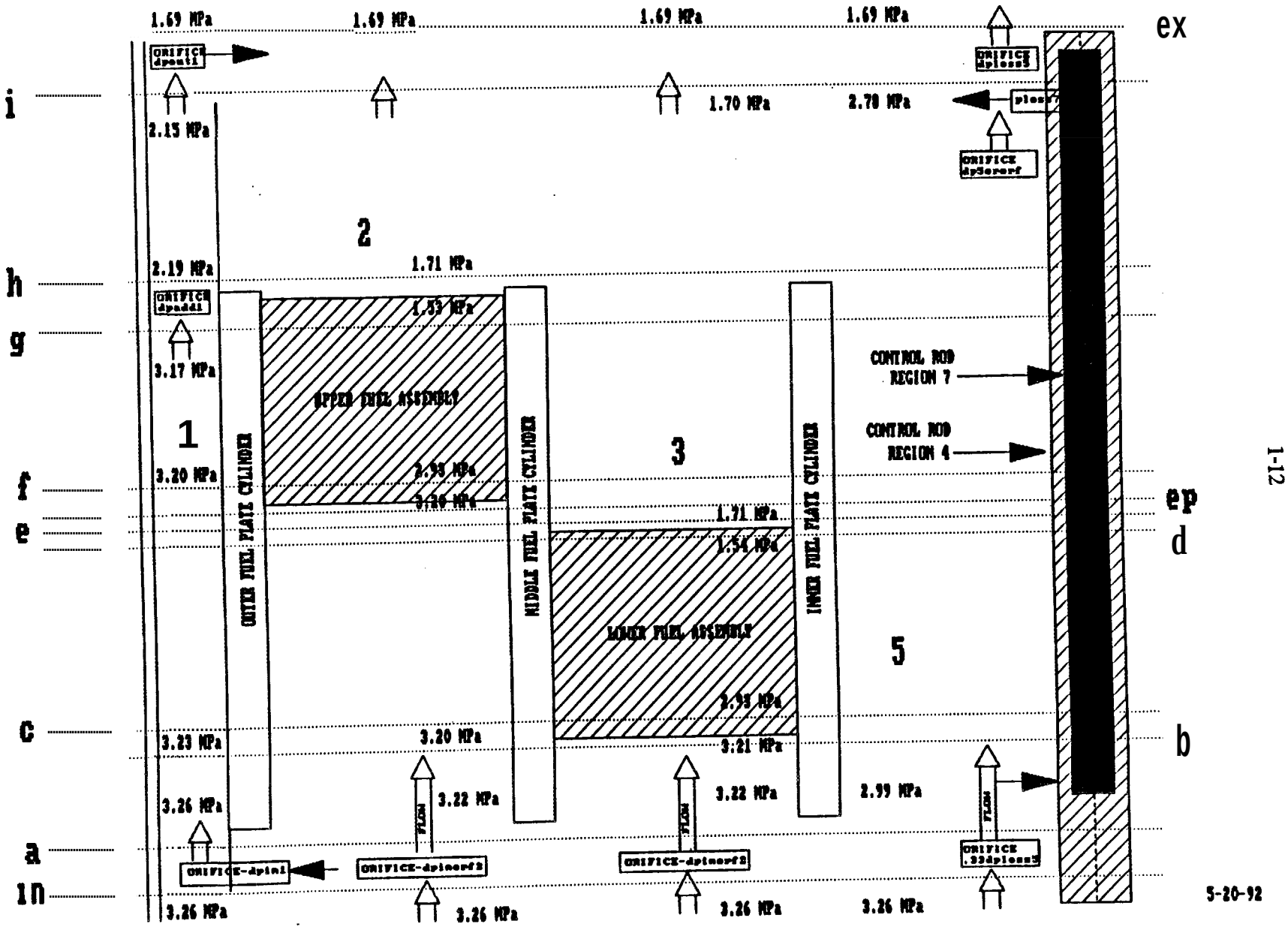

Fig. 1.8. TK Solver flow model diagram with corresponding control volumes,

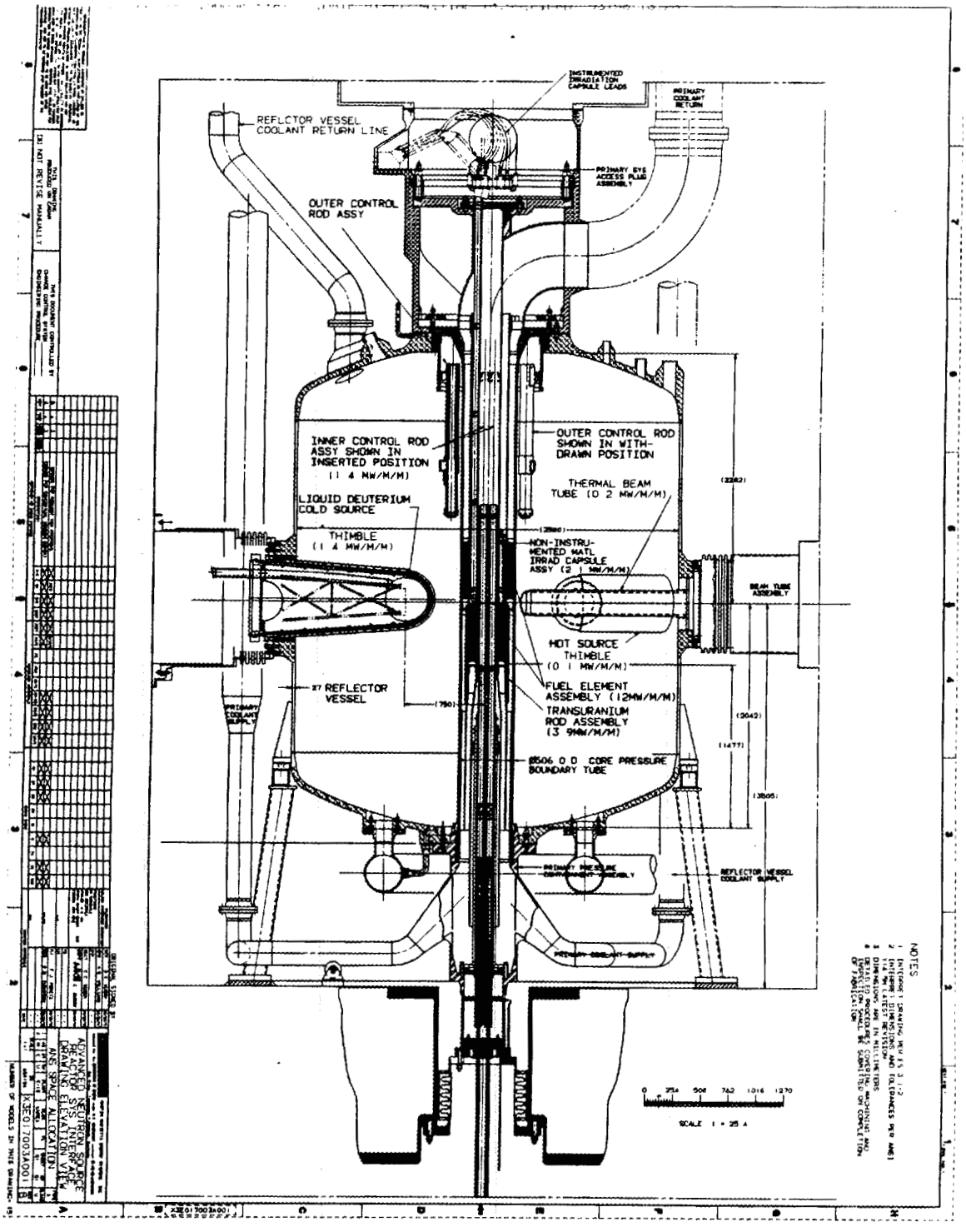

Fig. 1.9. Peak heat fluxes.

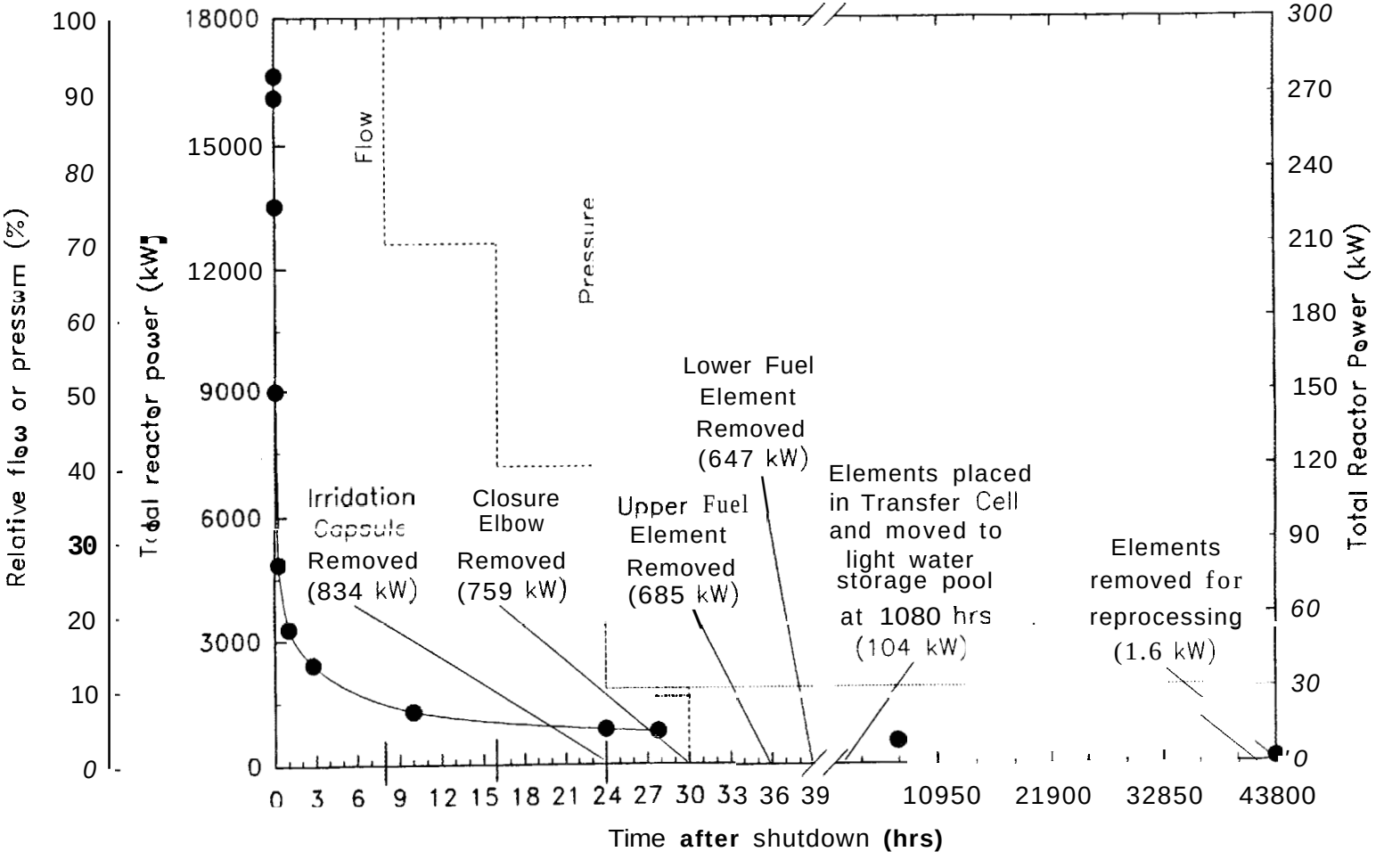

Fig. 1.10. Core heat loads after shutdown.

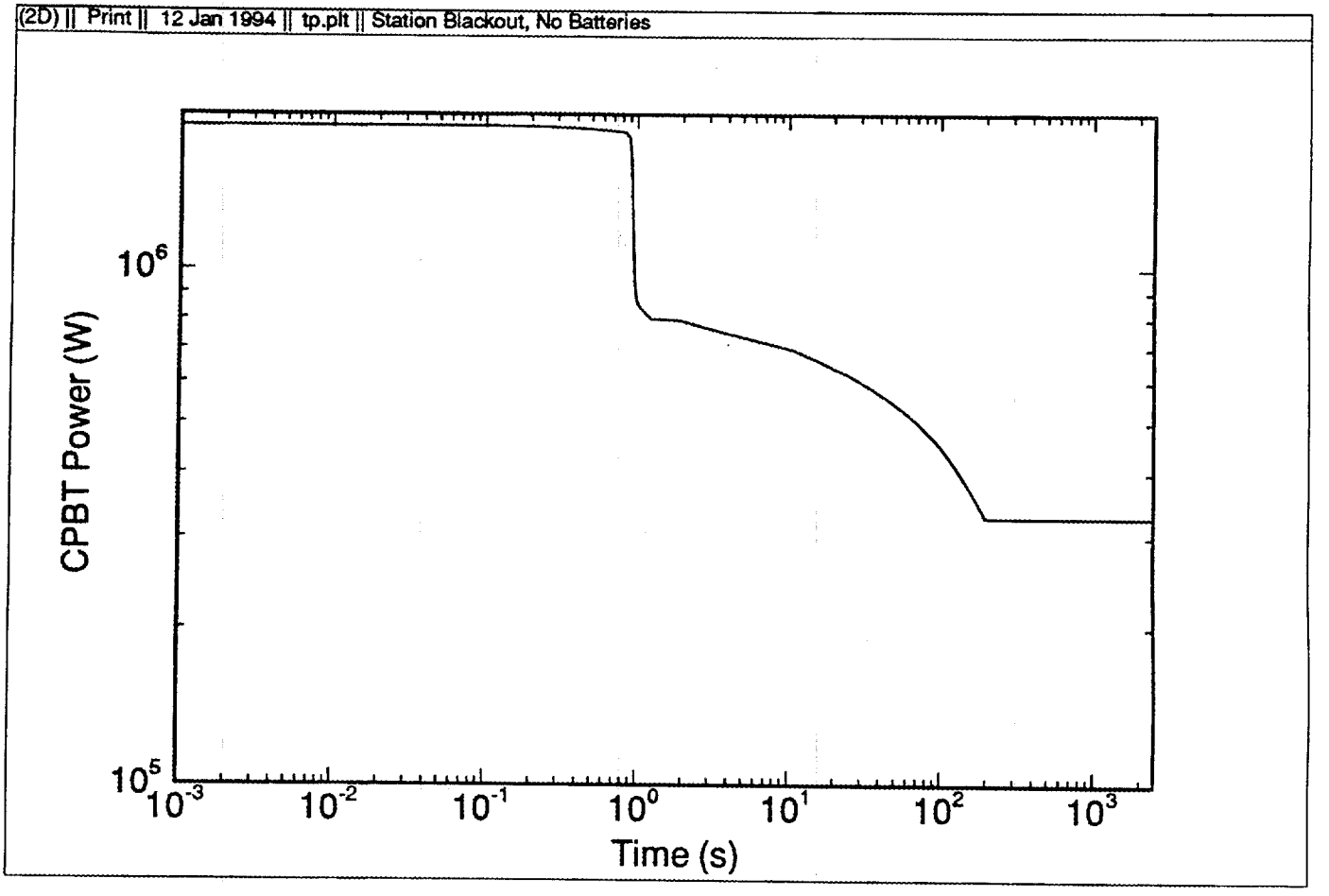

Fig. 1.11. Shutdown power—core pressure boundary tube.

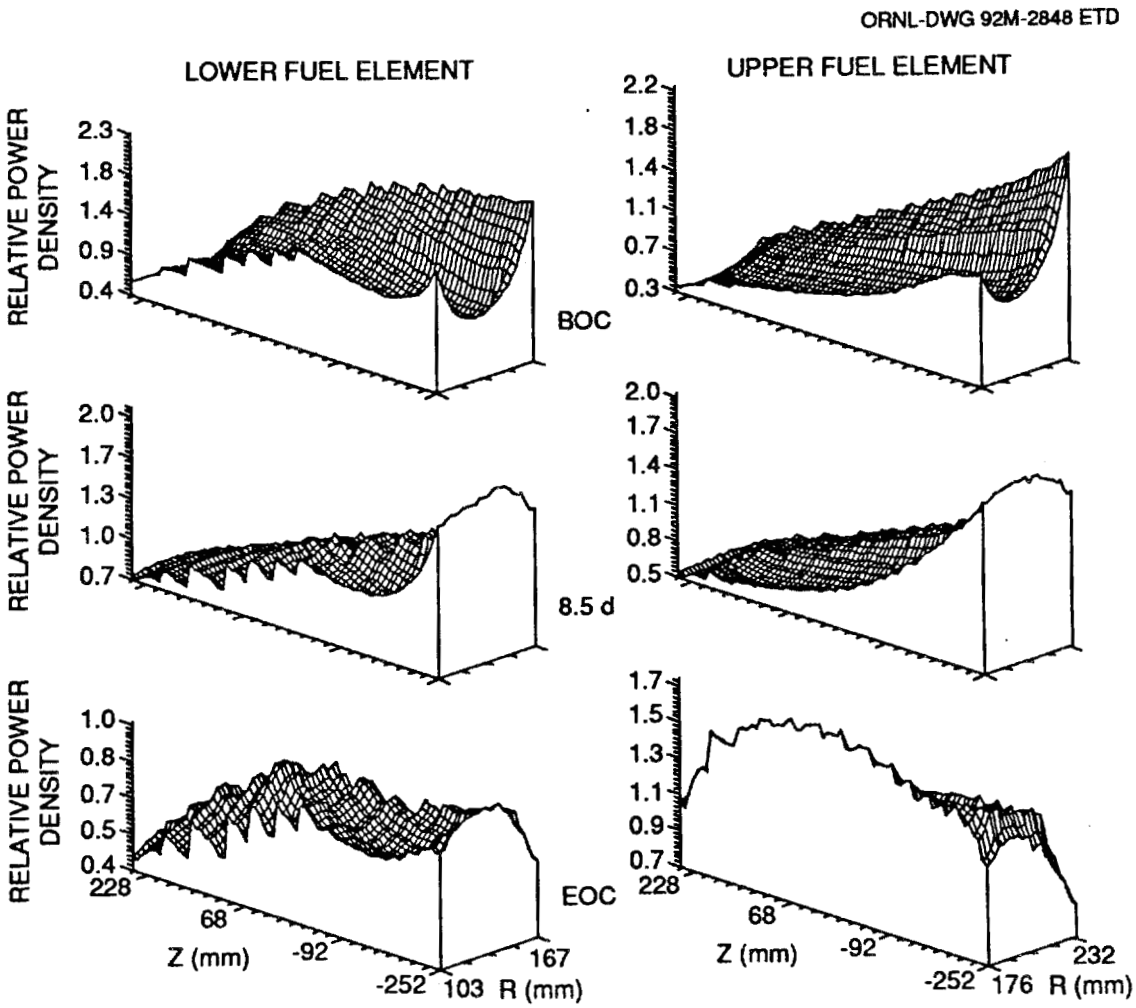

Fig. 1.12. Relative power density profiles for the L7 core design.

1.3 TRIP SIGNALS, SET POINTS, AND TIME DELAYS

Seven separate trip signals from the primary reactor system serve to cause scram of the reactor. These signals are described below.

1. The trip on power-equivalent-flux/flow ratio uses measurement of neutron flux (continuously calibrated to agree with the thermal power) and the coolant flow rate. This measurement is designed to prevent rapid overpower of the reactor. The scram set point for this variable is 115% of nominal. The overall time response of this signal is ~200 ms.
2. A trip is also generated on an excessive rate of change of neutron flux signal. This trip produces shutdown action significantly faster than does flux level for some very fast reactivity transients. A scram signal is generated when the rate of change is >20%/s.
3. A core thermal overpower trip is also included in the safety system. This trip signal is generated when the core thermal power (as defined by the flow rate-core temperature rise product) is 115% above normal. The time response of this signal is ~2 s.
4. A low core outlet pressure trip is activated when the core outlet pressure reaches 80% of nominal. The pressure sensor response has a 30-ms delay.
5. A high inlet temperature signal (defined as 120% of the nominal value) on any one of the three active coolant loops also initiates a scram signal. The time response of the temperature sensors is <2 s.
6. Low coolant flow rate (a tentative level has been set at <80% of nominal) also generates a reactor trip. This measurement has a time response of <1 s.
7. High fission product activity within the primary system also serves to trip the reactor. If the fission product levels exceed 150% of background, the scram signal is generated. The time response of this sensor is <2 s.

Other trip signals are also included in the safety system. These include trips generated by off-normal conditions in some of the reflector tank components or experimental facilities as well as seismic-activity trips. A detailed discussion of the safety shutdown system is presented in the conceptual safety analysis report (CSAR).

In addition to the response times discussed above, additional delays are caused by electronic processing (<5 ms) and the central control rod scram latch release mechanism (<25 ms). The control rods insert a minimum of $1 negative reactivity in 70 ms. This reactivity insertion rate requires two of the three central rods functioning (if the rod positions are initially at the minimum reactivity worth location). The full stroke insertion time of the central control rods is a maximum of 250 ms from any starting position.

The independent, outer shutdown rod system is located in the reflector tank region; each of the eight rods is in a withdrawn position under normal operation to avoid perturbing the neutron flux. This positioning places the rods in a region of relatively low differential reactivity and requires high accelerations and a large insertion movement to counteract transients.

1.4 DESIGN BASES AND ACCEPTANCE CRITERIA

Five criteria must be met to ensure adequate cooling of the reactor core. Together, these criteria constitute the acceptable fuel design limits defined in 10 CFR 50, Appendix A. The operational envelope addressed by these criteria includes steady-state or anticipated transient operation to any condition allowed by the reactor protection system. The criteria are enumerated below.

1. Heat flux from the fuel plates must not exceed the critical heat flux (CHF) or flow excursion (FE) limits, beyond which steam blanketing is possible. Should steam blanketing occur, this criterion must be met at a very high nonexceedance probability level because of the likelihood of fuel damage. A probability level of 99.9% is used for normal operation and anticipated events, while 95% is used for unlikely events.
2. Maximum fuel temperature for normal operation must remain below 400°C throughout the fuel cycle to prevent fission gas swelling of the fuel meat with accompanying reduction in plate-to-plate coolant gap. Short excursions >400°C for off-normal events are acceptable as long as the duration and magnitude are limited to prevent unacceptable fuel swelling.
3. The temperature drop across the oxide film on the fuel plates must remain <119°C during normal operation and anticipated events to prevent oxide spallation.
4. The inlet coolant velocity within the fuel plates must be limited to maintain fuel plate stability. The nominal design velocity of 25 m/s was established by applying uncertainties and margins to the limiting velocity (47 m/s). Criteria 2–4 are applied at a 95% nonexceedance probability level. (A 95% confidence level on the determination of nonexceedance probability was applied to both 95 and 99.9% probability levels.)
5. The temperature of all internal structures and components must be limited appropriately. For example, aluminum temperatures in components with structural responsibility must be maintained below 149°C.[1]

Two additional auxiliary design basis criteria have been established—one for normal operation and one for design basis rupture of the outer boundary of the double-walled CPBT. The first requires that, during normal operation (including minor variations from nominal conditions), no boiling shall occur at any point within the core. Operational benefits accrue from the no-boiling criterion because any detection of boiling may be interpreted as an indicator of abnormal operation that might benefit from automatic or manual intervention.

The other auxiliary design basis criterion is that the inner boundary of the dual-boundary CPBT must be maintained in compression during normal operation. If this is accomplished, there is no possibility for cracks to grow in the inner CPBT; in the event of a design basis rupture of the outer CPBT, the inner CPBT would be able to withstand primary coolant pressure during the ensuing blowdown. The compressive force on the inner CPBT during normal operation is determined by orifices in the core bypass path.

2. CODES AND MODELS USED TO DEVELOP THE THERMAL-HYDRAULIC DESIGN

This report documents only the codes and calculations used to design and evaluate normal operation, and some anticipated events. Other calculations[2-5] have been used to examine the transient T/H response of the reactor. The statistical methodology discussed here, however, covers both the methodology used in the codes and calculations documented in this report, as well as the transient calculations in the references cited above.

2.1 CORE REGION TURBULENT FORCED CONVECTION

A steady-state T/H code, TASHA (Thermal Analysis of Steady-State Heat Transfer for ANS) has been developed to perform core T/H design. The code is based upon an existing one developed in support of the HFIR.[6,7] Space- and time-dependent relative power density profiles, generated with detailed two-dimensional (2-D) (r,z) neutronics calculations, are used as input to this code. TASHA is designed to calculate maximum allowable powers using user selectable limiting criteria of maximum centerline temperature, maximum oxide temperature drop, incipient boiling (IB), CHF, and FE. Although the code includes two-phase limits, such as FE and CHF, the convective calculational capabilities (i.e., heat transfer coefficient and friction factors) are limited to single-phase conditions.

In the analysis, the radial coordinate within each fuel element (and the relative power density profile) is translated into the spanwise direction (along the arc length of the fuel plate). Coolant channels are then assumed to be bounded by flat plates with a width equal to the fuel plate span. Three separate channel types are analyzed—one with an average coolant gap, one with a minimum coolant gap, and one with the maximum allowable coolant gap.

Each channel is split into spanwise subchannels and axial cells forming a grid on the fuel plate (see Fig. 2.1 for a diagram and the equations solved). An energy balance and dynamic and frictional pressure gradients are calculated across each axial cell. Mass flow through each subchannel is iteratively solved by forcing the overall pressure drop across each subchannel to be equal to the specified core pressure drop. Losses resulting from entrance and exit effects are accommodated in the code using standard loss coefficients, while frictional pressure drop is calculated using a friction factor correlation. All appropriate property values are assumed to vary with temperature along the channel. Correlations for the properties of both light and heavy water have been developed and their errors quantified in ref. 8.

Each cell within the grid has an associated local relative power density within the fuel plate that is calculated via neutronics considerations. A forced convection heat transfer correlation is used to determine the local water/oxide interface temperature. Temperatures at the interfaces between the oxide and fuel clad, and the fuel clad and meat, along with the fuel centerline temperature are then calculated from their thermal properties with a one-dimensional (1-D) conduction model.

As described in Sect. 4.5.2, off-line 2-D conduction analyses have been performed to evaluate temperature and heat flux distributions around fuel defects for which more detailed modeling is required. These calculations will be used to "tune" (or replace) the 1-D model in TASHA and to provide the capability to predict limiting fuel plate temperatures accurately. Heat flux peaking resulting from fuel defects is specified in TASHA based on the 2-D analyses.

A significant number of revisions have been made to the original HFIR code, both to perform Monte Carlo uncertainty analysis and to update and to add thermal limit criteria for ANS design purposes.

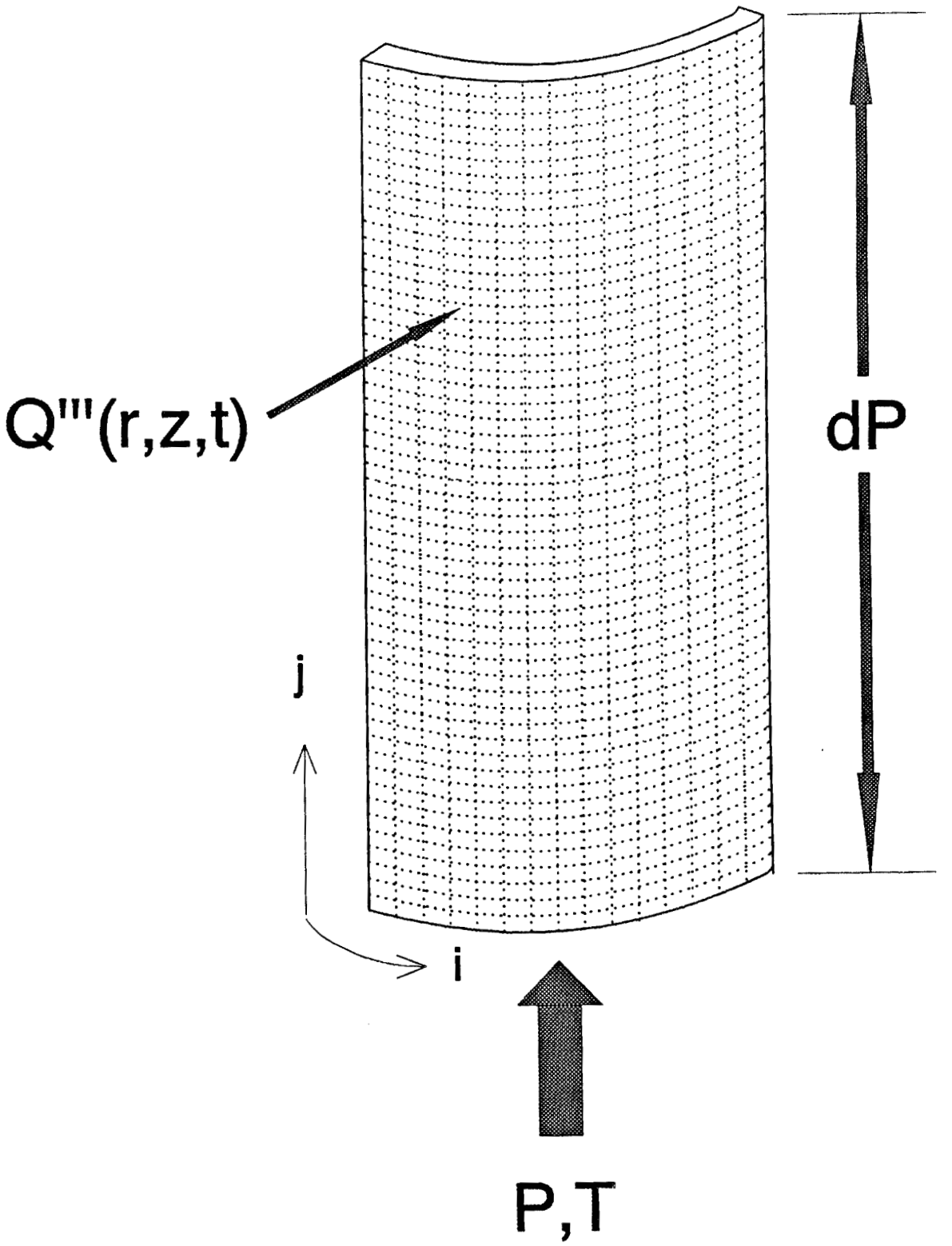

Fig. 2.1. Fuel plate grid geometry.

The series of correlations that are discussed in Sect. 3 were incorporated in the code by replacing existing correlations (exceptions noted below). Additional modifications include changes to the code logic, the addition of several new thermal limit criteria, and changes to allow basing oxide growth on the calculated maximum power, if desired.

The HFIR code was modified to include additional thermal limits based on fuel centerline temperature, oxide temperature drop (the onset of spallation), plate surface temperature less than the saturation temperature, and FE. Any number of these constraints can be used with or without the CHF or IB limits used in the HFIR versions of the code to calculate the core power limit. Maximum allowable centerline temperature and oxide temperature drop are now input to the code.

Two FE correlations have been installed in the code—one from Costa described in Sect. 3, which is the correlation presently used for design, and the Moritz[9] correlation, which is incorporated into the code for comparison purposes. The user may select either correlation. The Moritz correlation is formulated as:

$$q''_{Moritz} = \frac{9.995 \times 10^2 \, V \, (T_{sat} - T_b)}{(21.2 + 0.7708V)} \quad , \tag{2.1}$$

where

q''_{Moritz} = local heat flux (kW/m^2),
V = coolant velocity (m/s),
T_{sat} = saturation temperature (K),
T_b = bulk coolant temperature (K);

while the Costa correlation as used by ANS is:

$$q''_{Costa} = \frac{V^{1/2} \, (T_{sat,ex} - T_b)}{0.0128} \quad , \tag{2.2}$$

where

q''_{Costa} = local flow excursion heat flux (kW/m^2),
V = coolant velocity (m/s),
$T_{sat,ex}$ = saturated exit temperature (K),
T_b = bulk coolant temperature (K).

Either of these correlations can be selected for use where the calculated heat flux is compared to the hot streak or hot spot value at the user's option.

The code was also modified to enable calculation of an oxide film thickness that is "consistent" with the calculated maximum power (i.e., the oxide thickness is calculated based on the maximum power). This calculation provides a realistic estimate of the true maximum nominal (continuous) power level without exceeding the centerline temperature limit or spallation criteria. When the calculated maximum power is above nominal and the interest is in brief power excursion

margins or simply the margin from nominal conditions to the maximum power, this option should not be used.

The oxide growth rate correlation discussed in Sect. 3 was added to the code so that the user can select either the Griess correlation (originally in the HFIR code as given below) or the ANS Correlation I (Eqs. 2.4 and 2.5). The Griess correlation is:

$$x_t = 11252\ U9\ t^{0.778} \exp\ [-4600/(T_{x/c} + 273)] \quad , \tag{2.3}$$

where

x_t = oxide thickness at time t (μm),
$U9$ = the uncertainty factor for the oxide correlation (unitless),
t = time (h),
$T_{x/c}$ = oxide coolant interface temperature (K).

The ANS Correlation I is defined as:

$$x_t = U9(x_o^{1.351} + 1.351 \cdot k_t \cdot t)^{0.74} \quad , \tag{2.4}$$

where

x_t = oxide thickness at time t (μm),
$U9$ = the uncertainty factor for the oxide correlation,
x_o = oxide thickness at t = 0 (μm),
k_t = $6.992 \times 10^5 \exp\ [-7592/(T_c - 10\phi)]$ $\mu m^{1.351}/h$ [with T_c = bulk coolant temperature (K) and ϕ = local heat flux ($\mu W/m^2$)],
t = time (h).

A similar user selectable friction factor option was also incorporated. The two friction factor correlations in the TASHA code are the HFIR friction factor correlation (also in the original HFIR code)

$$f = F/Re^{0.2} \quad , \tag{2.5}$$

where

f = friction factor,
F = constant,
Re = Reynolds number;

and the Filonenko correlation:

$$f_D = \frac{[\,1.0875 - 0.1125\ (b/s)\,]}{(\,1.82\ \log_{10} Re_b - 1.64\,)^2} \left[\frac{7 - (\mu_b/\mu_w)}{6}\right], \tag{2.6}$$

where

f_D = friction factor (Darcy formulation),
b = gap of a rectangular channel or annulus (m),
s = span of a rectangular channel (m),
μ_b = bulk dynamic viscosity (Pa • s),
μ_w = wall dynamic viscosity (Pa • s),
Re_b = bulk coolant Reynolds number.

Other modifications to the HFIR code are described below.

1. In some cases, convergence problems occurred in calculating the wall temperature, $T_{x/c}$, using the Weatherhead correlation during a maximum core power search. The cause was a high guess (try) of the core power, which caused the calculated bulk coolant temperature, T_b, to be higher than the saturation temperature, T_{sat}, and resulted in a negative calculated CHF. This problem was fixed by checking to ensure the calculated CHF was >0, and, if not, it was set to 0. Checking the CHF allows the maximum core power search to continue and the valid maximum power to be determined. In addition, a check on the number of iterations used to calculate $T_{x/c}$ was implemented, and, if the number exceeded 100, the calculation was terminated and an error message written.

2. It was found for some cases that the code can converge to a maximum power that has subchannel(s) with exit temperatures greater than the saturation temperature. Since the code only accounts for single-phase flow, this is an erroneous solution. A new power limit flag was implemented to prevent such erroneous solutions.

3. During the investigation of the problem described in item 1, it was found that the convergence algorithm for core maximum power was not working properly (nonconverging oscillations) in some cases when CHF was limiting. For this limiting phenomenon, the Newton-Raphson method, which had been used, was replaced by a simple method that estimates the new maximum core power as the average of the previous and current estimates.

4. Revisions were made with regard to the treatment of hot streak uncertainties (see Sect. 4.2). The code was revised to allow unique integrated hot streak uncertainty factors for each axial position in the fuel element mesh. These factors are contained in an array. This array is normally divided into only two regions, each of which uses only one value for the factor [e.g., one for the entrance (lower half of each fuel element) region of the core and one for the exit (upper half of each fuel element) region]. The exit valve was developed by appropriately averaging "local" ($\sim$1.27 cm length), potentially above nominal fuel loadings (as high as +10%) along the entrance half of the fuel element. These factors are then used to account for hot streak uncertainties in the bulk coolant temperature. A different "hot streak" uncertainty factor is used in determining the oxide buildup and for evaluating FE limits. Since these phenomena can be limiting on a local basis, it is not conservative to use "length-averaged" values contained in the array. Thus, the code was revised so

that hot streak uncertainties are accounted for on both an "integrated" (bulk coolant temperature) and local (heat flux) basis. Additional changes were made with respect to the hot streak in the manner in which the fuel element temperature rise is calculated. The temperature rise is used to calculate the average channel temperature for the purpose of calculating coolant physical properties. Previously, the temperature rise was calculated based on an average of appropriate array values; it is now based on the exit array value. This calculational change is important because the limiting condition is generally near the exit, and since it will lead to a lower (and therefore conservative) calculated coolant velocity at locations away from the exit.

5. The code was revised to allow analysis of HFIR thereby providing a better code for HFIR analysis since the TASHA code contains correlations more appropriate to HFIR (i.e., Gambill/ Weatherhead CHF, modified Filonenko friction factor, and Petukhov forced convection heat transfer correlations). The code also allows the analysis of HFIR with the additional thermal limits provided. With the code, HFIR safety margins can be better estimated for comparison to those desired and eventually achieved for the ANSR. The HFIR option can be selected in the input field along with specification of the correct coolant. With this option, HFIR specific fuel deflection analysis and nonbond treatment are also invoked. Note that when the latter is invoked, the localized fuel nonhomogeneity factor is appropriately combined with nonbond effects (modeled with "hardwired" correlations) to provide a net hot spot peaking factor that accounts for variations in fuel meat thickness and in the forced convection heat transfer coefficient. For the purpose of evaluating nominal conditions in HFIR (i.e., "no uncertainties" calculations), the input can be altered so that this "hardwired" uncertainty treatment is bypassed. A corresponding nonbond model for ANSR has not yet been developed. Currently, this model is intended to employ a tighter nonbond inspection criterion for ANSR fuel plates than used for HFIR, thereby reducing the impact of nonbonds on ANSR performance. However, the impact of nonbonds will not be insignificant and will need to be accounted for, possibly with ANSR specific correlations as performed for HFIR. The combined effect of localized fuel nonhomogeneity and nonbonds is currently accounted for by evaluating their net effect off-line (in separate calculations) and then using this result (peaking factor) as input for the localized fuel nonhomogeneity factor.

The HFIR core code calculates the maximum achievable core power based on the most limiting location in the core that could be in either fuel element. This is the proper approach when worst case uncertainty assumptions are made. However, for Monte Carlo uncertainty analysis, limiting conditions for sample fuel plates are needed to determine the probability distribution characterizing the core maximum power if sampling is performed on a plate level.

The selection of an appropriate sampling strategy (i.e., plate, core, or combination) has not been made. If plate level sampling is used, then, in order to determine the core power distribution, the power distributions for plates in the upper and lower core must be determined. These two plate distributions can then be statistically combined to produce the core distribution. In this combination, consideration of the number of plates in each element is required.

Thus, with the requirements described above, it was necessary to modify the code to calculate power limits based on sample plates in both fuel elements **separately**. In addition, the code was modified to determine the maximum power limit for plates in each element throughout the fuel cycle. Then, again for plates in each element, the most limiting power calculated during the cycle is used to establish the maximum power limit. Alternatively, at the user's option, the code can also be executed using the original core limiting method (i.e., for sampling on a core level). In this case, the "worst" plate in either fuel element establishes the power limit. Additionally, as with the plate limiting method, the most limiting power calculated during the cycle is used to establish the maximum power limit.

The application of the hot streak uncertainty to the FE limit as discussed in item 4 is based on phenomenological considerations. The phenomenon of FE in a parallel channel configuration (as in the ANSR) occurs because of the pressure drop flow rate characteristics of two-phase flows. Because of additional flow resistance caused by void formation within a heated channel in excess of the single-phase flow resistance, the pressure drop/flow rate curve (for constant heat addition) has a region of negative slope where a slight decrease in mass flux within the channel causes an increase in pressure drop. This region of operation is unstable and could result in flow redistribution between the parallel channels leading to flow starvation, causing the fuel plate to overheat and eventually melt.

Because this phenomenon requires a certain amount of boiling (or two-phase flow) to exist within the channel before it can develop, a certain boiling length (as yet undetermined) would be required to initiate FE. In addition, because FE is typically applied to a single coolant channel, a certain width of channel must be affected before FE can initiate on a channel basis. For these reasons, the local hot streak factor has been applied to the local heat flux when evaluating the FE limit. This factor includes the possibility of having 10% excess fuel loading over a region 12.7-mm long and 2-mm wide. It is presently expected that this assumption will be conservative since the pressure drop imposed by boiling over this small region of the fuel plate would be small compared to the overall pressure drop within the channel. This assumption will be verified analytically and via planned experimentation as the project progresses. A detailed discussion of all of the factors entering into the uncertainty factor applied to the FE limit is presented in Sect. 4.

Currently, a fuel segregation/nonbond factor is applied to the local heat flux when evaluating the CHF and IB limits. This factor includes a component accounting for a 2-mm diam spot that can contain 20% excess fuel loading (or fuel segregation) and a factor that accounts for the possibility of a nonmetallurgical bond of 1-mm diam occurring between the fuel and the aluminum. (This nonbond is described more fully in Sect. 4.). These limits are enforced by the fuel inspection techniques discussed in Sect. 4.2. The two factors—fuel segregation and nonbond—combine to cause a localized, high heat flux region on the fuel plate. This treatment therefore assumes that the CHF limit is a local phenomenon. In fact, CHF limits for localized hot spots are generally much higher than those predicted using correlations developed for average channel conditions (as is the correlation used in this analysis), and this assumption should therefore lead to conservative results. The magnitude of the effect of the hot spot on the CHF limit will be addressed experimentally as the project progresses.

2.2 CORE REGION LAMINAR FORCED CONVECTION AND NATURAL CIRCULATION

Natural circulation calculations while the core is contained within the primary circulation loop have been performed using transient T/H codes. These calculations have been reported elsewhere[3] and are beyond the scope of this report. However, a brief discussion of natural circulation results with the core in the primary system is presented in Sect. 5. Natural circulation cooling of the core when it is external to the coolant loop and laminar core flow situations have been evaluated using a modified version of the code NATCON.[10] The NATCON code analyzes the steady-state natural convection thermal-hydraulics of plate-type fuel used in many research reactor designs. The code calculates the coolant flow rate and axial temperature distributions within the coolant, at the fuel plate surface, and at the fuel plate centerline. Flow is driven by density differences between the coolant and a surrounding constant temperature coolant pool. The flow velocity is obtained by equating the coolant buoyancy and viscous forces. The code was modified to improve its predictive capabilities by altering and extending both the Nusselt number and friction factor relationships. In addition, physical property subroutines for light water were replaced by heavy water subroutines.

The Nusselt number correlation for an upward vertical flow in a heated rectangular channel proposed by Sudo et al.[11] was used instead of the numerical data from Wibulswas[12] in the original code:

$$Nu = 2.0/(X^*)^{0.3} \quad (for\ 0.0 < X^* < 0.4) \quad , \tag{2.7}$$

where

Nu = the Nusselt number,
X^* = nondimensional length.

The above correlation takes into consideration the thermal entry length, and, for all cases investigated here, X^* remained < 0.4.

The friction factor correlations from Eckert and Irvine[13] were replaced by the following correlations. The correlation for fully developed laminar flow[14] ($Re < 2140$) is:

$$f_F = (23.532/Re)\ (\mu_b/\mu_w)^{-0.32} \quad , \tag{2.8}$$

where

f_F = Fanning friction factor,
Re = Reynolds number,
μ_b/μ_w = viscosity ratio term from Bonilla.[15]

For transitional flow, an interpolation between laminar and turbulent fraction factors is used ($2140 < Re < 4240$):

$$f_F = 0.011\ (\mu_b/\mu_w)^{-0.32} \quad . \tag{2.9}$$

For turbulent flow, the Filonenko[16] friction factor is used (see Sect. 3).

The inlet and exit pressure losses were calculated as half a dynamic head and one dynamic head respectively (based on inlet conditions).

2.3 NONFUEL COMPONENTS

Thermal analysis has been performed on a number of noncore components, including the core side plates, the CPBT, the inner shutdown and control rods, and the outer safety rods. Both 1- and 2-D finite element analyses have been performed. The general procedure at this point in the project has been to begin with hand calculations, proceed to 1-D analysis for initial scoping and sensitivity analysis, and then use 2-D finite element analysis when necessary.

Hand calculations have been effective for many first-cut, scoping type calculations and for checking code results. Because of complex internal heat generation rates, film coefficient correlations, and fluid properties, as well as the requirement for sensitivity studies to evaluate alternate conditions, several computer codes have been incorporated in the analysis. The major codes that have been used to date are TK Solver,[17] Mathcad,[18] PATRAN,[19] and P/THERMAL.[20] Each code is briefly described below.

2.3.1 TK Solver

TK Solver is an equation solving software that runs on several platforms, including DOS, Mac OS, and UNIX. The software is available from Universal Technical Systems, Inc., and is a rule-based programming language that can work directly with a mathematical description of the heat transfer problem without requiring sequencing of the operations to be performed. TK works with two major kinds of objects—rules (or equations) and variables. The following classes of objects are also available: lists of values; functions (built-in or user defined); unit conversions; and plot, table, and format specifications.

The modular nature of TK Solver has been ideal for setting up ANS heat transfer problems. Equations that describe material property correlations, transport properties, and other correlations, such as Reynolds number and convective film coefficient correlations, have been developed as TK functions. Functions are similar to subroutines in FORTRAN. The major difference between functions and FORTRAN subroutines is that the equations do not have to be sequenced. Information, such as heat generation tables, can be read directly into TK and used as table functions. Table functions are called like subroutines and relate empiric or descriptive data. The following is a partial list of the types of functions that have been developed for ANS work:

- D_2O properties (specific heat, conductivity, density, viscosity, saturation temperature),
- H_2O properties (specific heat, conductivity, density, viscosity, saturation temperature),
- forced and natural convection heat transfer coefficients,
- friction factor correlations,
- boiling correlations (incipient boiling, critical heat flux, etc.),
- oxide growth rate correlation, and
- internal heat generation tables for various components.

Each function can be copied into other models like subroutines and used in a modular fashion.

TK models have been developed for a variety of noncore components, but the generalized models can be applied to a variety of components. The following general models have been developed:

- 1-D cylinder with constant internal heat generation and forced or natural convection cooling on both sides;
- 1-D cylinder with linear radially distributed internal heat generation and forced or natural convection on both sides;
- 1-D cylinder with oxide corrosion layers on inner and outer surfaces and constant internal heat generation;
- 1-D cylinder with IB and CHF calculations on the inner and outer surfaces; and
- multisegmented cylinder with axially varying internal heat distribution, energy balance in cooling fluid with calculated bulk temperature used to determine convection coefficients, and varying annular coolant gap geometry.

A sample TK model for CPBT analysis is described below.

The TK model is based on the following assumptions.

- Property values for D_2O are a function of temperature and are based on correlations developed by Crabtree and Siman-Tov.[8]
- The CPBT is assumed to be cooled by forced convection on the core side and by natural convection on the reflector tank side.
- The Petukhov film coefficient correlation (discussed in Sect. 4) is used for core side forced convection film coefficients. The Dittus-Boelter correlation is included as a check and to improve initial convergence.

2.3.2 Heat Generation

The internal heat generation values were based on Idaho National Engineering Laboratory (INEL) generated curves [multiplied by a factor of 1.25 to account for the differences between the beginning-of-cycle (BOC) heating rates and those expected at end-of-cycle (EOC)].[21] In order to use these calculations, the axial stepped values were read off the curves, then entered into a TK list function. The values were then scaled to the required power levels for service levels A and B as follows:

- Service Level A at 355 MW(f) and an inlet cooling temperature of 51°C, and
- Service Level B at 399 MW(f) and an inlet cooling temperature of 55°C.

The heat generation tables were then converted from a mass basis (W/g) to volumetric basis (W/m^3).

2.3.3 Conduction Model

The conduction model was based upon the derivation given by El-Wakil.[22] The following assumptions were made.

- The volumetric heat generation rates were adjusted for a power level of 355–362 MW.
- The CPBT wall thickness was assumed to be 8 mm but can be varied from 8–16 mm.
- The inner gap annulus between the core and CPBT is either 3 or 5 mm depending on the axial location.
- The outer CPBT radius is cooled by natural convection on the reflector tank side.
- The CPBT is assumed to be a cylindrical shell of length 1.78 m.
- Aluminum properties, such as density and conductivity, are assumed to be constant.
- The internal heat generation term is assumed to be constant over the radial distance of the CPBT but can vary over the axial distance.

The steady-state heat conduction equation for a cylinder with constant internal volumetric heat generation is the 1-D Poisson equation in cylindrical coordinates:

$$\frac{d^2T}{dr^2} + \frac{1}{r}\frac{dT}{dr} + \frac{q'''}{k} = 0 \quad , \tag{2.10}$$

where

T = temperature (K),
q''' = volumetric heat generation rate (kW/m^3),
r = radius (m),
k = thermal conductivity (kW/m • K).

The solution of this differential equation is:

$$T = -q'''\frac{r^2}{4k} + C_1 \ln r + C_2 \quad , \tag{2.11}$$

where

T = temperature (K),
q''' = volumetric heat generation rate (kW/m^3),
r = radius (m),
k = thermal conductivity (kW/m • K),
C_1 = constant of integration,
C_2 = constant of integration.

The constants of integration C_1 and C_2 are evaluated from the boundary conditions for the system: $T = T_i$ at $r = r_i$, and $T = T_o$ at $r = r_o$.

After substituting the boundary conditions and solving for the constants of integration the following expressions are derived:

$$C_1 = \frac{(T_o - T_i) - \frac{q'''}{4k}(r_i^2 - r_o^2)}{\ln\frac{r_o}{r_i}} \quad ,$$

$$C_2 = T_i + q'''\frac{r_i^2}{4k} - C_1 \ln r_i \quad , \tag{2.12}$$

where

T_o = outside temperature (K),
T_i = inside temperature (K),
q''' = volumetric heat generation rate (kW/m^3),
k = thermal conductivity (kW/m · K),
r_i = inside radius (m),
r_o = outside radius (m).

The maximum temperature within the CPBT wall can be determined by setting dT/dr to 0 at $r = r_m$ as follows:

$$\frac{dT}{dr} = -\frac{q'''}{2k} r + \frac{C_1}{r} \quad ,$$

$$0 = -\frac{q'''}{2k} r_m + \frac{C_1}{r_m} \quad , \tag{2.13}$$

$$r_m^2 = 2\frac{k}{q'''} C_1 \quad ;$$

where

T = temperature (K),
r = radius (m),
q''' = volumetric heat generation rate (kW/m^3),
k = thermal conductivity (kW/m · K),
C_1 = constant of integration from Eq. (2.12),
r_m = maximum radius (m).

The surface heat flux can be calculated from the Fourier equation as follows:

$$q = -kA \frac{dT}{dr} \quad ,$$

and (2.14)

$$\frac{dT}{dr} = -\frac{q'''}{2k} r + \frac{C_1}{r} \quad ;$$

where

q = surface heat flux (kW/m^2),
k = thermal conductivity (kW/m^3),
A = area (m^2),
T = temperature (K),
r = radius (m),
q''' = volumetric heat generation rate (kW/m^3),
C_1 = constant of integration from Eq. (2.13).

Substituting for the inside and outside radii gives the following expressions:

$$Q_i = -kA_i\left(-\frac{q'''}{2k}\,r_i + \frac{C_1}{r_i}\right) , \tag{2.15}$$

and

$$Q_o = -kA_o\left(-\frac{q'''}{2k}\,r_o + \frac{C_1}{r_o}\right) ;$$

where

Q_i = inside heat flow (kW),
k = thermal conductivity (kW/m^3),
A_i = inside area (m^2),
q''' = volumetric heat generation rate, (kW/m^3),
C_1 = constant of integration from Eq. (2.13),
r_i = inside radius (m),
Q_o = outside heat flow (kW),
A_o = outside area (m^2),
r_o = outside radius (m).

2.3.4 Convection Model

The heat transferred to the coolant can be expressed as:

$$Q = h_{FC}\,A(T_w - T_b) , \tag{2.16}$$

where

Q = heat flow (kW),
h_{FC} = forced-convection heat transfer coefficient (kW/m^2 · K),
A = area (m^2),

T_w = wall temperature (K),
T_b = bulk coolant temperature (K).

For the outside and inside surfaces of the CPBT the following expressions apply:

$$Q_o = h_{FC,o} A_o (T_o - T_{b,o}) \quad ,$$

and

$$Q_i = h_{FC,i} A_i (T_i - T_{b,i}) \quad ; \tag{2.17}$$

where

Q_o = outside heat flow (kW),
$h_{FC,o}$ = forced-convection heat transfer coefficient, outside (kW/m^2 · K),
A_o = outside area (m^2),
T_o = outside temperature (K),
$T_{b,o}$ = outside bulk temperature (K),
Q_i = inside heat flow (kW),
$h_{FC,i}$ = forced-convection heat transfer coefficient, inside (kW/m^2 · K),
A_i = inside area (m^2),
T_i = inside temperature (K),
$T_{b,i}$ = inside bulk coolant temperature (K).

2.3.5 Heat Transfer Film Coefficient

The single-phase turbulent Nusselt number relationship for the inside surface of the CPBT model is discussed in Sect. 3.

2.3.6 Heat Balance

The heat balance on the inner channel between the core side plate and CPBT is expressed as follows:

$$Q_{tot} = \rho \, V \, C_p \, (T_{ex} - T_i) \quad , \tag{2.18}$$

where

Q_{tot} = total heat flow (kW),
ρ = coolant density (kg/m^3),
V = coolant velocity (m/s),
C_p = mean coolant specific heat (kJ/kg • K),
T_{ex} = exit temperature (K),
T_i = inlet temperature (K).

For this analysis, it was assumed that all of the heat generated in the core side plate would be deposited in the coolant annulus between the side plate and CPBT according to the following energy balance:

$$Q_{tot} = Q_{sp} + Q_i \quad , \tag{2.19}$$

where

Q_{tot} = total heat flow (kW),
Q_{sp} = side plate heat flow (kW),
Q_i = inlet heat flow (kW).

2.3.7 Corrosion Layer

The aluminum oxide corrosion layer was assumed to follow the Kritz[23] correlation, which was developed under low heat flux conditions:

$$x = 6.531 \cdot q'' \cdot t^{0.778} e^{(-1880.0/T_{xc})} \quad , \tag{2.20}$$

where

x = oxide thickness (μm),
q'' = local heat flux (kW/m^2),
t = 8736 h (1 year of operation),
e = 2.71828,
T_{xc} = oxide coolant interface temperature (K).

2.3.8 Model Setup and Execution

The TK Solver model calculates the surface and maximum temperatures within a cylindrical shell with constant internal heat generation. The energy balance determines the outlet coolant temperature in the shell segment with a given inlet temperature. Since the internal heat generation rates depend on the axial distance from the core midplane, the CPBT model was broken into 100 cylindrical elements starting at the lower seal area to an area 586-mm above the core midplane. The top and bottom distances and the number of axial segments are input into the model. A setup function is then run that builds tables of the heat generation vs axial position interpolating values from the INEL tables. The setup function then adjusts the power level for the service condition and calculates the velocity in the CPBT/side plate annulus based on the appropriate coolant channel gap. Lists are then generated for the velocity, area, and hydraulic diameter for each segment.

The TK Solver program solves simultaneous equations with a modified Newton method. It requires initial guesses for some variables. For the CPBT model, the following variables were assigned initial guess values:

- T_{bs}, the average bulk coolant temperature;
- T_i, the inside CPBT surface temperature;

- $T_{s/x}$, inside surface temperature of oxide layer; and
- $T_{x/c}$, oxide/coolant interface.

In the list solve mode, the equations are solved in a function named "IF SOLVED." This function determines if every equation has been solved and then calls a "switch" function. The switch function saves the element number that has just been solved and places the exit temperature of this element into the inlet temperature array for the next element. This continues for all 100 elements, providing a running energy balance on the coolant flow. The calculated average bulk temperature is, in turn, used to determine the fluid properties and the film coefficients.

2.3.9 Mathcad

Mathcad is an equation solving software package developed by MathSoft, Inc. This software package allows for the input of equations as they are generally presented. Mathcad has been used as a verification tool for TK Solver models and to evaluate results of finite element models.

2.3.10 PATRAN P/THERMAL

The PATRAN P/THERMAL combination is a finite element analysis code developed by PDA Engineering. PATRAN is the pre- and postprocessing code that is used to create the analysis geometry. Grids, points, lines, 2-D patches and three-dimensional (3-D) hyperpatches can be generated to describe the component geometry. The model can then be meshed with various automatic or manual meshing tools and appropriate boundary conditions, such as surface convection coefficients, and initial conditions, such as internal heat generation rates, can be applied. The geometry is then output in the form of a generic ASCII file called a "neutral file." The neutral file is then converted by P/THERMAL into a resistor capacitor type of network and solved for steady-state or transient temperature distributions. The resulting nodal results file can be read back into PATRAN, and fringe or contour plots of the thermal solution can then be generated.

A number of components have been analyzed with finite element methods. Models include the CPBT, the core side plate, the inner control rod, and the outer control rod. The typical procedure is to build a 2-D geometry of the component with the PATRAN preprocessor. The geometry is then meshed. Material identity numbers are assigned to the geometry and boundary conditions, such as constant coolant temperatures and convection surface boundaries. An input template is then prepared that contains material identification (ID) numbers and convective boundary conditions. Other files are generated that contain the material properties and inputs, such as heat generation rates and coolant velocities. The model is then submitted to the P/THERMAL analysis code for the steady-state solution. P/THERMAL produces a nodal temperature file. This file is read back into PATRAN, and contour or fringe temperature distribution plots are then prepared.

A unique capability of P/THERMAL is the ability to include fluid elements within the finite element geometry. These elements represent the coolant channels. Convective boundary conditions can then be applied to the fluid elements, and convective configurations can be selected from an extensive list of functions. For the ANS work, the heat transfer configuration that calculates film coefficients is based on the Petukhov correlation. The edges of fluid elements can be meshed with advective bar elements. These are special elements that will use an energy balance to determine the bulk fluid temperature as the coolant heats up. The bulk and surface temperature nodes are then used to determine properties and the convective film coefficient.

When a long axial model is built (e.g., the CPBT model), it is desirable to include the axial heat generation profile in the model. PATRAN can include this profile in a number of ways. One method

that has been used for ANS is to generate a 2-D table of heat generation rates vs axial position and then apply it to the PATRAN geometry. PATRAN then determines the centroids of each element, interpolates the table, and assigns a volumetric heating rate to each element.

In PATRAN, geometric models are built, meshed, and then boundary conditions are applied. As each step is performed, a session file is produced including every command that was issued. A 2-D model can contain ~24 commands that describe grid position, lines, 2-D patches, meshing of patches, material identification, and applied boundary conditions. The session file can be input to PATRAN, and the model can be recreated. This capability allows easy modification of input parameters by editing the session file and rerunning it. The effects of changing parameters, such as heat generation rates, materials, and coolant velocities, can be determined by editing the session file, processing it to make a new model, and submitting the model to P/THERMAL for analysis.

Some components, such as the inner and outer control rods, require both an axisymmetric and r/Θ model to provide an adequate analysis of the temperature distribution. Figure 2.2 is a model of one of the recent control rod configurations. The figure shows the material sections of the rod and the constant heat generation rates that were applied. The axisymmetric model has been rotated 180° and shaded to show how the components are connected. Figure 2.3 is the temperature distribution in the completed model. In this particular model, the contact region between the outer Inconel and the aluminum carrier tubes shows an elevated temperature that exceeds the design temperature of the aluminum.

2.3.11 Other Codes

On occasion other codes have been used for verification and checking. These codes include the Advanced Continuous Simulation Language (ACSL).[24] ACSL is a differential equation solver package and was used to evaluate natural circulation for transient shutdown conditions.

HEATING 7[25] is another finite difference code that has been used for verification of P/THERMAL results. The HEATING 7 code was developed at ORNL.

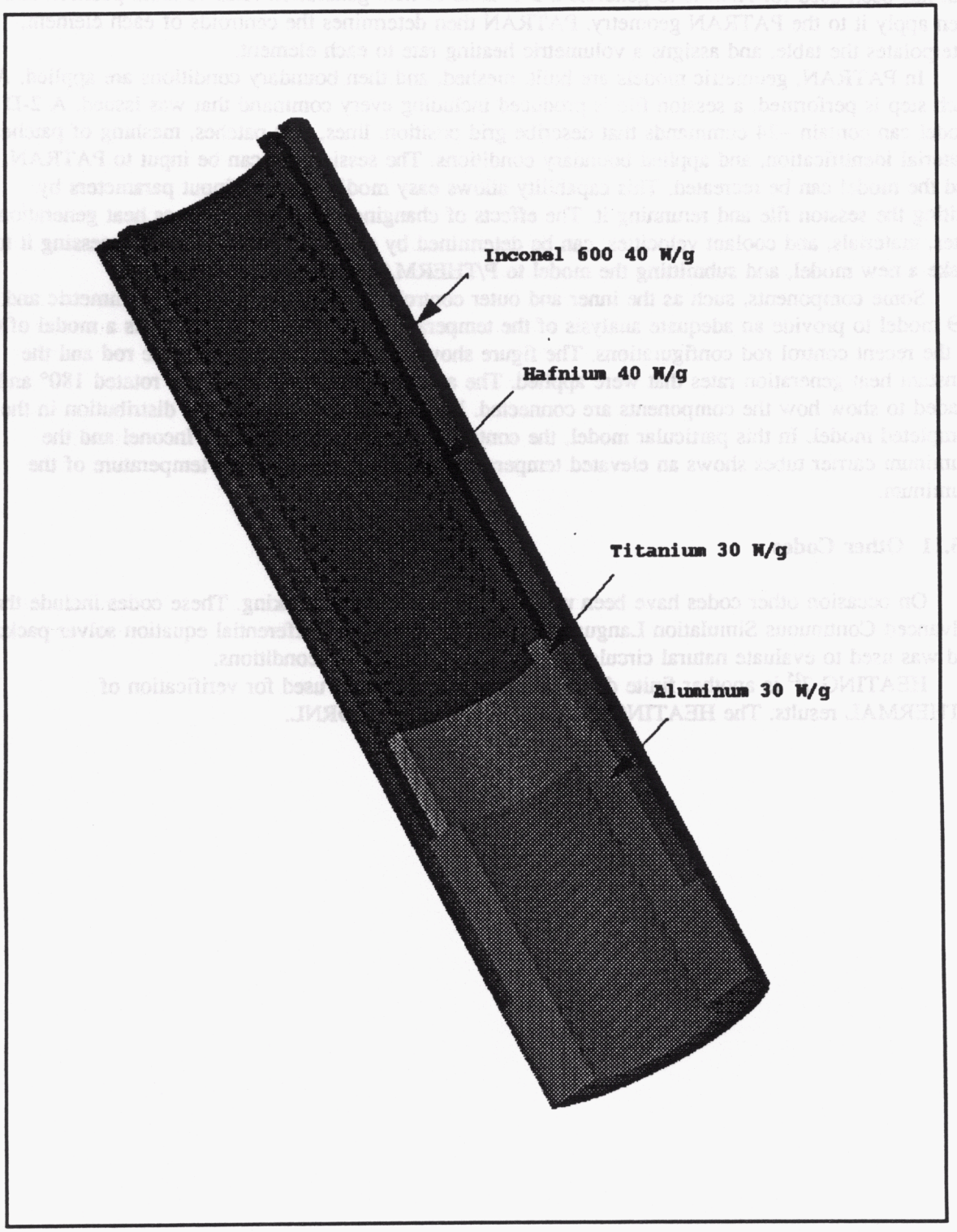

Fig. 2.2. Axisymmetric model of a section of an inner control rod showing materials and heat generation rates.

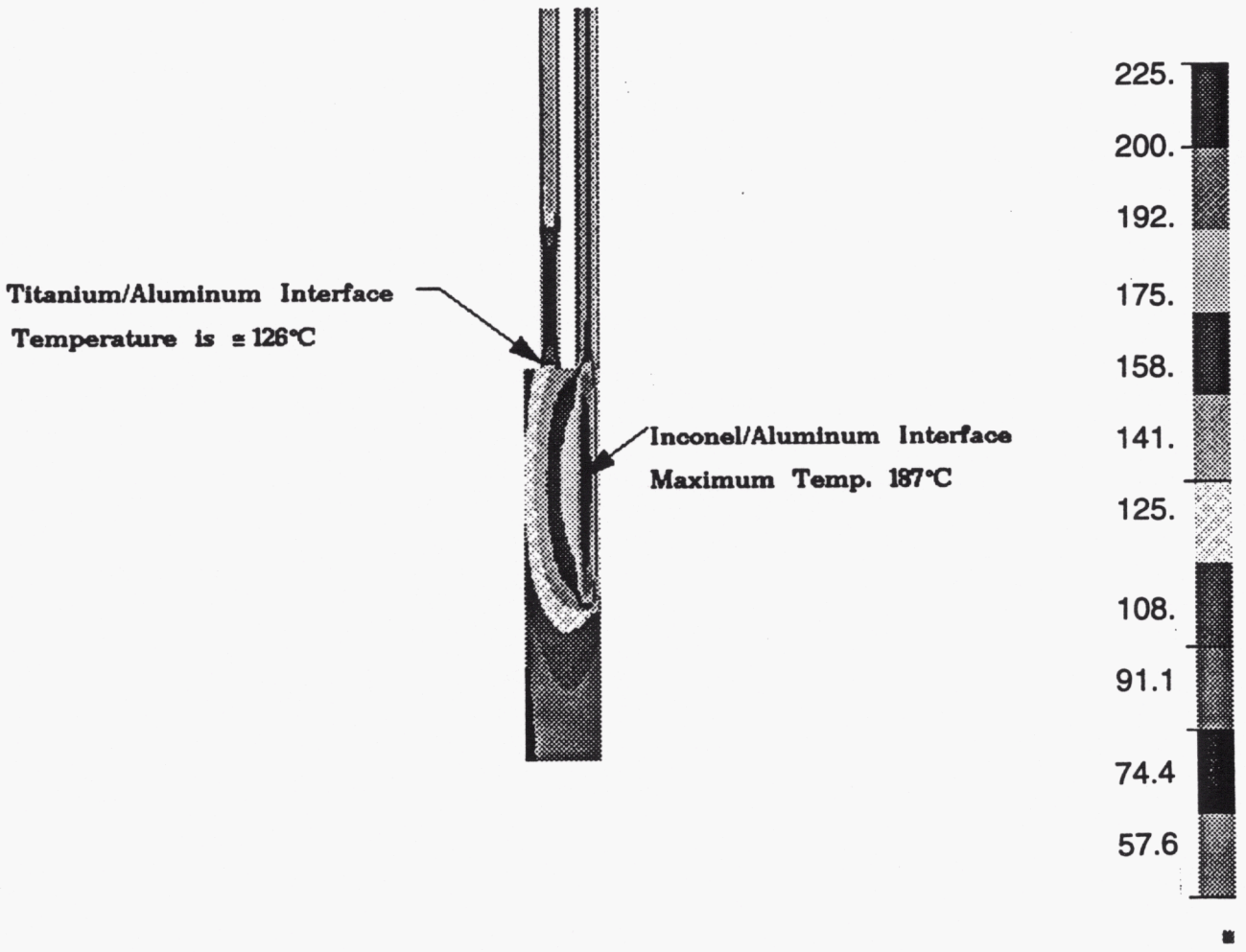

Fig. 2.3. Finite element model of an inner control rod showing temperature distributions in the aluminum/Inconel screwed connection.

3. CORRELATIONS AND PHYSICAL DATA

The T/H correlations and the physical data involved in performing the T/H design of the reactor are listed and described in this section. The basis for this T/H design, including thermal limits, the choice between CHF vs FE as a thermal limit, and the application of these limits, is described in Sects. 2 and 6. The statistical uncertainty analysis, including the statistical peaking factor approach, is described in Sect. 4.

3.1 CORRELATION SELECTION

This section describes the T/H correlations currently used for the ANSR T/H nominal steady-state design and analysis. These correlations were initially selected based on literature evaluation and subsequently compared with a data base that was compiled specifically for the ANS range of conditions. Because the ANS T/H design is based on a statistical/probabilistic uncertainty analysis for determining the desired safety margins (see Sect. 4), there was a need to quantify the uncertainties involved through statistical evaluation of the data against a selected number of correlations in each T/H category. This evaluation was performed in a preliminary way based on the correlations and data collected so far and reported in more detail by Siman-Tov et al.[26] Table 3.1 lists the most promising correlations for comparison and evaluation that were selected in each T/H category.

Based on statistical evaluation of the current data base, the mean and standard deviations for each correlation were determined, thus providing the probability distributions and a comparative measure of how well the correlations agree with the data[26] (see Sect. 4.). An extensive data collection and correlation evaluation is still under way to select the best correlations for the ANS conditions and to both minimize and quantify the uncertainties. As part of that effort, an experimental T/H test facility has been built at ORNL to provide data specifically in the ANS range of conditions[27] (see Sect. 5). These improvements will be implemented as the reactor design is being detailed and will be reported accordingly. The following T/H correlations currently in use in the ANSR design and safety analysis are described in this section—Gambill-w/Weatherhead[26,28] for the CHF, Costa[29] for the FE heat flux, Bergles-Rohsenow (B-R)[30] for the IB heat flux, Petukhov[31] for the forced-convection heat transfer coefficient, and Filonenko[16] for the forced-convection friction factor.

3.1.1 Critical Heat Flux

The CHF (or the point of departure from nucleate boiling) is determined based on the Gambill additive CHF correlation,[28] the Weatherhead correlation[32] for CHF wall temperature, and the Petukhov correlation[31] for calculating the forced-convection heat transfer coefficient (see Eq. 3.6). These three correlations are iteratively solved to arrive at the appropriate CHF value and the corresponding wall temperature.

Table 3.1. Promising correlations in each thermal-hydraulic category for comparison and evaluation

Investigator[a]	Value[b]	Investigator[a]	Value[b]
CHF[c] (MW/m²)		**IBHF[f] (MW/m²)**	
Gambill-w/Weatherhead[28,33]	38.18	Bergles and Rohsenow[30]	25.46
Bernath[34] (modified by Oh[35])	51.83	Papell[48]	26.51
Thorgerson[36] (modified by Gambill[33])	57.60	Davis and Anderson[49]	25.85
Labuntsov[37]	*d*	Frost and Dzakowic[50]	26.13
Shitsman[38] (modified by Gambill[33])	*d*	Hino and Ueda[51]	*d*
Bowring[39]	*d*	**FCHTC[g] (kW/m²K)**	
Katto[40]	*d*	Dittus-Boelter[52]	153.8
Weisman and Ileslamlou[41]	*d*	Sieder and Tate[53]	146.2
Komori et al.[42]	*d*	Petukhov[31]	178.9
FEHF[e] (MW/m²)		Hausen[54]	182.3
Bowring[43]	183.17	Gnielinski[55]	167.4
Whittle and Forgan[44]	85.43	**FCFF[h] (unitless)**	
Costa[29]	48.78	Pandtl,[56] von Karman,[57] and Nikuradse[58]	0.015604
Saha and Zuber[45]	95.78	Filonenko[16]	0.015580
Moritz[46]	51.21	Techno et al. [59]	0.015617
Moritz (modified)[47]	77.27	Colebrook[60]	0.014384
		Chen[61]	0.015616

[a]Complete citations are located in Sect. 7.
[b]Calculated values using the Advanced Neutron Source channel exit nominal value.
[c]CHF = critical heat flux.
[d]Correlation not yet programmed in SAS.
[e]FEHF = flow excursion heat flux.
[f]IBHF = incipient boiling heat flux.
[g]FCHTC = forced-convection heat transfer coefficient.
[h]FCFF = forced-convection friction factor.

This combination is designated as the Gambill-w/Weatherhead correlation and is implemented as follows:

$$
\begin{aligned}
q_{CHF} &= q_{pool,sub} + q_{conv,sub} \ , \\
q_{pool,sub} &= 0.18\, h_{lv}\, \rho_v (\sigma g \Delta\rho/\rho_v^2)^{0.25} F_{sub} \ , \\
F_{sub} &= 1 + (\rho_l/\rho_v)^{0.75}\, [C_p \Delta T_{sub}/(9.8\, h_{lv})] \ , \\
q_{conv,sub} &= h_{FC}\, (T_w - T_b) \ ;
\end{aligned}
\tag{3.1}
$$

where

q_{CHF} = critical heat flux (kW/m^2),
$q_{pool,sub}$ = subcooled pool boiling heat flux (kW/m^2),
$q_{conv,sub}$ = subcooled convective heat flux (kW/m^2),
h_{lv} = latent heat of vaporization (kJ/kg),
ρ_v = vapor coolant density (kg/m^3),
σ = surface tension (N/m),
g = acceleration due to gravity (9.81 m/s^2),
$\Delta\rho$ = liquid to vapor density difference (kg/m^3),
F_{sub} = subcooling factor,
ρ_l = density of pure U_3Si_2 (12.2 mg/mm^3),
C_p = mean coolant specific heat (kJ/kg • K),
ΔT_{sub} = subcooling temperature difference (K),
h_{FC} = forced-convection heat transfer correlation (kW/m^2 · K),
T_w = wall temperature (K),
T_b = bulk coolant temperature (K).

In this equation, T_w at the CHF point being calculated by iteration using Weatherhead's correlation[32] for fully developed nucleate boiling of water is calculated as follows:

$$
T_w = [47.7\text{-}0.127\ (T_{sat}\text{-}273.16)]\ (q_{CHF}/3154.6)^{0.25} + T_{sat} \ , \tag{3.2}
$$

where

T_{sat} = saturated temperature (K),
q_{CHF} = critical heat flux (kW/m^2);

and by using the Petukhov correlation[31] for the turbulent forced-convection, nonboiling, heat transfer coefficient in combination with the Filonenko correlation[16] for the Darcy friction factor [see Eqs. (3.6) and (3.7)].

All the physical properties in the boiling term are evaluated at the wall temperature but are not allowed to exceed the saturation temperature, except C_p, which is evaluated at 0.5 (T_{sat} + T_b). For the convective component, all properties are evaluated at the liquid bulk temperature, except μ_w, which is evaluated at the saturation temperature for evaluation of CHF.

The range of applicability of the Gambill-w/Weatherhead correlation as well as comparison of the correlation with other correlations and with data are described in ref. 26. Statistical uncertainties for the correlation are discussed in Sect. 4.

3.1.2 Onset of Flow Excursion (or Static Flow Instability)

The cooling channels in the ANSR fuel assembly are all parallel to each other and share common inlet and outlet plena, which impose a common pressure drop on all of the channels. This flow configuration is subject to FE and/or flow instability, which may occur once boiling is initiated in any one of the channels. The FE phenomenon constitutes a different thermal limit from the stable CHF or departure from nucleate boiling limit. In a system like the ANSR core, initiation of boiling in one of the channels can cause redistribution of the flow between the parallel channels, leading to continued flow reduction in that channel. This reduction in flow can lead to an actual departure from nucleate boiling phenomenon, but at reduced mass flow compared to the nominal value. This phenomenon can possibly occur before a true departure from nucleate boiling (at the nominal flow) occurs,[62] but not necessarily so.[63]

It is accepted that FE will probably occur near the conditions where sustained net vapor first appears or where net vapor generation starts. Because the margin between the occurrence of net vapor generation and actual onset of FE is narrow and uncertain, it is conservatively assumed in this design that FE will occur at the point of onset of net vapor generation (ONVG). Many of the correlations developed in the past for CHF and reported today in the open literature may actually reflect data for FE, since some researchers were not careful to distinguish between the two phenomena. The Costa FE correlation used in the ANSR design[29] was uniquely developed for the FE phenomena. The correlation developed from rectangular channel data is:

$$q''_{COSTA} = \frac{V^{1/2}\,(T_{sat,ex} - T_b)}{0.0128}\ , \tag{3.3}$$

where

q''_{COSTA} = local flow excursion heat flux (kW/m^2),
V = coolant velocity (m/s),
$T_{sat,ex}$ = saturated exit temperature (K),
T_b = bulk coolant temperature (K).

In this equation, q''_{COSTA} is determined by the start of net vapor generation. $T_{sat,ex}$ is evaluated at the exit pressure, as opposed to numerical design calculations, where $T_{sat,ex}$ is evaluated at local pressure. T_b is evaluated at the local ONVG point, and the liquid-phase velocity, V, is evaluated at local bulk conditions.

The constant 0.0128 in Eq. (3.3) would be replaced by 0.018 for circular tubes. The range of applicability of the Costa correlation and a comparison of the correlation with other correlations and with data are described in ref. 26. Statistical uncertainties for the correlation are discussed in Sect. 4.

3.1.3 Onset of Incipient Boiling

The onset of IB, which is used as one of the thermal limits at steady-state nominal operation, is determined by the B-R[30] correlation in combination with the Petukhov[31] forced-convection correlation for calculating the corresponding wall temperature:

$$q_{IB} = (F_{D_2O}) \times 1.7978 \times 10^{-6} P^{1.156} [1.8 (T_w - T_{sat})]^{(2.8285/P^{0.0234})} ,$$

$$q_{IB} = h_{FC} (T_w - T_b) , \tag{3.4}$$

$$F_{D_2O} = 0.9 ;$$

where

q_{IB} = local incipient boiling heat flux (kW/m^2),
F_{D_2O} = correction factor for applying the Bergles-Rohsenow correlation for heavy water,
P = pressure (Pa),
T_w = wall temperature (K),
T_{sat} = saturated temperature (K),
h_{FC} = forced-convection heat transfer coefficient (kW/m^2 • K),
T_b = bulk coolant temperature (K).

T_w is calculated by iteration through the Petukhov[31] correlation for the forced-convection heat transfer coefficient and the Filonenko correlation[16] for the Darcy friction factor, as modified for rectangular channels [see Eqs. (3.6) and (3.7) in Sect. 3.1.4].

All parameters are evaluated locally. For the Petukhov convective portion, all properties are evaluated at the bulk temperature except μ_w, which is evaluated at the wall temperature but is not allowed to exceed the saturation temperature.

The B-R correlation was derived for light water only, but the method is applicable to other fluids. Using the Davis and Anderson[49] correlation for IB, a comparison was made between heavy water and light water. Based on this comparison, a correction factor was developed as a function of pressure for using the B-R correlation for heavy water rather than light water:[64]

$$F_{D_2O} = (a+c\cdot P+e\cdot P^2+g\cdot P^3)/(1+b\cdot P+d\cdot P^2+f\cdot P^3) . \tag{3.5}$$

From this correlation, it can be concluded that a correction factor of 0.9 can be used with good approximation for the pressure range of 1.7–6.0 MPa, which covers the nominal ANS conditions.[64] In order to use the correction factor for off-normal or transient conditions, the full equation should be used. This equation is represented graphically in Fig. 3.1.

The B-R correlation seems to be broadly accepted for predicting the IB heat flux for "commercial surfaces," where a wide range of cavity sizes is represented. The range of applicability of the B-R correlation and a comparison of the correlation with other correlations and with data are described in ref. 26. Statistical uncertainties for the correlation are discussed in Sect. 4. Since the Davis/Anderson correlation is quite similar to the Bergles/Rohsenow correlation when used for the same medium (at given pressure and wall superheat), it might be preferable to use the Davis/Anderson correlation directly for heavy water rather than the Bergles/Rohsenow correlation with the correction factor.

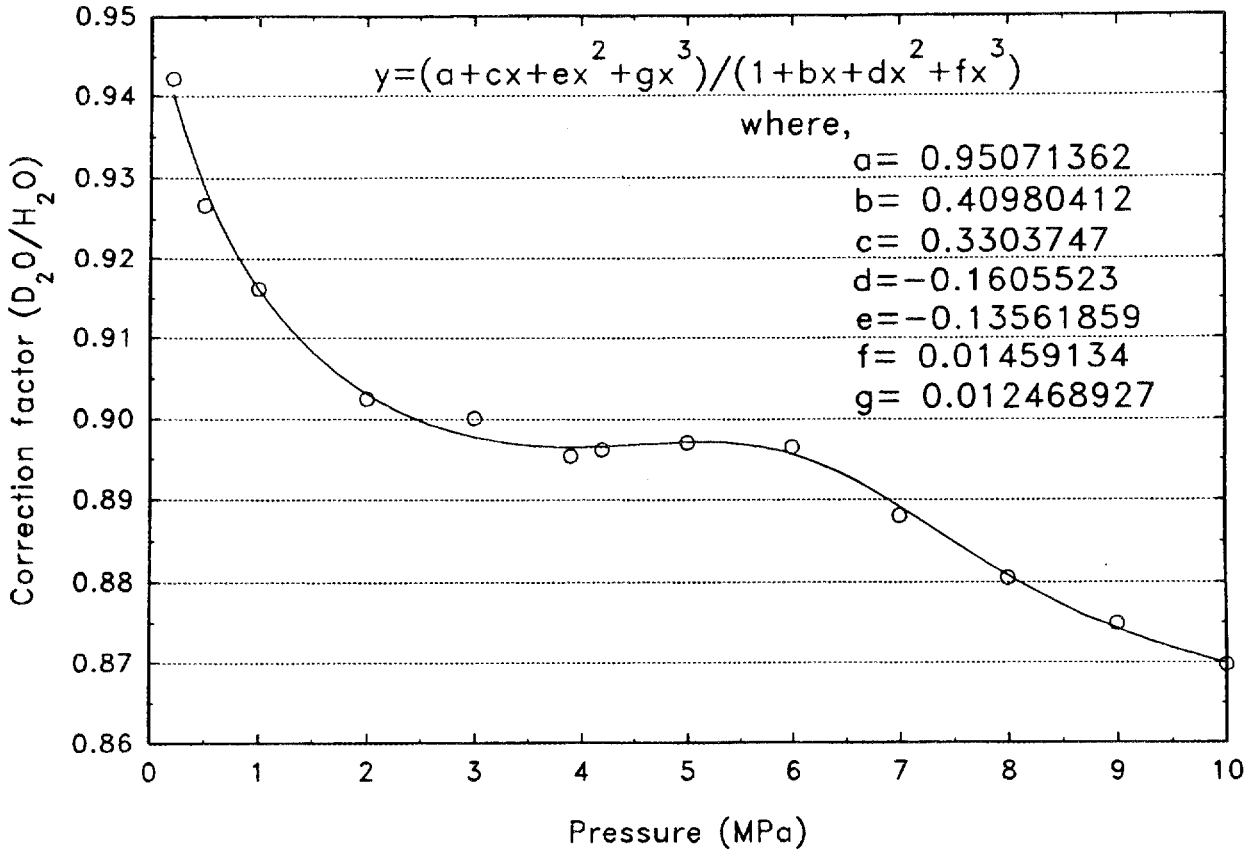

Fig. 3.1. A correction factor as a function of pressure for using Bergles/Rohsenow[30] correlation with heavy water.

3.1.4 Single-Phase Forced-Convection Heat Transfer Coefficient

The forced-convection heat transfer coefficient, required for most T/H calculations including thermal limits, is determined by the Petukhov and Popov correlation,[31] with some modifications for variable physical properties and rectangular channels. The coefficient is determined as follows:

$$h_{FC} = \frac{k_b}{D_e} \frac{(f_d/8)\, Re_b\, Pr_b\, (\mu_b/\mu_w)^{0.11}}{(1+3.4f_d) + [11.7 + \frac{1.8}{Pr_b^{1/3}}]\, (f_d/8)^{1/2}\, (Pr_b^{2/3} - 1)}, \tag{3.6}$$

where

h_{FC} = forced-convection heat transfer coefficient (kW/m^2 · K),
k_b = bulk coolant thermal productivity (kW/m • K),
D_e = equivalent channel diameter (m),
f_d = Darcy friction factor,
Re_b = bulk coolant Reynolds number,
Pr_b = bulk coolant Prandtl number,
μ_b = bulk coolant dynamic viscosity (Pa • s),
μ_w = wall dynamic viscosity (Pa • s);

with the Filonenko correlation[16] used for the Darcy friction factor:

$$f_d = \frac{[\,1.0875 - 0.1125\,(b/s)\,]}{(\,1.82\,\log_{10} Re_b - 1.64\,)^2}, \tag{3.7}$$

where

f_d = Darcy friction factor,
b = gap of a rectangular channel or annulus (m),
s = span of a rectangular channel (m),
Re_b = bulk coolant Reynolds number.

Since all parameters are either dimensionless or ratios, any consistent units can be used. All parameters and physical properties are evaluated at local bulk conditions, except μ_w, which is evaluated at the wall temperature.

The correction factor in the Petukhov correlation for variable physical properties during heating (the wall to bulk viscosity ratio) should be used in Eq. (3.6) without modifying the Filonenko friction

factor correlation Eq. (3.8). Equation (3.7) includes a correction factor for rectangular channels as applied to the ANSR (see Sect. 3.1.5). Entrance effects are conservatively neglected for the ANS calculations. The range of applicability of the Petukhov correlation as well as comparison of the correlation with other correlations and with data are described in ref. 26. Statistical uncertainties for the correlation are discussed in Sect. 4.

3.1.5 Single-Phase Pressure Drop and Friction Factor

The friction factor correlation for single-phase forced convective flow is determined by the Filonenko correlation,[16] with some modifications for heating in rectangular channels and the conversion to the Darcy rather than Fanning formulation, as follows:

$$f_d = \frac{[1.0875 - 0.1125\ (b/s)]}{(1.82 \log_{10} Re_b - 1.64)^2} \left[\frac{7 - (\mu_b/\mu_w)}{6}\right], \tag{3.8}$$

where

f_d = Darcy friction factor,
b = gap of a rectangular channel or annulus (m),
s = span of a rectangular channel (m),
Re_b = bulk coolant Reynolds number,
μ_b = bulk coolant dynamic viscosity (Pa • s),
μ_w = wall dynamic viscosity (Pa • s).

Eq. (3.8) includes a correction factor for rectangular channels based on the Bhatti and Shah[65] correlation using the channel span-to-gap aspect ratio. The correction factor for heated liquids was proposed later by Petukhov[31] in conjunction with his forced-convection correlation.

$$K_H = \left[\frac{7 - (\mu_b/\mu_w)}{6}\right], \tag{3.9}$$

where

K_H = correction factor for heated liquids,
μ_b = bulk coolant dynamic viscosity (Pa • s),
μ_w = wall dynamic viscosity (Pa • s).

Note that this last correction factor **should not** be used with Petukhov's forced convection correlation [Eqs. (3.6) and (3.7)], because Petukhov's correlation already includes a separate correction for variable physical properties (see Sect. 3.1.4). The fuel plates are currently considered "hydraulically smooth." This consideration is based on a preliminary laminar sublayer thickness comparison with a surface roughness of 0.5 μm, measured for the HFIR fuel plates.[66] This assumption will be reevaluated to see if another friction factor correlation should be used that includes

the effects of surface roughness as well. The range of applicability of the Filonenko correlation and a comparison of the correlation with other correlations and with data are described in ref. 26. Statistical uncertainties for the correlation are discussed in Sect. 4.

3.1.6 Nucleate Boiling and Void Fraction

No boiling is expected under reactor nominal steady-state operating conditions. Therefore, correlations for nucleate boiling heat transfer and two-phase pressure drop, as well as for void fraction, are not included here. Evaluation of two-phase correlations will be made as the project progresses.

3.1.7 Oxide Growth Rate and Spallation

The oxide growth rate during the fuel cycle is determined by a correlation developed using data taken specifically for the ANS—Correlation I.[67-70] This correlation is based on the general rate equation:

$$\frac{dx}{dt} = \frac{k_t}{x^n} \quad , \tag{3.10}$$

where

x = oxide thickness (μm),
t = time (h),
k_t = rate constant,
n = constant (mechanism number).

Early kinetic results for the ANS steady-state experiments were consistent with the assignment of n = 0.351, so that the integrated form of the equation is:

$$x_t = (x_o^{1.351} + 1.351 \cdot k_t \cdot t)^{0.74} \quad , \tag{3.11}$$

where

x_t = oxide thickness at time t (μm),
x_o = oxide thickness at t = 0 (μm),
k_t = rate constant,
t = time (h).

The shape of the growth rate curves is essentially identical to those of Griess, Savage, and English[71] (and Kritz[23]) who reported a growth exponent of 0.778. Using the model defined in Eq. (3.10), Eq. (3.11) can be used to predict oxide layer thicknesses for any set of specified

conditions, providing the rate constant, k_t, can be assigned for the conditions involved. Thus, a "correlation" essentially defines the rate constant as a function of its critical variables (in this case, mainly the T/H parameters that control temperatures across the reacting system).

Since Eq. (3.11) was first presented,[67] several additional experiments that meet its requirements were added to the data base. These have reinforced its applicability. A conservative equation for k_t (except at very low growth rates) was developed from this data and is given by:

$$k_t = 6.992 \times 10^5 \exp\left[-7592/(T_b + 10\phi)\right] \quad \mu m^{1.351}/h \quad , \tag{3.12}$$

where

k_t = rate constant,
T_b = bulk coolant temperature (K),
ϕ = heat flux (μW/m^2).

The experiments contributing to this data base were all conducted under conditions where the nominal coolant pH was 5, the coolant velocity, V_c, was 25.6 m/s, and the coolant inlet temperature, $T_{c,i}$, was between 39 and 49°C.

Spallation of the boehmite films was observed toward the end of some of the more aggressive loop experiments. Metallographic examinations of such specimens showed that spallation was followed by the onset of internal reactions in the metal beneath the oxide. The presence of an extensive internal reaction zone is clearly detrimental to efficient heat flow as well as structural integrity and should not be allowed to occur in the ANS fuel cladding. Steady-state experiments indicate that spallation will not occur if the temperature drop across the growing oxide film is maintained at < 119°C, and this limit is currently used as a criterion for core calculations. Additionally, spallation was not induced by moderate temperature cycling at or near the end of the tests.

3.2 SUPPORTING DATA BASE

An extensive data collection and correlation evaluation was performed (and is continuing) to select the best correlations possible, as supported by statistical evaluation and comparison. A limited number of correlations have been selected that may prove to be the most applicable to specific ANSR conditions. A wide variation in reporting details of the experimental data exists in the literature, from tabulation of actual experimental data to plotting comparative results using calculated dimensionless groups. To evaluate the data and examine it statistically in different ways, the collected data were incorporated into a statistical software program (SAS).[72] The correlation selection process, based on statistical evaluation and comparison against a multisource data base, can be very complicated even if it is assumed that all the collected data are of high quality.

Recognizing that the data base is not yet complete, the correlations were evaluated against the collected data. Table 3.2 lists the various sources from which the data base was complied for each of the T/H categories, the number of data points compiled from each source, and the number of data points that were within the acceptance criteria range (see ref. 26). Table 3.3 provides a summary of the mean and standard deviation for each of the correlations evaluated against all of the data collected to date and against the data within the range of the acceptance criteria. Figures 3.2–3.6 provide a closer look at the comparison of all of the data collected with correlation predicted values for some of the T/H correlations currently used in the ANS Project and discussed above. A more detailed discussion of the correlations selected and the current status of the experimental data base can be found in ref. 26.

Table 3.2. Data base for each of the thermal-hydraulic categories and acceptance criteria for screening data

Data set source[a]	No. of points[b]	No. of "good" points[c]
CHF[d]		
Knoebel et al.[73]	84	0
Gambill et al.[74]	23	0
Gambill and Bundy[75]	7	0
Mirshak et al.[76]	65	0
Babcock and Hood[77]	63	0
Burck and Hufschmidt[78]	135	0
Jens and Lottes[79]	13	0
Schaefer and Jack[80]	3	0
Mayersak et al.[81]	1	0
Gambill and Greene[82]	6	0
Bergles and Rohsenow[30]	46	0
Dormer and Bergles[83]	13	0
Bergles[84]	56	0
Skinner and Loosmore[85]	111	0
Reynolds[86]	6	0
Wessel[87]	34	0
Scarola[88]	9	4
Ornatskii[89]	77	8
Vandervort[90]	211	6
Ornatskii and Kichigan[91]	122	0
Boyd[92]	5	0
Ornatskii and Vinyarskii[93]	137	0
Celata et al.[94]	43	0
Boyd[63]	5	3
TOTAL	1275	21

Data set source	No. of points	No. of "good" points
FEHF[e]		
Lafay et al.[95]	35	0
Lafay[96]		
Costa et al.[29]	117	0
Courtaud et al.[97]	6	0
Courtaud et al.[98]	15	0
Courtaud et al.[99]	12	0
Vernier[100]	19	0
Courtaud et al.[101]	12	0
Whittle and Forgan[44]	88	
Schleisiek and Dumaine[102]	14	0
Lafay et al.[103]	18	0
Waters[62]	18	0
TOTAL	354	0
IBHF[f]		
Papell[48]	3	0
Sato and Matsumura[104]	39	0
Sudo et al.[105]	27	0
TOTAL	93	0
FCHTC[g]		
Petukhov[31]	56	55
Hufschmidt and Burck[106]	45	45
Webb[107]	38	38
TOTAL	139	138
FCFF[h]		
Hartnett et al.[108]	69	69
Jones[109]	25	25
Jones[110]	7	7
Schiller[111]	29	14
Eckert and Irvine[112]	2	0
Washington and Marks[113]	15	8
TOTAL	147	100

[a]Complete citations are located in Sect. 7.
[b]Total number of data points = 2008.
[c]Number of data points within the acceptance criteria range. Total number of "good" points = 259.
[d]CHF = critical heat flux.
[e]FEHF = flow excursion heat flux.
[f]IBHF = incipient boiling heat flux.
[g]FCHTC = forced-convection heat transfer coefficient.
[h]FCFF = forced-convection friction factor.

Table 3.3. Means and standard deviations of experimental-to-correlation-calculated ratios

Correlation[a]	No. of data points[b]	Mean[b]	Standard deviation[b]
Gambill-w/Weatherhead[28]	1275/21	1.381/1.343	0.531/0.131
Bernath modified[34]	1275/21	1.427/0.885	0.731/0.072
Thorgerson modified[36]	1275/21	1.257/0.820	0.962/0.089
FEHF[c]			
Bowring (1962)[43]	284/-	0.485/-	0.164/-
Whittle and Forgan[44]	284/-	0.120/-	0.389/-
Costa[29]	284/-	0.942/-	0.364/-
Saha and Zuber[45]	284/-	1.300/-	0.443/-
Moritz[46]	284/-	0.884/-	0.283/-
Moritz (modified)[47]	284/-	0.839/-	0.273/-
IBHF[d]			
Bergles and Rohsenow[30]	69/-	1.202/-	0.230/-
Papell[48]	69/-	2.233/-	1.670/-
Davis and Anderson[49]	69/-	1.243/-	0.394/-
Frost and Dzakowic[50]	69/-	1.059/-	0.246/-
FCHTC[e]			
Dittus-Boelter[52]	139/138	0.986/0.986	0.127/0.127
Petukhov[31]	139/138	0.996/0.996	0.033/0.033
Gnielinski[55]	139/138	0.979/0.979	0.037/0.037
Sieder and Tate[53]	139/138	1.110/1.111	0.213/0.214
Hausen[54]	139/138	0.977/0.976	0.065/0.063
FCFF[f]			
Prandtl,[56] von Karman,[57]	147/100	0.998/1.004	0.053/0.055
and Nikuradse[58]	147/100	0.985/0.997	0.054/0.053
Filonenko[16]	147/100	0.998/1.004	0.053/0.055
Techo et al.[59]	147/100	0.997/1.003	0.053/0.055
Colebrook[60]	147/100	0.998/1.004	0.053/0.055
Chen[61]			

[a]Complete citations are located in Sect. 7.

[b]The first number is for the total data base to date, and the second is for data within the acceptance criteria range for the Advanced Neutron Source.

[c]FEHF = flow excursion heat flux. Excluding data with velocity <2 m/s and subcooling <8°C.

[d]IBHF = incipient boiling heat flux. Insufficient data within the applicable range of the compared correlations.

[e]FCHTC = forced-convection heat transfer coefficient.

[f]FCFF = forced-convection friction factor. Excluding data with a Reynolds number <4240.

As can be seen from these results, there is very good agreement between the data collected so far and the correlations selected, for both friction factor and forced-convection heat transfer coefficients. The comparisons also seem to justify the selection of the Filonenko correlation for friction factor and the Petukhov correlation for forced convection, with standard deviations of 5.4 and 3.3%, respectively. On the other hand, the comparisons are not as conclusive for the boiling-related correlations. The agreement with the data is not very good, and the various correlations do not closely agree with each other. Possible reasons for these discrepancies include the broad range of data, the use of correlations outside their original limits, and, in some cases, insufficient data within these limits. In addition, the complexity of performing good experiments under boiling conditions also adds to the data scatter. The comparison indicates the areas of agreement and deficiencies and provides a basis for a more thorough and final selection of the correlations. The actual correlation means and standard used in this report and in the CSAR and the justification for using them are discussed in Sect. 4.2.

3.3 PRESENT STATUS, LIMITATIONS, AND PLANNED ACTIVITIES

The T/H correlations presented in this report are those currently used for conceptual design and analysis of the ANSR. As the project progresses, these correlations (and others) will be reviewed, modified, and replaced as necessary. These actions will be performed based on additional data (both from the available literature as well as from new experiments), additional evaluation, and future needs of the project. Specific activities will include:

- further expansion of the data base to include more data in the specific range of ANSR conditions;
- assessment and minimization of the uncertainties associated with the data collection and back calculations used to establish uncertainty probability distributions;
- statistical comparison and evaluation of the candidate correlations using various approaches to data base screening, with special attention to the applicability of each correlation;
- revision of the selected correlations, if necessary, as the project progresses to detailed design;
- expansion of the work to include T/H correlations for ANSR transient, off-design conditions (e.g., lower pressures, velocities, and heat fluxes, as well as other flow regimes—laminar, transition, and natural convection) and evaluation of the applicability of the correlations to transient conditions; and
- incorporation data from the ANS T/H test facility and corrosion test loop constructed at ORNL.[27]

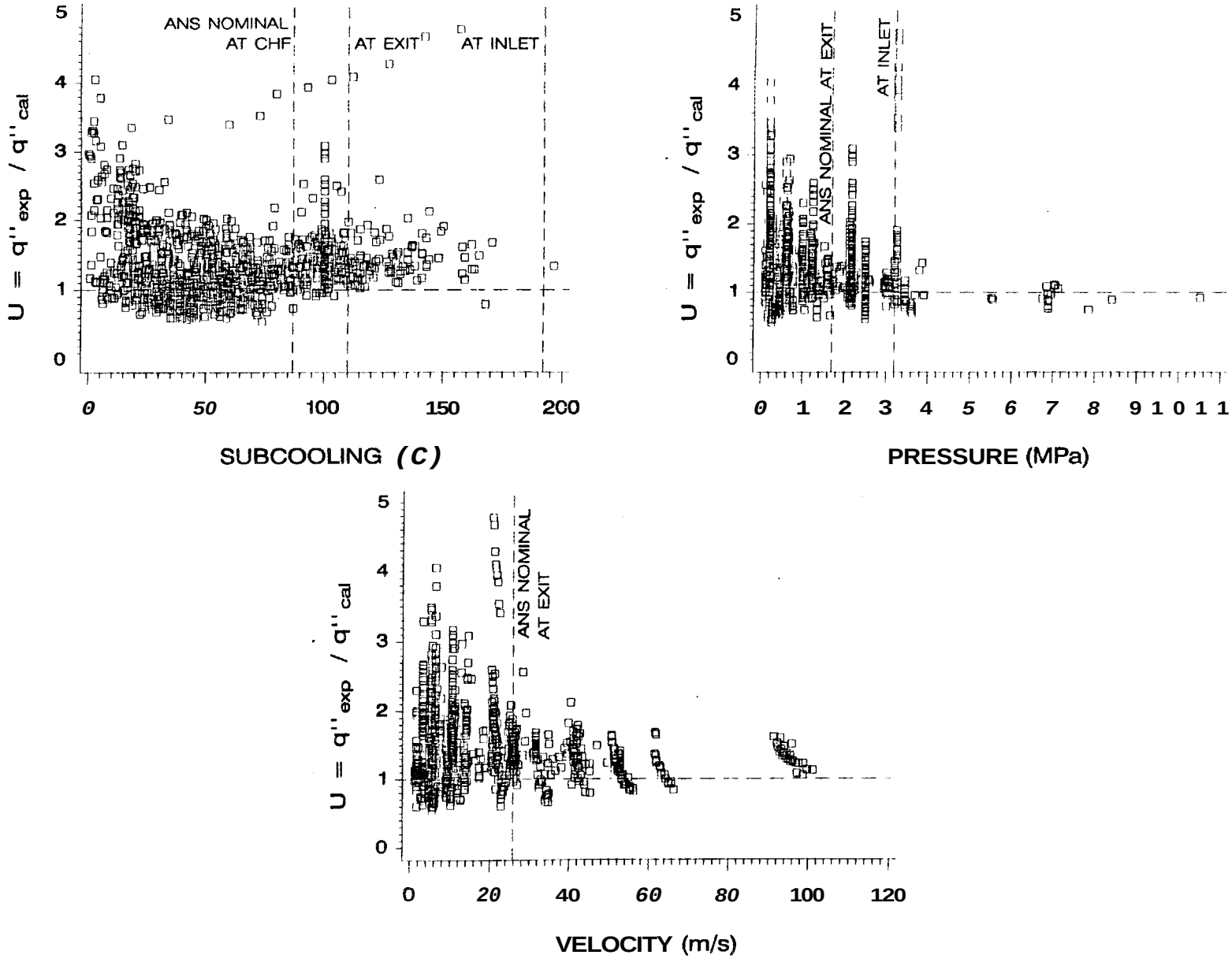

Fig. 3.2. Critical heat flux preliminary experimental-to-calculated ratios for all the data points using the Gambill-w/Weatherhead correlations.

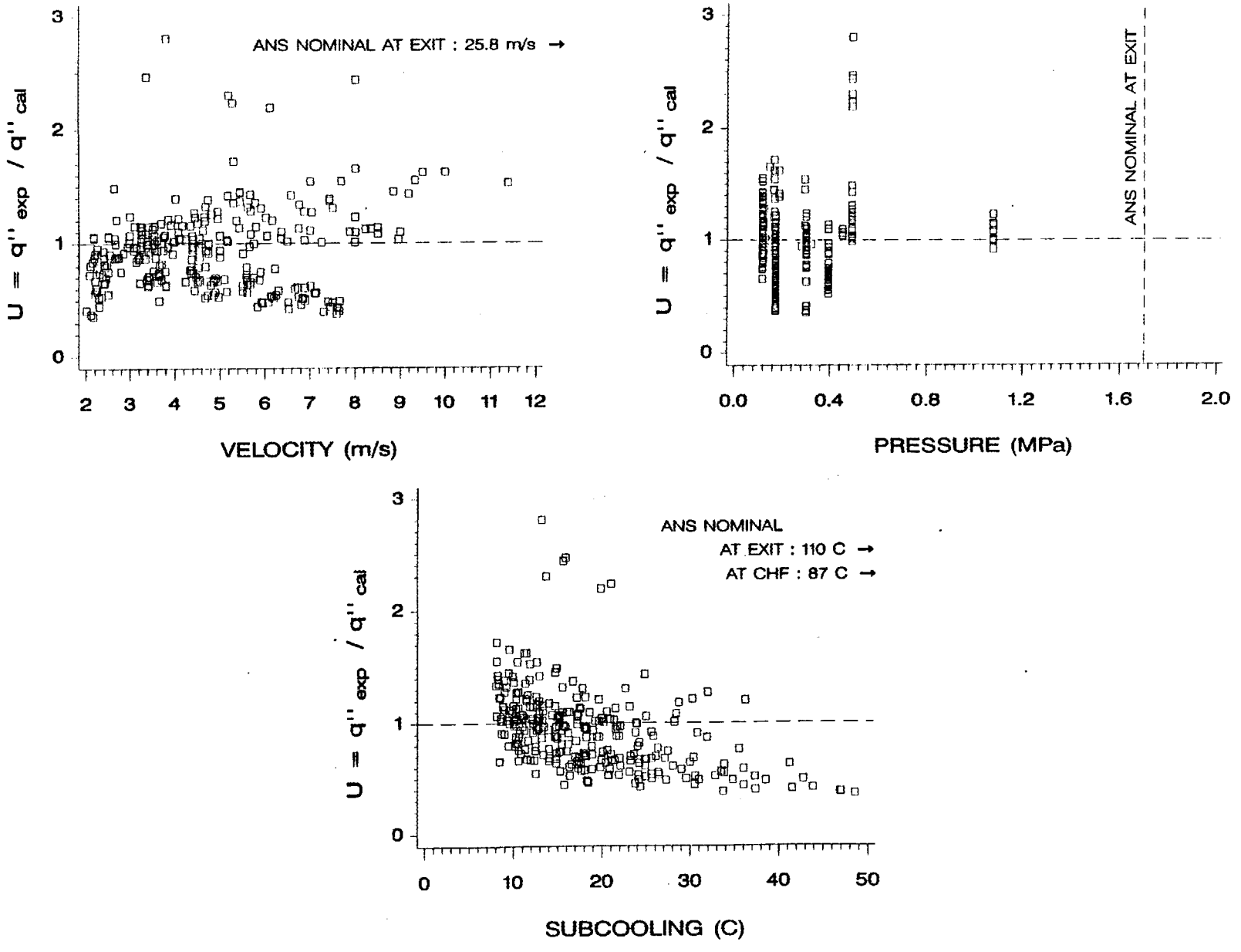

Fig. 3.3. Flow excursion heat flux preliminary experimental-to-calculated ratios for all the data points using the Costa correlation.

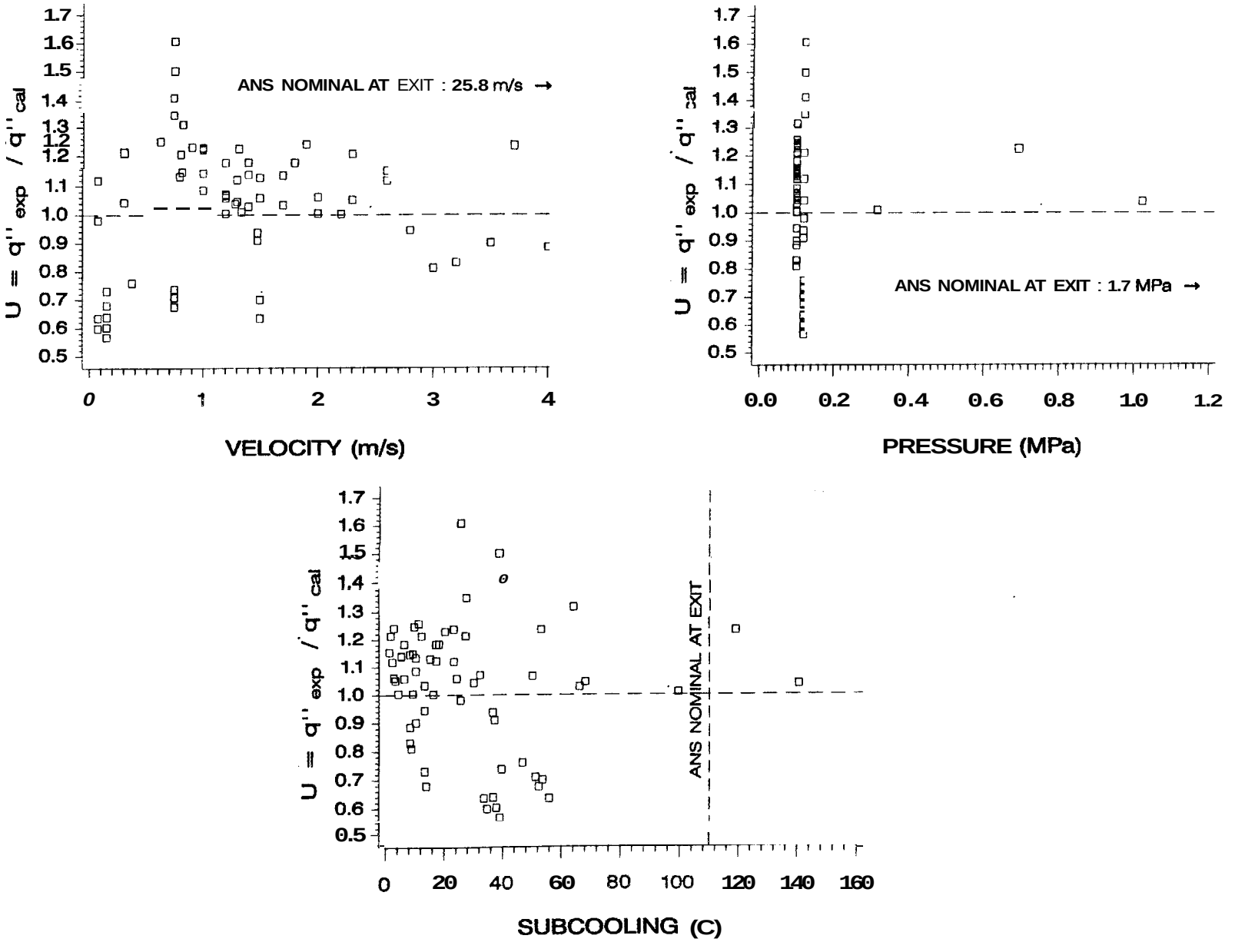

Fig. 3.4. Incipient boiling heat flux preliminary experimental-to-calculated ratios for all the data points using the Bergles and Rohsenow correlation.

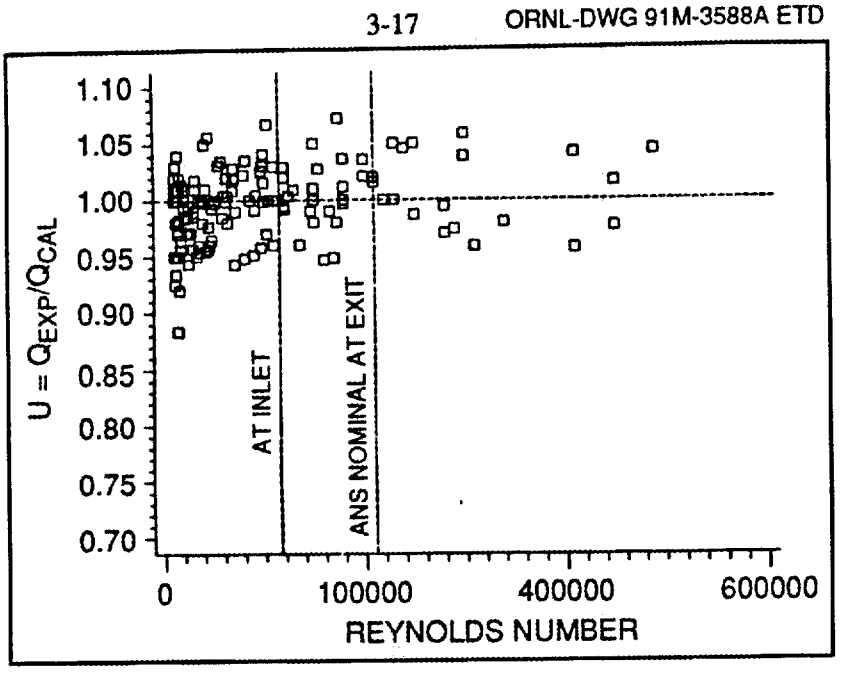

Fig. 3.5. Forced-convection heat transfer coefficient preliminary experimental-to-calculated ratios for all data points using the Petukhov correlation.

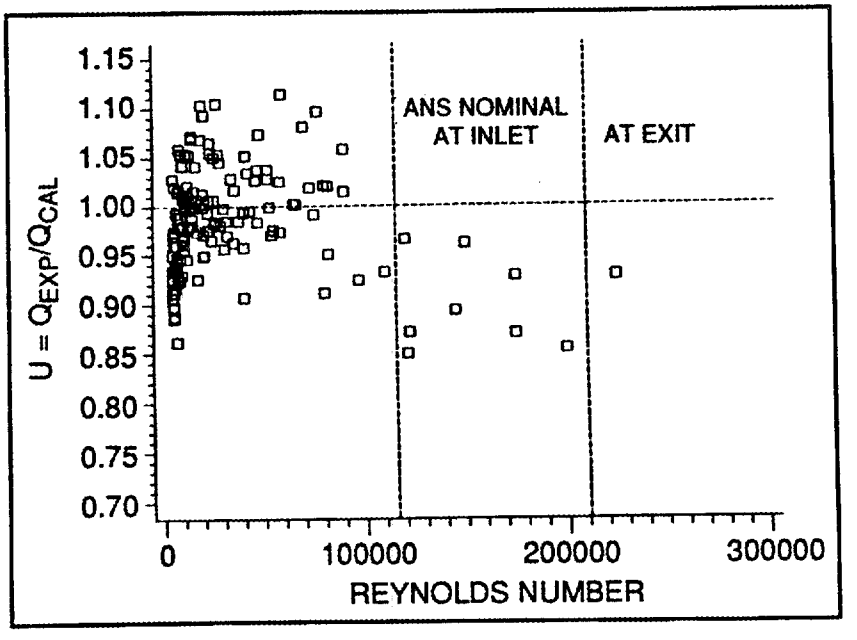

Fig. 3.6. Forced convection friction factor preliminary experimental-to-calculated ratios for all the data points using the Filonenko correlation.

4. EVALUATION OF THERMAL-HYDRAULIC UNCERTAINTIES

The uncertainty analysis of the ANSR was initiated in FY 1990 to determine the maximum operating power limits while simultaneously accounting for uncertainties and providing safety margins compatible with an acceptable quantified probability level. To avoid an overly conservative design that normally results from applying the worst case methods used in the past, it was determined that a statistical/probabilistic approach to the uncertainty analysis would be pursued. It is necessary to minimize uncertainties, design around uncertainties, and, as indicated above, use a better (i.e., less conservative) treatment of uncertainties to meet the power goal for ANS. An estimate of the penalty for using the worst case approach rather than a statistical approach (applying a 95% probability level) for ANS is ~23% for nominal operation based on IB as the thermal limit. Using oxide associated temperature limits as the criteria, the penalty is ~11%. The penalties would be larger using a more complete statistical approach (which is currently being implemented). Obviously, as the probability level for the statistical approach increases, the penalty decreases.

The statistical approach for reactor design was later integrated with the probabilistic risk assessment (PRA) to achieve the safety goals adapted by the ANS Project. The risk being considered results from uncertainties in the input parameters, including manufacturing parameters (e.g., fuel-plate fabrication tolerances) and operating parameters (e.g., inlet pressure and temperature), and in the models (e.g., the CHF correlation) used when performing the best estimate design and analysis. The major uncertainty analysis steps performed include:

- evaluation and selection of a cost-effective statistical method;
- determination of the key parameters and correlations most influencing the reactor performance through a sensitivity study;
- evaluation and selection of the input parameters and analytical models (correlations) to be used in the design and analysis of the reactor;
- quantification of the uncertainties involved in the key parameters and correlations by determining the error probability distributions for each;
- modification of the ANS steady-state T/H code and integration with a statistical sampling code (SAMPLE[114]), thus allowing selection of an appropriate power level for a given probability and confidence level; and
- performing a preliminary analysis to determine the maximum nominal operating power consistent with adequate safety margins (see Sect. 5).

4.1 THE STATISTICAL APPROACH

The merits of several methods to perform uncertainty analysis, both statistical and nonstatistical, were evaluated. Four of these methods are described below.

1. The **worst case approach**, in which each parameter is assigned a conservative constant value reflecting the "maximum" (i.e., typically 2 or 3 standard deviations from the mean) deviation from nominal, and all of the uncertainties are assumed to exist simultaneously at their maximum value. This method was very common in the past and was used for the HFIR design.[6] However, this approach was judged to be unnecessarily conservative, and it does not provide any quantitative measure of the level of risk involved. The primary advantage of the approach is the conceptual simplicity because detailed uncertainty distributions for the input parameters and correlations are not required.

2. The **statistical square root of sum of squares (SRSS) approach**, where all the uncertainties are assumed to be independent and are incorporated via standard deviations. Although this approach is statistical, it generally provides only an approximation of the relationship among uncertainties and may, therefore, provide nonconservative results. This approach does have the advantage of relative simplicity by not requiring a computer code for implementation, but it does require determination of the uncertainty distributions for the input parameters and correlations.

3. **A full statistical approach** combining input uncertainties randomly (via sampling of individual uncertainty distributions) in repeated simulations. The most basic technique for implementing this approach is the Monte Carlo (MC) technique. This method has the advantage of being fully statistical and providing a definitive statement of the safety margins or probability levels achieved. The disadvantages include the need to provide detailed error distributions for each of the parameters and correlations that appreciably affect the reactor performance and the computer time that might be involved in performing the many statistical sampling combinations. For steady-state analysis and a probability level that is not overly high (95–99.9%), the computer time necessary in applying the MC technique is manageable. The technique can then be directly applied in combination with the TASHA code described previously.[6,7] For higher probability levels, as well as for transient analyses that apply complex T/H codes, this approach is not cost effective. In these situations, more advanced sampling techniques or analytical approaches are necessary.

4. **Latin hypercube sampling (LHS), response surface techniques, etc.** This type of sampling may greatly improve the efficiency of simple MC sampling and response surface techniques, which use a surrogate to the complex T/H programs (such as RELAP5). These techniques were investigated in consultation with experts from Sandia National Laboratory (SNL) and INEL. The LHS technique is based on the stratified sampling approach that greatly reduces the number of random combinations necessary for a given confidence level, yet does not introduce new approximations. This approach can probably be used for most steady-state cases and some transients. The response surface technique introduces new sources of errors since the surrogates to the original codes are only simpler simulators of those complex programs. These and other advanced statistical techniques, such as fast probability integration (FPI),[115] are being investigated for application in more difficult situations.

Based on the above considerations, the fully statistical approach was adopted. The MC technique, in combination with LHS, is being implemented with the steady-state T/H code for the steady-state analysis. Unfortunately, this tool is not completely ready for extensive application to ANS T/H calculations. Tools to implement fully the statistical approach for transients have not been developed. Currently, the more advanced techniques are still being studied for the more complex transients. Hence, a shortcut technique, which involves a combination of statistical and deterministic peaking factors, was used in most steady-state analyses instead of the integrated TASHA code/sample code. (A few steady-state analyses, however, used the integrated codes.) This approach was also used exclusively in transient analysis and is discussed in this section.

4.2 DETERMINATION OF UNCERTAINTIES

The effort required to characterize process parameter uncertainties with probability distributions for inclusion in full statistical analysis can be very large. Thus, a preliminary sensitivity analysis was performed to determine the most significant parameters (of the many candidate parameters)[116] affecting the code performance. This analysis served to reduce the number of parameters with uncertainties that will be treated statistically. (The remaining parameters are considered through predetermined conservative values or neglected.) The TASHA code was used to perform this

sensitivity analysis. The uncertainties are taken into account in the code by multiplying the nominal value (either an input parameter or a best estimate calculated value) by an uncertainty factor (U) that represents the ratio between the possible value (e.g., worst case value or values sampled from a probability distribution) and the nominal value. The uncertainties involved are many and include manufacturing parameters (such as fuel plate fabrication tolerances), operating parameters (such as inlet pressure and temperature), and analytical models used (such as the CHF correlation). By exercising the T/H code repeatedly for each of the existing U factors one at a time, all the U factors were sorted and ranked in order of increasing effect on reactor maximum power (order of significance).

Selected results from this sensitivity study are presented in Table 4.1. Analysis was performed at BOC for the G3 core design (a design before the L7 design). The values of the U factors are generally representative of worst case values. Although the ranking of U factors obviously depends on the core design and the time in the cycle (among other aspects), the U factors presented in Table 4.1 will remain among the important parameters that will be accounted for in analysis. Although not addressed in the sensitivity study, a number of other important parameter uncertainties have been identified. These include oxide correlation, fuel-plate nonbond, fuel extending beyond normal boundaries, channel gap, and code uncertainty.

For analysis of transient events, the list of important parameter uncertainties includes those above plus a number of others. Identification of these additional parameter uncertainties has been and will continue to be guided by phenomena identification and ranking table (PIRT) studies proceeding generally as outlined in the Code Scaling, Applicability, and Uncertainty (CSAU) methodology.[117] An initial list of parameters (phenomena) with associated uncertainties will need to be addressed, including break modeling, choking, pressure wave propagation, pump performance, and numerics.

Of the many parameters involved in the analysis, 16 factors have been identified as significant for the current preliminary evaluation. Depending upon their nature and/or the level of understanding, uncertainties in these factors have been described with probability distributions or worst case values. Those with distributions are provided in Table 4.2; those with worst case values are provided in Table 4.3. Note that in Table 4.2, uncertainty distributions are identified as applying on a plate level (i.e., variations that occur from plate to plate within a core) or on a core level (i.e., variations that are the same for all plates within a core).

To quantify statistically the uncertainty levels associated with the correlations used in the T/H analysis, a task was initiated to evaluate the correlations and develop a data base for the significant T/H phenomena. An evaluation of several correlations for each of these factors has led to preliminary selection of correlations for the ANS T/H analysis. These correlations included the Gambill-w/Weatherhead[26,28,32] correlation for CHF limit (U22), the Costa[29] correlation for FE heat flux limit (U25), the B-R[30] correlation for IB heat flux (U23), the Petukhov[31] correlation for forced-convection heat transfer coefficient (U8), and the Filonenko[16] correlation for forced-convection friction factor (U7). Uncertainty levels for each correlation U factor were determined based on a comparison with the data base as discussed in Sect. 3 and presented in Table 3.1.

In several instances (e.g., CHF, FE, and IB correlations), uncertainties in Table 4.2 represent extrapolations to values expected and achievable in the future with a specific ANS experimental data base. In those cases, uncertainty values selected are significantly smaller than determined in the analysis of the existing data base.[26] The evaluation discussed in Sect. 3 shows that the uncertainties for both Petukhov and Filonenko correlations are not large and do not change much with the conditions tested for either steady-state or transient conditions. The mean was in the narrow range of 0.996–1.00 and the standard deviation in the range of 3–6% (see Table 3.1). On the other hand, the uncertainties for the Gambill/Weatherhead, Costa, and Bergles/Rohsenow correlations are quite wide and do depend considerably on the conditions and sources used for comparison. The mean for the Gambill/Weatherhead correlation ranges from 0.9–1.6 and the standard deviation from 13–53%. The

Table 4.1. Selected preliminary sensitivity study results for nominal operating conditions

U[a] factor	Uncertainty	Effect (%)
U22 (critical heat flux correlation)	0.80	18.80
U18 (fuel segregation)	1.30	14.30
U3 (power density)	1.10	9.10
U24 (hot streak)	1.10	4.36
U8 (local heat transfer correlation)	0.94	3.81
U7 (friction factor)	1.05	2.04
U1 (reactor power)	1.02	1.96
U2 (total heat transfer)	1.02	1.96
U23 (incipient boiling correlation)	0.90	0.73
U6 (inlet coolant temperature)	1.01	0.36

[a]U = uncertainty.

Table 4.2. Probability distributions used in Monte Carlo uncertainty analysis

Parameter	U factor[a]	Probability distribution	Distribution level	Mean	Standard deviation
CHF[b] correlation	U22	Normal	Core	1.0	0.10
FE[c] correlation	U25	Normal	Core	1.0	0.10
Local power density distribution	U3	Normal	Core	1.0	0.03
Streak-average power density distribution	PSAR[d]/FSAR[e]	Normal	Core	1.0	0.02
Integrated hot streak	U24m	Log-normal	Plate	1.030	0.00425
Forced-convection heat transfer correlation	U8	Normal	Core	1.0	0.0283
Friction factor correlation	U7	Normal	Core	1.0	0.05
Reactor power	U1	Normal	Core	1.0	0.018

Table 4.2 (continued)

Parameter	U factor[a]	Probability distribution	Distribution level	Mean	Standard deviation
Fuel plate heated length	U2	Normal	Plate	1.0	0.0036
IB[f] correlation	U23	Normal	Core	1.0	0.10
Inlet coolant temperature	U6	Normal	Core	1.0	0.006
Exit pressure	PSAR/FSAR	Normal	Core	1.0	0.025
Flow	PSAR/FSAR	Normal	Core	1.0	0.0033
Channel gap	PSAR/FSAR	PSAR/FSAR	Plate	PSAR/FSAR	PSAR/FSAR
Oxide correlation	U9	PSAR/FSAR	Core	PSAR/FSAR	PSAR/FSAR

[a]SS thermal hydraulic code U factor. U = uncertainty.
[b]CHF = critical heat flux.
[c]FE = flow excursion.
[d]PSAR = preliminary safety analysis report.
[e]FSAR = final safety analysis report.
[f]IB = incipient boiling.

Table 4.3. Deterministic values used in Monte Carlo uncertainty analysis

Parameter	U factor	Worst case value
Local fuel segregation plus nonbond	U18/U19 and U20/U21	1.313
Fuel beyond radial boundary	U26 (array)	1.02
Fuel beyond axial boundary	U25 (array)	1.05
Hot streak fuel segregation	U24	1.10

mean for the Bergles/Rohsenow correlation is 1.02 and standard deviation is 23%. The mean for the Costa correlation ranges from 0.96–1.35 and the standard deviation from 26–48%. The data collected so far for IB is insufficient, and this data base needs to be expanded.

Table 4.4 provides the results of a more extensive and detailed statistical evaluation made for the FE and the CHF correlations. As can be seen in this table, comparing the Gambill/Weatherhead correlation with Boyd's data,[63] which are the best data for the ANS conditions, provides a mean of 1.07 and standard deviation of 20%, and comparing the Costa correlation to his own data[29] provides a mean of 0.98 and standard deviation of 8.4%. The table also indicates that both correlations are in reasonable agreement with Boyd's data. Similar observation can be made from Fig. 4.1, which compares all of the FE and CHF correlations with Boyd's data on a common plot.

Investigation thus far suggests that the two correlations are, in all probability, on the conservative side, specifically the Costa correlation at the higher velocities [compared to Saha & Zuber (S&Z) correlation,[45] for instance], as is also demonstrated in Fig. 4.2. The standard deviations of these correlations seem to be very high. However, other specialized correlations like that of Costa,[29] Babcock and Wilcox (B&W)[118] and Westinghouse[119] correlations, and the more recent general correlations by Weisman[120] and Katto[121] demonstrate that correlations for both CHF and FE can be developed with standard deviations as low as 7–9% when derived from carefully designed in-house experiments tailored for a given set of conditions.

It is hard to reconcile all these results without considerable additional work, i.e., more data from additional sources, in-house experiments, and more evaluations and comparisons. For the purpose of this report, it was decided to base the uncertainties for the CHF, FE, and IB correlations on a mixed approach using the current evaluations, engineering judgement, and extrapolation to values that can be expected or achievable in the future, by performing high quality and dedicated in-house experiments specifically designed for the ANS conditions. The logical sequential justification for this selection can be summarized as follows.

- The Costa correlation is more optimistic than S&Z at low velocities and more conservative than any other correlation, including S&Z, at high velocities. The S&Z correlation, which is the most widely used in the literature, gives twice as high a heat flux prediction as the Costa correlation at the ANS nominal velocity range (see Fig. 4.1).
- This conservatism is not reflected in this data base comparison because 97% of the data are below 8.3 m/s, which is far below the ANS nominal and transient velocity range (see Fig. 4.2).
- These trends can be detected in a data plot and in the statistical comparison, by separating data below and above 8.3 m/s, giving a mean and a standard deviation of 0.93/35.8% and 1.42/23%, respectively (see Table 4.4).
- The Costa correlation data comparison using Costa data only gives a mean and standard deviation of 0.98/8.4% (see Table 4.4). This value reflects very careful experimentation with a very low spread of experimental data.
- Taking all of the above considerations into account, a mean value of 1.2 (conservative) and a standard deviation of ~20–30% seem to be reasonable choices for the Costa correlation.

However, comparisons of correlations required the modification of some of the assumptions, as explained below.

- Comparing the Costa correlation against Boyd's CHF data, which is quite close to the ANS conditions and is considered very reliable, shows a relatively close agreement, with a mean of 1.13 and a standard deviation of 26% (see Table 4.4). With Boyd's data being for CHF rather than FE, the assumed conservatism was reconsidered, and a mean value of 1.0 was assumed.

Table 4.4. Statistical observations of flow excursion and critical heat flux uncertainty distributions for the conceptual safety analysis report[a]

Data base application	Selected data	(No. data points/mean/% standard deviation)			
		CHF[b]	FE[c]	FE[d]	U(Q) ratio[e]
All CHF DB[f]	Re[g] > 4240	1274/1.38/53.1	NA[h]	NA	NA
All FE DB (Re > 4240)	dT[i] > 5	NA	302/0.98/42.7	283/1.33/51.3	0.74 (NA)
All FE DB (Re > 4240)	dT > 8	NA	284/0.94/36.4	269/1.30/45.1	0.72 (NA)
All FE DB (Re > 4240, dT > 8)	G[j] < 8000	NA	276/0.93/35.8	261/1.30/45.6	0.72 (0.75)
All FE DB (Re > 4240, dT > 8)	G > 8000	NA	8/1.42/23.0	8/1.27/26.9	1.12 (1.27)
ANS[k] nominal, CHF		21/1.34/13.1	NA	NA	NA
ANS nominal, FE		NA	No data	No data	No data (2.0)
Boyd data only (CHF)[l]		10/1.07/20.1	10/1.13/26.0	10/0.83/36.2	1.36 (1.65)
Costa data range (FE)[m]		NA	31/0.81/21	31/1.21/32	0.6 (0.83)
Costa data only (FE)[m]		NA	43/0.98/8.4	43/1.12/34.6	0.88 (NA)
ANS transient, CHF		44/1.61/35.6	NA	NA	NA
ANS transient FE	5 < dT < 55	NA	40/1.02/48.6	40/1.02/42.4	1.0 (1.7)
ANS transient FE	5 < dT < 25	NA	24/1.33/35.6	24/1.31/29.3	1.0 (1.7)
Applicable data/rectangular		58/0.78/18.9	292/1.07/658	269/1.4/550[n]	
Applicable data/tube + annulus		1216/1.41/52	23/1.66/62.9	23/1.64/86.2[n]	
Applicable data/H_2O		1233/1.39/54	315/1.11/634	292/1.42/528[n]	
Applicable data/D_2O		41/1.19/14.0	No data	No data	
Applicable data/Aluminum		89/1.07/24.0	No distinction	No distinction	
Applicable data/other materials		1185/1.4/54	No distinction	No distinction	

[a] *Conceptual Safety Analysis Report,* ORNL/ANS/INT-33, Martin Marietta Energy Systems, Inc., Oak Ridge National Laboratory, June 1992.

[b] CHF = critical heat flux. [*Source:* W. R. Gambill, "Generalized Prediction of Burnout Heat Flux for Flowing, Subcooled, Wetting Liquids," *Chem. Eng. Prog. Symp. Series* 59(41), 71–87, (1963).]

[c] FE = flow excursion. (*Source:* J. Costa, "Movement of the Momentum Pressure Drop and Study of the Appearance of Vapor and Change in the Void Fraction in Subcooled Boiling at Low Pressure," presented at the Meeting of the European Group Double-Phase, Winfrith, England, 1967. Translated from French as ORNL/LRT-90/21, Martin Marietta Energy Systems, Inc., Oak Ridge National Laboratory, 1990.)

[d] *Source:* P. Saha and N. Zuber, "Point of Net Vapor Generation and Vapor Friction in Subcooled Boiling," *Proc. of 5th Intl. Heat Transfer Conf.*, Tokyo, Japan IV, 175–179, (1974).

[e] U(Q) ratio = ratio of the Costa mean to the Saha and Zuber mean. *Sources:* Costa 1967 and Saha and Zuber 1974.

[f] DB = data base.

[g] Re = Reynolds number.

[h] NA = not applicable.

[i] dT = superheat (°C).

[j] G = mass flux ($kg/m^2 \cdot s$).

[k] ANS = Advanced Neutron Source.

[l] *Source*: R. D. Boyd, "Subcooled Water Flow Boiling at 1.66 MPa under Uniform High Heat Flux Conditions;" *Fusion Technol.* **16**, 324 (November 1989).

[m] *Source:* Costa 1967.

[n] *Source:* R. S. Smith and W. L. Woodruff, *A Computer code, NATCON, for the Analysis of Steady-State Thermal-Hydraulics and Safety Margins in Plate-Type Research Reactors Cooled by Natural Convection,* ANL/RETR/TN-12, Argonne National Laboratory, Chicago, December 1988.

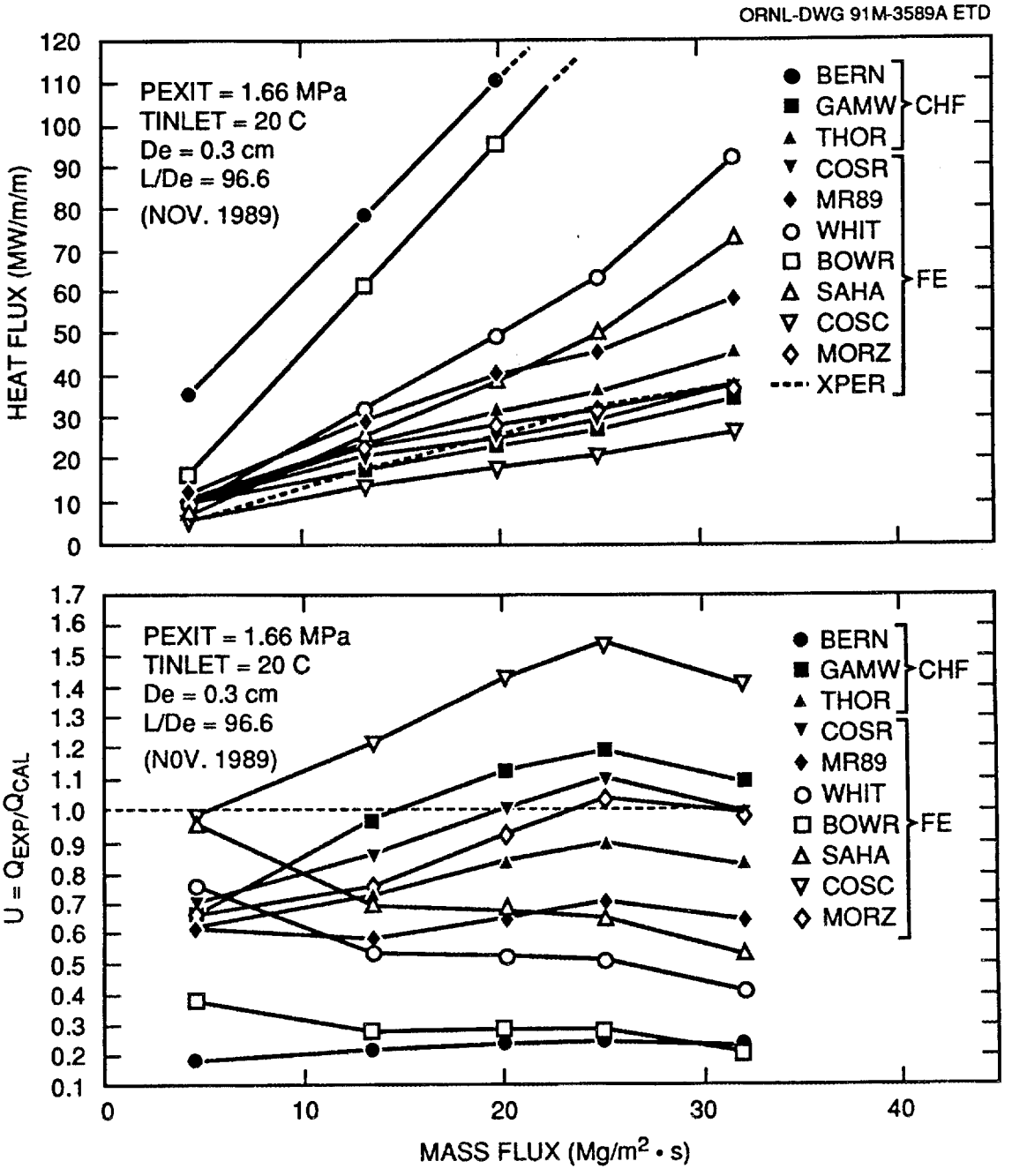

Fig. 4.1. Comparison of all critical heat flux (CHF) and flow excursion (FE) correlations with Boyd CHF data.[63]

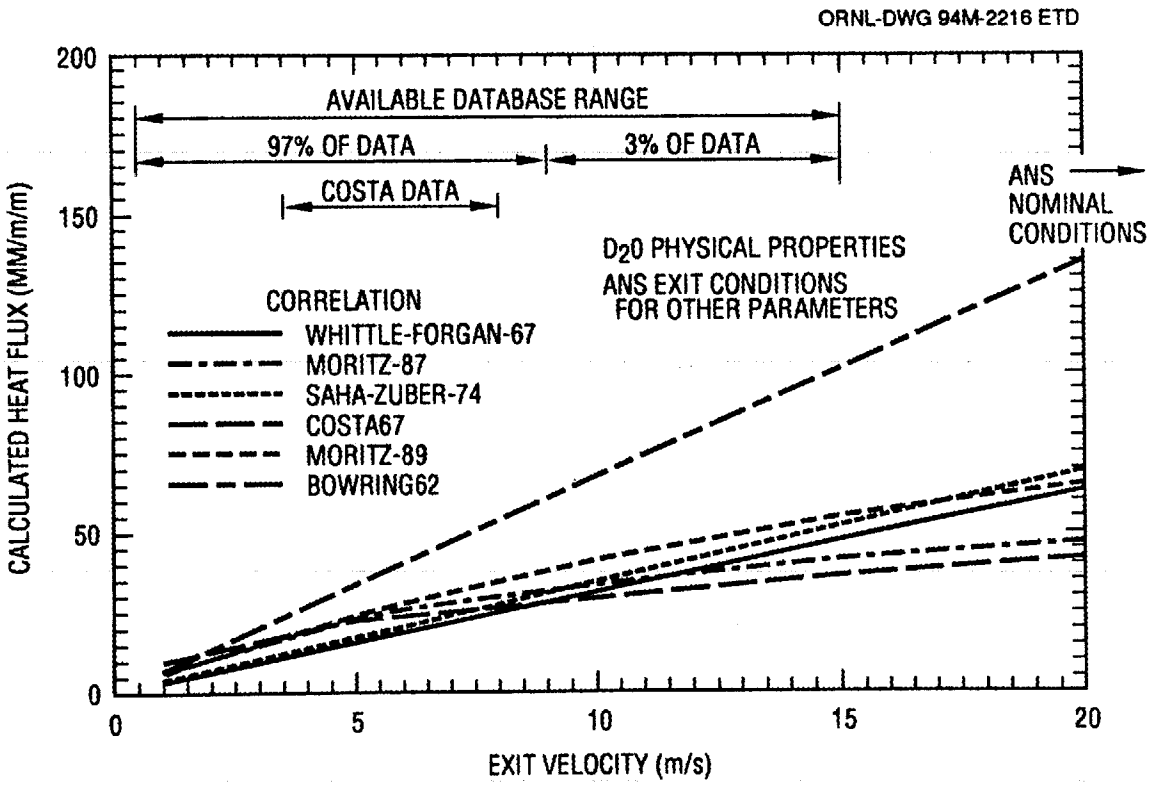

Fig. 4.2. Comparison of flow excursion correlations.

- Comparing the Gambill/Weatherhead correlation against Boyd's CHF data shows a close agreement, with a mean of 1.07 and a standard deviation of 20% (see Table 4.4). With Boyd's data being of high quality and very close to the ANS conditions, the assumed conservatism was reconsidered, and a mean value of 1.0 was assumed.
- Comparing the B-R correlation for IB to the total data base results in a mean of 1.02 and standard deviation of 23%. A mean value of 1.0 was assumed in spite of the small number of points in the data base. This assumption is justified in part by the insensitivity of the predictions to large deviations in the correlation. Sensitivity is caused by the high subcooling and the domination of the results by the forced convection heat transfer correlation. In addition, the B-R correlation is widely used in T/H codes for reactor licensing and is generally considered to be conservative.
- Encouraged by the Costa experiment, where a standard deviation of 8.4% was achieved in a dedicated and high quality experiment, and similar achievements by B&W and Westinghouse for their respective CHF experiments,[118,119] as well as by Weisman[120] and Katto,[121] it was agreed that similar standard deviations can eventually be achieved through high quality and dedicated ANS experiments. On the basis of this kind of **future expectation**, a standard deviation of 10% was assumed for all three correlations.

Following this line of integrated judgement, a common uncertainty distribution was selected for all three correlations, where the mean U factor is 1.00 and the standard deviation is 10%, as reflected in Table 4.2. It is recognized that, as new experimental data become available, new correlations will likely be needed and developed. The extrapolated uncertainties will have to be examined in light of those new correlations. It is believed, however, that the correlations currently used will be shown to be conservative.

Uncertainties in reactor physics parameters, which include local and streak-average power density distributions, and fuel beyond normal boundaries, (see Tables 4.2 and 4.3) are engineering estimates. The streak-average distribution reflects the integral uncertainty in calculations along a significant length along the core (approximately half of the core length) and narrow width ($\sim$2 mm); and, hence, a standard deviation smaller than for the local distribution is used. Although not indicated in these tables, upper limits on the uncertainty probability distributions for power density U factors were used—namely 1.10 for local and 1.05 for streak-average. These factors obviously reflect the belief that calculations will never be in error above them. Uncertainty values for fuel beyond normal boundaries (which results in a higher than nominal heat flux because of gradients in the thermal neutron flux) consider current HFIR fuel plate manufacturing limits. The axial boundary uncertainty value selected for ANS is much lower than values used in HFIR (which are a function of span position). This difference exists because of the heavy water (D_2O) moderator in ANS vs light water (H_2O) in HFIR. Also, ANS employs poisons at the fuel plate ends (and may use edge poisons as well) to suppress neutron flux peaking.

There are a number of very significant parameter uncertainties associated with the fuel element. These uncertainties include fuel segregation/nonbond (see Sect. 4.5 for a description of the defects), hot streak fuel segregation, integrated hot streak, fuel plate heated length, channel gap width, and oxide thickness.

The effect of fuel segregation and nonbonds on heat flux and temperature peaking has been analytically investigated rather thoroughly (see Sect. 4.5); however, fuel plate manufacturing data that are sufficiently detailed to characterize the frequencies and magnitudes of these defects are only beginning to become available. In some early stages,[122] uncertainty probability distributions were estimated for local fuel segregation alone (no nonbond) using a HFIR fuel plate rejection fraction ($\sim$1% of plates)[123] resulting from the defect. The defect fraction was assumed to comprise the "tail"

of a log-normal distribution with an assumed mean value (which was varied) that represented the highest fuel segregation anywhere on the plate. Although the distributions were crude estimates, they suggested that at least one fuel plate in the core would contain a fuel segregation defect near the inspection tolerance limit. For this reason, and because of the lack of detailed fuel plate manufacturing data, the uncertainty associated with this defect is treated deterministically. Further, its uncertainty is lumped with that associated with a nonbond.

The selected uncertainty value (1.313) is the highest value possible corresponding to the anticipated ANS fuel plate manufacturing tolerance limits for the worst possible configuration of the defects, their location on the plate (e.g., in a thin fuel meat region), and the time in the cycle. (See Sect. 4.5.2 for the derivation of the uncertainty value selected.) However, the value used for ANS is significantly lower than that used in HFIR (typically 1.8).[6] This discrepancy is the primary result of fuel plate design and manufacturing improvements anticipated for ANS including fuel meat centered within the fuel plate thickness, a maximum 1-mm-diam nonbond (vs 1.5 mm for HFIR), and a maximum 20% excess local spot fuel segregation (vs 30% for HFIR).

The ANS local fuel segregation/nonbond uncertainty value reflects all of the above improvements. Of all of these improvements, centering the fuel meat has the most impact.

The hot streak fuel segregation uncertainty represents average fuel loading variations in segments 1.27-cm long (along the length of the fuel plate) and 2-mm wide over the entire fuel plate. (This geometry represents that which is presently measured during inspection of HFIR fuel plates.) This uncertainty is treated deterministically as indicated in Table 4.3 with a U factor (U24) value of 1.10, which corresponds to the HFIR fuel plate manufacturing tolerance limit for this defect.

The integrated hot streak uncertainty accounts for average fuel loading variations (above or below nominal) along the length of the fuel plate and is used to calculate the effect of these variations on the coolant bulk temperature rise axially along the core. Note that the integrated average value of loading variations along the fuel plate up to the axial location of interest determines the effect on coolant bulk temperature rise. As indicated in Table 4.2, this uncertainty (U factor U24m) is treated with a probability distribution (plate level) that was developed as follows. Based on previous analysis, it was determined that the location of the limiting heat flux (i.e., IB, CHF, or FE) in the L7 core design occurs in the exit half of the core (or fuel plates). Thus, averaging was performed conservatively over the entrance 40% of the fuel plates and then was assumed to apply at all axial locations in the last (exit) 60% of the fuel plates. This averaging was statistically performed based on HFIR fuel plate inspection data, which indicates that 1% of the plates are rejected because of an average +10% or more loading variation over a region 1.27-cm long (in the axial direction of the fuel plate) and 2-mm wide.[123]

The 1% rejection fraction was conservatively assumed to comprise the "upper" tail of a normal distribution with a mean of zero (no excess loading) representing fuel loading in a 1.27-cm-long segment. The corresponding standard deviation, σ_{seg}, is 0.0429. However, the interest here is in the integrated average distribution through the first 40% of the core (i.e., the core inlet region). This distribution is obtained by statistically "stacking-up" the 1.27-cm segments to form a continuous hot streak. This new distribution is the distribution that represents the average of this segment stack over the first 40% of the core. This distribution is also normal with a mean of zero and a standard deviation, σ_{streak}, given by:[124]

$$\sigma_{streak} = \sigma_{seg} / \sqrt{N_{seg}}$$
$$\sigma_{streak} = 0.0429 / \sqrt{16} = 0.0107 \quad , \tag{4.1}$$

where

σ_{streak} = standard deviation for a continuous hot streak,
σ_{seg} = standard deviation of the hot streak distribution,
N_{seg} = number of stacked segments.

Note that along the width of the plate there are ~220 potential hot streaks, assuming each streak spans ~0.4 mm of the plate width. The 0.4-mm value is based on the HFIR fuel plate inspection procedure in which a 2-mm-diam inspection beam is used to scan lengthwise down the plate in a series of passes proceeding from one edge (radial) of the plate to the other. The procedure calls for a 0.4-mm-wide overlap, which was interpreted to mean that the inspection beam only moves radially 0.4-mm per pass; thus, ~220 passes would be required to transverse the entire plate. However, it was subsequently recognized that the 0.4-mm-width overlap means that adjacent beam passes only overlap each other 0.4-mm. In this case, only ~55 passes would be required to transverse the entire plate. The use of the 220 vs 55 potential hot streaks in the development of the probability distribution is conservative and will be revised for future T/H analyses. Note that the 1% plate rejection value indicated above is tied to this procedure.[123]

Thus, in order to determine the distribution that describes the highest (loaded) streak in a plate, MC analysis was used in which the single streak distribution was sampled 220 times (per plate), and the worst value for the sample plate was determined and saved. This procedure was performed multiple times in order to develop another distribution, this one presenting the worst streak on a fuel plate. This distribution was found to match quite well to log-normal distribution with the distribution parameters given in Table 4.2. Although not indicated in the table, values resulting from this distribution that are > 1.10 (e.g., the tails) are not used since the plate would be rejected. However, a value > 1.10 is very unlikely to occur since the statistical averaging approach employed here greatly reduces the integrated hot streak uncertainty, even for very high probability values. As detailed fuel plate manufacturing data become available, the validity of the developed integrated hot streak distribution will be assessed and revised.

The fuel plate heated length uncertainty accounts for variations in the length of the fueled portion of the fuel plate. In addition to causing heat flux peaking (i.e., fuel beyond normal axial boundary uncertainty described previously), this variation causes an increase in the coolant bulk temperature rise. As indicated in Table 4.2, this uncertainty (U2) was represented with a probability distribution (plate level). This probability distribution was developed based on HFIR fuel plate manufacturing limits and rejection data associated with the heat transfer area of the fueled portion. The data[123] indicate that ~1.2% of the plates are rejected because of deviations $> \pm 4.5\%$ from nominal. The corresponding span and length defect limits are 2.1 and 2.4%, respectively. Assuming that the defects in span and length dimensions are equally likely and independent, then:

$$\begin{aligned} P_{nr}^{T} &= P_{nr}^{s} \times P_{nr}^{l} = P_{nr}^{s} \quad , \\ P_{nr}^{s} &= 1 - 1.2\% \quad , \\ P_{nr} &= 0.99398 \quad , \\ P_{rej} &= 1 - P_{nr} = 0.00602 \quad , \end{aligned} \tag{4.2}$$

where

P_{nr}^{T} = probability plate not rejected because of a heat transfer area defect,
P_{nr}^{s} = probability plate not rejected because of a "span defect,"
P_{nr}^{l} = probability plate not rejected because of "length defect,"
$P_{nr} = P_{nr}^{s} = P_{nr}^{l}$,
P_{rej} = probability of rejection because of the length of the defect.

Next, assuming length variations are normally distributed with a mean of 1.0 (no variation), the standard deviation of the distribution can be determined as follows:

$$F = 1 - P_{rej}/2 = 0.99699 , \tag{4.3}$$

where F is the value of the cumulative distribution function at the upper inspection limit, from which the value of the standardized random variable, Z, is 2.75.[26] Hence, using the random variable, x, for length variations and, μ, its mean, the standard deviation, σ_l^{HFIR}, is:

$$\begin{aligned} Z = 2.75 &= (x - \mu)/\sigma_l^{HFIR} , \\ 2.75 &= (1.024 - 1)/\sigma_l^{HFIR} , \\ \sigma_l^{HFIR} &= 0.00872 . \end{aligned} \tag{4.4}$$

Now, for ANS, the maximum heat transfer area uncertainty is anticipated to be 2%: 1% span and 1% length. Therefore, if the HFIR P_{rej} (i.e., Z value) is applied to ANS, then the ANS standard deviation, σ_l^{ANS}, for its length deviation is:

$$\begin{aligned} Z = 2.75 &= (x - \mu)/\sigma_l^{ANS} , \\ 2.75 &= (1.01 - 1)/\sigma_l^{ANS} , \\ \sigma_l^{ANS} &= 0.0036 . \end{aligned} \tag{4.5}$$

This series of equations obviously implies that significant improvements in the control of variations in the fueled length parameter will be achieved in the ANS fuel plate manufacture; these estimates will be revised as what can be achieved becomes clear. Although not indicated in Table 4.2, values resulting from the fuel plate heated length uncertainty probability distribution that are $> \pm 1\%$ from nominal are not used because the plate would not be used in the core.

Uncertainties in the fuel element channel gap widths significantly impact the ANS maximum safe achievable power level. Power decreases roughly proportionally with decreases in the gap width, with CHF or FE as the thermal limit (see Sect. 5.1.1). Variations in the gap width are determined by the

manufacturing process and the operating environment. For the latter, factors affecting the gap width variability include oxide buildup on the fuel plates, fuel plate stresses resulting from pressure differences across the plates, temperature variations, flow frictional force, and fuel swelling during burnup. Investigations to address both manufacturing and operating environment factors affecting gap variations are in progress. Results of some of these investigations are summarized below. These results provide a flavor of the approach being taken by ANS to characterize channel gap size variations in the longer term and provide support to the manner in which these variations were handled in the CSAR. As indicated in Table 4.4, the channel gap width uncertainty is treated deterministically, with a 10% reduction in the nominal width.

Coolant channel gap variability associated with the manufacturing process has been studied by analyzing HFIR fuel element coolant channel gap variations since these variations are representative of what is expected for ANS, and no ANS data are presently available. The HFIR manufacturing tolerance gap width limits are 1.27 ± 0.254 mm locally and 1.27 ± 0.152 mm average across the channel span.[123] Note that HFIR fuel plate thickness tolerance limits of 1.27 ± 0.0254 mm[123] influence gap width variations. For ANS, a goal has been set to modify the HFIR manufacturing average gap width tolerance limit to be slightly more stringent, at 1.27 ± 0.127 mm. Additionally, it is intended that this average be applied along the channel length rather than (or in addition to) the width. The reason for this modification is that flow along subchannels with significant axial variations would likely be affected more than if the same variations were across the span. In the latter case, the total channel flow would be less, but individual subchannel flows would be higher than those in the subchannel with significant axial variations.

Preliminary statistical analysis of HFIR channel gap width measurements has been performed, as well as companion T/H analysis to assess the impact of gap variations on the ANS maximum achievable core power.[125,126] In a simplified analysis, the behavior of a fuel plate bounded by a wide channel on one side and a narrow channel on the other side was performed using a code developed specifically for this purpose.[126] This modified code facilitated assessment of the additional cooling provided by the wide channel as opposed to a fuel plate bounded by two narrow channels. This benefit is currently overlooked in the TASHA code.

The HFIR channel gap width data base (in electronic digital form) for statistical analysis includes measurements from two inner and three outer fuel elements. These measurement sites correspond to 1449 channels. Gap width is measured at five span positions continuously along the channel length.[124] Data reported include the minimum, maximum, and average widths for each span position. Statistical analysis has been performed on each of these three measures of gap width. Statistical analysis of the average gap size in one of the outer fuel elements (369 channels) at each of the five positions indicates that variations are normally distributed with means very close to nominal and standard deviations ranging from 0.017–0.025 mm. The smallest variation occurs at the span position nearest the outer sideplate; however, the variation nearest the inner sideplate was larger than one of the middle span positions. Thus, based on this limited set of data, average gap size variations may tend to be smaller near sideplates. Analysis was also performed on the minimum average gap width within each channel. This measurement is felt to be a conservative, but reasonable, indication of average gap width variations. Analysis indicates that variations in this measurement are also normally distributed with a typical mean and standard deviation of 1.26 and 0.018 mm, respectively.

Statistical analysis was performed to determine if a narrow channel is more likely to be adjacent to a wide channel than a channel that is nominal, as might be expected. However, analysis indicates that this tendency is weak as indicated by a correlation coefficient (for the interdependence of gap size between adjacent channels) of –0.1. As an example, however, the analysis indicates that, given a 1.143-mm average gap width for a channel (i.e., at the manufacturing tolerance limit), then the probability is 95% that each of the channels adjacent to it will be ≥ 1.26 mm.

Statistical analysis was performed to determine the minimum average gap size distribution on a whole core basis; that is, the distribution would represent the minimum average gap size for the worst (or smallest) channel in the entire core. A distribution of this type could be sampled at the core level (although with some additional conservatism) in full MC analysis (rather than the plate-level analysis), which would expedite the process (see Sects. 2.1 and 4.3). This distribution was found to be log-normal. As an example, at a 95% probability level, the core minimum average gap size was found to be 1.17 mm.

As mentioned previously, thermal analysis was conducted to determine the cooling benefit provided by a channel with a near nominal sized gap adjacent to a narrow one (e.g., 1.26-mm channel adjacent to a 1.14-mm channel; see above), as opposed to assuming that two narrow channels exist together. It was determined that the benefit results in an ~2% increase in the core maximum power level for this case, based on FE as the thermal limit.

One can also compare the power benefit of using a statistically based treatment of average channel gap size variations vs the worst case (i.e., manufacturing tolerance limit) value of 1.14 mm. For the core level distribution described above, a minimum gap size of 1.17 mm was indicated for a 95% probability level, which implies an increase in the maximum core power of ~2.5% (assuming power increases proportionally with gap-size increase).

As indicated previously, the other cause of channel gap-size variations is the operating environment. It appears that the most significant source of variations resulting from the plate environment for the current ANS design is thermal stress, which has been evaluated with analysis.[127] Although thermal and plate-stress analyses are interdependent, the initial thermal stress calculations are based on thermal conditions with assumed channel gap-size variations. Results of the thermal calculations were then used as boundary conditions for the stress analysis. Thermal conditions were based on steady-state operation at the scram set point (LSSS) limits and included appropriate uncertainties (99.9% probability level). The corresponding power level was 351 MW(t). Plate-to-plate temperature differences drive thermal deflections, and the two factors that dictate plate temperature differences are channel gap size and plate fuel loading. For this analysis, a hot plate was assumed to be adjacent to a narrow, 1.143-mm-wide channel and to contain 1% above the nominal fuel load (1% overload is also the HFIR manufacturing tolerance limit); a cold plate was assumed to be adjacent to a 1.40-mm-wide channel and to contain 1% below the nominal fuel loading. To provide conservative estimates of the fuel plate temperatures, which results in lower plate strength, EOC conditions (with maximum oxide growth) were assumed.

Thermal stress analysis calculations, which were performed using a finite element model, provided the following results regarding fuel plate deflections. Fuel deflections:

- are a function of span and axial position,
- are not significantly affected by sidewall temperature variations,
- are largest at the center of the span and midway along the fuel plates with ~17% deflection,
- have an average deflection along the axial length at center span position of ~13%, and
- are small near sidewalls (where they are supported).

The next obvious step would be to revise thermal calculations with the results of these stress calculations and to recalculate thermal deflections. The process would continue until thermal/stress results do not change. However, this revision has not been undertaken.

ANS fuel plate stability to hydraulic loads has been investigated by analysis[128] and experimentation.[129] Although there are differences in results between the two, with the experimental study indicating that the plates are more stable than the analysis shows, both studies indicate that a sudden collapse of the fuel plates does not appear to be the limiting condition imposed by the fluid

flow for current ANS design conditions. Indications are that flow-induced plate deflections are not large at nominal flow conditions as well. For example, given a 10% preoperation channel gap width defect (or 0.0635 mm/plate), the maximum plate deflection induced by the fluid is only ~0.03 mm. Additionally, the induced deflection is directed opposite to the preoperational defect (i.e., it acts to open the channel).[128]

The effect of fuel plate oxide buildup on channel gap width is accounted for in TASHA. The maximum effect of this on the gap width is on the order of 9 μm (for 22-μm oxide growth on each fuel plate) or 0.7% of the nominal gap width.

The effect of fuel swelling on channel gap width could be significant under some conditions. Maximum width reductions of ~6% (see Sect. 4.5.2) could occur in locations where thick fuel meat exists, but much smaller reductions would occur in thin meat regions, which is where heat fluxes are highest. ANS fuel plate temperature criterion (i.e., fuel plate centerline temperature) was selected to limit fuel swelling. More study is needed to characterize this effect on gap width.

Based on the results of the studies described above addressing the factors controlling channel gap width variations and recognizing that the current L7 core design is thermally limited near the sideplates, the deterministic gap uncertainty value of 10% (reduction in nominal, but not including oxide buildup) is felt to be reasonable. The L7 power distribution is very peaked near the sideplates so that, even with significantly larger gap width variations along the center span portion of the plate, the core is not anticipated to be limited in this area. Efforts to characterize channel gap-size variations more realistically and to perform more accurate thermal analyses of the effect of these variations on maximum achievable core power will continue.

There have been limited statistical investigations of the uncertainties associated with the ANS fuel plate oxide growth rate correlation. Initial statistical analysis showed the correlation to overpredict the data with a U factor (U9) mean of 0.89 and a standard deviation of 0.18. It was found that the correlation was most conservative at high oxide thicknesses, which are obviously of most concern. Thus, for CSAR analysis, a deterministic value of 1.10 was used, providing a 10% margin on the conservative correlation values.

The uncertainties for inlet temperature, exit pressure, flow, and reactor power in Tables 4.2 and 4.3 (and Table 4.5 discussed subsequently) are those applicable to the operating margin (window). Thus, these uncertainties include both measurement and control uncertainties and, as indicated in the tables, are small deviations around the nominal operating point.

The net uncertainty values in the tables were derived from both measurement and control uncertainties using the values for each presented in Table 4.6.[130] This derivation used the SRSS method. In performing this derivation, the control margin uncertainties were interpreted as two standard deviation values (measurement uncertainties as three standard deviation values as indicated in Table 4.2) for the purpose of calculating the one standard deviation net values given in Table 4.6. Further, as indicated in Table 4.2, the corresponding net uncertainty probability distributions were assumed to be normal. For the deterministic net uncertainty values given in Table 4.7, the values given in Table 4.6 were simply used as given in the SRSS calculations; thus, they represent two to three standard deviation values.

Investigation of thermal limits was also performed for the safety margin (or window), which allows variations in these parameters to the LSSS limits. For the safety margin analysis, each parameter was set to its LSSS limit plus measurement and control uncertainties except for the reactor power, which was the calculated parameter. Measurement and set point uncertainties were combined using the SRSS method to calculate deterministic net uncertainty values as described above for measurement and control uncertainties. The trip set point values presented in Table 4.6 were then multiplied by these uncertainty values to give the net values provided in Table 4.7.

In addition, correlations for heavy- and light-water properties were developed and their errors were quantified. A more detailed description of this correlation and data evaluation process is given in ref. 8.

Table 4.5. Additional parameters treated with peaking worst case values in statistical peaking factor method

Parameter	U[a] factor	Worst case value
Inlet coolant temperature	U6	1.014
Exit pressure	PSAR[b]/FSAR[c]	0.949
Flow	PSAR/FSAR	0.99
Forced convection heat transfer correlation	U8	0.94
Friction factor	U7	0.90
Channel gap width	N/A[d]	1.14 mm[e]
Oxide correlation	U9	1.10

[a]U = uncertainty.
[b]PSAR = preliminary safety analysis report.
[c]FSAR = final safety analysis report.
[d]N/A = not applicable.
[e]10% reduction in nominal (1.27-mm) gap width.

Table 4.6. Advanced Neutron Source set points and instrumentation and controls related uncertainties[a]

Response	Design point (%)	Trip set point (%)	Set point uncertainty (%)[b]	Measurement uncertainty (%)[b]	Measurement response time (ms)	Control margin stainless steel (%)	Over-shoot typical (maximum) (%)
Flux/flow ratio	1.0	>1.15	±1	±3	1 (flux) 200 (flow)	<3	3(10)
Thermal power	100	>115	±1	±2	2000	<2	3(10)
Primary outlet pressure	100	<80	±1	±1	30	<5	5
Reactor inlet temperature	100	>120	±1	±1	2000	<1	5(20)
Flux rate	0	>20	±1	±5	N/A[c]	N/A	5 ms
Primary flow	100	<87[d]	±1	±1	200	*e*	NA

[a]*Source:* J. L. Anderson, Martin Marietta Energy Systems, Inc., Oak Ridge, Tennessee, letter to M. Siman-Tov, Martin Marietta Energy Systems, Inc., Oak Ridge, Tennessee, March 4, 1992.
[b]Measurement and set point uncertainties are interpreted as three standard-deviation values.
[c]N/A = not applicable.
[d]Trip point for 100% power.
[e]Flow is not a controlled variable but is determined by pump characteristics and system pressure drops. Nominal full flow will vary with core irregularities, oxide buildup, etc.

Table 4.7. Safety margin values for inlet temperature, exit pressure, and flow

Parameter	Safety margin value[a]
Inlet temperature	1.22
Exit pressure	0.79
Flow	0.99

[a]Multiplier relative to nominal.

4.3 INTEGRATION OF MONTE CARLO ANALYSIS CODE WITH THE TASHA CODE

The MC technique is well known as a technique for statistical analysis of systems that are too complex for analytic solution. An early example is the reactor safety study WASH-1400,[131] for which a simple generic driver program was written in FORTRAN to allow a user-written function to be added easily. That program, named SAMPLE,[114] was used to determine probability distributions and confidence intervals for various functions throughout the reactor safety study. The driver routine was sufficiently general and has been used in many other studies as a result of the incorporation of improved sampling techniques and other performance enhancements and generalizations.

The TASHA code was incorporated into the Science Applications International Corporation version of SAMPLE as the "user function." The integrated code functions as outlined in Fig. 4.3. The result of the analysis is the determination of the maximum power level at a given probability and confidence level.

A series of quality assurance test calculations have been performed to ensure the integrated code is functioning as desired. Initial simulations include an example calculation with the integrated codes. In the calculation, plate-level uncertainties (e.g., localized fuel segregation and hot streak) were treated as if they were core-level, which produces nonconservative results. However, this treatment is being revised. The example calculation examined maximum ANSR core power (G3 core design) assuming the fuel centerline temperature is limiting at EOC. The maximum core power probability distribution function (PDF) and cumulative distribution function (CDF) are presented in Figs. 4.4 and 4.5, based on 1000 trials. Currently, the latest version of TASHA is being integrated with the SAMPLE code.

4.4 THE STATISTICAL PEAKING FACTOR METHOD

As indicated previously, a simplified method was used to incorporate uncertainties in most of the steady-state analyses and all of the transients. This method is the statistical peaking factor approach and is outlined in Fig. 4.6. In this approach, two statistically based peaking factors are first generated separately (as discussed below) and then are input to the TASHA code along with a number of other parameter uncertainties that are treated as worst case values. In contrast to the procedure used with the fully integrated TASHA and SAMPLE code, only one TASHA code calculation is required to determine the core maximum power level at each probability and confidence level.

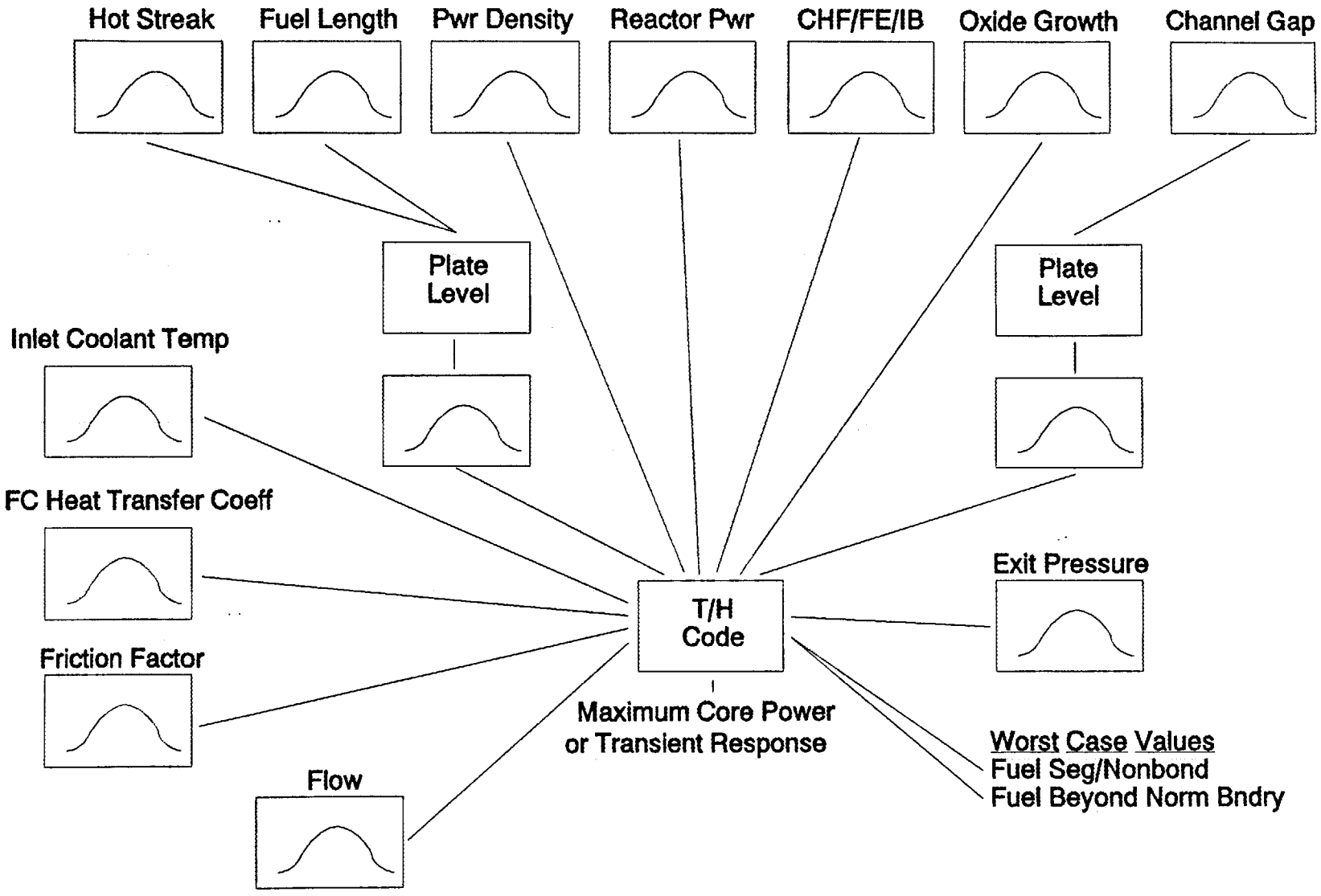

Fig. 4.3. Schematic of procedure for direct input of uncertainty distributions to thermal code via the sample code.

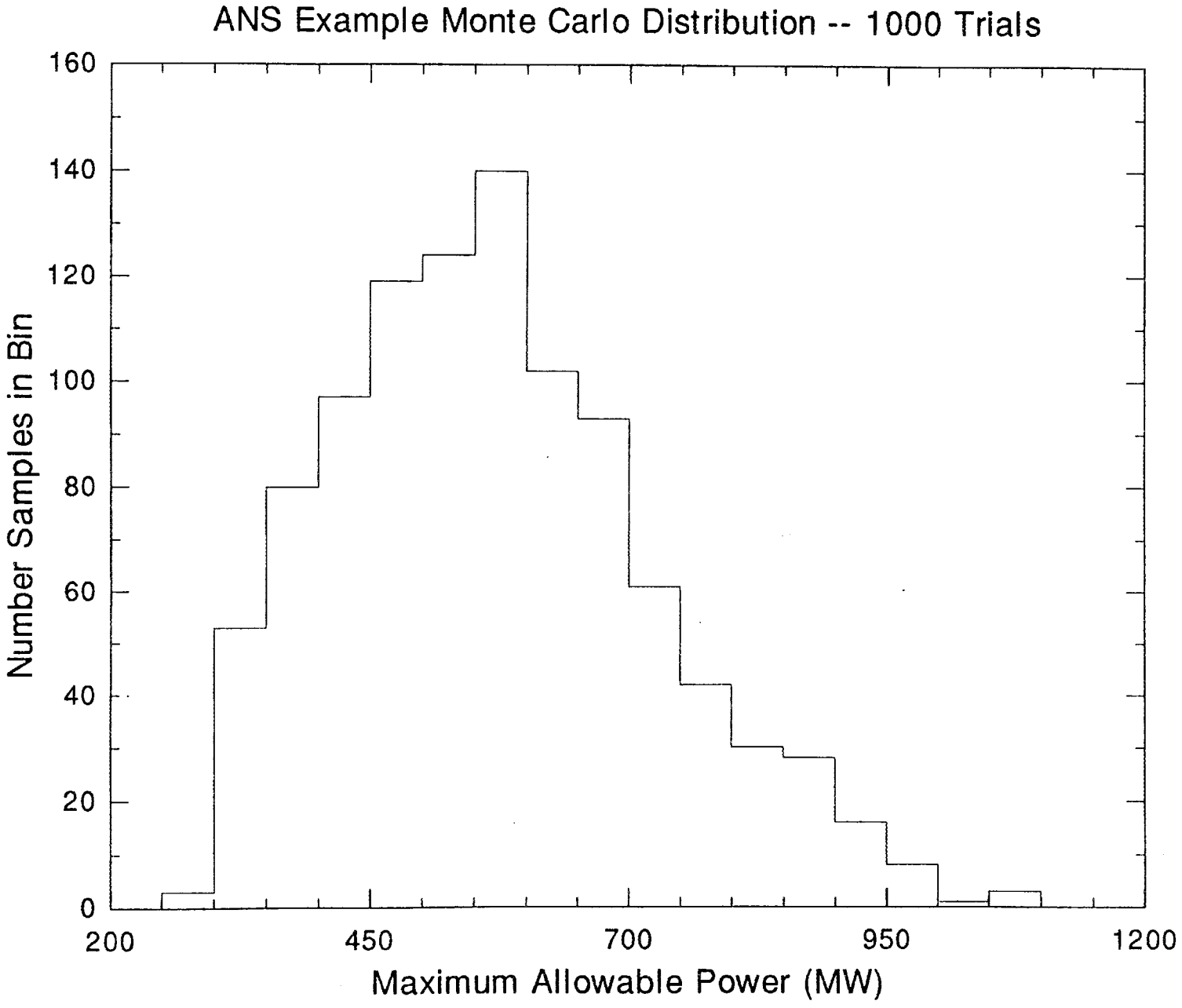

Fig. 4.4. Example core maximum power probability distribution function based on fuel plate centerline temperature limit at end-of-cycle.

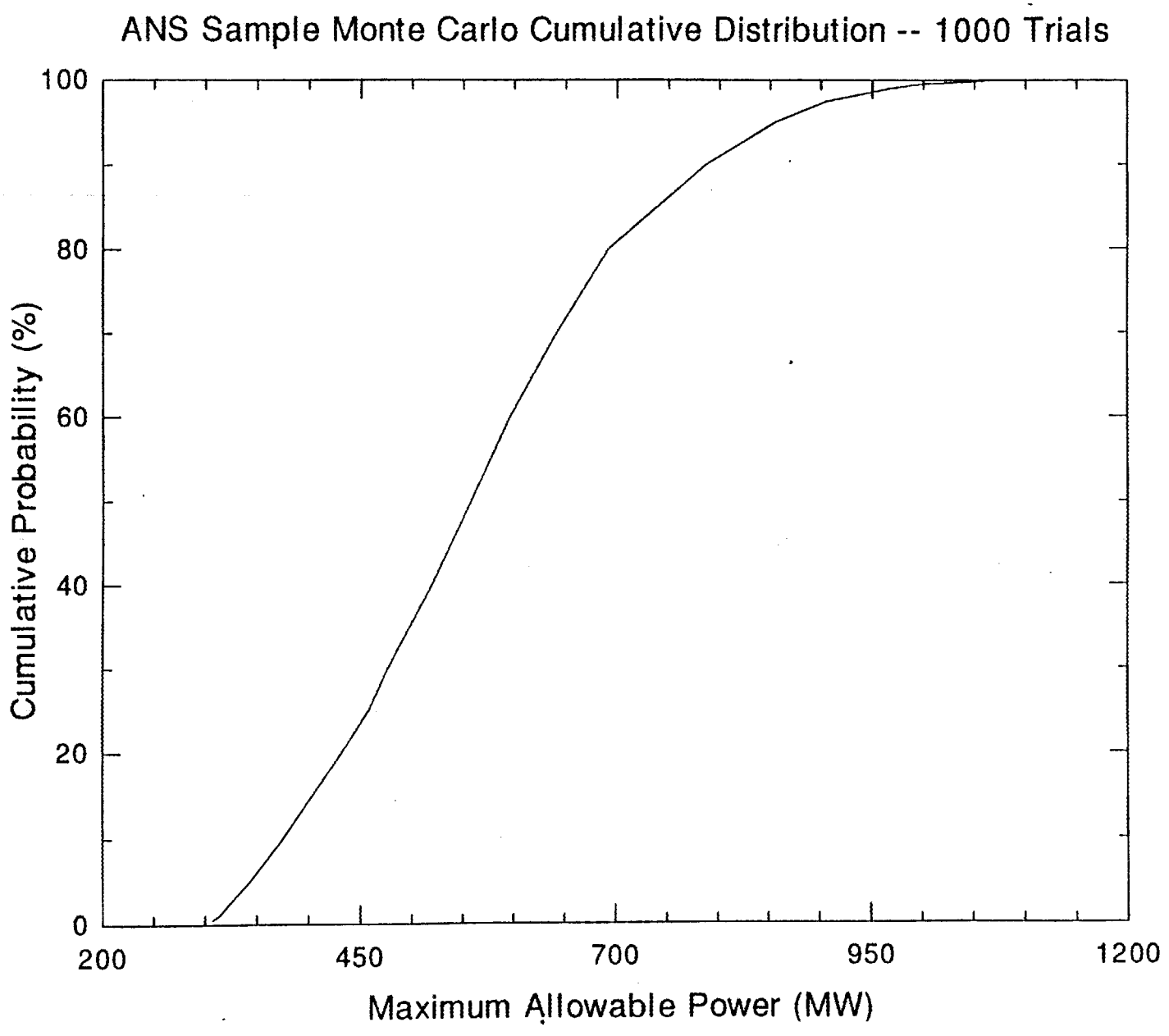

Fig. 4.5. Example core maximum power cumulative distribution function based on fuel plate centerline temperature limit at end-of-cycle.

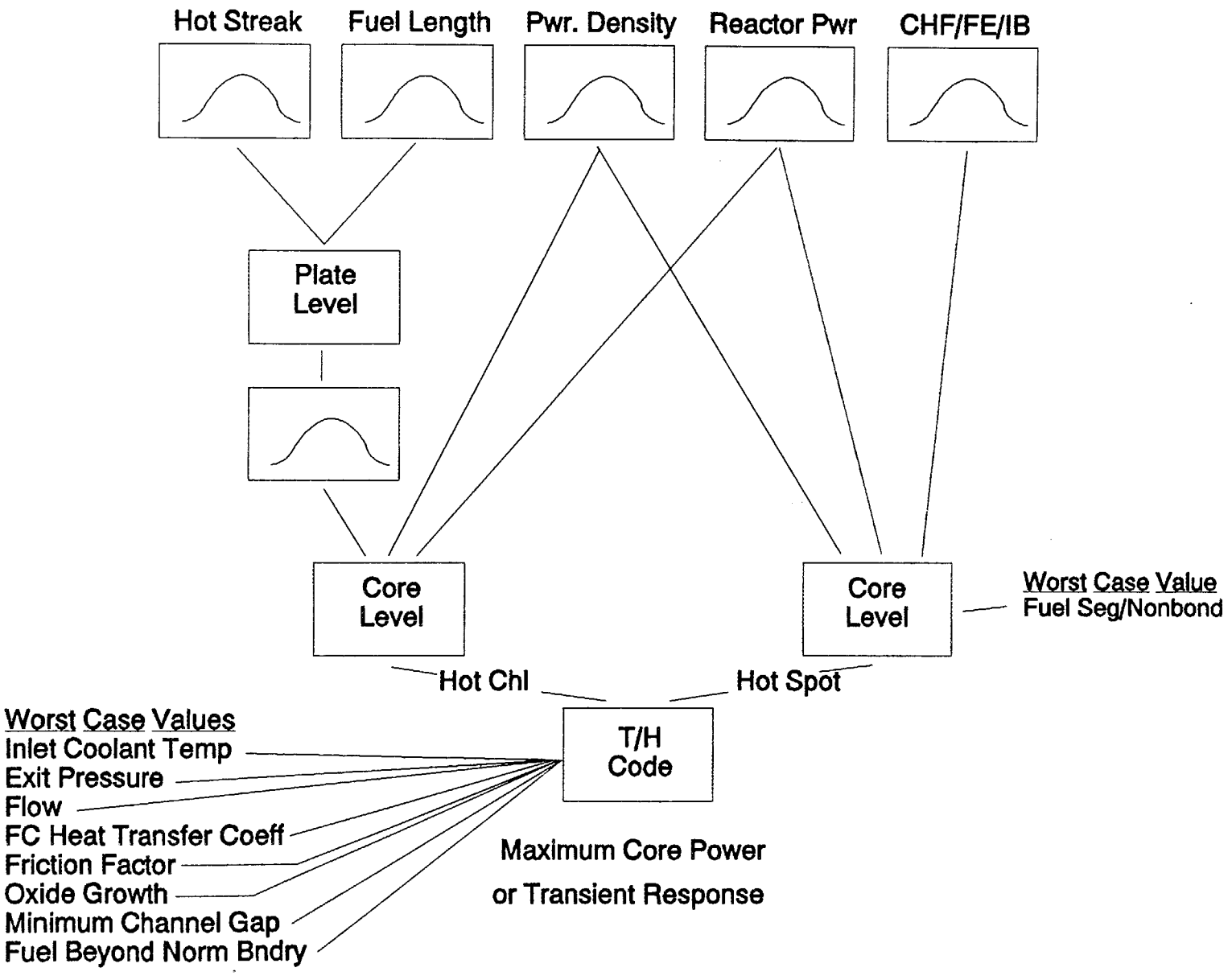

Fig. 4.6. Schematic of procedure for peaking factor based statistical analysis.

One peaking factor is defined to account for uncertainties in parameters directly affecting the fuel plate heat flux and is denoted as the hot spot peaking factor. The other is defined to account for uncertainties in parameters directly affecting the bulk coolant temperature rise along the core and is denoted the hot channel peaking factor. (These factors are also discussed in Sect. 2.) Uncertainties in parameters that scale proportionally with power directly affect either the fuel plate heat flux or the bulk coolant temperature rise.

For the hot spot, these parameters include reactor power; local power distribution; IB, CHF, or FE limit; and fuel segregation with or without nonbond. For the hot channel, the affected parameters include reactor power, streak-average power distribution, fuel plate heated length, and integrated hot streak.

As an example, the hot spot factor for CHF, f_{hs}^{CHF}, is defined by:

$$f_{hs}^{CHF} = U1 \times U3/U22 \times U_{sn} \ , \tag{4.6}$$

where U_{sn} denotes the combined effect of local fuel segregation plus a nonbond. Note that U_{sn} is treated deterministically here, but future analyses will treat this factor statistically. The three remaining U factors, which are core-level parameters (see Table 4.2) are sampled once in MC analysis (see Fig. 4.6) for each core trial and then are used to calculate f_{hs}^{CHF}. Then, based on 10^6 trials, a PDF and CDF for f_{hs}^{CHF} are produced. The IB hot spot factor is calculated in the same manner, but with U22 replaced by U23; however, the uncertainty probability distribution for them is currently the same, thus the hot spot factor for both is the same. For the FE hot spot factor, f_{hs}^{FE}, U_{sn} is replaced by the hot streak fuel segregation uncertainty (i.e., 1.10) described in Sect. 4.2. For temperature limit calculations, two other factors are calculated that are the same as f_{hs}^{CHF} and f_{hs}^{FE}, but without U22 and U25, respectively. Two peaking factors are used for the oxide limit because of the form of the oxide correlation [Eq. (3.10)]. The oxide is assumed to grow based on the hot streak heat flux (i.e., using FE without U23) because conduction tends to wash out localized heat flux peaks (such as that imposed by fuel segregation and nonbonds) as the oxide thickness grows.[132] However, the temperature rise through the fuel plate is calculated based on the localized peak heat flux (i.e., using f_{hs}^{CHF} without U22). As mentioned in Sect. 2.1, calculations such as those described in Sect. 4.5.2 will be used to "tune" this calculation method (or to show that it is conservative).

The hot channel factor, F_{hc}, is defined by:

$$F_{hc} = U1 \times U_{pd} \times (U2 \times U24m)_{\max} \ , \tag{4.7}$$

where U_{pd} denotes the streak-average power distribution, and the brackets denote that the maximum value of $U2 \times U24m$ (plate-level parameters) for all plates in a given core is to be used. This value is used with the values for the other two parameters, which, as indicated previously, are core-level parameters. Thus, for a given core trial, the values of $U2$ and $U24m$ are sampled 684 times (the total number of plates in the core), the product calculated, and then the maximum value multiplied by values of $U1$ and U_{pd}. The result is a single (core-level trial) value of F_{hc}. Then, as with the hot spot factors, based on 10^6 core-level trials (684×10^6 plate-level trials), a PDF and CDF are produced.

Next, the peaking factor CDFs are used to define the appropriate peaking factors at the desired probability and confidence level. As previously indicated, these and the other parameter uncertainties are used in the TASHA code to determine the maximum core power.

The other parameter uncertainties are treated with worst case values. These parameters include those given in Table 4.3 in addition to those that could not be included in the peaking factors. These additional worst case values are provided in Table 4.6. (Note that these values were treated with probability distributions in the full MC analysis.) Table 4.8 presents peaking factors for the limiting criteria at both 95 and 99.9% probability levels.

Table 4.8. Hot spot and channel peaking factors at 95/95 and 99.9/95% probability/confidence levels

Peaking factors 95/95%	
Hot spot (IB,[a] CHF[b])	1.59
Hot spot (FE[c])	1.33
Hot spot (oxide)	1.17 and 1.39
Hot channel	1.10
Peaking factors 99.9/95%	
Hot spot (IB, CHF)	1.94
Hot spot (FE)	1.63
Hot channel	1.14

[a]IB = incipient boiling.
[b]CHF = critical heat flux.
[c]FE = flow excursion.

Off-line peaking factor models, such as those used in ANS studies, have been used in a number of other reactor studies.[133-136] These studies complement each other and address many of the issues that have been identified in ANSR uncertainty studies. The papers clearly identify the different levels of uncertainties (e.g., plate, assembly, and core) involved in analysis and the statistical complications that result. They offer alternative means to deal with them, generally through simplifying assumptions. In these studies, peaking factor models were evaluated using MC analytical techniques. Although the thermal limits were only the bulk coolant temperature (and fuel surface temperature in some studies), the concept is the same as that used in ANSR statistical peaking factor models, hot channel and spot. It is reassuring to find previous studies employing the same general technique.

One of the papers[134] shows that for high probability calculations ($\sim$0.999+), ignoring the difference in the level (i.e., plate and core) of the uncertainties results in little error (i.e., only slightly conservative); however, this relationship only holds true for the probability of plates not failing. If the probability of multiple plates failing is considered, the above simplification can be nonconservative. Given the currently assumed propagation of a fuel plate failure in the case of ANSR, this simplification can be used to enable high probability analysis. It is expected that such analysis may be required for establishing nominal operation (steady-state) power limits. An initial check of the penalty paid in ignoring the uncertainty levels was made using the ANSR hot spot statistical peaking

factor model. Results indicate that the assumption introduces conservatism that does decrease with increasing probability. At 95%, the conservatism is 17%, while at 99.999%, it is only 2.2%.

4.5 THERMAL ANALYSIS OF FUEL PLATE DEFECTS

Various perturbations from the design conditions on the peaking factors and maximum temperatures for the new ANS fuel plate design and their effect on peaking factors have been considered. These perturbations include lack of a metallurgical bond, local power excess resulting from fuel segregation, coolant temperature variations, thermal physical property variations, and fuel meat location.

4.5.1 Advanced Neutron Source Fuel Plate Design

The ANS fuel plates are thin composite plates that are manufactured in an involute shape. The plate cross section is composed of two outer clad layers that are of equal thickness with a central volume that contains fuel filler and/or fuel meat. The borders of the plate contain no fuel volume. The clad layers are aluminum (Al 6061) sheets that are metallurgically bonded to the filler meat by a rolling process that compresses the filler meat and produces a fuel plate of the desired thickness. The filler is pure Al 6061 powder, while normal fuel meat is a powder mixture of U_3Si_2 (11.2% by volume) and Al 6061 powder. Table 4.9 contains the pertinent geometric parameters of the ANS fuel plate. The fuel meat can be located next to one of the clad layers or centered in the fueled volume. The fuel meat in the HFIR design is located next to one of the clad layers in an offset location. The new ANS design specifies a centered position for the fuel meat layer. Figure 4.7 compares these two designs for the minimum fuel meat thickness condition.

Table 4.9. Advanced Neutron Source fuel plate dimensions for hot spot investigations

Geometric parameter	Dimension (m)
Clad thickness	0.000254
Filler meat volume thickness	0.000762
Total plate thickness	0.001270
Design maximum fuel thickness	0.000762
Design minimum fuel thickness	0.0001778

4.5.1.1 Heat Generation

The heat generation in the fuel meat is a function of the average local heat flux, the maximum design power density, and the meat thickness or

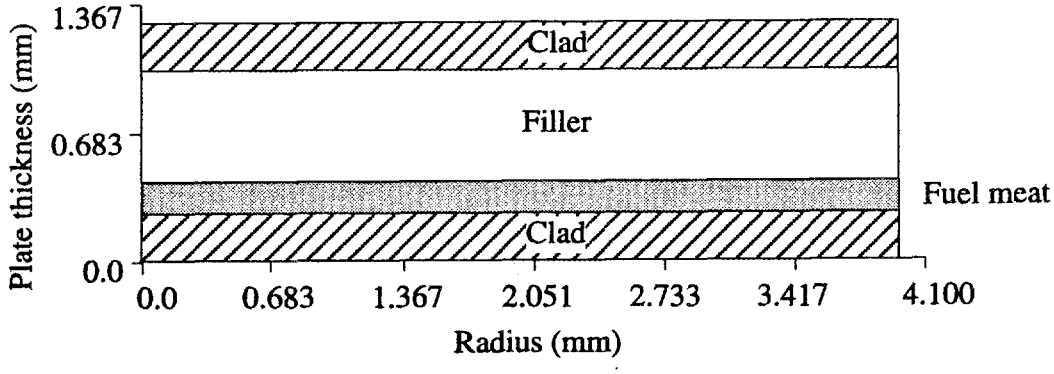

(a)

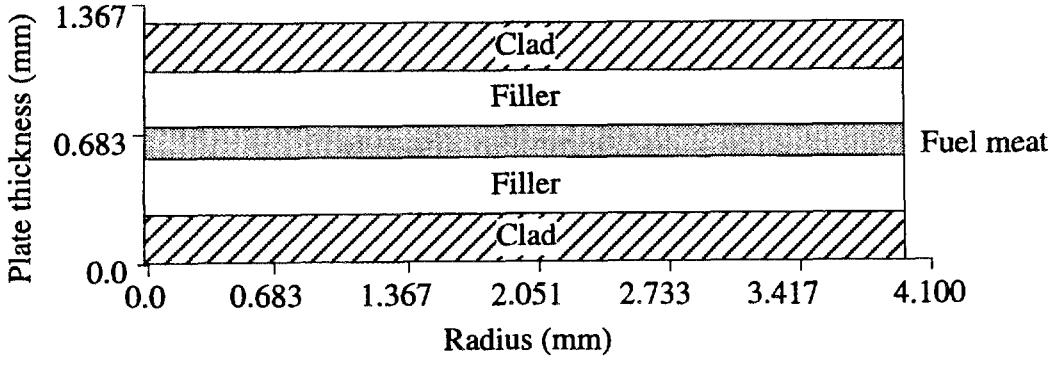

(b)

Fig. 4.7. Advanced Neutron Source fuel plate design: (a) offset and (b) centered fuel meat designs.

$$q''' = \frac{MP_d \, \phi_a}{t_m} \quad , \tag{4.8}$$

where

q''' = volumetric heat generation rate (MW/m^3),
MP_d = maximum relative power density (unitless),
ϕ_a = average local heat flux (MW/m^2),
t_m = meat thickness (m).

The heat generation in the clad and filler is not known and is assumed to be zero for these calculations. This assumption produces conservative estimates of the peaking factor and maximum temperature since increasing the fuel meat heat generation increases the calculated peaking factor and the maximum temperature.

4.5.1.2 Thermal Conductivities

A summary of the thermal conductivities that were not varied during these analyses is included in Table 4.10.

Table 4.10. Thermal conductivity

Material	Thermal conductivity (W/mm • °C)
Filler	0.17
Oxide	0.0023
Clad	$0.15693 + 1.8738 \times 10^{-4}\,T^a - 2.5238 \times 10^{-7}\,T^2$

[a]T = temperature (K).

4.5.1.3 Coolant Parameters

The fluid properties for D_2O flowing in a gap 1.27-mm wide and 70.29 mm in span were used in the Petukhov[31] correlation (see Sect. 3) to estimate the heat transfer coefficient. The D_2O properties were obtained from ref. 8. The Petukhov correlation for heat transfer coefficient as a function of temperature is used with the parameters in Table 4.11.

Table 4.11. Coolant boundary condition parameters

Parameter	Value
Velocity	2.5×10^4 mm/s (25
Hydraulic diameter	m/s)
Gap height	2.494 mm
Gap span	1.27 mm
Bulk temperature	70.29 mm
Reynolds number	90°C
Friction factor	1.8×10^5
Prandtl number	0.0173
Absolute viscosity	2.4
Fluid conductivity	2.44×10^{-10} (Ns/mm^2)
	0.0634 (W/mm • K)

The properties at the specified state were obtained by evaluating the functions defined in ref. 8 using a FORTRAN code. This code was used to generate a table of the heat transfer coefficients as a function of the average of the bulk and wall temperatures using Eqs. (3.5) and (3.6). This average temperature was used to accommodate input requirements of the thermal analysis code employed.

Calculations were performed for a range of bulk temperatures from 49–90°C. All results reported in this document used the 90°C bulk temperature.

4.5.2 Variations from Design Conditions Investigated

4.5.2.1 Lack of Metallurgical Bond

One of the major manufacturing flaws that can occur is a failure to form a metallurgical bond (nonbond) in the plate during the rolling process. This flaw can produce a major modification of the local heat flow and the heat flux from the surface of the clad into the coolant channel. Proposed inspection procedures will limit the maximum allowable nonbond to 1-mm diam. The heat transfer across a nonbond depends on many parameters, such as contact pressure between the surfaces of the nonbond void, gas composition and pressure in the void, fuel composition at the void surface, clad or filler, as well as fuel hardness and yield strength, fuel swelling, local burnup, and void surface emissivities. Most of these parameters are not known to any precision for the conditions in the ANSR, and the models that use these parameters are not necessarily precise. Although there will be some heat transfer across the nonbond, an adiabatic assumption (no heat transfer) will result in a higher peaking factor and maximum temperature and is, therefore, conservative. Although no data exist for the dimension of the nonbond thickness, it is assumed to be 0.1 mm in this analysis. Since it is assumed to be adiabatic across this gap anyway, the exact thickness assumed for the nonbond is not vital as long as the thickness is a small fraction of the diameter.

The most conservative position for a nonbond depends upon the type of plate design. For fuel offset from the center, the nonbond void position that produces the most severe thermal conditions is at the meat-filler interface closest to the center of the plate. This position produces the maximum peaking factor and fuel temperature. For the centered design, the worst location is at the meat-filler interface.

4.5.2.2 Excess Local Power

Proposed inspection procedures require that the maximum allowable local excess fuel loading be no more than 20% over a fuel plate area of 2-mm in diam. Several mechanisms can be postulated to produce this excess. The assumption that would produce the most concentrated uranium volume would be a dense lump of pure ^{235}U located at the center of the 2-mm diam spot. This scenario appears to be unlikely to occur in the manufacturing process. The next most concentrated segregation spot assumption would be a solid lump of U_3Si_2 at the center of the spot. Since the U_3Si_2 powder is controlled to have particles $< 150\ \mu m$, it is also unlikely that this condition will occur. The fuel manufacturing process is such that 50% U_3Si_2 is the maximum density that can be formed, and fuel manufactured at this density will also include 15% void and 35% Al 6061. Therefore, a segregation spot is assumed to be made up of a cylinder of 50% density U_3Si_2 extending the thickness of the fuel meat layer, surrounded by normal fuel, with a segregation cylinder diameter of 0.47-mm. This cylinder segregation model was the basis of the T/H analyses reported in this document; however, other configurations were also studied.

An alternative, and perhaps more conservative, assumption of surrounding the segregated spot with an annular volume containing only filler (no fuel) was not used since no mechanism has been proposed that can produce this condition. (This assumption may not be more conservative since the much higher conductivity of the filler would reduce the effect of the larger 50% U_3Si_2 spot.)

The ratio of heat generation in the segregated fuel to that of normal fuel is assumed to be equal to the ratio of the densities of ^{235}U in segregated and normal fuel.

$$R_s = \left[\frac{p\rho_s}{\rho_n}\right] , \tag{4.9}$$

where

R_s = ratio of heat generated in segregated fuel to that of normal fuel (unitless);
p = volume fraction of U_3Si_2 (0.50);
ρ_s = ^{235}U density in segregated fuel (10.472 mg/mm^3),
= Mu • En,
Mu = mass of uranium (all isotopes) in U_3Si_2 per volume of U_3Si_2 = $r_u\rho_1$ (mg/mm^3),

$r_u = 0.921\left[\frac{^TU}{U_3Si_2}\right]$, mass of total uranium per mass of U_3Si_2,

ρ_1 = density of pure U_3Si_2 = 12.2 mg/mm^3,

En = enrichment = $0.932\left[\frac{^{235}U}{^TU}\right]$;

ρ_n = ^{235}U density in normal fuel (1.1184 mg/mm^3),
= En ρ_m,
ρ_m = ^TU density in normal fuel (1.2 mg/mm^3).

For 50% U_3Si_2, R_s = 4.68.

The diameter of the segregation spot (d_s) is calculated from the relation:

$$1.0A_i + (R_s - 1.0)\frac{d_s^2\pi}{4} = 1.2A_i \quad , \tag{4.10}$$

where

A_i = area of the inspection spot (3.24×10^{-6} m^2),
R_s = ratio of heat generated in segregated fuel to that of normal (unitless),
d_s = diameter of the segregation spot (0.471 mm).

The excess local heat generation is also a function of the average local power or:

$$q'''_{sat} = \frac{R_s\, p_d\, \phi_a}{t_m} \quad , \tag{4.11}$$

where

q'''_{sat} = at volumetric heat generation (MW/m^3),
R_s = ratio of heat generated in segregated fuel to that of normal fuel (unitless),
p_d = local relative power density (unitless),
ϕ_a = average local heat flux (MW/m^2),
t_m = meat thickness (m).

Since a segregation spot in the fuel meat is a possible cause of the metallurgical bond failure, a segregation volume and a nonbond could be coincidental. If the segregation spot causes a nonbond, then it is logical to assume that both would have the same diameter. If the nonbond was the same diameter as the cylinder model, then this nonbond size would not be detected. Since it is not possible to ensure that the nonbond size will be smaller than the maximum allowable, the nonbond is presently assumed to be the maximum (1 mm). Therefore, the segregation spot could be assumed to be the same diameter as the maximum allowable nonbond. Since the maximum allowable segregation volume is less than that of a cylinder with the nonbond diameter (1 mm), the simplest segregation region to meet these conditions is a disk adjacent to the nonbond. The nonbond/segregation spot is located at the interface between the fuel meat and filler. Figure 4.8 compares the geometry of a cylinder segregation model with a disk segregation model for the thickest fuel meat zone. Figure 4.9 presents the cylinder segregation models, and Fig. 4.10 presents the disk segregation models for various fuel meat thicknesses ranging from 0.762–0.178 mm. Although the disk segregation model is less conservative, it may be more reasonable and was used in a few analyses.

The local power excess can also be produced by a uniform distribution of higher power fuel material in the inspection area. Although this assumption is probably the least conservative, it was also investigated to quantify the benefits of better control of the manufacturing process.

4.5.2.3 Fuel Thermal Conductivity

The conductivity of the U_3Si_2 fuel particles changes under irradiation resulting from generation of gaseous fission products. This phenomenon causes the conductivity of normal fuel to decrease almost

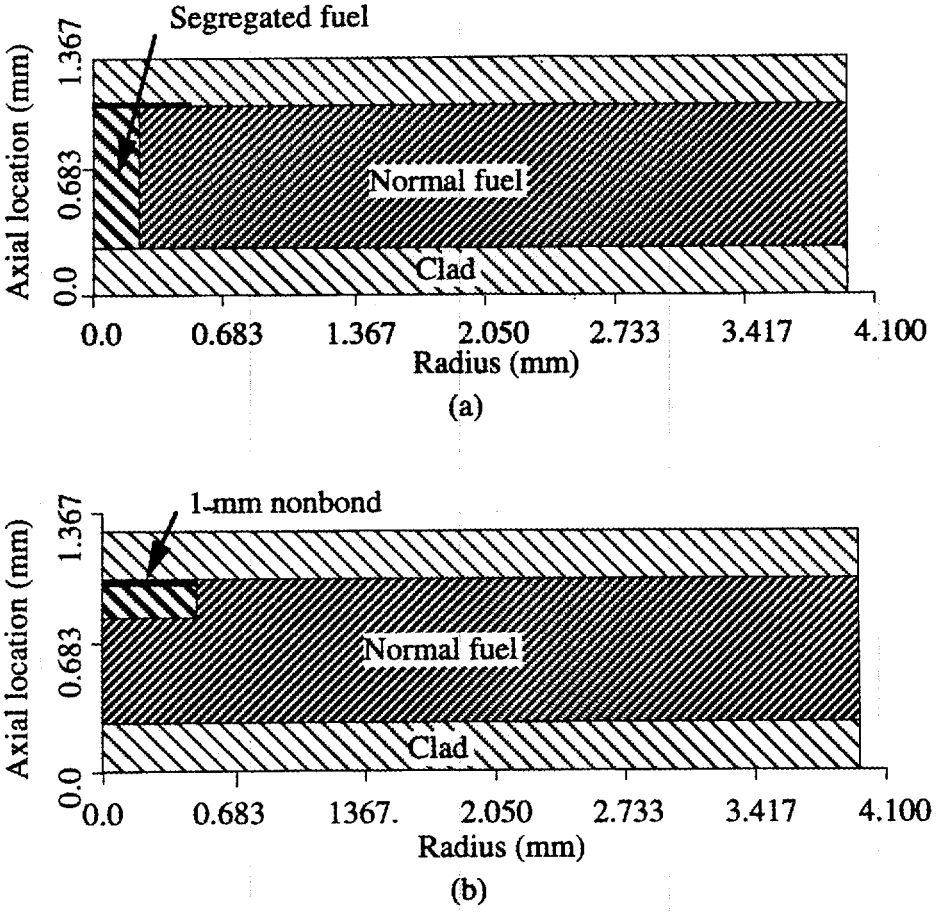

Fig. 4.8. Comparison of (a) cylinder and (b) disk segregation models with 0.762-mm meat.

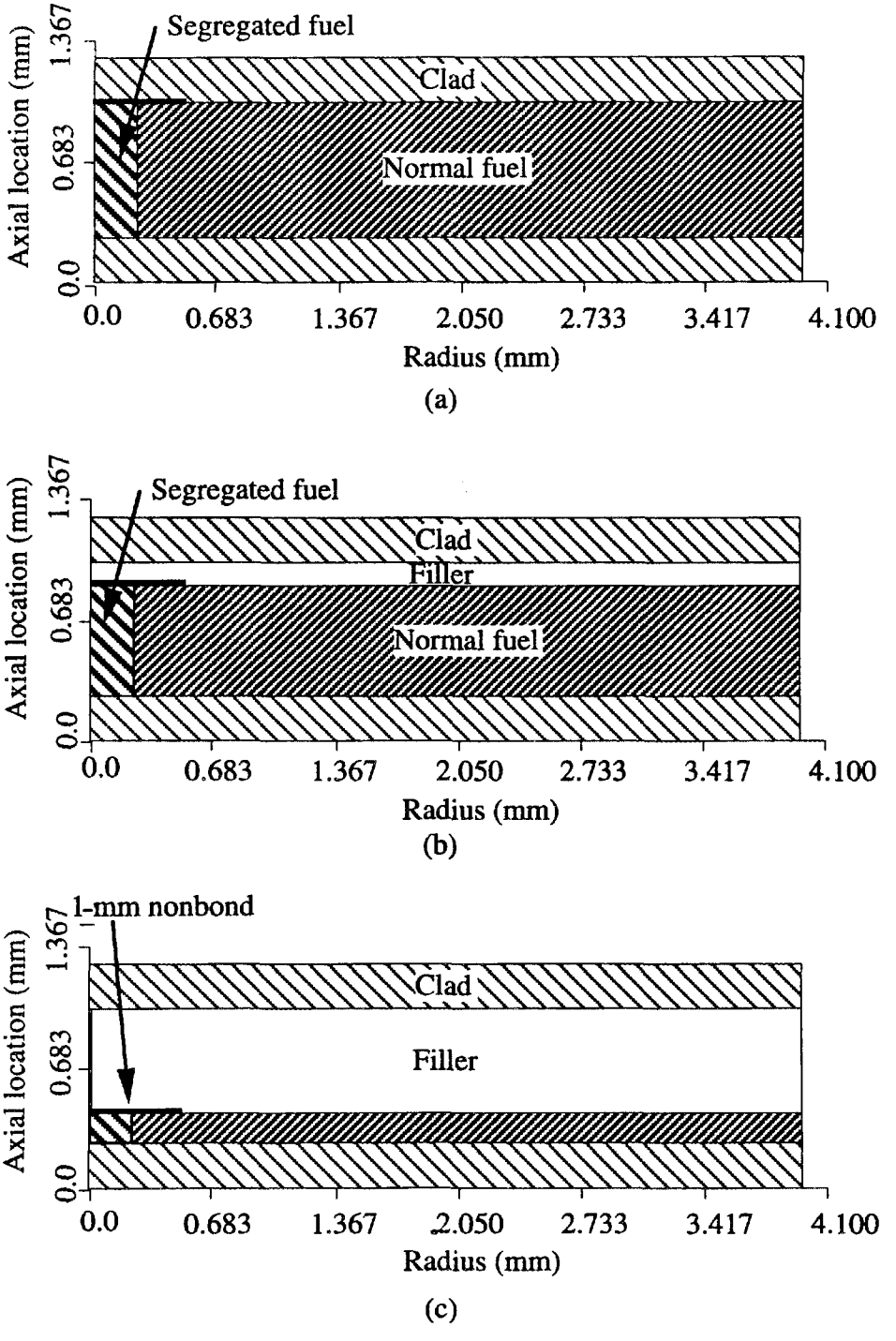

Fig. 4.9. Cylinder segregation models with different fuel meat thicknesses: (a) 0.762-, (b) 0.64-, and (c) 0.58-mm meat.

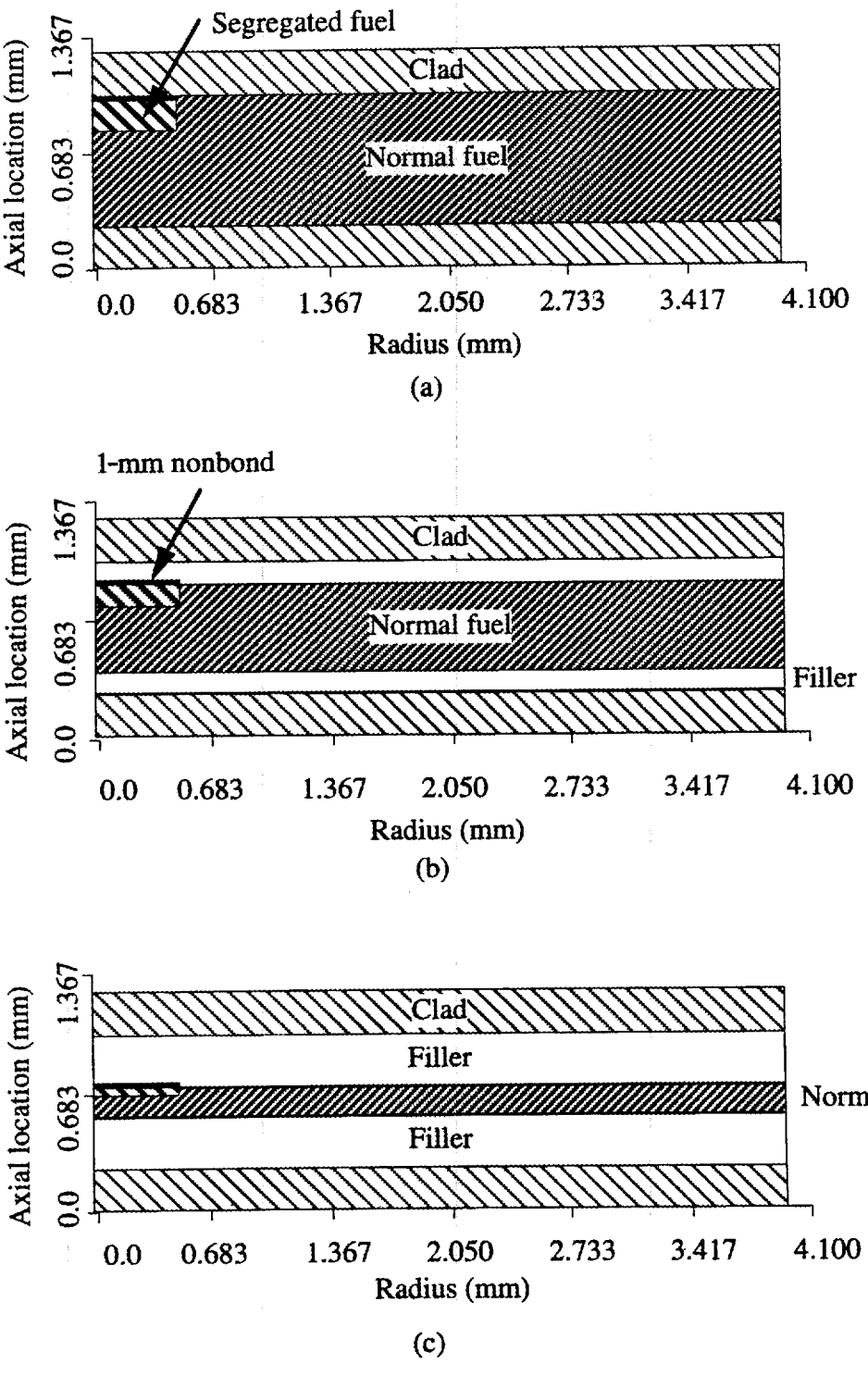

Fig. 4.10. Disk segregation models with different fuel meat thicknesses: (a) 0.762-, (b) 0.508-, and (c) 0.1778-mm meat.

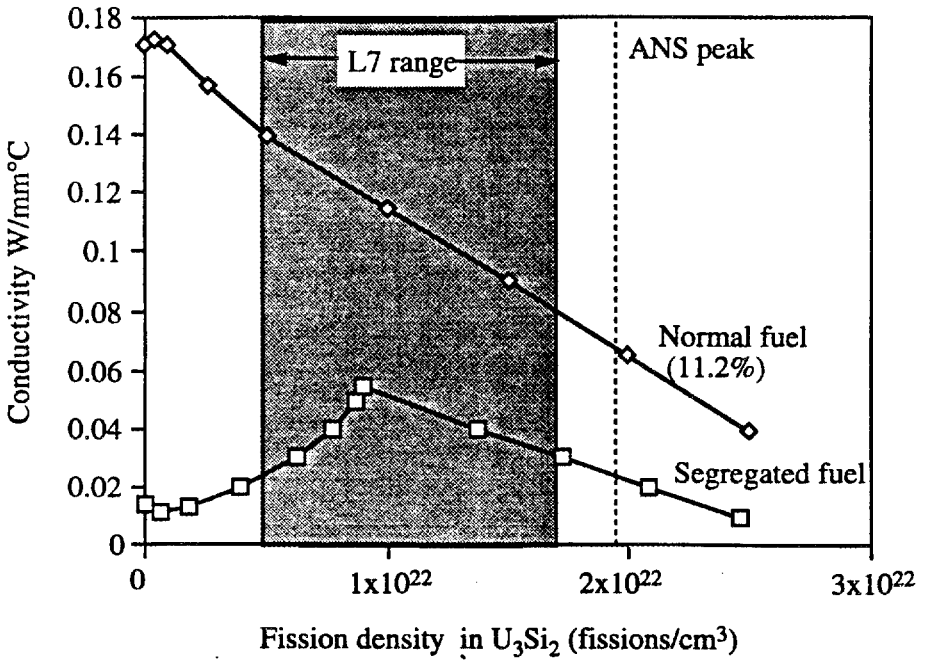

(a)

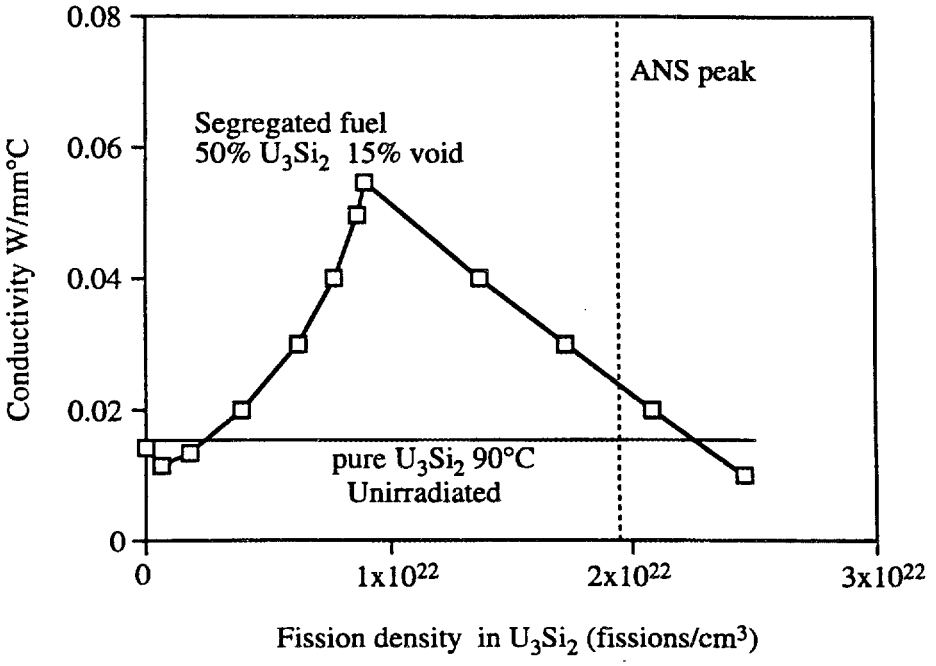

(b)

Fig. 4.11. Comparison of thermal conductivity of (a) normal fuel and segregated fuel as a function of fission density (both sets of results were produced by the DART code) and (b) segregated fuel and unirradiated U_3Si_2.

linearly with increased fission density (increased burnup). However, segregated fuel exhibits a more complex behavior. J. Rest[137] used the DART code to calculate the thermal conductivity of the 50% U_3Si_2 material as a function of fission density. Conductivities calculated by the DART code for both types of fuel are shown in Fig. 4.11. The gray region on the figure represents the span of fission densities found in the L7 core design, and the vertical line represents the ANS design limit fission density. The thermal conductivity of the normal and segregated fuel is evaluated from these curves by knowing the fission density in the U_3Si_2 particles. The fission density, F_d, is calculated from the initial surface density of ^{235}U and the burnup:

$$F_d = \frac{S_d B_u}{t_m v_f} \left[\frac{A_v}{M_w}\right] , \tag{4.12}$$

where

F_d = fission density (fissions/mm^3),
S_d = initial surface density (g ^{235}U/mm^2),
B_u = burnup (ρ_{uf}/ρ_{um}),
t_m = meat thickness (m),
v_f = volume fraction of fuel (0.112),
A_v = Avogadro's number (6.023×10^{23} molecules/g • mole),
M_w = molecular weight (^{235}U g/g • mole).

A summary of the range of thermal conductivities used in these analyses is included in Table 4.12.

Table 4.12. Thermal conductivity

Material	Thermal conductivity (W/mm • °C)
Normal fuel	(see Fig. 4.11)
Beginning-of-cycle	0.17
End-of-cycle at ANS[a] design limit (ANS peak)	0.0663
Segregated fuel—50% U_3Si_2, 15% void, 35% Al	(see Fig. 4.11)
Beginning-of-cycle	0.0145
End-of-cycle	0.0245
U_3Si_2 (unirradiated)	$0.01336 + 2.4 \times 10^{-5}$ T[b]

[a]ANS = Advanced Neutron Source.
[b]T = temperature (K).

4.5.2.4 Fuel Meat Location

The location of the fuel meat layer at the precise center of the fuel volume is difficult to achieve. Assumed displacement of 0.0254 mm (1 mL) and proportional displacements of 25, 50, and 100% from this ideal location were investigated.

4.5.3 Phenomena Not Included In These Investigations

4.5.3.1 Fuel Swelling

The fuel swells under irradiation as a result of the production of gaseous fission products. Although individual fuel particles increase 50% in size, this increase produces a maximum of only 6% (0.07-mm) growth in total plate thickness during the fuel cycle. This thickness change was not included in these studies, and its effect on fuel plate maximum temperature and peaking factor has not been evaluated. The increase in fuel volume will produce a reduction in local heat generation, while the reduction in the channel gap width will result in higher bulk coolant temperatures (as a result of lower coolant velocities).

4.5.3.2 Plate Bowing

Plate bowing can affect the coolant channel width, the bulk temperature, the heat transfer coefficient, and the local plate geometry. The curvature of the fuel plate is ignored in these studies since the hot spot model radius is small, and the plate surfaces are essentially flat over this region. The small changes in the local curvature that can be produced by bowing should not affect these analyses. Local changes in the thicknesses of the plate components are not expected because of the small amount of bowing allowed. Although ignoring the changes in coolant heat transfer is not conservative, it should be possible to use uncertainty factors derived in the same manner as those for HFIR in conjunction with these analyses to incorporate this phenomenon. Plate deflection is accounted for, however, in the overall T/H analysis and is discussed in Sect. 4.2.

4.5.3.3 Hot Streaking

The coolant bulk temperature was assumed to be the exit coolant temperature. This assumption neglects the possibility of the upstream coolant being heated to higher than the exit temperature by a sequence of hot spots or other phenomenon. Again, techniques for incorporating this effect should be investigated.

4.5.4 HEATING 7.2 Finite-Volume Model

HEATING 7.2[25] is a finite-volume general heat transfer analysis computer code developed at ORNL. This code was used to analyze detailed, 2-D, axisymmetric, nonlinear, steady-state models of the fuel plate at the location of a nonbond or segregation spot. A typical model using 2640 nodes is shown in Fig. 4.12. The calculations are performed simultaneously for this model and a companion model that only has 1-D heat flow. The temperatures from the companion model are used for ease of comparison and in the calculation of the peaking factors. The temperature at the surface of the models (on the coolant channel) was used to calculate the local heat flux and therefore the hot and cold side peaking factors. The maximum temperature in the model is also reported. This temperature is always located in the fuel or segregated fuel volume, if present.

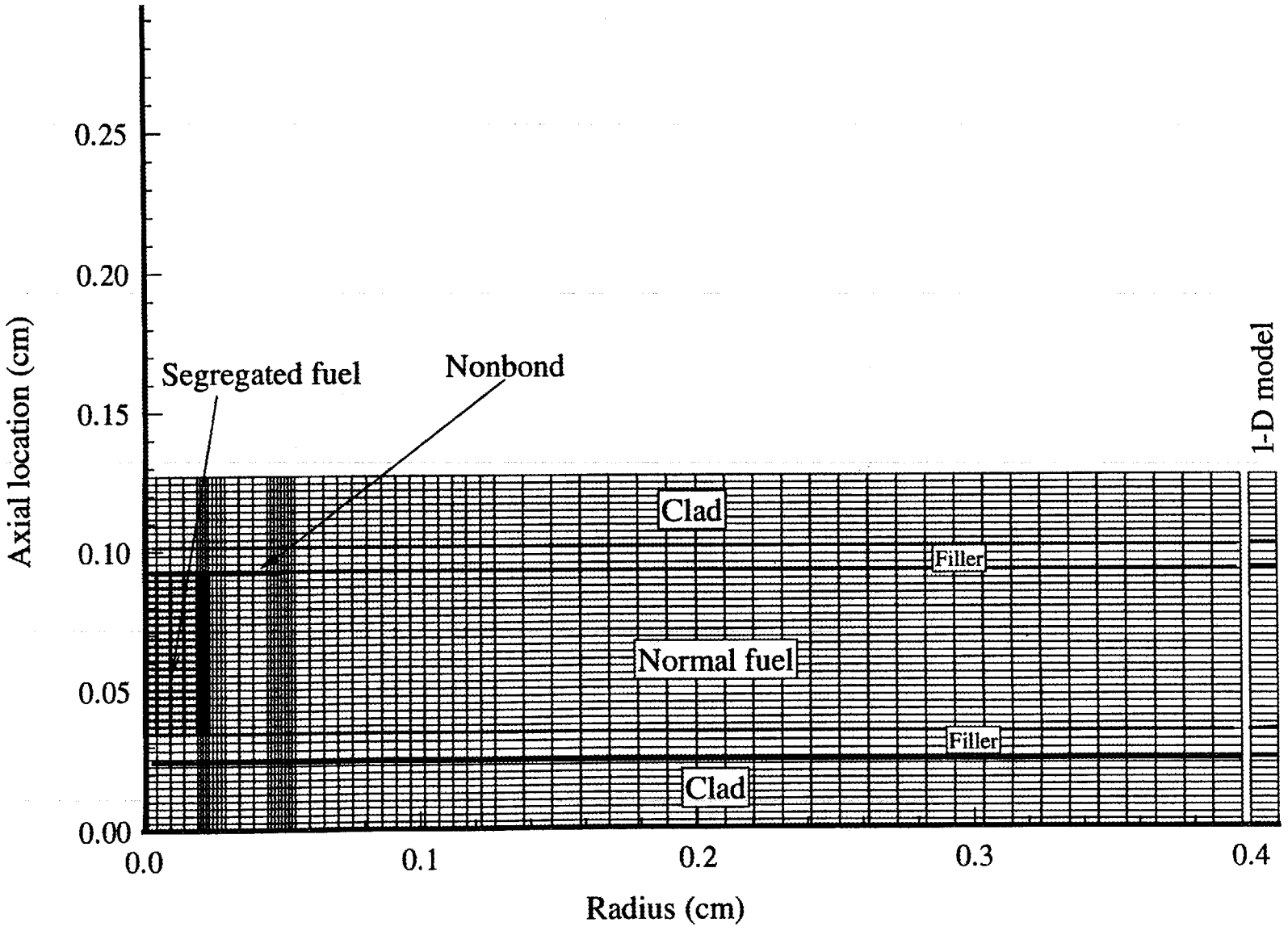

Fig. 4.12. HEATING 7.2 model of an axisymmetric hot spot with nonbond and a segregation cylinder.

Grid and convergence studies have also been performed.

4.5.4.1 Peaking Factor

Kirkpatrick[132] reported the effects of a hot spot produced by segregated fuel or nonbond on the hot side peaking factor. The hot side peaking factor was defined as "the ratio of maximum [heat] flux . . . to the flux that represents the average of the hot and cold sides." This definition is consistent with ANS and HFIR steady-state T/H codes and is the definition used in this study.

4.5.5 Analyses

4.5.5.1 Meat Thickness Variation Analyses

Previous HFIR[6,138] and ANS[132,139-141] hot spot studies have used the design limits for various parameters in analyses that vary the meat thickness from the minimum to the maximum. The other design limits used in these analyses are the maximum relative power density and fuel burnup, the maximum and minimum coolant bulk temperature, the coolant flow rate, and the oxide layer thickness. The fuel burnup determines the normal and segregated fuel conductivities. The coolant conditions determine the forced convection heat transfer coefficient.

4.5.5.2 Design Limits Studies

These studies involved a series of thermal analyses using HEATING 7.2 with the current ANS thermal design limits (Table 4.13). Nonbond size, segregation factor, fuel meat location, coolant conditions, thermal conductivities, segregation models, and the oxide layer have been investigated in these studies. Figure 4.13 reports a summary of the hot side peaking factor as a function of fuel meat thickness for models, including a 1-mm-diam nonbond, a segregation spot (cylinder.segregation model), and nonbond with a segregation spot (disk segregation model) for clean fuel (oxide thickness = 0). Figure 4.14 presents the maximum temperature results from these analyses. The addition of a 30-μm layer was also studied, and the results are reported in Figs. 4.15 and 4.16. Since it is not possible to center the fuel layer precisely in the fuel volume, an investigation of the effects of displacement from the design location was performed. These results are reported in Figs. 4.17 and 4.18.

Table 4.13. Advanced Neutron Source thermal design limits pertinent to hot spot investigations

Parameter	Limit
Relative power density	2.31
Maximum burnup (B_u) EOC[a]	0.925
Fuel conductivity (max. B_u)[a]	0.0663 W/mm · °C
Segregated fuel conductivity (max. B_u)[a]	0.0245 W/mm · °C
Minimum meat thickness	0.1778 mm
Maximum meat thickness	0.762 mm
Maximum oxide thickness EOC	30.0 μm
Minimum oxide thickness EOC	0.0 μm

[a]Estimated from ORNL-DWG 90Z-9704. B_u = burnup, and EOC = end-of-cycle.

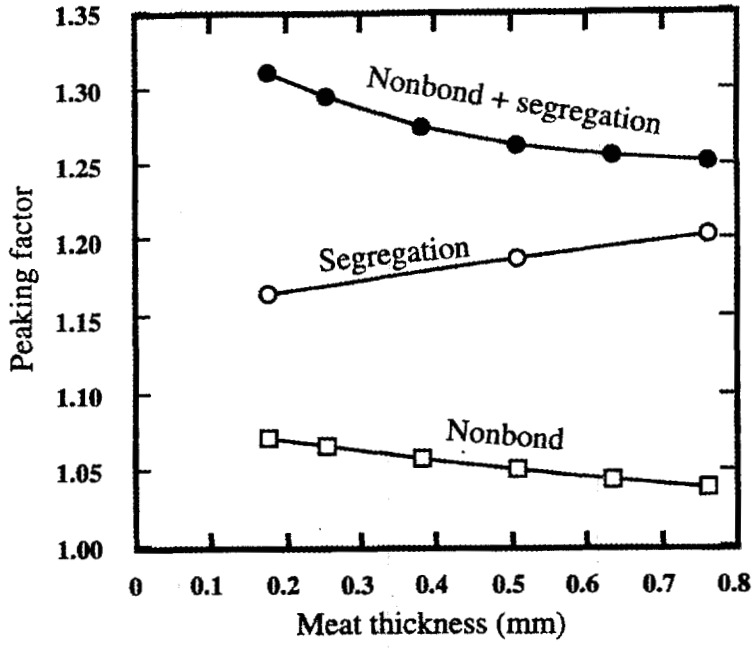

Fig. 4.13. Peaking factor as a function of meat thickness for design limits without oxide layer.

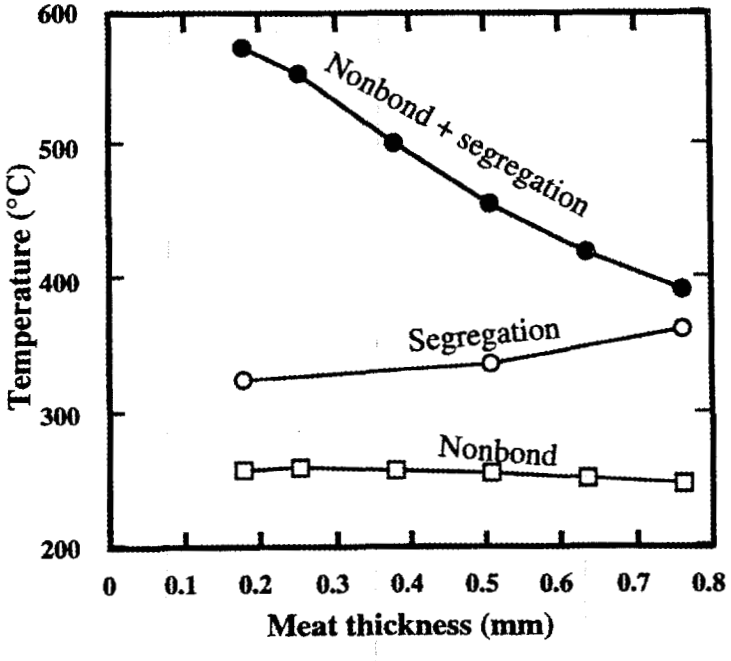

Fig. 4.14. Maximum temperature as a function of meat thickness for design limits without oxide layer.

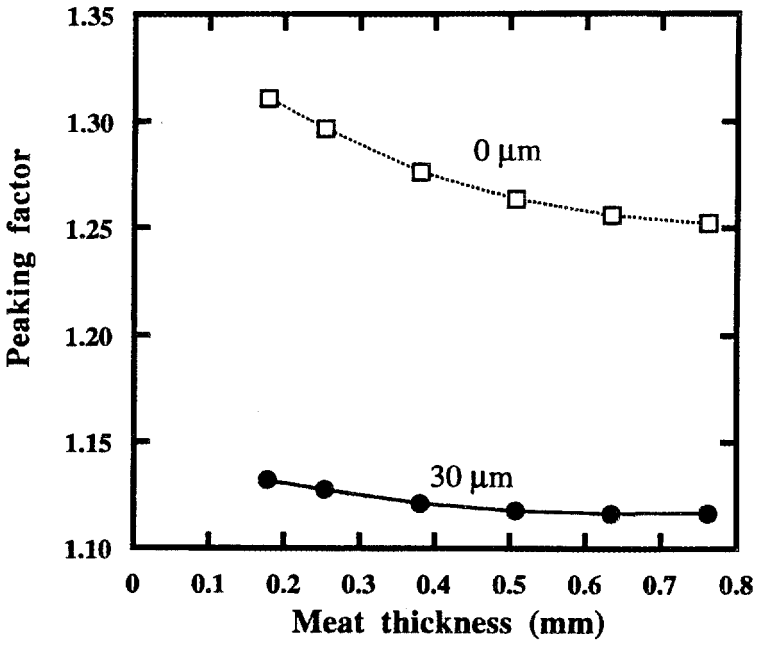

Fig. 4.15. Peaking factor as a function of meat thickness for design limit values with maximum and minimum oxide thickness.

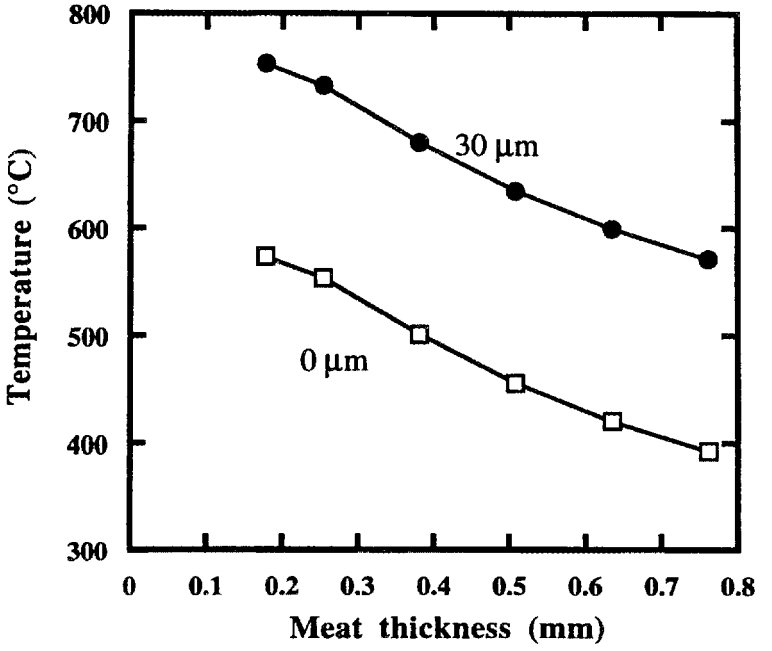

Fig. 4.16. Maximum temperature as a function of meat thickness for design limit values with maximum and minimum oxide thickness.

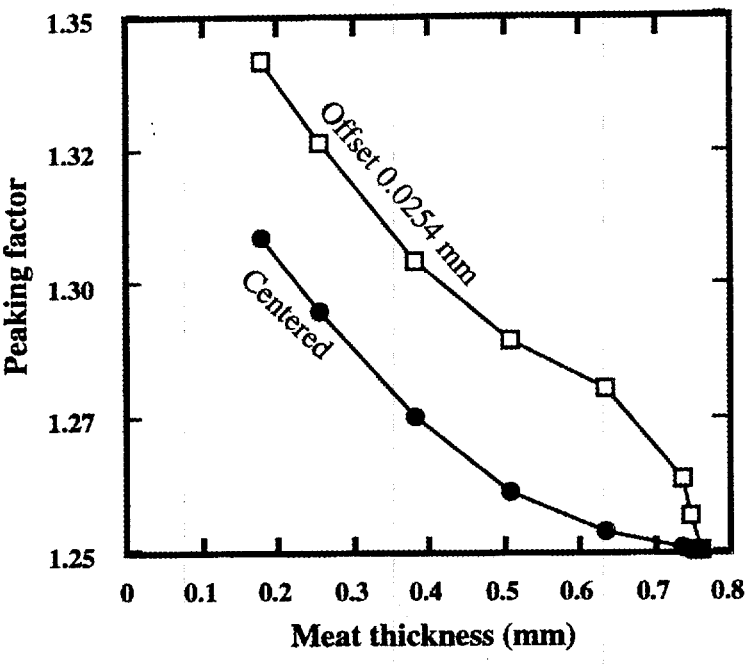

Fig. 4.17. Peaking factor as a function of meat thickness for centered and offset meat layers.

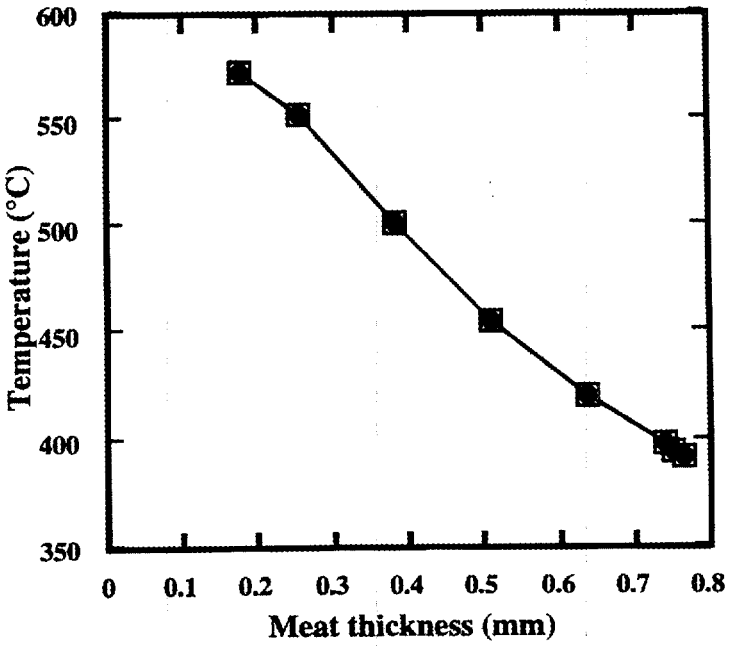

Fig. 4.18. Maximum temperature as function of meat thickness for centered and offset meat layers.

4.5.5.3 L7 Design Values Studies

A specific fuel plate design may not approach the above design limits because other constraints may control the design. The latest ANS core design is called the L7 core, and, from Table 4.14 it can be seen that the maximum and minimum meat thickness are not equal to the design limits. Also, the maximum power density occurs early in the fuel cycle. The maximum relative power density when the fuel conductivities are lowest (at EOC) is much lower than the design limits. The meat thickness variation studies were repeated for the maximum and minimum values found in the L7 core design for EOC. Table 4.14 presents a summary of the values that were used in the analyses. Figure 4.19 presents a comparison of the hot side peaking factor for the actual L7 core design and design limit meat thickness variation studies. Figure 4.20 presents a comparison of the approximate maximum temperature for these studies. These studies were designed to determine the maximum peaking factor and not necessarily the maximum temperature. The maximum forced convection heat transfer coefficient was used to produce the maximum peaking factor estimate. The minimum coefficient should be used for more conservative maximum temperature estimates. Although the temperatures are not strictly conservative, trends in results between models should be accurate.

Table 4.14. Summary of L7 core design values at end-of-cycle

Parameter	Design value
Maximum relative power density	1.7803
Maximum fuel burnup	0.799
Fuel conductivity at maximum burnup	0.0795 W/mm • °C
Segregated fuel at maximum burnup	0.0309 W/mm • °C
Minimum meat thickness	0.2214 mm
Maximum meat thickness	0.7366 mm
Minimum oxide thickness	1.431 μm
Maximum oxide thickness	22.334 μm

This comparison demonstrates that a small but significant reduction in the peaking factor is possible. The estimated maximum temperatures do not show significant change and remain higher than desired.

The investigation of offsetting the meat layer was also performed for the L7 values and the results are reported in Figs. 4.21 and 4.22. The amount of offset for each curve is labeled in Fig. 4.21. The centered meat model is labeled 0% offset. The curve labeled "0.0254 mm" is from a case with a constant offset of 0.0254 mm. The offset fuel layer makes a significant difference in the peaking factor but no difference in the maximum temperature. The data in Fig. 4.22 (plotted as circles with different radii) lay right on top of each other.

4.5.5.4 Local analyses—L7 design values

The meat thickness variation studies assume that the worst case values occur at the same point in a fuel plate and for all the meat thickness range in the design. Although this condition is the worst possible combination of values, it may not occur. In fact, for the latest ANS fuel plate design, this condition does not occur. Appendix A describes the nonuniformity of the ANS L7 core design fuel plate at EOC. Using a combination of more realistic local values and conservative assumptions at

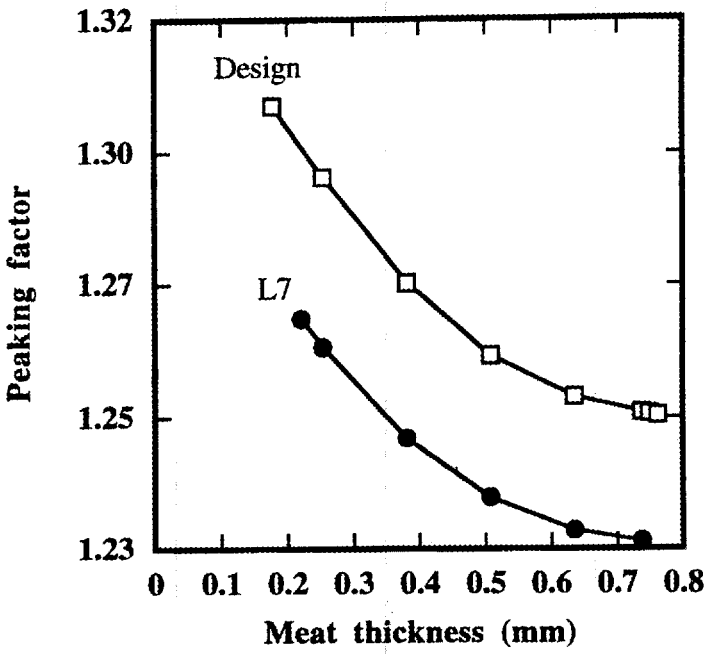

Fig. 4.19. Comparison of peaking factor for L7 design values with design limits. (Minimum oxide thickness: design limit = 0 μm, L7 = 1.4 μm.)

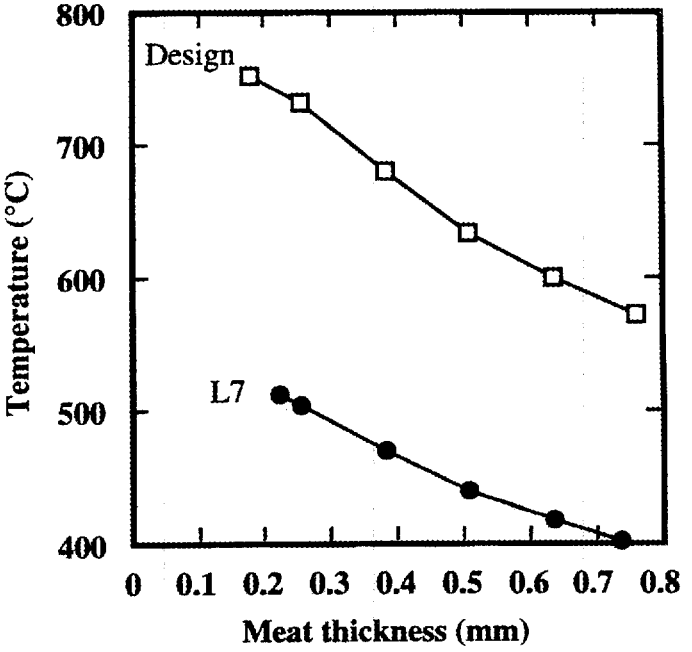

Fig. 4.20. Comparison of maximum temperature for L7 design values with design limits. (Maximum oxide thickness: design limit = 30 μm, L7 = 22 μm.)

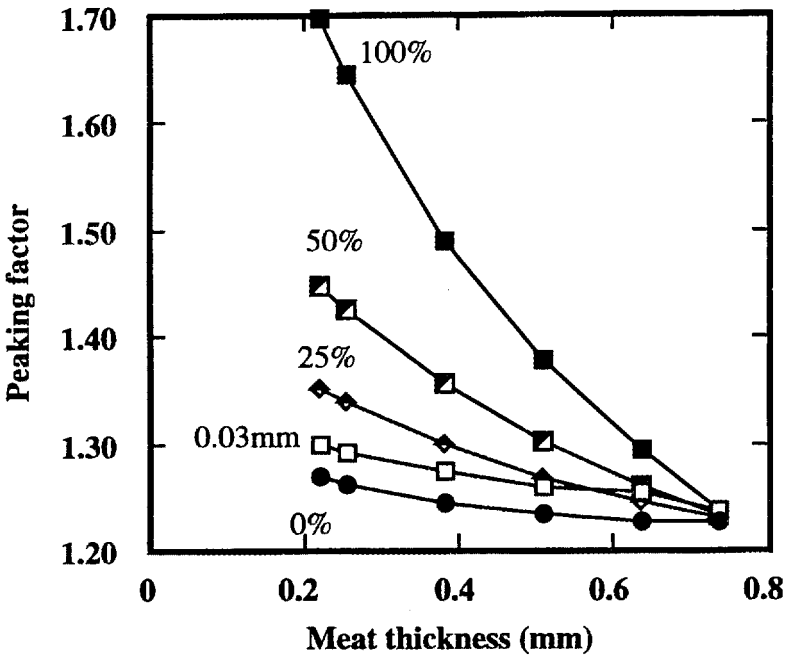

Fig. 4.21. Comparison of peaking factor for L7 design values with offset meat layers.

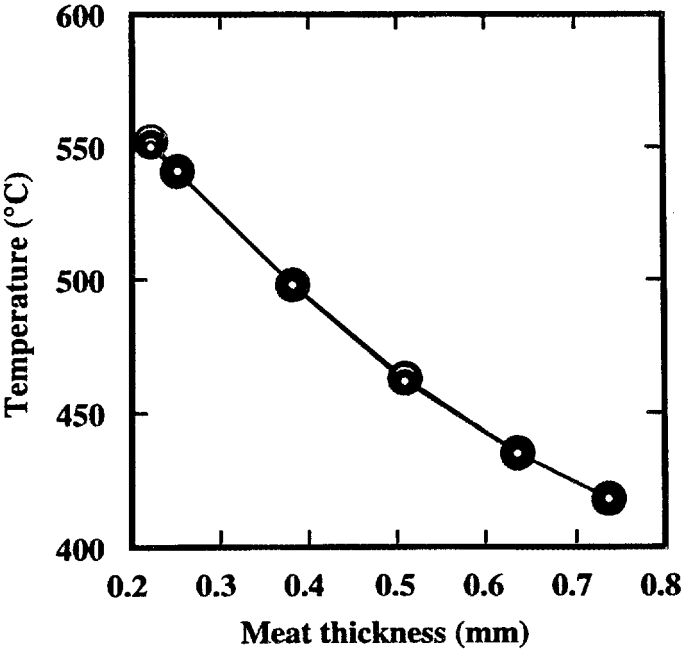

Fig. 4.22. Comparison of maximum temperature for L7 design values with offset meat layers and minimum oxide thickness.

every point in the L7 core design tables, a more realistic (but still conservative) estimate of the maximum peaking factor and fuel temperature can be obtained.

Figures 4.23 and 4.24 present the peaking factors and approximate maximum temperatures at EOC for local heat transfer analyses. These results are compared with those produced by the design limits and L7 worst case values. Large reductions in the peaking factors and maximum temperatures are obtained. Since the maximum fuel temperature is required to be $< 400°C$, the large reduction in maximum temperature to a level well below 400°C is very important. Table 4.15 presents the thermal parameters for the point that produced the highest peaking factor of 1.235.

Table 4.15. L7 maximum peaking factor point at end-of-cycle using local calculations

Parameter	Value
Relative power density	0.4845
Local burnup	0.7095
Fuel conductivity	0.0891 W/mm • °C
Segregated fuel conductivity	0.0360 W/mm • °C
Oxide thickness EOC[a]	3.052 μm
Meat thickness	0.234 mm
Radius	131.0 mm
Axial coordinate	−28.8 mm

[a]EOC = end-of-cycle.

This series of analyses was repeated for a 0.0254-mm fuel meat offset. The peaking factor results are included in Fig. 4.25 with the estimated maximum temperature in Fig. 4.26. The maximum peaking factor is increased slightly by 0.018, while the temperatures are not changed significantly. For comparison, these analyses were performed for a full offset fuel meat (100% offset) model where the fuel meat is next to one of the clad layers. The peaking factor results for the 100% offset model are compared with a centered model in Fig. 4.27. As with the previous global analyses, these results show the significant reduction in peaking factor possible with the centered meat design. The maximum temperature shown in Fig. 4.28 is less sensitive to the meat location.

As a demonstration of the flexibility of the local analysis technique, the series was repeated to investigate the effect of varying the fuel thermal conductivities by ±10%. This arbitrary variation was chosen since the uncertainties in the conductivities of the normal and segregated fuel are not known. The increase in maximum peaking factor is not large (0.006). The results presented in Figs. 4.29 and 4.30 show only slight increases in the peaking factor and maximum temperatures for a large variation in these properties.

These analyses were performed for only the EOC values, and, although they demonstrate sizable reductions in peaking factors and maximum temperatures, there is no certainty that the worst case occurs at EOC. In addition, the oxide layer that is used is calculated from the TASHA code. The estimates for surface heat flux calculated using the TASHA code are more conservative than these local analyses. These studies should be repeated for each time step to determine more accurately the local heat flux and, thus, the oxide layer thickness for each time step. These analyses could then determine a more accurate (but still conservative) estimate of the maximum peaking factors and temperatures.

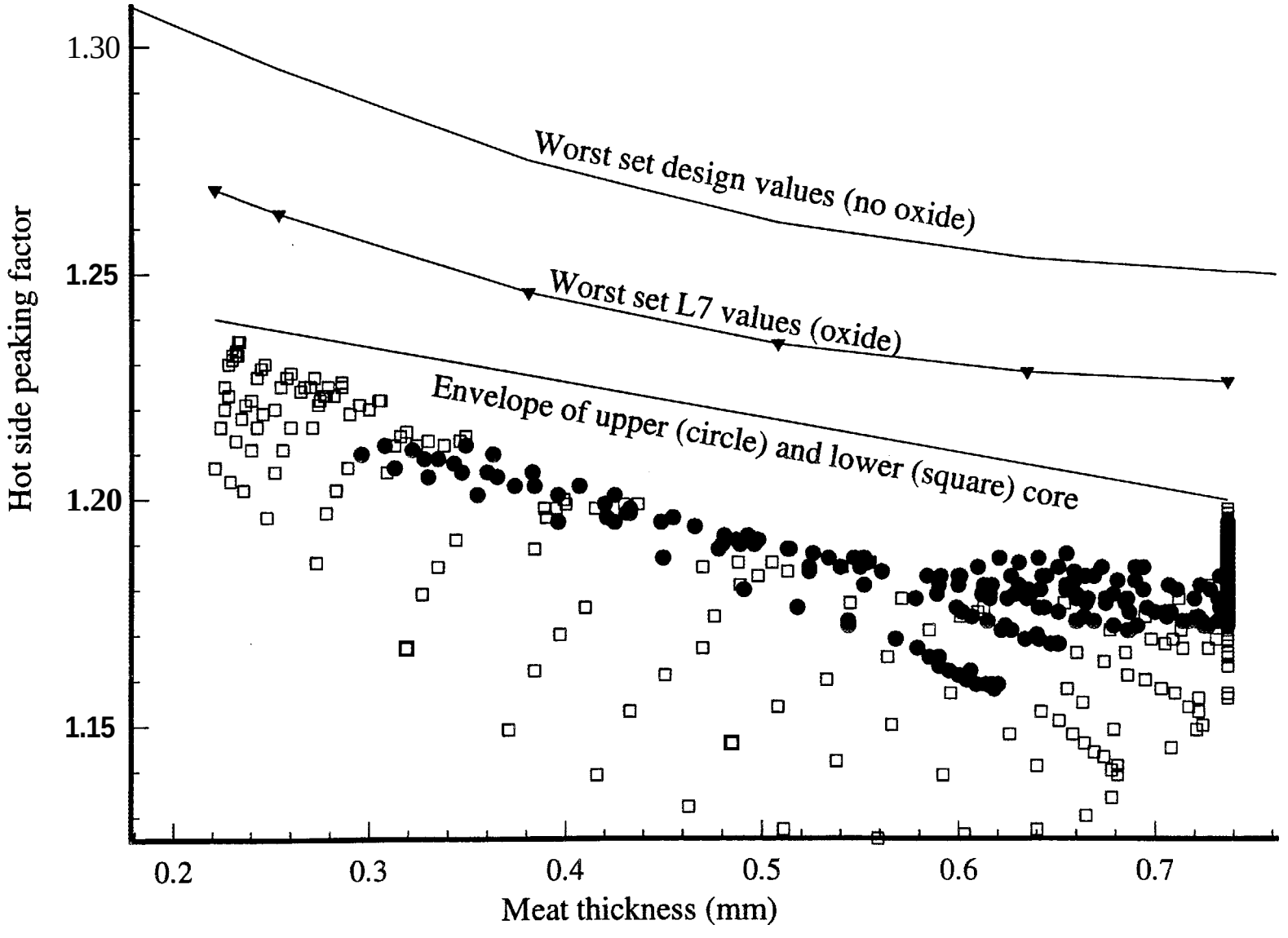

Fig. 4.23. Peaking factor for centered local and global calculations.

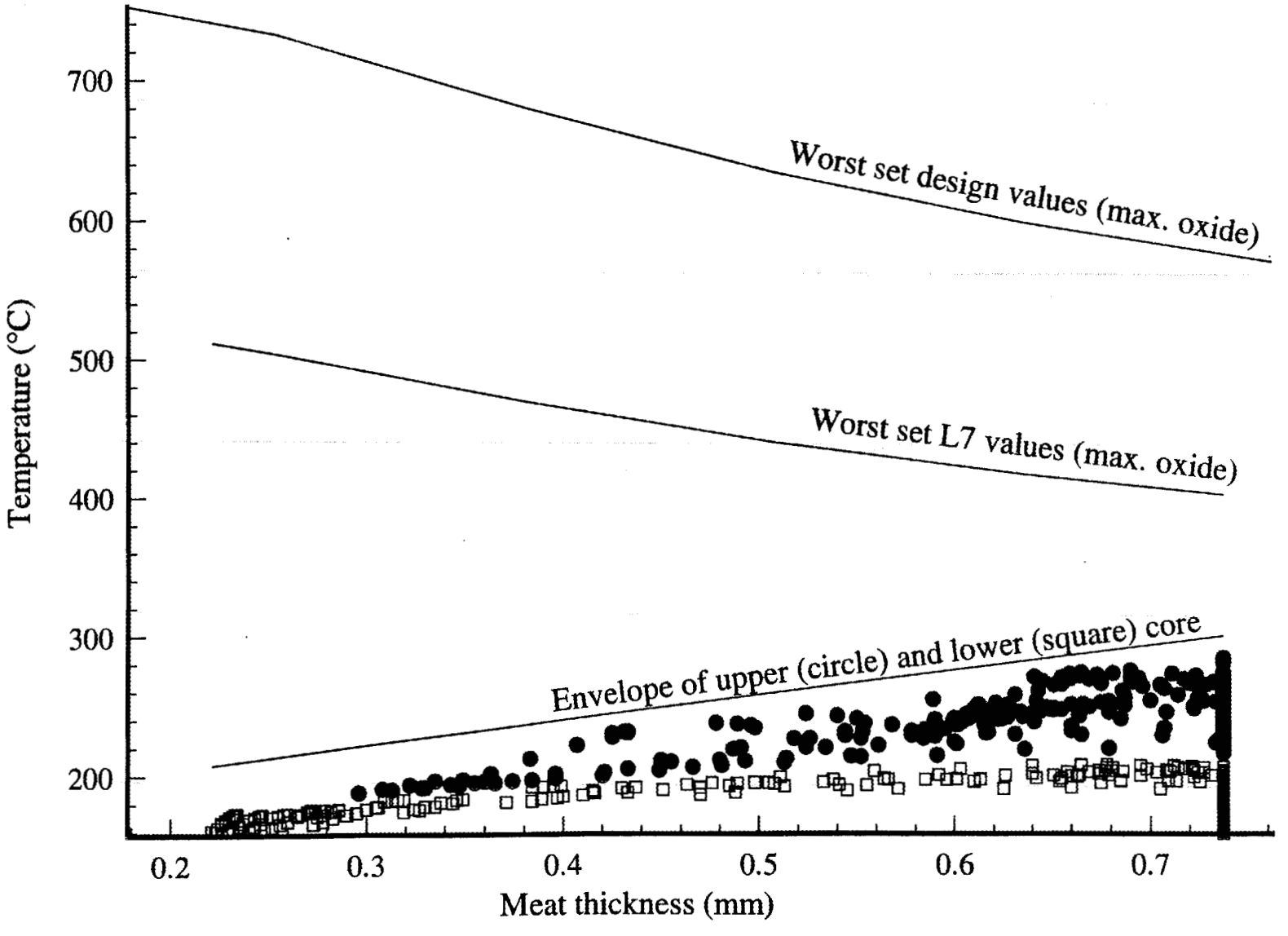

Fig. 4.24. Maximum temperature for centered local L7 and global L7 and design limit calculations.

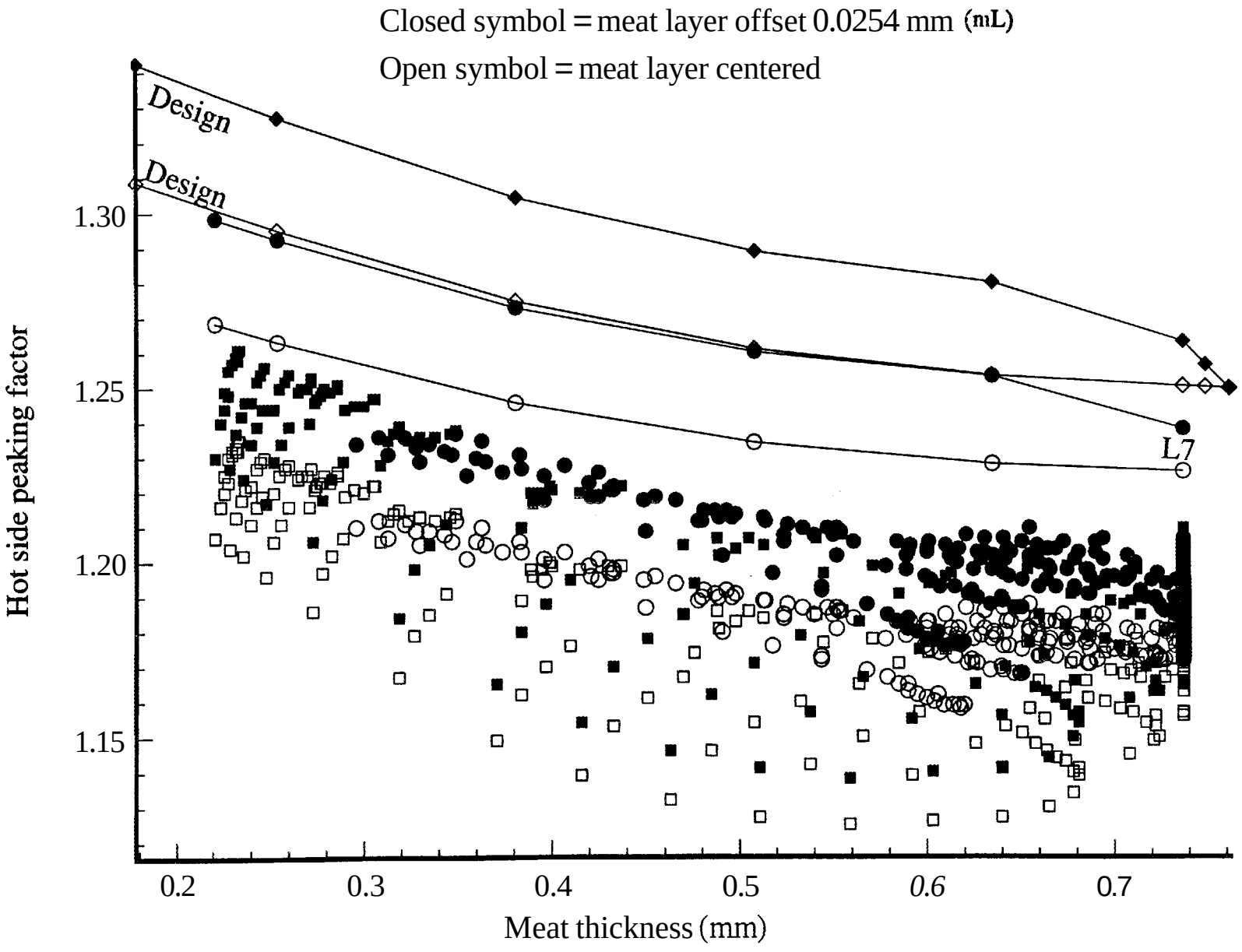

Fig. 4.25. Comparison of peaking factor from centered and offset calculations global and local.

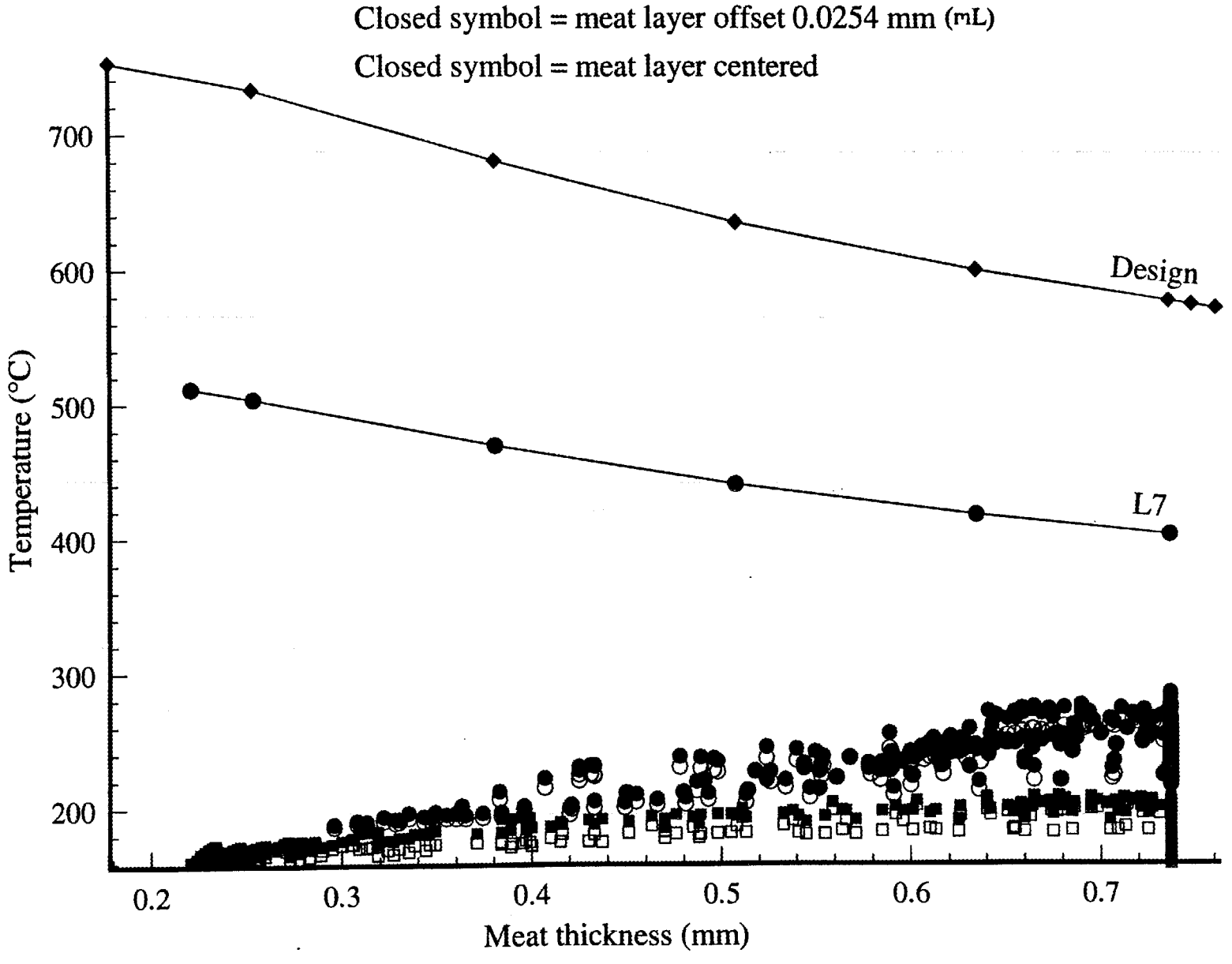

Fig. 4.26. Comparison of maximum temperature from centered and offset calculations global and local.

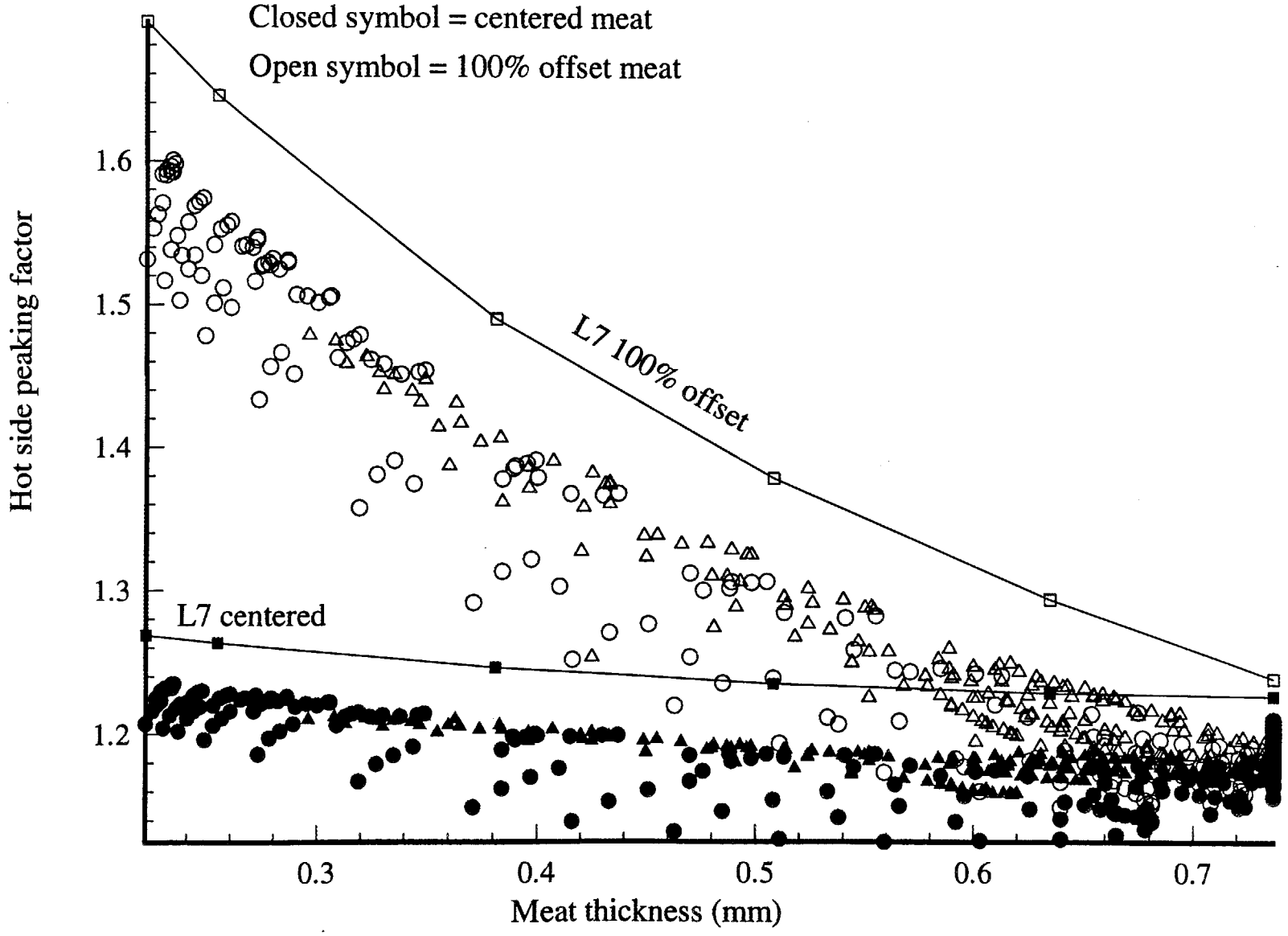

Fig. 4.27. Peaking factor for centered and offset L7 local calculations.

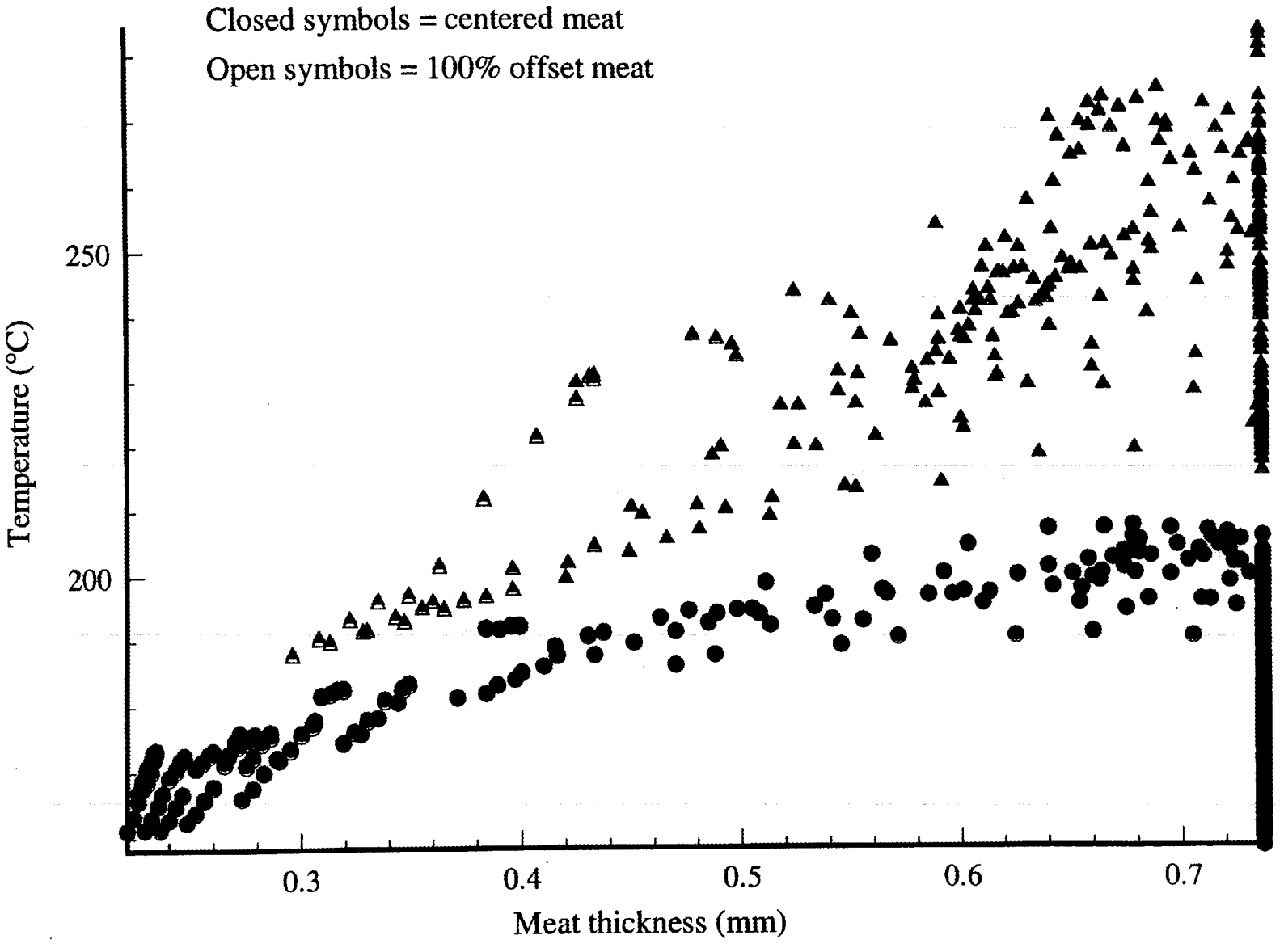

Fig. 4.28. Maximum temperature for centered and offset local L7 calculations.

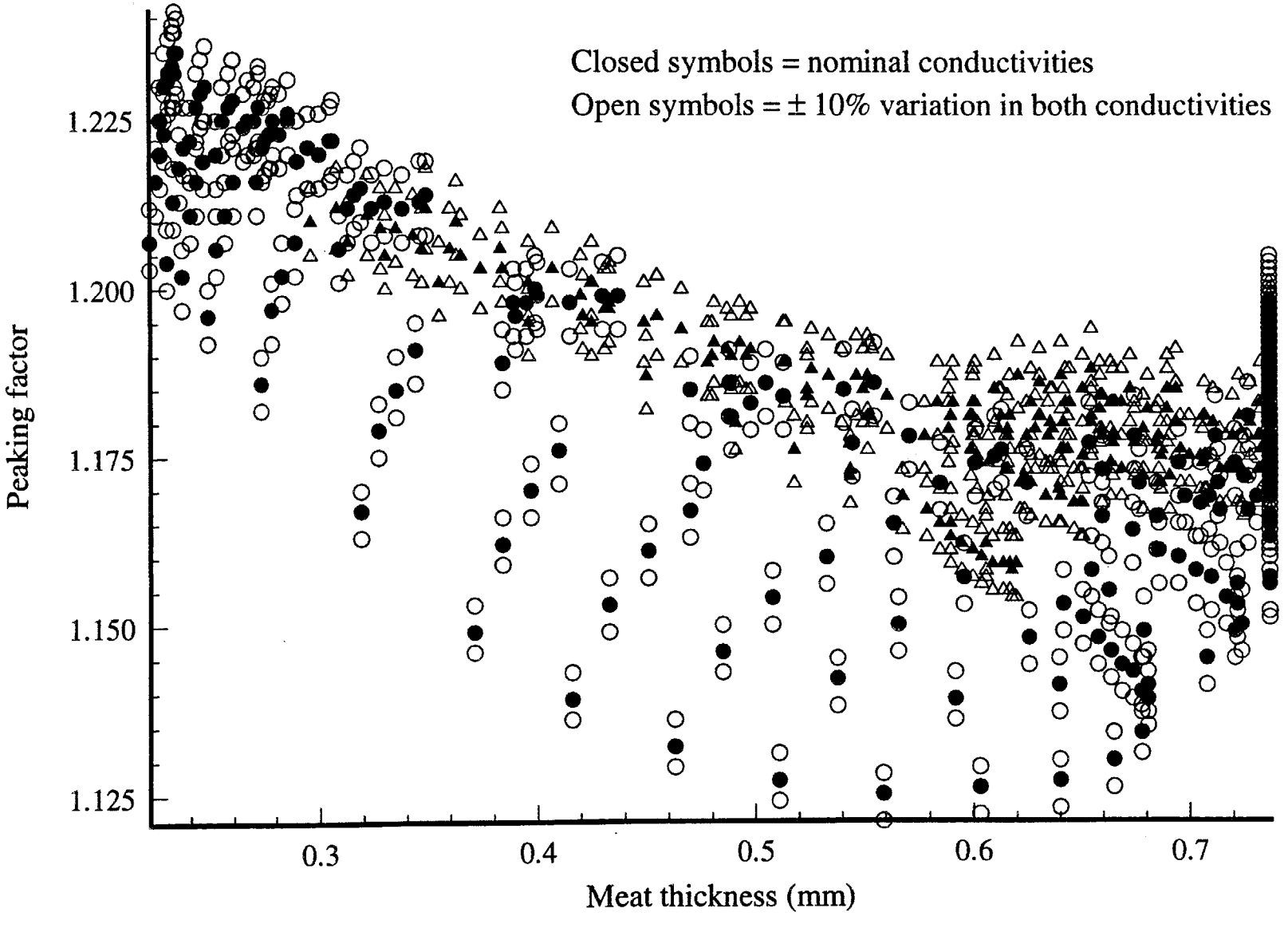

Fig. 4.29. Peaking factors from local analyses with ±10% variation in conductivities.

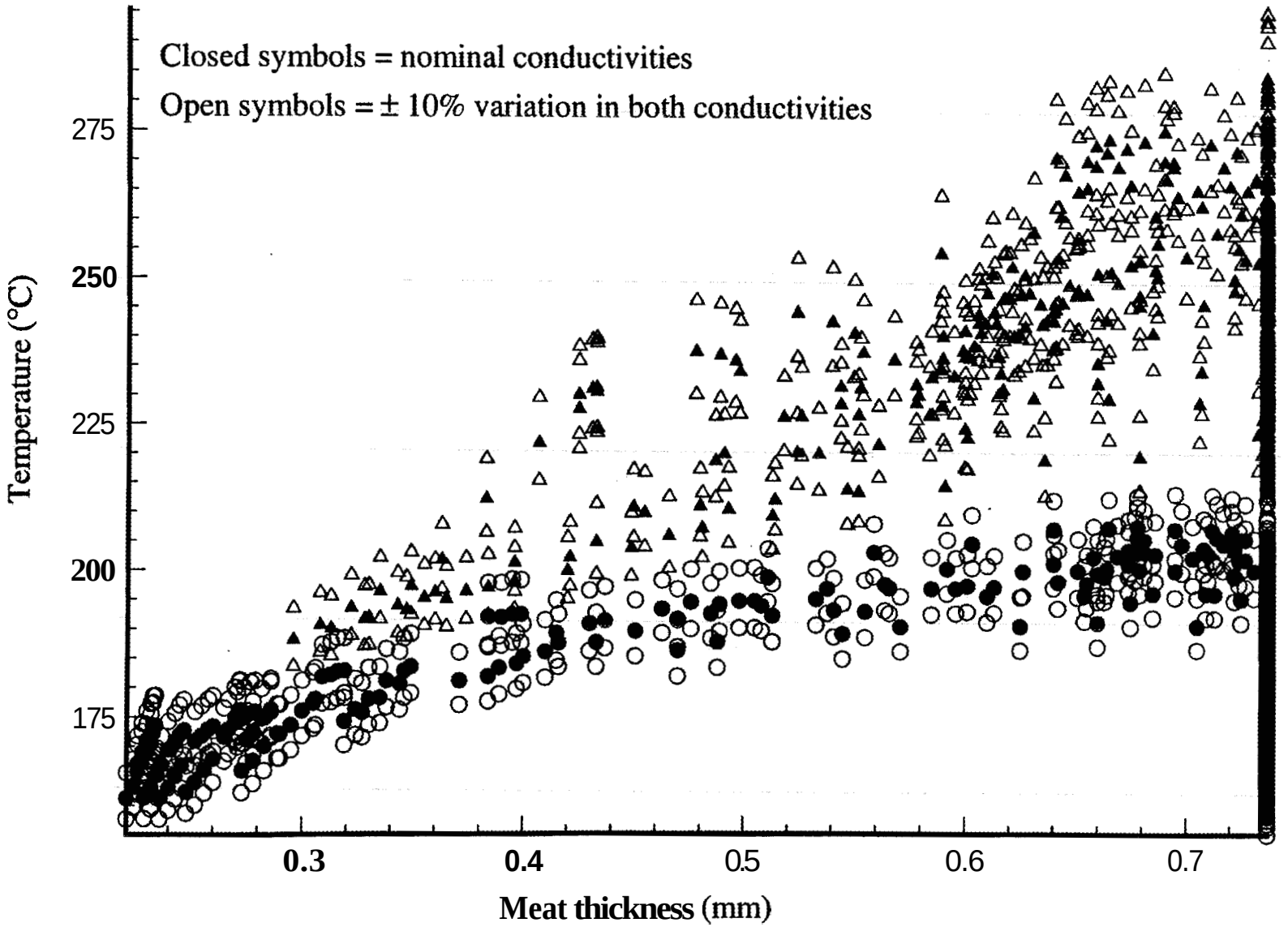

Fig. 430. Maximum temperature from local analyses with ±10% variation in conductivities.

4.6 CONCLUSIONS, LIMITATIONS, AND COURSE OF ACTION

The maximum reactor operating power was statistically determined (see Sect. 5), providing safety margins compatible with an acceptable quantified probability/confidence level and simultaneously accounting for uncertainties in assumptions, correlations, and input parameters. At this preliminary stage of the reactor design, neither the data collected nor the methodology used allowed the elimination of all worst-case parameters as desired. While the extreme conservatism normally involved in the worst-case methods used in the past was avoided, some excess conservatism was retained in the analysis. At the same time, it is not likely that all of the significant parameter uncertainties have been included. The statistical peaking factor methodology applied in the conceptual design is quite progressive but is still a combination of deterministic and statistical methods. The data base collected for determining the uncertainties is relatively extensive, going beyond what was considered normal practice, but is not yet complete. Extensive experimental data from in-house experiments planned for the project at the specific range of the ANS conditions are not yet available.

The following are some activities planned for future development that will improve the statistical treatment of uncertainties as well as allow further optimization of the design.

1. Further develop the statistical uncertainty methodology to allow a fully statistical approach incorporating the integrated SAMPLE/T/H code along with MC, LHS, or FPI statistical techniques. This methodology will replace the statistical peaking factor approach used in the CSAR.
2. Incorporate all other significant uncertainties that were not considered in the current phase into the analysis through phenomena identification and sensitivity analysis.
3. Consider modifications in the assumptions or the design that will allow more flexibility in maximizing the power or increasing the demonstrated safety margin.
4. Further expand and improve the experimental data base by incorporating additional data from the open literature and from specific in-house experiments. This addition will improve the accuracy and reliability of the uncertainty distributions, emphasizing fuel plate manufacturing defects and boiling-related correlations (see Sect. 3).
5. Further improve the correlation selection through additional statistical evaluation and comparisons with data (see Sects. 3.1.8 and 4.1).
6. Perform prototype and full-scale experiments to achieve and confirm the expected uncertainty levels projected in this CSAR for CHF, FE, and IB correlations (Sect. 4.2).

Most of the activities indicated above are either currently in progress or planned. As work progresses toward the PSAR and the FSAR stages, the results of all these activities will be integrated in the reactor design and analysis.

5. THERMAL-HYDRAULIC DESIGN AND SAFETY ANALYSIS

Analysis results presented in this section are divided into several subsections primarily related to the codes used. As mentioned previously, transient analysis is beyond the scope of this report, and only steady- or quasi-steady-state results are discussed.

5.1 STEADY-STATE DESIGN

5.1.1 Fuel Loading Design and Core Region Thermal-Hydraulic Parametric Studies

The configuration of the ANSR (small core volume, D_2O coolant and reflector, etc.) is such that the location and magnitude of the neutron flux is relatively insensitive to the fuel location. Present fuel manufacturing techniques also allow the fuel to be graded in both the axial and radial directions within the fuel plates. These two features allow the fuel grading design to be tailored to accommodate T/H characteristics. The neutronics and T/H design have, therefore, been integrated within the project, and cooperation between the neutronic and T/H design teams has led to significant improvements in core design.

Once inlet conditions have been specified, two T/H parameters that vary within the core significantly affect the thermal limits. These parameters are the local bulk coolant temperature and the local fluid pressure. Since each of the thermal limits is affected by one or both of these parameters, core power profiles can be imagined that maximize the power output of the core without exceeding a specified thermal limit (if the effect of fuel burnup and control rod movement are temporarily ignored). Ideal axial power profiles were generated for design purposes that cause the desired limit criteria to be met at all points on the fuel plate. (The oxide limits of fuel centerline temperature and oxide temperature drop were forced to be met at all points on the fuel plates at the EOC by allowing the oxide thickness to grow throughout the fuel cycle and determining the power density profile that meets the criteria.) This ideal scenario allows for the achievement of maximum power from the core or maximum margins in the core design. These profiles were generated by treating the bulk coolant temperature as an initial value problem, integrating along the fueled length of the core using a Runge-Kutta scheme, and determining the local heat flux that forces the centerline temperature to reach 400°C at EOC (or the spallation temperature drop limit, IB limit, etc. to be met at all points on the fuel plate) assuming that the oxide grows according to Eq. (3.10).

These ideal power profiles were used as an initial guide for the fuel loading design. In reality, these ideal profiles cannot be achieved for all radial locations of the fuel element or all times within the fuel cycle. Therefore, the neutronics calculations were aimed at producing radially and time averaged power distributions that followed the ideal shape. Figure 5.1 shows one of these averaged distributions (symbols) that was optimized to the spallation temperature drop limited ideal profile. Also shown on this figure are ideal profiles for the maximum centerline temperature limit and the IB limit. Once an initial fuel grading was established using the ideal distribution, the T/H calculations were performed using the TASHA code. Results of the T/H code calculations (as ratios representing how near the local power densities were to the thermal limits) were then used to refine the fuel loadings, and the neutronics calculations were repeated. A comparison of three ANSR fuel designs is presented in Fig. 5.2, with designs progressing from G3 to I3. This figure shows the IB limited powers as a function of time in the cycle as well as the oxide limited powers for these fuel designs. For case G3, axial grading of the fuel was allowed only within the first and last 100 mm of the fuel plate heated length, and optimization was for the IB limit. For the "I" cases, grading was performed along the

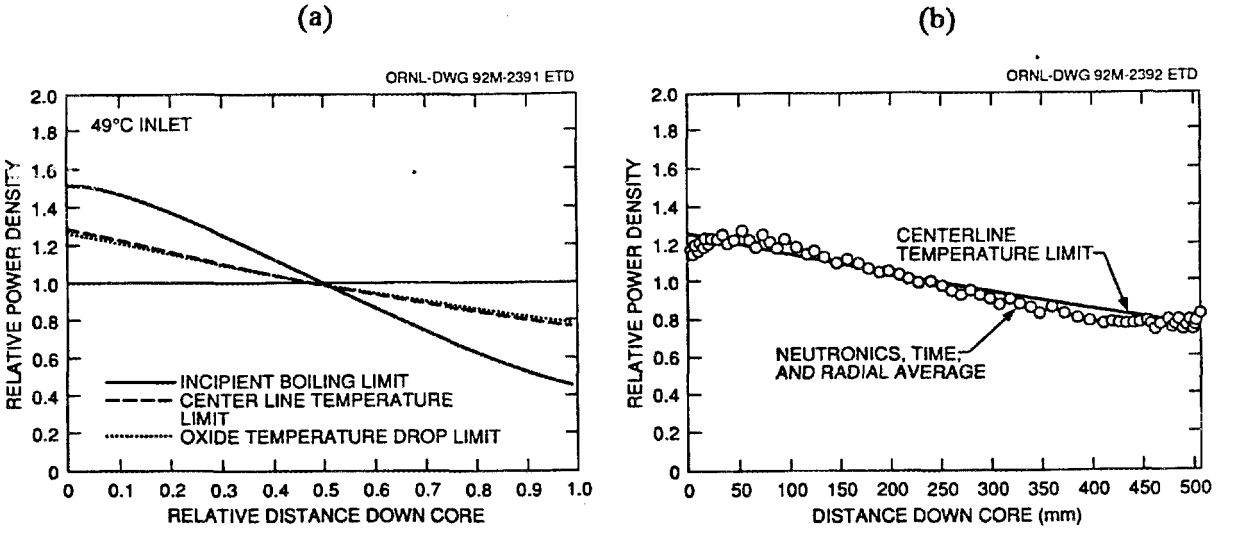

Fig. 5.1. Relative power density profiles: (a) ideal and (b) ideal and actual optimized.

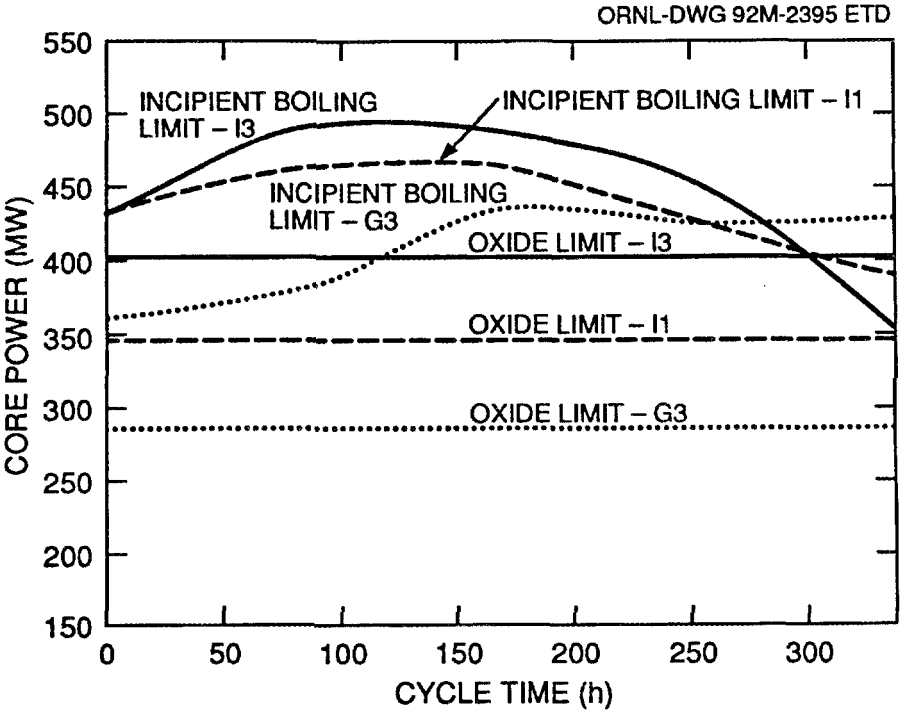

Fig. 5.2. Performance of three Advanced Neutron Source reactor fuel designs.

entire fueled region, which should better approximate the ideal profiles—case I1 was optimized for the ideal IB profile, while I3 was optimized for the ideal oxide profile. In progressing from design G3 to I1, both the oxide and IB performance improve as the region of fuel grading encompasses the entire fuel plate heated length since both oxide and IB ideal profiles are biased toward the core inlet where pressure is highest and temperature is lowest. An additional increase in oxide performance is achieved by optimizing with respect to the ideal oxide profile (I3); however, a decrease in the IB limited power is also noted. This decrease can be anticipated by examining Fig. 5.1.

A core design that represents a fuel loading more typical of the ideal IB profile would be limited by oxide growth near the core inlet at powers lower than a design that more closely represents the ideal oxide distribution. The reverse is true if the fuel design more closely represents the ideal oxide profile. The design of the core with respect to oxide limitations is very complicated, depending on both local instantaneous thermal conditions as well as the time dependent nature of these conditions. However, as Fig. 5.2 shows, increases of up to 40% can be achieved by careful tailoring of the fuel loading. The grading of the L7 core chosen for the conceptual design was based on optimizing the oxide performance. The power distribution for this design at various times throughout the operating cycle is shown in Fig. 1.12.

The TASHA code has been used to perform several T/H parametric studies of the core region to establish the combination of operating parameters and core geometry noted in Sect. 1. These studies have included the effects of core heated length, channel gap, coolant inlet pressure and temperature, and coolant velocity on the thermal performance of the core. In addition, since the fuel is being graded in both the axial and radial directions in the fuel plates, T/H analyses have been used to evaluate and alter fuel loading within the core.

An example showing the effect of the heated length of the core on the T/H performance is shown in Fig. 5.3. This figure shows the maximum thermal power density at which the core can operate without exceeding the IB limit at any point in the core. These curves represent the performance of two early fuel grading designs (designated G3 and F4) at two differing inlet temperatures. (Uncertainty levels in these early calculations are somewhat different from those described in Sect. 4, and, therefore, these results are presented only for illustration.) As this figure illustrates, increasing the fueled length (for a fixed inlet pressure) decreases the IB limited power level. This phenomenon occurs because of the increased pressure drop through the core with increasing fueled length and the correspondingly lower local pressure at the core exit where IB is limiting. The fuel grading also impacts the behavior of these curves since both the local bulk temperature and the local heat flux are dependent on the relative power density profile (which is dependent on the fuel loading). Other considerations also enter into selecting the fueled length, including fuel plate stability, the effect of core volume and length on the neutron flux, etc. These considerations are discussed in the ANS CSAR.

The coolant channel gap has also been studied parametrically. Table 5.1 shows the sensitivity of the minimum of critical heat flux and flow excursion limited power to a decrease in channel gap thickness. A 30% decrease in the minimum channel gap causes an ~30% decrease in maximum power.

The effect of coolant inlet temperature on IB power is also represented in Fig. 5.3. These calculations indicate an ~0.5% increase in average allowable power density for every degree of coolant temperature decrease. This increase results from the impact of the local bulk temperature on the IB limit. The choice of design inlet temperature of 45°C also considered other factors, including heat exchanger cost, etc.

The impact of core inlet pressure and coolant velocity is illustrated in Figs. 5.4 and 5.5. Figure 5.4 shows the effect of increasing the core inlet velocity on the maximum IB limited power.

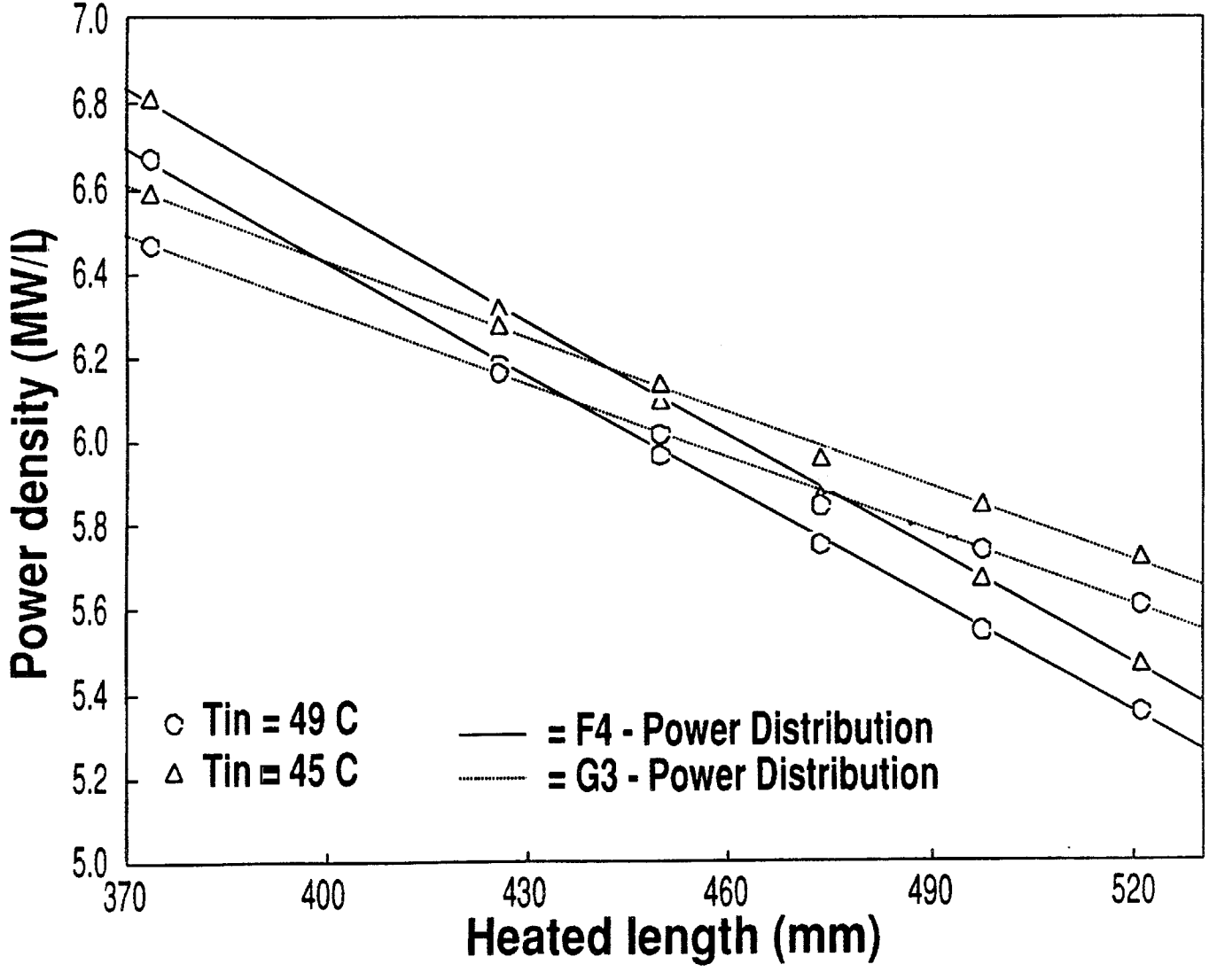

Fig. 5.3. Effect of heated length on maximum power.

Table 5.1. Variation of Advanced Neutron Source reactor maximum power with coolant channel gap

Gap width (mm)	CHF[a] or FE[b] limiting power [MW(t)]
1.27	456
1.14	416
0.889	317

[a]CHF = critical heat flux.
[b]FE = flow excursion.

(Again, this figure represents an early core design with uncertainties differing from those in Sect. 4 and is shown for illustrative purposes only.) The maximum allowable power initially increases with increasing coolant velocity, peaks, and then decreases. The peak is caused by the competing effects of improved heat transfer and decreasing local pressure with increasing velocity and their effects on the IB criterion.Increasing the heat transfer coefficient (with increased coolant velocity) increases the IB limit, while decreasing the local pressure decreases the IB heat flux. Other factors alter the shape and location of the maximum power curve on such a plot. As indicated on the figure, as core inlet pressure increases, the peak in these curves tends to move to the right. As inlet pressure is increased for the same coolant velocity, the local pressure is increased by approximately the same amount; thus, the IB flux tends to increase. Although not presented here, the effect of increasing the heated length is similar to the effect of decreasing the core inlet pressure (and therefore local pressure); that is, IB power decreases as the heated length increases (because the local pressure decreases).

Another way of examining the effect of coolant velocity on IB limited power is to maintain the core outlet pressure constant (i.e., increasing the inlet pressure) as the velocity is increased. This type of analysis is shown in Fig. 5.5. (Again, this figure should be used for illustration only.) In this case, because the local pressure at the limiting location is held constant, increasing the coolant velocity does not cause a maximum in the maximum IB limited core power curves.

Because the power distribution changes during the fuel cycle, the T/H limits and, therefore, margins also change. This variation is illustrated in Fig. 5.6, which shows oxide, IB, FE, and CHF limits over the fuel cycle. (These calculations were performed with the uncertainty treatment and values discussed in Sect 4.) For comparison, these values were all calculated at 95% probability levels. The oxide limiting power can be interpreted as being the maximum power at which the core can operate for the entire 17-d fuel cycle without exceeding either the 119°C oxide temperature drop limit or the 400°C centerline temperature limit. Also indicated in this figure are the relative magnitudes of the various limits. The CHF limit normally is ~35–40% higher than the IB limit, while the FE and CHF limits are approximately the same at normal operating conditions. (At lower pressures, the FE limit is much lower than the CHF limit). Although not shown on the figure, the power at which the local fuel plate surface temperature equals the local saturation temperature is ~7% lower than the IB limit.

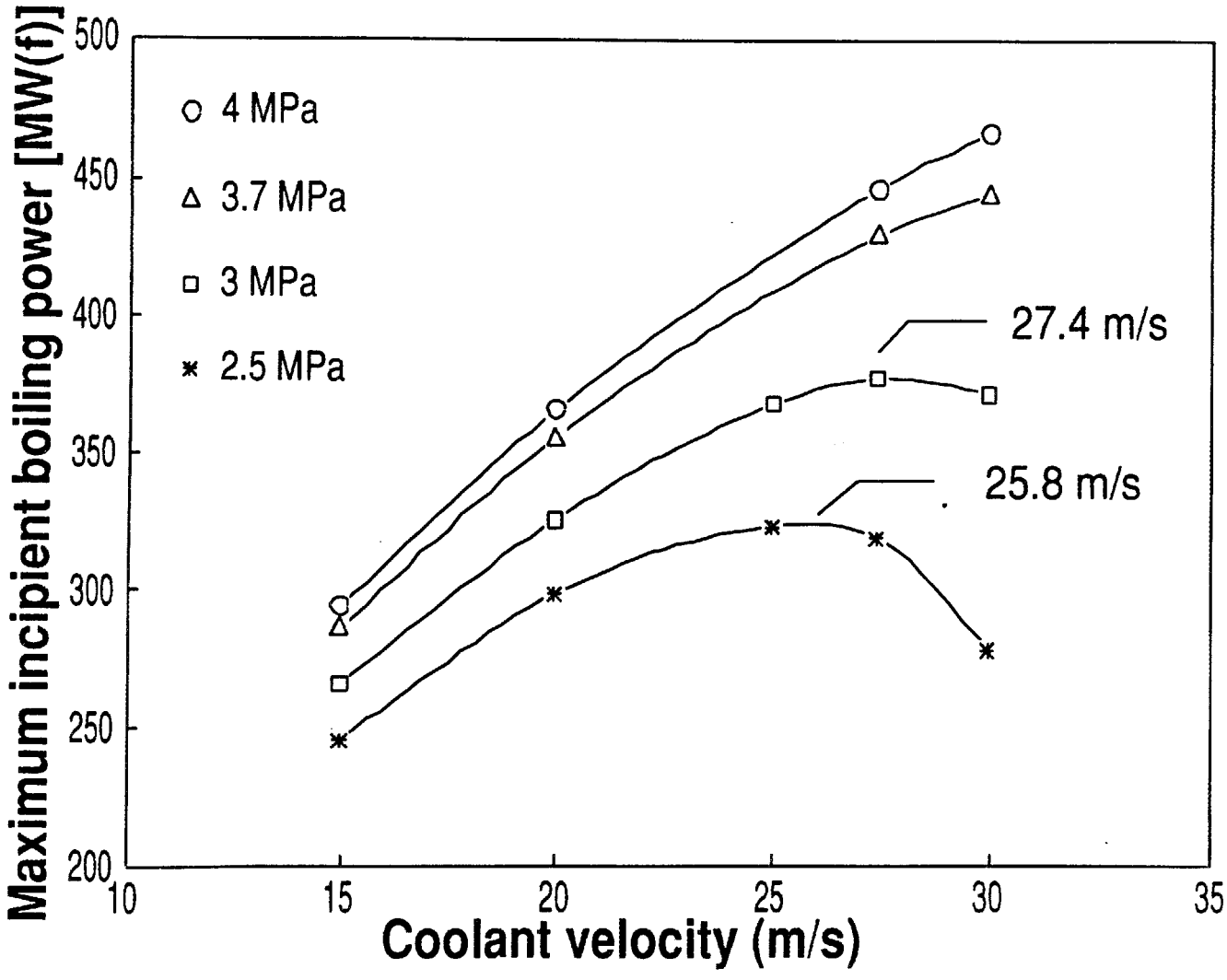

Fig. 5.4. Parametric study of I1 core operating parameters.

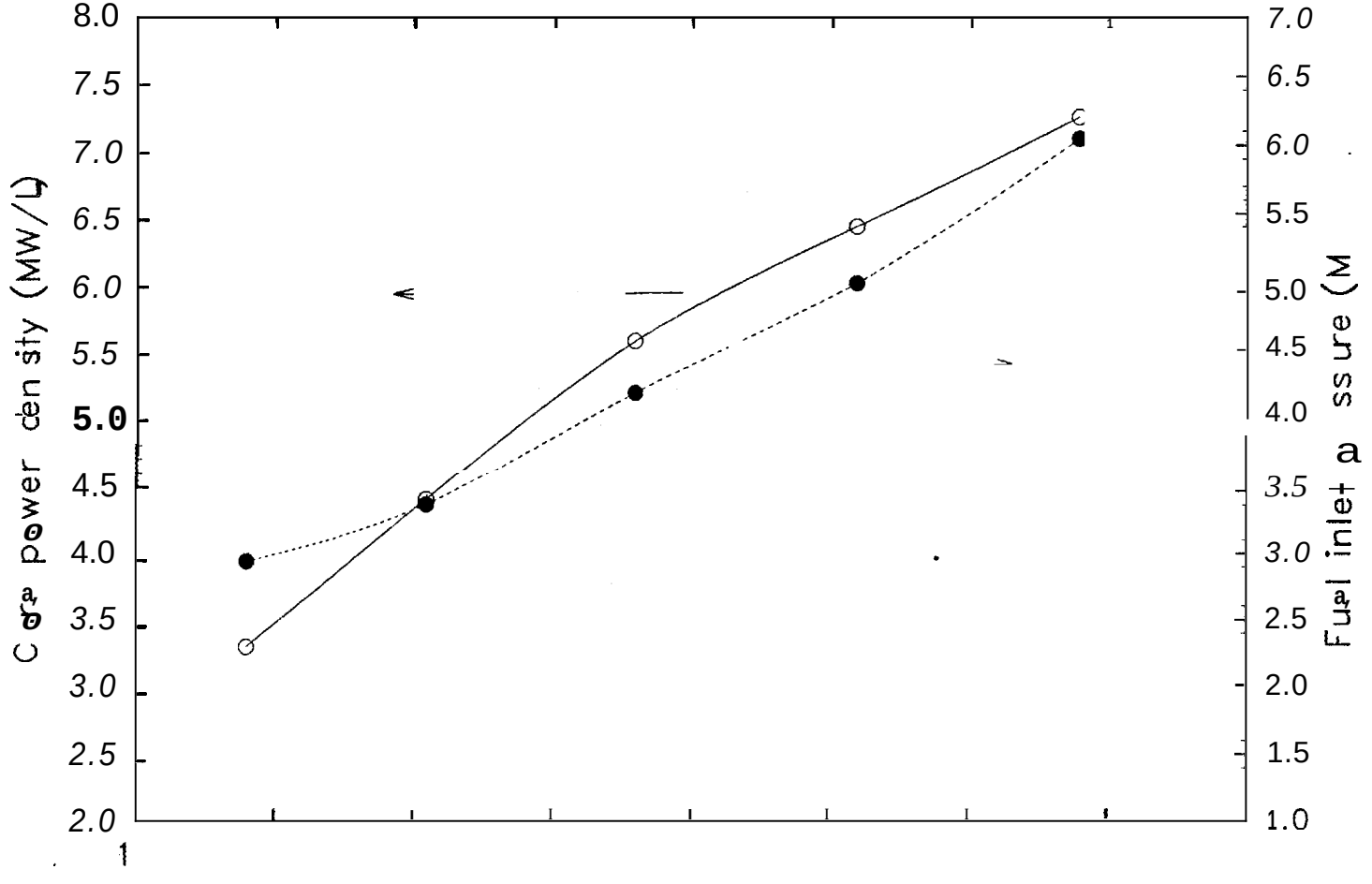

Fig. 5.5. Effect of coolant velocity on power density. {Case 6,50 1, heated length = 379 mm, inlet = 49°C, and outlet = 2.32 MPa ± 0.16.)

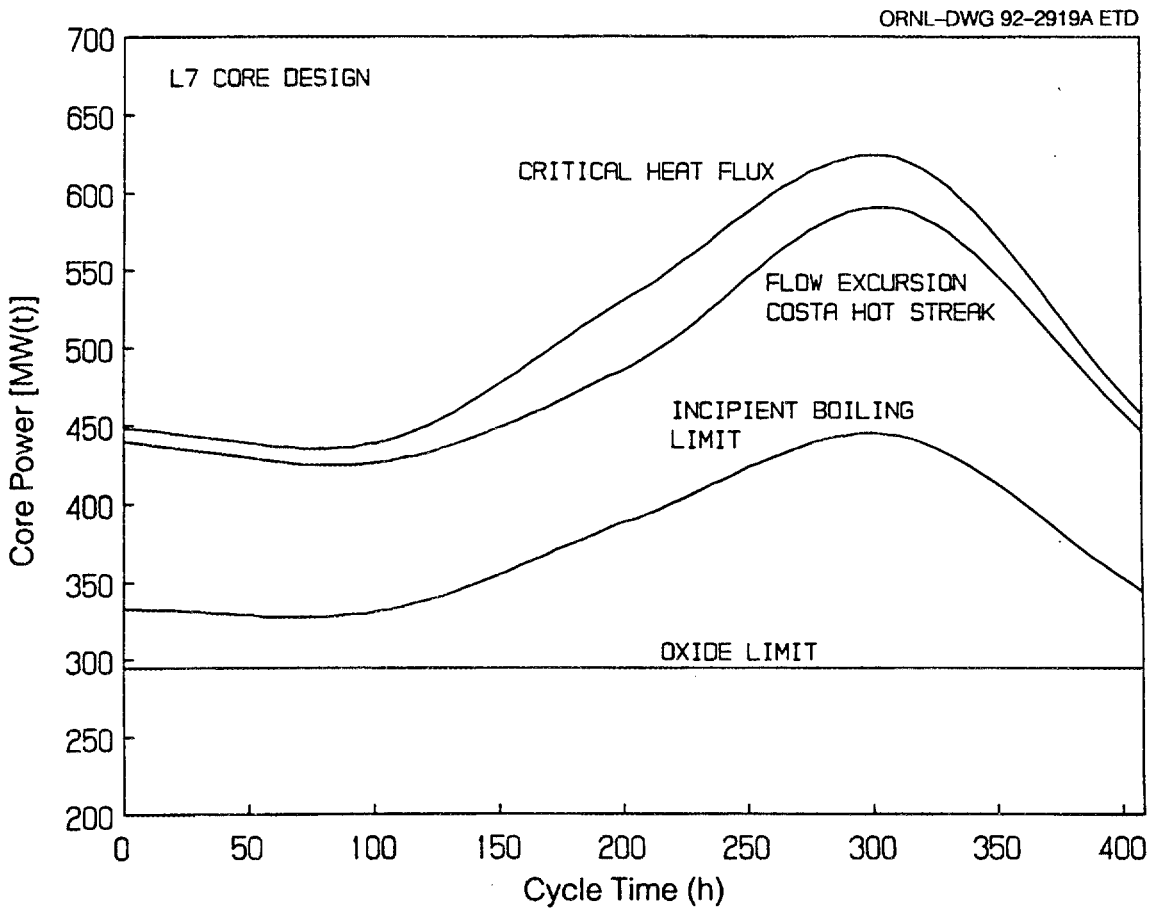

Fig. 5.6. Thermal limits during the fuel cycle (L7 core design).

Oxide thickness as a function of position on the fuel plate over the 17-d fuel cycle for the L7 fuel design (power distribution shown in Fig. 1.12) is shown in Fig. 5.7. A constant 303-MW(t) power level over the entire 17-d fuel cycle was assumed for these calculations. As the figure indicates, the maximum oxide thickness for this fuel design is 22.4 μm and occurs at the outer fuel radius of the lower core. A more complete discussion of the design aspects of oxide growth is given by Yoder et al.[142]

5.1.2 Natural Circulation Behavior

In-loop, steady-state natural circulation behavior is discussed in Sect. 5.2, Safety and Margin Analysis. However, under refueling conditions, several parametric studies have been performed. Since the ANS fuel cycle will last only 17 d with ~4 d allowed for refueling, it will be necessary to remove and install ~17 cores (i.e., both elements) per year. A refueling machine will be used to remove the element from the primary coolant loop and place it into a heavy water, short-term storage pool.

Each core half will be removed separately, and an absorber within the central hole and/or outer region of each core half will be used to control core reactivity while it remains submerged within D_2O. Figure 5.8 shows one possible design for the removal path. The region marked "1" is filled with D_2O and will be open to the primary system during refueling. The absorber will be installed and each core half will be moved from its normal position within the primary system (A) and moved to position (B). After a cooldown period, it will be placed within a D_2O/H_2O lock. The lock, initially filled with detritiated D_2O, will open to the transfer tunnel and accept an element, after which it will be resealed and flushed with H_2O. At this point, the element can be moved to the light water storage pool until it is removed for reprocessing.

Even some time after shutdown, the residual core power will be several hundred kilowatts, and some means of core cooling will be required in order to prevent overheating. The effectiveness of natural convection cooling during this process is discussed here. The object of this study is to determine the length of time required after reactor shutdown before the cores can be cooled by natural or forced convection with no boiling. The no boiling condition is presently used to provide a significant safety margin before the possibility of fuel damage might occur. For this initial investigation, it has been assumed that the core is stationary and is submerged within an infinite coolant pool.

Uncertainty levels that affect calculation of the bulk coolant temperature and the local hot spot conditions were also included in the analysis. For initial analysis, hot channel and hot spot uncertainty values were set at their 95% probability levels (see Sect. 4). In addition, a heat transfer coefficient correlation multiplier of 0.94 was used deterministically. This multiplier forces the Sudo correlation to skirt the lower bounds of the data envelope presented in ref. 11. These factors were incorporated into the analysis by multiplying the local temperature rise, the heat flux, and the heat transfer coefficient by the appropriate factor.

To provide some conservatism in the present initial calculations, IB was used as the thermal design limit and was calculated using Eq. (3.4). Because many details of the refueling process have yet to be determined, a parametric study was performed. The present analysis assumes no obstruction to the flow either at the bottom or top of the coolant channel, and that flow is supplied to each core half from an infinite coolant pool. Three parameters were examined—the effect of core location within the pool [i.e., the pool depth where the core half is located (defined from the top surface of the pool liquid to the bottom of the core half)], the effect of coolant temperature, and the effect of adding a chimney above the core to improve natural circulation performance. Since ANSR uses two separate

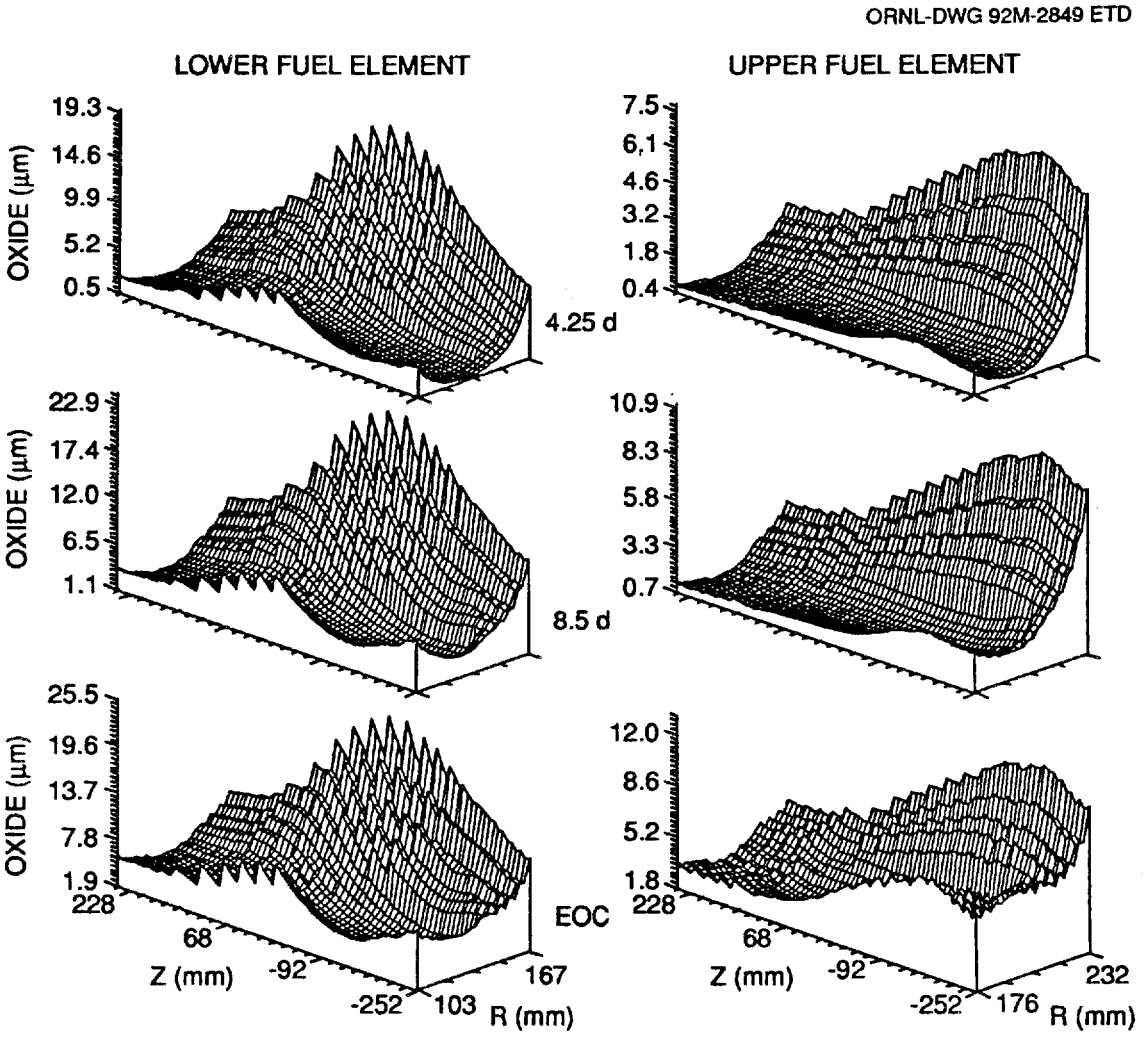

Fig. 5.7. Oxide profiles for both cores at three times in the fuel cycle.

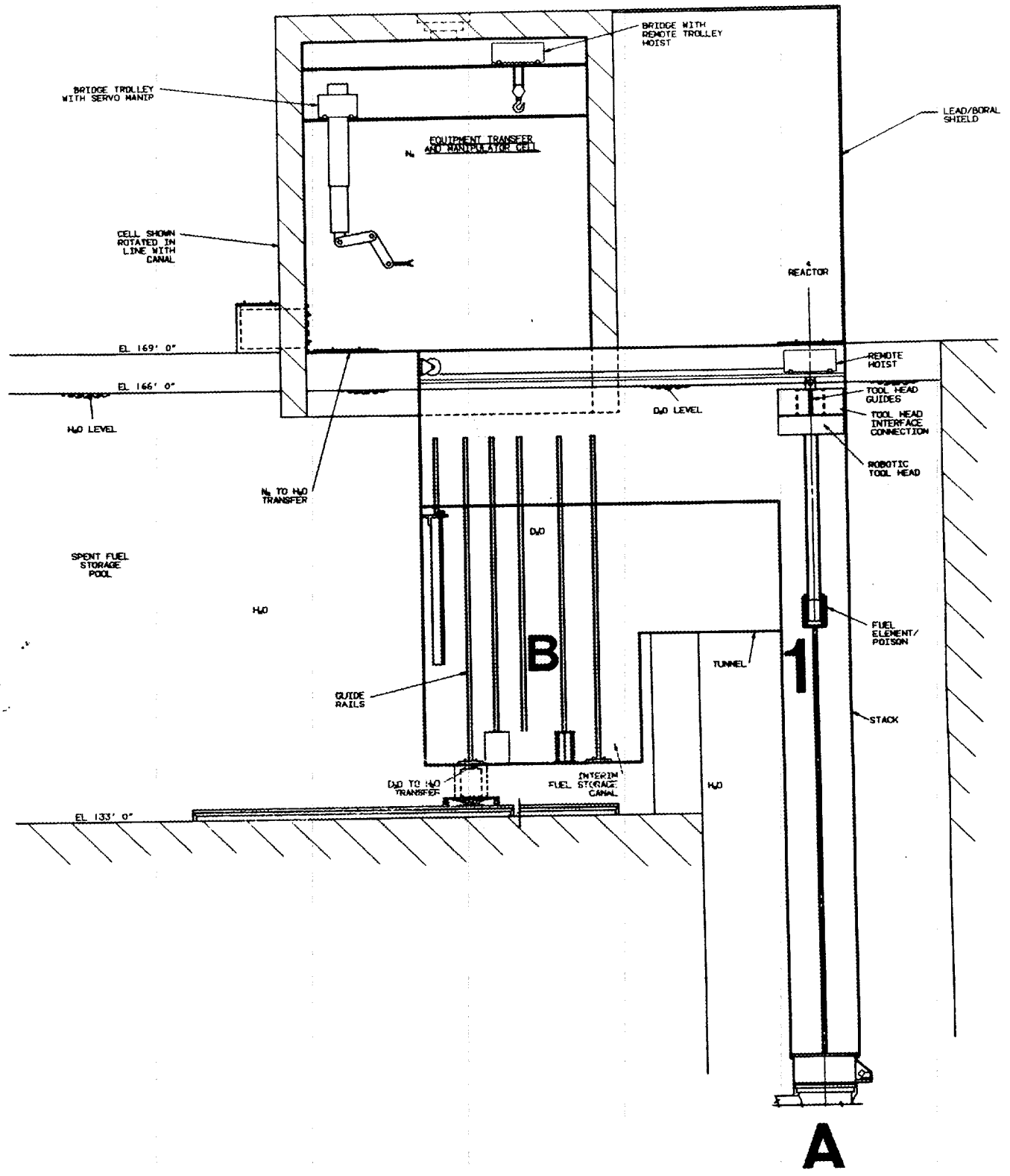

Fig. 5.8. One proposed refueling layout for the Advanced Neutron Source reactor.

core halves, each of which will be separately cooled by pool water, the maximum power (the power where one point in the core is at the IB limit) for each core half was first calculated based on the beginning of cycle power distributions, since that is the limiting condition. The limiting core half was then used to determine the maximum operating power for a given set of coolant conditions. The time after shutdown was then determined by comparing this power to the decay heat curve.

Figure 5.9 shows the margin to IB in degrees celsius (defined as the difference between the IB wall temperature and the calculated wall temperature) as a function of the coolant pool temperature and depth at 24 h after shutdown. As Fig. 5.9 indicates, a pool depth of $\sim$20 m is required for a pool coolant temperature of 35°C before natural circulation is adequate to prevent IB. Figure 5.10 indicates that a chimney placed above the core is effective at improving the IB margins.

Many of the same recommendations to improve the ANS steady-state T/H code that were discussed in Sect. 3 apply to the natural circulation code as well. In addition, review of the uncertainty values used in natural circulation calculations will be performed as the project progresses.

5.2 SAFETY AND MARGIN ANALYSIS

Table 5.2 presents maximum IB limited, CHF limited, and flow instability limited operating powers at several times in the fuel cycle. These calculations were performed with the TASHA code using core inlet conditions corresponding to the operating margin described in Sect. 4. The IB limit calculated at a 95% probability level is shown in the table, while CHF and FE limits are shown at both the 95 and 99.9% probability levels.

In addition, a best estimate calculation of CHF and FE is also presented with core inlet conditions at their nominal values. As indicated in the table, the core design currently meets the alternate design criterion for IB discussed in Sect. 1, and the best estimate limiting FE power level is a factor of 1.6 above nominal.

Calculations examining the FE and CHF limits using the 99.9% probability level and coolant inlet conditions established by the safety margin (also discussed in Sect. 4.) are presented in Table 5.3. These calculations represent a drift of all controlled parameters to the safety set point. (This condition would be considered an anticipated event.)

The reactor protection system provides scram on both power and flux-to-flow ratio to protect against inadequate primary coolant flow as well as excessive power. Primary coolant pressure and core inlet temperature scram settings have been tentatively set at 79% of normal core outlet pressure and 122% of the normal core inlet temperature. For the calculations presented in Fig. 5.11, the core exit pressure was varied parametrically while the core inlet temperature was assumed to remain at the scram set point, the worst possible value for IB, FE, or CHF. The friction factor was assumed to be at its 2 σ value to establish pressures conservatively within the core region. Results of calculations are illustrated in Fig. 5.11. Also shown in Fig. 5.11 is the region of normal operation about which there is no boiling. As defined in Sect. 4.1, the no-boiling criterion applies only to normal operation, whereas the no-CHF or -FE criterion applies to all anticipated events at a 99.9% probability level (3.09 σ away from the best estimate value, if the distribution was normal) and to all unlikely events at a 95% probability level (a 1.65 σ away from the best estimate value, assuming a normal distribution). It should be noted that, in fact, the appropriate distribution is not a normal distribution; proper evaluation of actual standard deviation values will be performed at a later date.

Figure 5.11 is constructed to illustrate the relationships between nominal conditions, anticipated operating conditions allowed by the reactor protection system, and design basis accidents. The

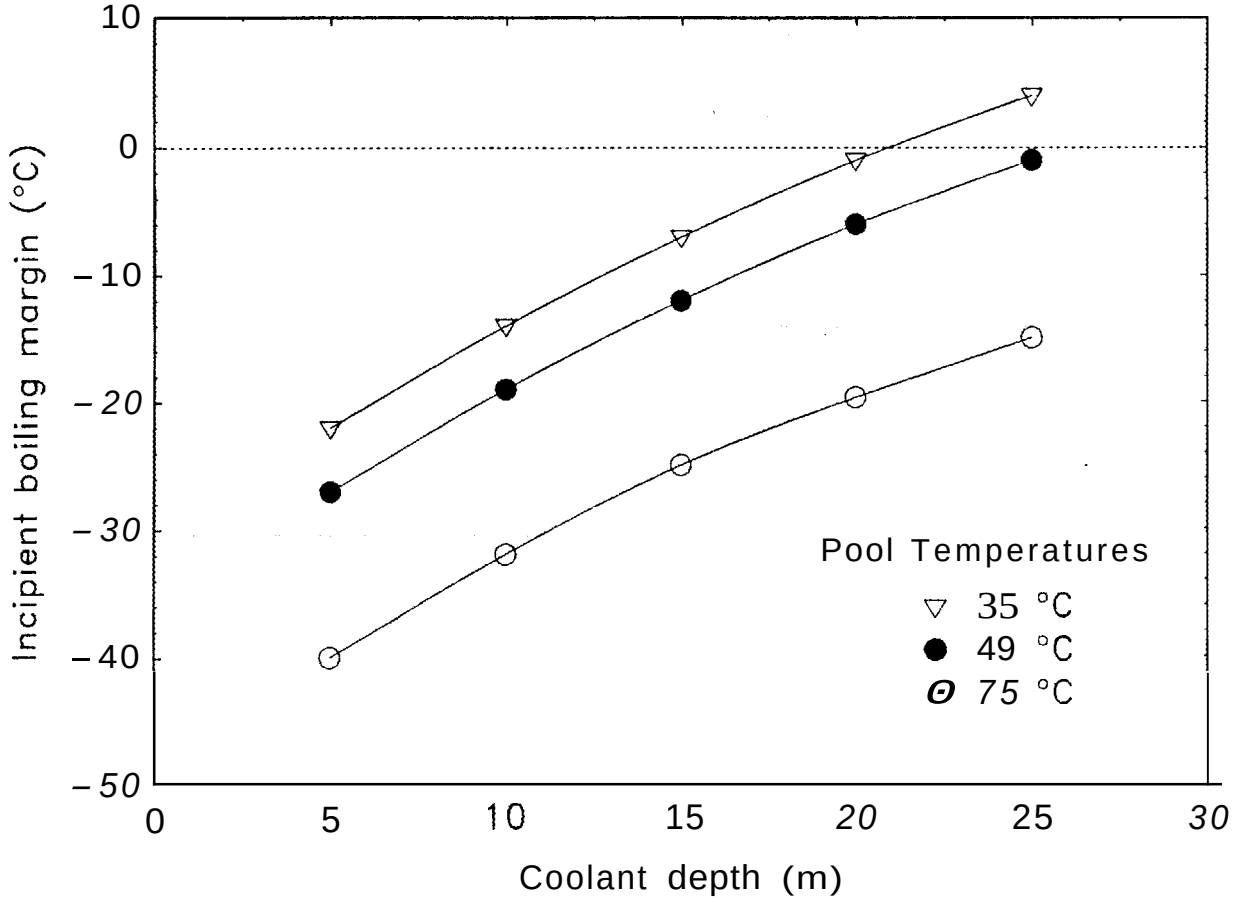

Fig. 5.9. Incipient boiling margins 24 h after shutdown.

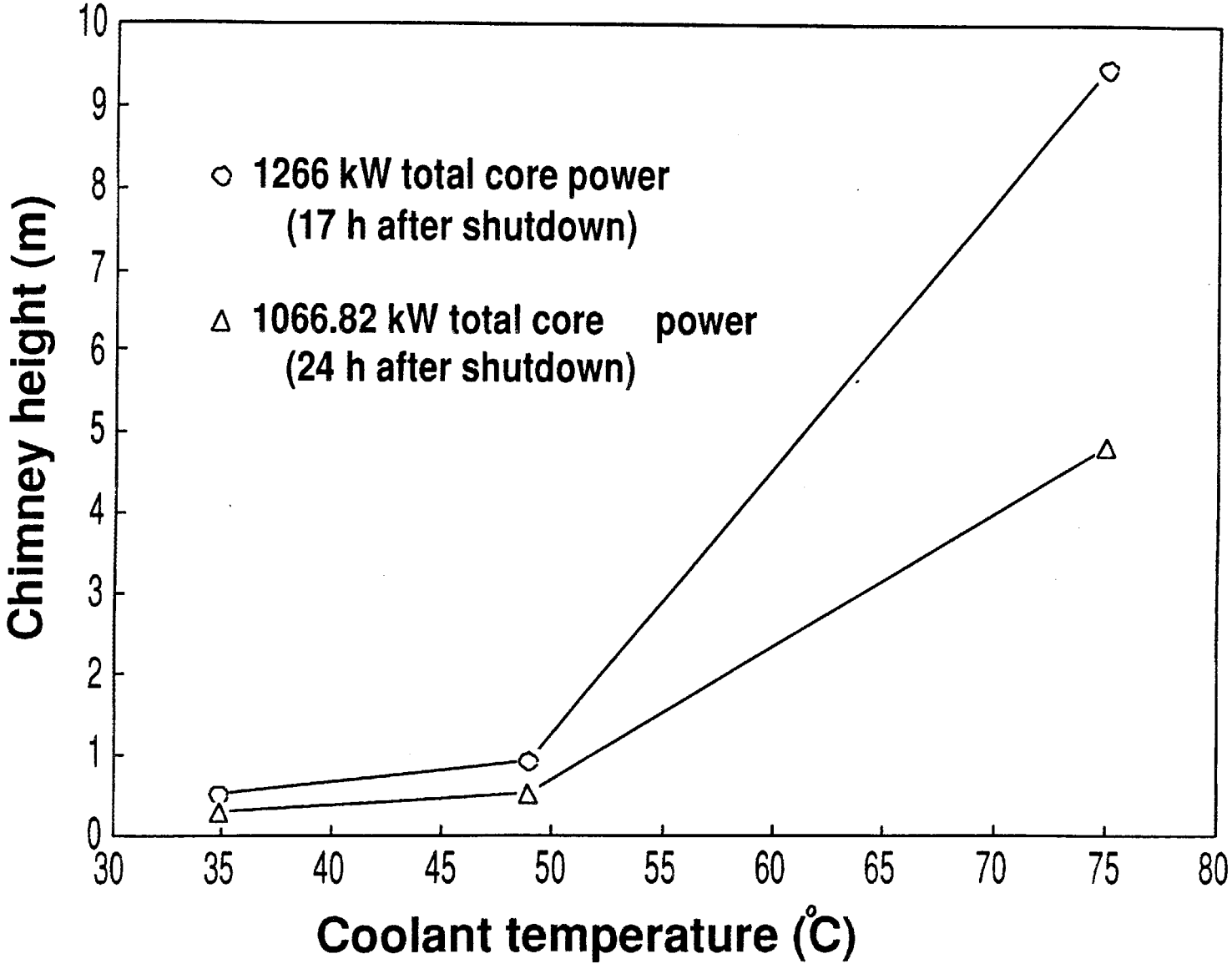

Fig. 5.10. Chimney height required at point of incipient boiling.

Table 5.2. Limiting power level [MW(t)] normal operating margin

Limited	IB[a]	CHF[b]			FE[c]		
Probability	95%	95%	99.9%	Best estimate	95%	99.9%	Best estimate
BOC[d]	333	448	396	521	439	414	494
4.25 d	332	440	390	511	427	402	482
8.5 d	391	535	479	611	490	459	555
12.75	445	624	567	712	592	550	668
EOC[e]	345	458	407	533	448	415	511
Nominal operation	303	303	303	303	303	303	303

[a]IB = incipient boiling.
[b]CHF = critical heat flux.
[c]FE = flow excursion.
[d]BOC = beginning-of-cycle.
[e]EOC = end-of-cycle.

Table 5.3. Limiting power levels 99.9% probability at the safety margin

Time	CHF[a] limiting power [MW(t)]	FE[b] limiting power [MW(t)]
0	363	365
4.25 d	358	355
8.5 d	440	406
12.75 d	515	486
EOC[c]	371	366
Nominal operating	303	303

[a]CHF = critical heat flux.
[b]FE = flow excursion.
[c]EOC = end-of-cycle.

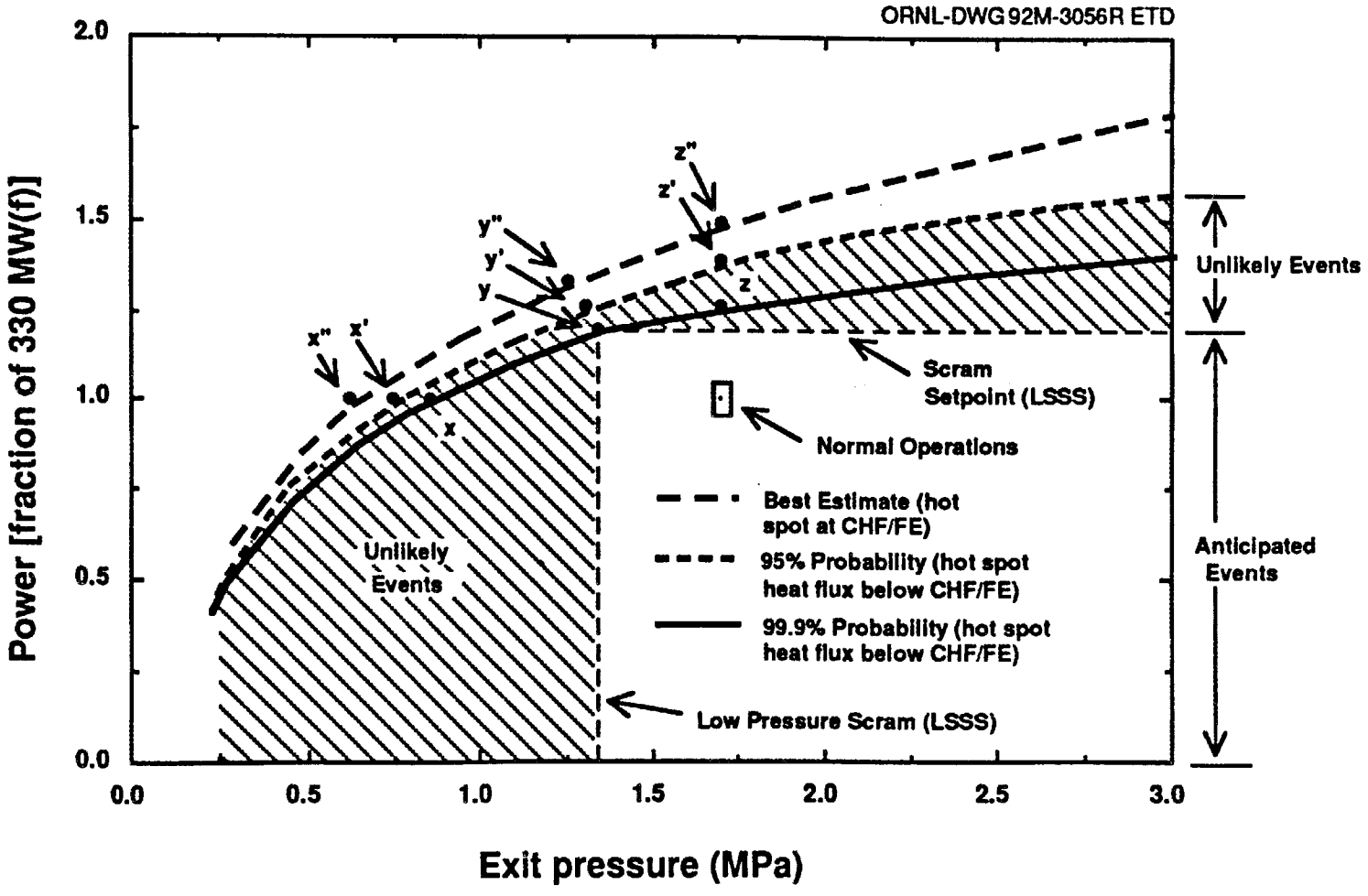

Fig. 5.11. Advanced Neutron Source operating map for three-pump operations.

smallest and innermost region is that of normal operation. Throughout this region, there is no boiling at any point in the core. The small square around the nominal operating conditions represents possible instrument errors and minor control variations. Anticipated events perturb pressure or power in a wide region around the nominal, but are interrupted with little overshoot after LSSS is exceeded. The more severe challenges represented by design basis accidents may push the power-to-flow ratio and/or pressure beyond LSSSs into the unlikely event region indicated on Fig. 5.11. The results of Fig. 5.11 are accurate for steady-state, nonboiling conditions; reasonably accurate in a quasi-steady-state sense to transients in the anticipated event category; and less accurate for accidents in the unlikely event category.

Three accident paths are illustrated on Fig. 5.11. Path X-X′-X″ represents a loss of pressure without change in flux-to-flow ratio. Path Y-Y′-Y″ could be a pump coastdown or another accident involving simultaneous degradation of core outlet pressure and flux-to-flow ratio. Path Z-Z′-Z″ would be typical of a power excursion, with the flux-to-flow ratio increasing without any concomitant loss of core outlet pressure.

Path Y-Y′-Y″ of Fig. 5.11 was chosen hypothetically and, therefore, is not guaranteed to represent any specific event. Pressure decay with flux-to-flow increase traces a path toward the CHF safety limit curve. When the edge of the IB curve is reached, there is a 5% chance of IB at the worst location within the core. IB is defined as the point (or time) where the first bubble is formed on the fuel surface. Further progression toward point Y may result in some void production by the time that the CHF/FE safety limit curve is reached. Before point Y is reached, automatic control action would insert control rods in an attempt to maintain a flux-to-flow ratio of one, and the letdown valves would close in an attempt to maintain a constant core outlet pressure. If these control actions are not effective, continued degradation of the control parameters would result in the set point for flux-to-flow scram being exceeded, and the most likely event at that point would be reactor scram and rapid power reduction with a consequent rapid improvement in the safety margin. But if measurement and set point errors are at their worst condition in two of the three scram channels, the scram might not be initiated until the actual power reaches the CHF safety limit curve.

When point Y is reached, the probability of CHF or FE at the hot spot is 0.1%, or 10^{-3}. Although the ANS scram systems are very fast, a rapidly developing accident (i.e., an unlikely event or an extremely unlikely event) might force the trajectory to point Y′. The probability of hot spot CHF at point Y′ is 0.05. This probability is acceptable when considering the frequency of initiating events capable of causing significant overshoot past the scram settings. Continued degradation of reactor pressure and flux-to-flow ratio would lead to a rapid increase in the probability of FE or CHF until, at point Y″, there would be an even chance of exceeding the FE or CHF limit.

Table 5.4 shows the oxide limited power at all times in the fuel cycle. As is indicated by the minimum power level of 299 MW(t), this core is limited by the oxide temperature drop (spallation) at 4.25 d into the fuel cycle. The limiting location is at the outside edge of the lower core. Additional work on the fuel design in the future should show additional improvement in core performance with respect to oxide growth behavior.

The L7 core design, therefore, does not currently meet the design criterion No. 3 discussed in Sect. 1, either at nominal conditions or for an anticipated event where all controlled parameters drift to their set-point limits. The combination of sharp peaks in the L7 power distribution and the significant dependence of the oxide growth rate correlation [Eq. (3.10)] on local heat flux limits the core power early in the fuel cycle. It is felt that this limit can be improved by several means. Three of the most promising means of improvement are increased time-step and fuel-meat grading resolution and improved fuel grading. To examine the impact of these effects, a sensitivity study was performed.

Table 5.4. Oxide limits at all time steps

Time	ΔT limited [MW(t)]	T_{el} limited power [(MW(t)]
0		
4.25 d	295	308
8.5 d	295	318
12.75 d	308	341
EOC[a]	326	370
Nominal operating	303	303

[a]EOC = end-of-cycle.

The neutronics calculations currently use a coarse mesh to grade the fuel and a much finer mesh to calculate relative power densities. This combination results in a rather jagged and peaked power density distribution as evidenced by Fig. 1.12. To examine the effect of increasing the fuel thickness mesh on oxide growth calculations, the oxide limiting channel (the channel located at the outer radius of the lower core and designated as channel 26) was smoothed and the case was rerun. The results are shown as case 2 in Table 5.5 (the original case is shown as case 1 and is used to normalize the other power levels). A gain of 1.4% over nominal was achieved via this change alone.

Table 5.5. Sensitivity of oxide limiting power to fuel design issues

Case	Calculation	Relative limiting power	Limiting:		
			Core	Pos.	Time (h)
1	Nominal	1	lower	26,31	102
2	26 smoothed	1.014	lower	26,24	204
3	26 smoothed, alternate oxide growth	1.065	lower	26,24	102
4	26 suppressed	1.075	lower	24,31	204
5	26 suppressed, alternate oxide	1.126	lower	24,31	204

To examine the effect of shortening the neutronics timestep, an alternate method of calculating the oxide growth (case 3, Table 5.5) was used. Normally, the oxide growth is calculated from time t to time $t + 1$ based on the power distribution for time t; the oxide limits of maximum centerline temperature and maximum oxide temperature drop are calculated based on the time t power

distribution. This method is conservative if the power at the limiting position decreases from time t to time $t + 1$. To get an idea of how conservative this might be for the L7 core, an alternate method was used to calculate the oxide growth. In this alternate method, the oxide growth was calculated from time t to time $t + 1$, based on the time t power distribution as is normally done, but then the limiting temperature conditions were calculated based on the $t + 1$ power distribution. In reality, neither of these methods is exactly correct, because a continuous description of the power density variation is needed from time t to time $t + 1$ to get an exact solution to this problem. However, it does give some idea how conservative the calculations might be, and how much improvement might be available with power distribution information in smaller time step increments. Of course, if for some reason the power distribution actually went through some maximum from time t to time $t + 1$, then it is possible that neither calculation would be completely conservative. Calculation in this manner increases the limiting power level an additional 5% over the smoothed channel 26 case.

Case 4 is like the nominal (case 1) calculations, except that channel 26 in the lower core has not been allowed to limit. To do this, any relative power density in channel 26 with a value over 1 was set to a value of 1. The idea in this calculation was to see what the effect of moving some fuel out of this region would be on the limiting power. An increase of 7.5% over nominal was achieved by preventing channel 26 from limiting. If channel 26 is suppressed and the alternate oxide treatment is used, a gain of 12.6% over nominal is achieved.

These calculations are intended to show the magnitude of improvement that might be expected with further fuel grading work.

In this report, discussion of natural circulation while the core remains within the primary coolant system will be limited to only steady or quasi-steady conditions. Transient studies of natural circulation capabilities of the ANS have been performed and are reported elsewhere (see refs. 2-5). Figure 5.12 indicates that pony motor flow would be sufficient to cool the core immediately after shutdown without exceeding the IB limit even if the system were at pool pressure (0.3 MPa) and that natural circulation would be sufficient after ~1 h. The power-time curve shown in this figure reflects the total decay heat of the core. Because all of this heat would not be deposited to the coolant directly from the fuel plates, using this curve as a reference introduces some conservatism into the conclusions.

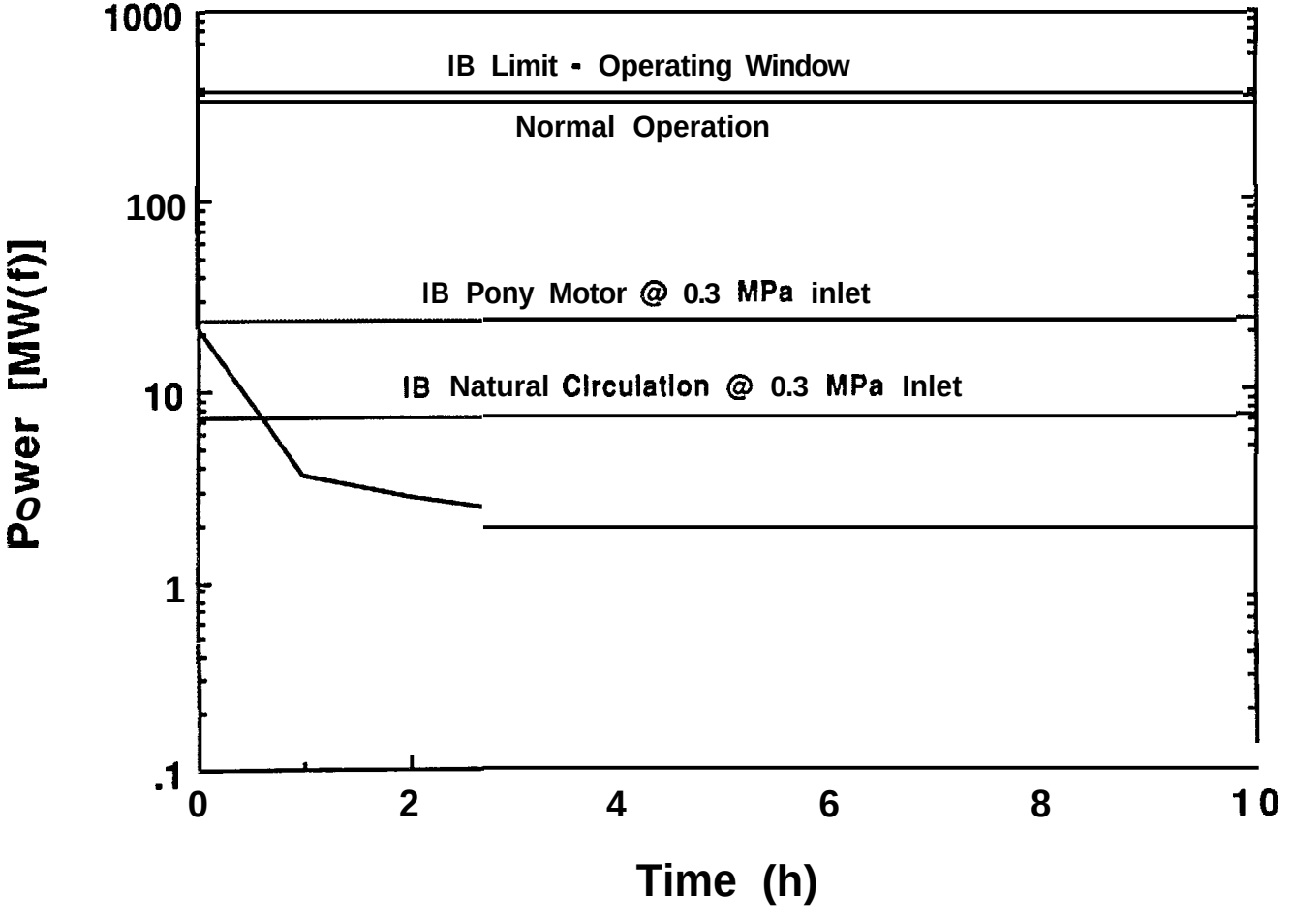

Fig. 5.12. Power decay heat curve after 17 d of full power operation. (IB = incipient boiling.)

6. EXPERIMENTATION IN SUPPORT OF THE ADVANCED NEUTRON SOURCE REACTOR DESIGN AND SAFETY ANALYSIS

Extensive testing of operating thermal limits and other T/H correlations will be undertaken to support the T/H design and safety analysis of the ANSR. In areas where supporting data is limited or nonexistent, experimental test facilities are planned to verify safety margins in the design. Additional T/H experiments are planned to establish the safety-related performance limits of the ANSR. The majority of the safety-related transient T/H of the ANSR will be done using RELAP5. The TASHA code will be used for detailed T/H design and analysis of the fuel assembly under steady-state nominal conditions, including statistical evaluation of the uncertainty involved. Other analytical tools will be used for special situations. A multidimensional fluid code may be used to evaluate flow blockage in the fuel assembly. A lumped parameter code using a high-level simulation language is used extensively for control system and coolant system design studies and will be used for evaluation of some safety-related transients as a check of consistency between analysis tools. However, RELAP5 will be the main analytical tool to perform most of the reactor safety-related transient analyses presented in the FSAR.

RELAP5 has been developed over many years for the simulation of transient T/H behavior of power reactors. Many of the models and correlations in RELAP5 are specific to the conditions encountered during typical power reactor transients. Some situations expected during safety-related transients in research reactors are quite different from those analyzed for power reactors. Therefore, both RELAP5 and the TASHA codes were modified to be applicable to the ANSR configuration and operating conditions. Models and correlations have been identified and incorporated into the codes as appropriate to accommodate these situations. Verification and validation exercises will be required to ensure that these models are properly implemented in the codes and that the resulting integral modeling program (i.e., code and system models) is capable of representing ANSR transients.

A preliminary experimentation plan has been developed to define the type and scope of experiments needed to support the design and safety analysis of the reactor as well as to provide a basis for the verification and validation of the major codes used in the analysis.

Four areas dictated the direction of the experimentation plan: (1) the thermal phenomena that are limiting the reactor thermal performance within accepted safety margins, (2) the design and safety criteria used for the analysis, (3) the availability of reliable T/H correlations and their supporting data base, and (4) uncertainty distributions and tolerance requirements. These areas will be briefly discussed here, followed by a discussion of the facilities and the experiments that have been performed or that are currently planned.

6.1 PHENOMONOLOGY OF THERMAL LIMITS IN THE ADVANCED NEUTRON SOURCE REACTOR FUEL ASSEMBLY

This section will review the limiting thermal conditions in the reactor fuel assembly (i.e., CHF, FE, and IB as related to hot stripes and hot spots) and the models and data available and/or needed to evaluate these thermal limits. This background is necessary to justify the experiments that are subsequently described. The requirements for verification and validation of a complicated system code in conjunction with the complexity of the T/H phenomena that control the thermal limits in the fuel assembly must be understood to appreciate which experiments are needed and the basis of the structure for such experiments.

6.1.1 High Mass Flux Conditions ($G > 2000\ kg \cdot m^{-2} \cdot s^{-1}$)

The cooling channels in the ANSR fuel assembly are all parallel and share common inlet and outlet plena, imposing a common pressure drop along all the channels. This core configuration is subject to a potential excursive instability, called FE, that may occur once boiling is initiated in any one of the channels.[143,144] The FE phenomenon constitutes a different thermal limit from a true CHF or departure from nucleate boiling (DNB). In such a system, initiation of boiling in one of the channels (e.g., the hot channel) can result in flow redistribution to the other cooler channels. This process can very rapidly lead to flow starvation, which, in turn, leads to a DNB in the hot channel at flows lower than the nominal flow rate. The FE phenomenon is in contrast to a primary DNB that occurs at a nominally constant flow rate, referred to here as a "true CHF." Unfortunately, many of the CHF correlations are based on some combination of primary DNB where the mass flux at the position and time of the DNB are known, and FE where the mass flux at the time and position of the DNB are not known (i.e., the researchers recorded the mass flux at the onset of FE, not at DNB). This situation undoubtedly contributes to the wide scatter in reported CHF data. Only data taken with appropriate channel pressure drop characteristics (constant pressure boundaries) should be used to establish the conditions at the onset of FE in the fuel assembly of a research reactor. Similarly, only data taken with constant and known mass flux conditions should be used to establish true DNB (or CHF) conditions.

The more complete way to predict the occurrence of FE is to perform flow vs pressure-drop analysis of the parallel channels involved and to predict the subsequent flow redistribution under constant and common pressure-drop boundary conditions. Performing this prediction is quite complex because of the uncertainties involved in predicting void fractions and pressure drops in two-phase flow. In reality, after boiling starts, the flow resistance of the channel increases drastically, leading to flow reduction in the channel. The flow reduction promotes more boiling, which rapidly leads to FE. Therefore, it is normally accepted that FE [also referred to as the onset of flow instability (OFI)] will most likely occur near the point where sustained net vapor first appears. This point is called the ONVG point[25] or the point of onset of significant void (OSV).

Since FE is a pressure-drop driven phenomenon, it can be expected that anything that affects the pressure drop characteristic of the channel (both single- and two-phase) will influence the position where FE is initiated. The conditions leading to the onset of this instability can be expected to vary with the ratio of heated perimeter to channel cross-section area, the amount of pressure drop in the unheated sections upstream and downstream of the heated section (but included in the section where the pressure drop is held constant), and the length of the unheated section downstream of the heated section (caused by condensation that results in some pressure recovery).[25]

Maulbetsch and Griffith[145] and other investigators[146,147] analytically and experimentally demonstrated the conditions under which excursive instability will occur. They have determined that such instability will occur "if the slope of the (demand) pressure drop vs flow rate is more negative than that of the external supply system." This statement is expressed mathematically as:

$$\frac{d(\Delta P_{ext})}{dV} > \frac{d(\Delta P_{is})}{dV} \quad , \tag{6.1}$$

where

ΔP_{ext} = external supply pressure drop (Pa),
ΔP_{ts} = test section pressure drop (Pa),
V = coolant velocity (m/s).

Figure 6.1 presents a typical plot of the pressure drop vs flow rate relationship under various boundary conditions. In the case of many parallel channels between large common headers, as is the case in the ANSR, the slope of the external supply system is practically zero and is represented in Fig. 6.1 by horizontal lines (A and B). This relationship means that, in order to properly simulate the true FE phenomenon in an experiment, the test section supply system must have a very shallow pressure drop/flow rate slope. This simulation has been achieved in past experiments by using a large bypass around a single heated channel. As the supply system "stiffens" (or the supply side pressure drop/flow rate slope approaches infinity), the experiment becomes capable of simulating a true CHF condition. In this case, the flow rate to the test section is independent of the test section pressure drop.

Knowing which of the two types of limiting phenomena—true CHF or FE—should be used as a thermal limit for the ANSR configuration is crucial. In most cases, FE will precede true CHF in such a configuration.[62] However, the sequence of these phenomena depends on the specific conditions involved. It was demonstrated that FE will occur at heat fluxes much lower than the CHF (as low as half) at low pressure, low velocities, and low subcooling.[144] Some recent data taken at conditions of very high local subcooling and heat flux at pressures near the operating pressure for the ANS (Boyd,[92] and Celata et al.[94]) indicate the pressure drop in the channel may not increase appreciably prior to DNB. These data are consistent with the trend reported in the data of Inasaka, Hariai, and Shimura[148] and Rohsenow and Clark,[149] which show that the increase in pressure drop in the channel with subcooled boiling is less significant as pressure and local subcooling is increased. Unfortunately, the exit pressure measured by Boyd was actually measured 5 to 6 L/D downstream of the heated length. The pressure drop resulting from the change in momentum flux may have been recovered in this length, as discussed earlier. It remains unclear if a similar situation existed in the data taken by Celata et al.[94] If the possibility of having missed the pressure drop because of the change in momentum flux is ignored, this data indicate that, as exit subcooling and pressure are increased, the thermal limit changes from an FE leading to decreased mass flow and burnout to a primary departure from nucleate boiling. Since the ANS normally operates at moderate pressures and very high mass flux and subcooling levels, one of the main goals of testing is to determine this relationship between CHF and FE under ANS conditions. There may exist a locus of subcooling, pressure, and velocity values that denote where the FE limit and the primary DNB limit converge for the ANS. Care must be taken to resolve this issue in the safety related T/H experiments.

Several assumptions are made while establishing thermal limits in research reactors like ANSR. It is assumed here that the involute shape of the span of the cooling channel can be replaced with a simple rectangular channel cross section. This assumption is reasonable since the minimum radius of curvature of the involute profile is over thirty times the channel gap. Some offset of flux profiles occurs in the involute channel that is lost in the rectangular model. However, this is not an important effect for the ANS as shown in analysis contributed by Doderlein.[9]

The orientation of the flow (i.e., upflow or downflow) can normally be expected to influence the pressure drop in the channel once vapor is generated in the heated channel. However, in subcooled boiling water flowing at low pressure (i.e., subcooling $>5°C$ and pressure <2.5 MPa), the buoyancy

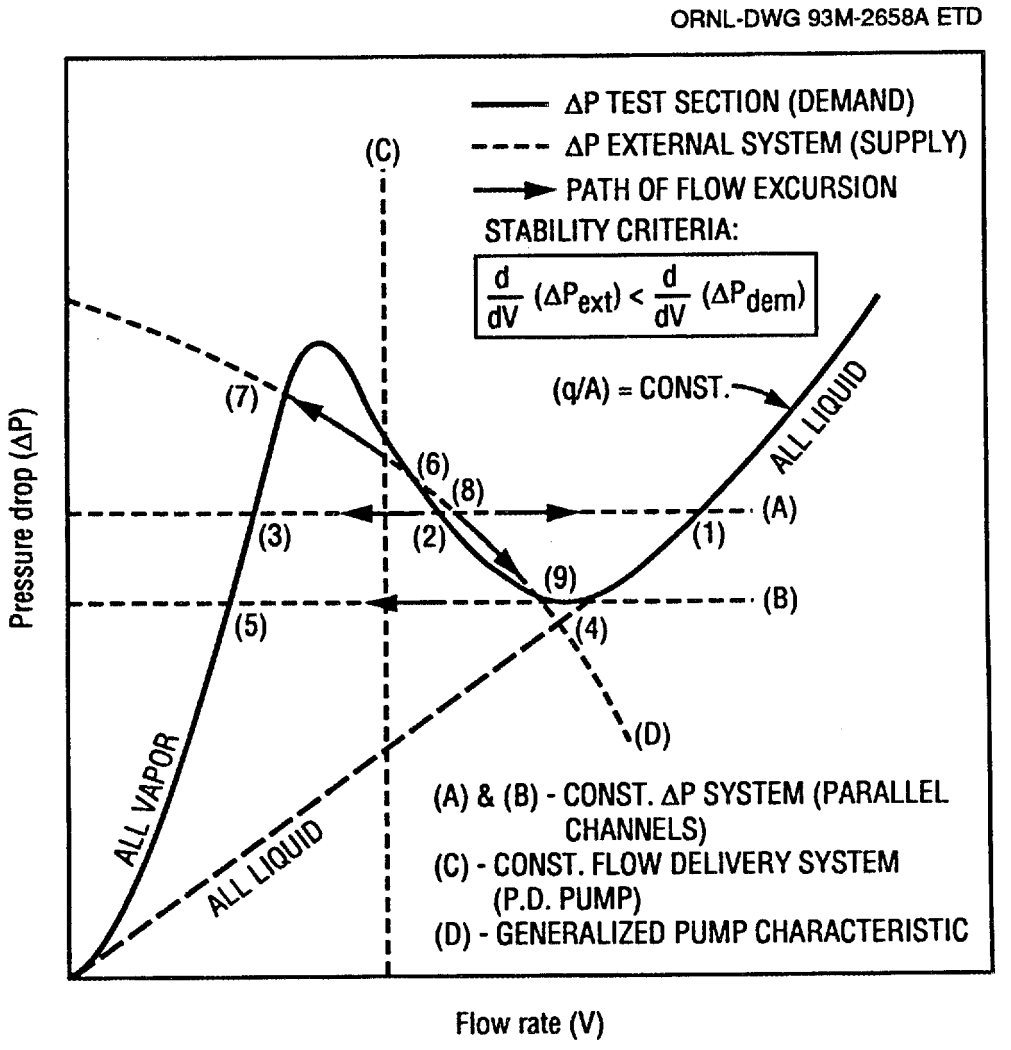

Fig. 6.1. Typical plot of pressure drop vs flow rate.

terms are not important relative to the momentum flux terms until the flow velocity is <3 m/s. Thus, the flow orientation is not important to high mass flux situations as in the ANSR nominal conditions.

The flux profile is also expected to influence the pressure drop characteristic of the channel. A significant assumption is made when conventional models for thermal limits are applied to a cooling channel with both spanwise and axially varying flux profile. The majority of data used to generate the models for thermal limits were generated in uniformly heated tubes, some in uniformly heated rectangular channels, and very few in nonuniformly heated channels. Costa[29] consolidated results of several experiments where nonuniform flux profiles were tested and found that the onset of FE was predicted well if 0.94 times the peak flux in the channel was used to compare with the model developed to predict the onset of FE in a uniformly heated channel. Some flux profiles that were tested are shown in Fig. 6.2. Waters[62] found the exit bulk temperature profiles in his experiments followed the spanwise flux profiles of the channel.

The explanation for these results and conclusions can be explained with the aid of Fig. 6.3, which represents hot stripe conditions in a rectangular channel. Local vapor generation along the hot stripe causes significant increase in the local resistance to flow because of increased momentum flux and increased viscous pressure losses. This increased resistance motivates the bulk fluid stream lines to bypass the region where vapor is being generated. This situation is somewhat analogous to FE in a heated subchannel. The major portion of the large channel is functioning as a bypass, maintaining constant pressure drop boundary conditions on the subchannel. It should be noted that the short subchannel does not have the long stabilizing single-phase flow length available that existed in the uniformly heated channel case. Thus, a local FE upstream of the hot stripe could be envisioned to occur before that observed in a uniformly heated channel. Note that this analogy is not strictly correct since it is actually the **local pressure gradient** that is imposed along the hot stripe by the cooler bypass flow in the channel. Gunther[150] conducted thermal limit experiments on a uniformly heated strip 3.2-mm wide in an otherwise wider adiabatic channel. The situation he tested was analogous to the hot stripe since boiling on the heated strip had a limited influence on the total channel pressure drop (i.e., the heated perimeter over the adiabatic perimeter was 0.18). Interestingly, the model developed by Gunther has the same functional form as that proposed by Costa. However, Gunther's measured burnout values are, on average, 3% lower than those predicted by Costa in uniformly heated channels. The bulk fluid exit temperature is used in this comparison since it is not possible to define a hot streak temperature for the geometry in this experiment.

A series of tests were conducted at the Savannah River Laboratory (SRL) in the 1960s[151] examining burnout fluxes in channels with hot stripes. The channel cross section was 50×3 mm with a heated length of 0.6 m. Results of these experiments indicate that the burnout heat flux along the hot stripe is underpredicted by as much as 30% for stripes with widths <10 mm and is equal to or slightly over that predicted for stripes with widths >10 mm, when using the hot stripe heat flux and corresponding hot stripe bulk fluid temperature in a correlation developed from uniformly heated channel data. The underprediction vanishes as the stripe width approaches or exceeds ~ 10 mm.

Figure 6.4(a) shows the pressure gradient in a channel with a hot stripe similar to that pictured in Fig. 6.3. The pressure gradient in a uniformly heated channel at the hot stripe heat flux value is also shown. The channel with the hot stripe has single-phase pressure drop behavior up to the point where net vapor is produced along the hot stripe. The channel pressure gradient decreases somewhat (i.e., becomes a larger negative value) at this point. The magnitude of this decrease depends on the amount of the channel perimeter devoted to the hot stripe. The case where the channel is uniformly heated at the hot stripe value shows a slight decrease in pressure gradient at the incipience of boiling followed by a large decrease at ONVG.[83,148] The channel with the hot stripe approaches the behavior of the uniformly heated channel as the amount of perimeter devoted to the hot stripe is increased to 100%.

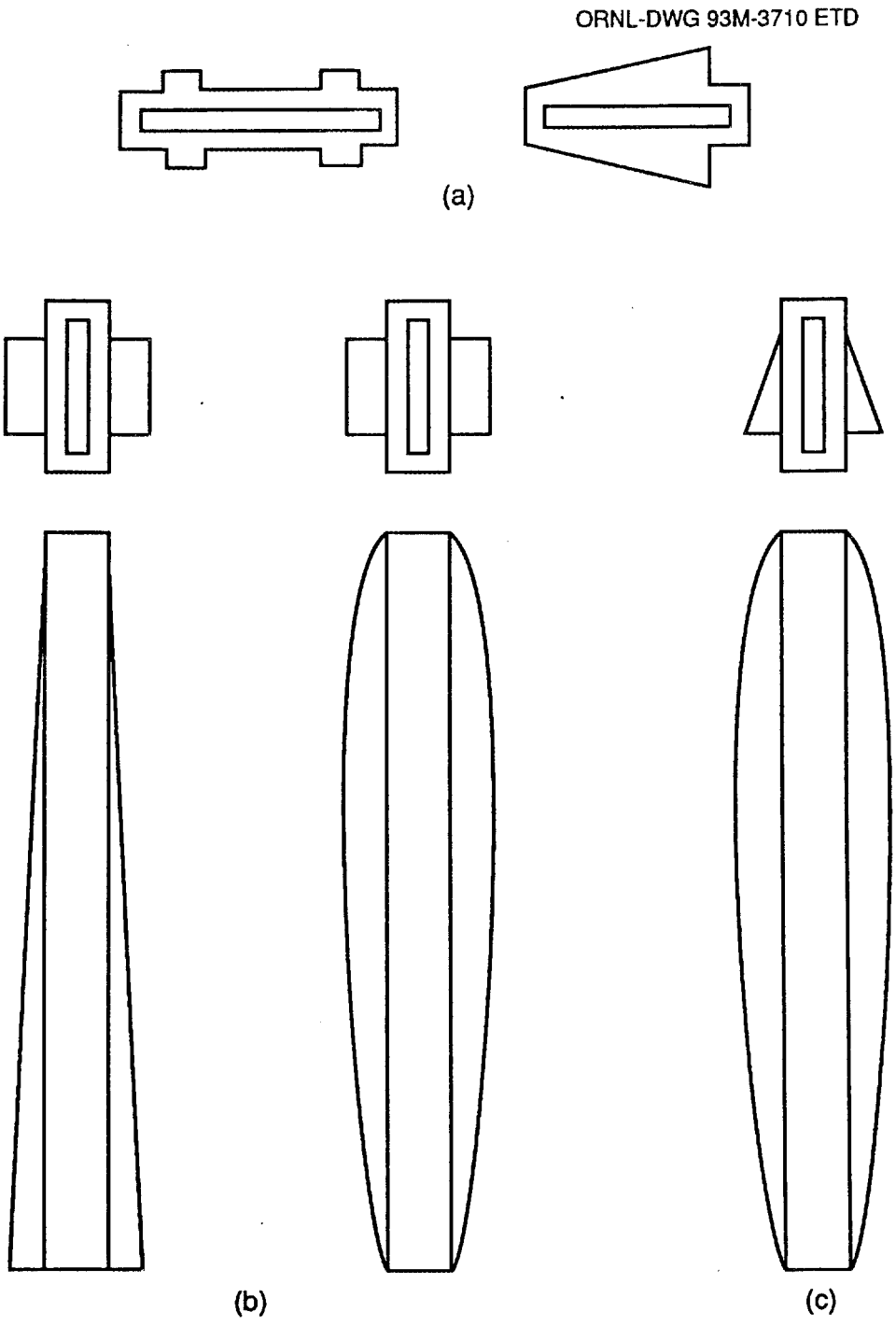

Fig. 6.2. Nonuniform heat flux test section configurations used by Costa for flow excursion: (a) uniform axial flux, with variation in spanwise flux distribution; (b) uniform spanwise flux with variation in axial flux distribution; and (c) combined variation of the spanwise and axial flux profiles that can be used in future experiments.

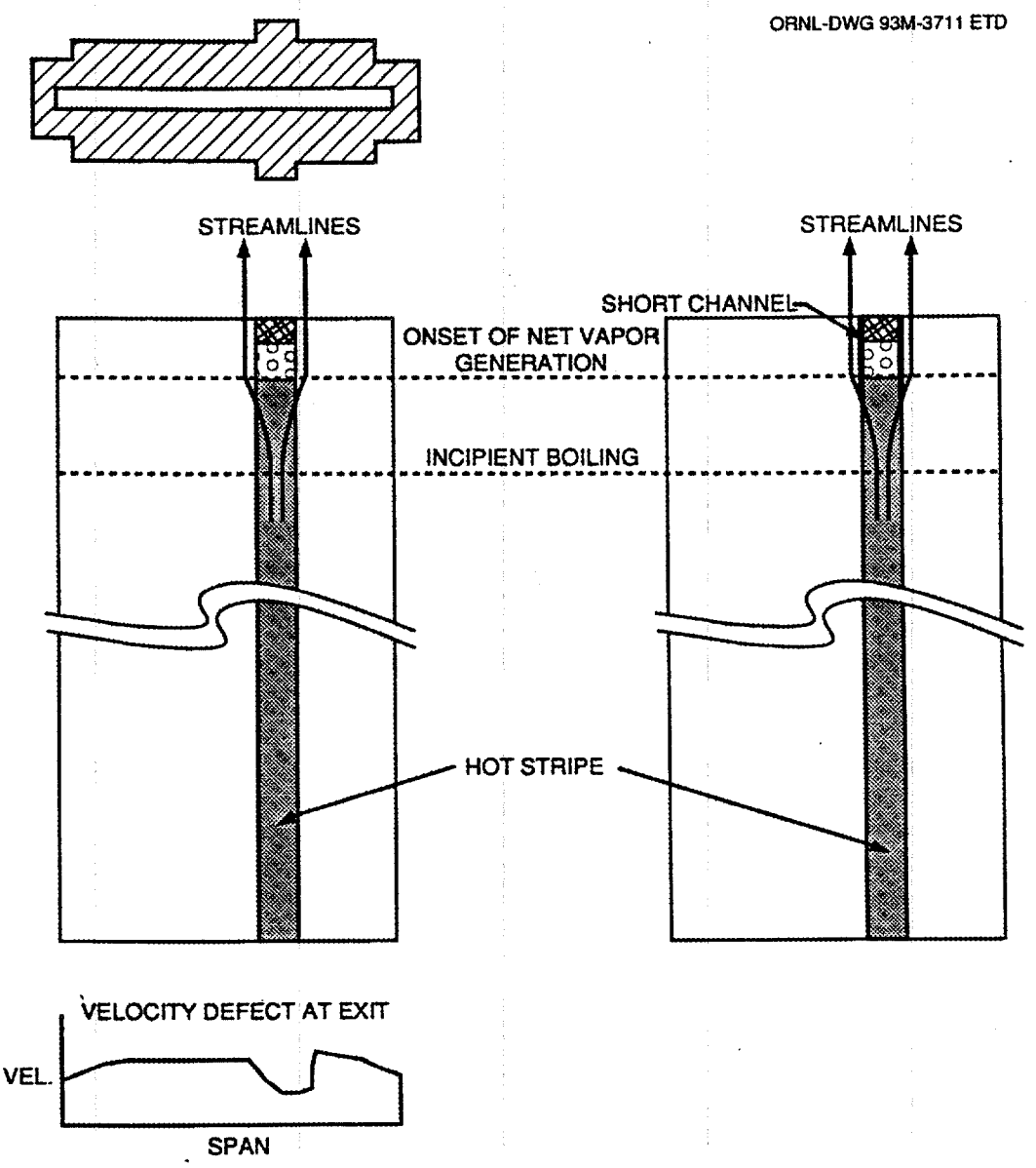

Fig. 6.3. Hot stripe effect on local mass flux in a rectangular channel.

The mass flux along the hot stripe is shown schematically in Fig. 6.4(b) where the total channel mass flux is held constant. The local increase in the flow resistance along the hot stripe results in a local decrease in the mass flux as was shown in Fig. 6.3. A constant pressure gradient is imposed along the hot stripe and the fluid stream lines in the hot stripe diverge into the adjacent cooler parts of the channel. The decrease in mass flux along the hot stripe can be expected to be a function of the width and the length of the hot stripe and the ratio of the hot stripe flux to the flux in the remainder of the channel.

Most experiments studying subcooled boiling pressure drop characteristics and the associated excursive flow instability use direct electrical heating of the test section. This technique results in channels with unheated entrance and exit lengths. The vapor generated in the heated length may condense in the unheated exit length. A major portion of the pressure drop caused by vapor generation in the channel results from the change in momentum flux. Thus, significant pressure recovery will occur in the unheated exit length of the channel as reported by Costa[29] and shown in Fig. 6.5. This pressure recovery can significantly increase the heat flux at the onset of FE in uniformly heated channel tests. Note that the reactor fuel assembly cooling channels have unheated entrance and exit lengths. However, the reactor cooling channels also have both spanwise and axial flux profiles. Thus, the local FE, as shown in Fig. 6.3, is the limiting T/H phenomenon. Condensation downstream of a hot stripe will allow the flow to recover downstream of the hot stripe. (However, the pressure recovery is not significant relative to the total channel pressure drop, and the upstream divergence of stream lines and resulting velocity defect will remain, as illustrated in Fig. 6.3.) Thus, experiments in uniformly heated channels with unheated exit lengths at bus bar attachments may not give conservative results when applied to hot stripes.

The discussion offered above deals primarily with data gathered in the early 1960s in France to support the design of the High Flux Reactor at Grenoble. These data were taken with a clear understanding that the onset of FE would lead rapidly to channel burnout in high mass flux subcooled boiling flows. Therefore, the parameters likely to influence the pressure drop characteristic of the channel were studied carefully in a variety of experimental facilities. No similar comprehensive study of the pressure drop characteristics of narrow channels typical of those used to cool research reactor fuel assemblies exists. The following general conclusions can be derived from this body of information.

1. Unheated exit lengths on channels with uniform heat flux can result in data predicting the onset of FE that is not conservative when applied to hot stripes.
2. Experiments with nonuniform spanwise and axial flux profiles indicate that onset of FE was predicted well if 0.94 times the peak flux in the channel was used in the model developed to predict the onset of FE in a uniformly heated channel. However, it was cautioned that this result is only applicable to the specific flux profiles tested.

Item 2, along with the variation in the hot stripe burnout flux with stripe width measured at SRL, may be caused by combined spanwise bulk fluid mixing, which would lower the fluid temperature along the hot stripe, and conduction in the heater material, which would drive the local flux peak down from the reported ideal value. Further, vapor generation along the hot stripe will have increasing influence on the total channel pressure drop as the hot stripe width is increased.

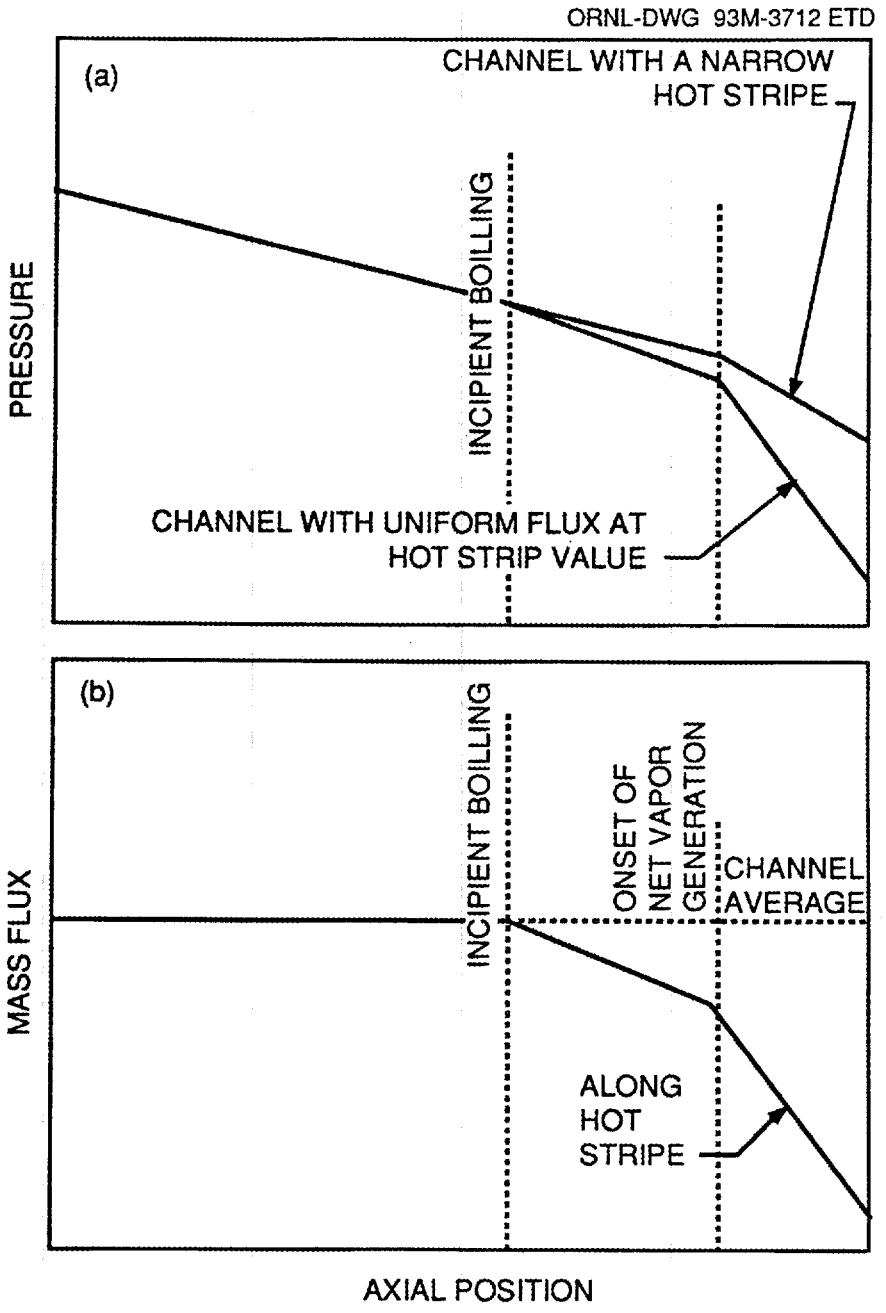

Fig. 6.4. Local hydraulic conditions associated with hot stripe and uniform heat flux tests: (a) pressure gradient and (b) mass flux in a channel with a hot stripe operating under steady-state conditions.

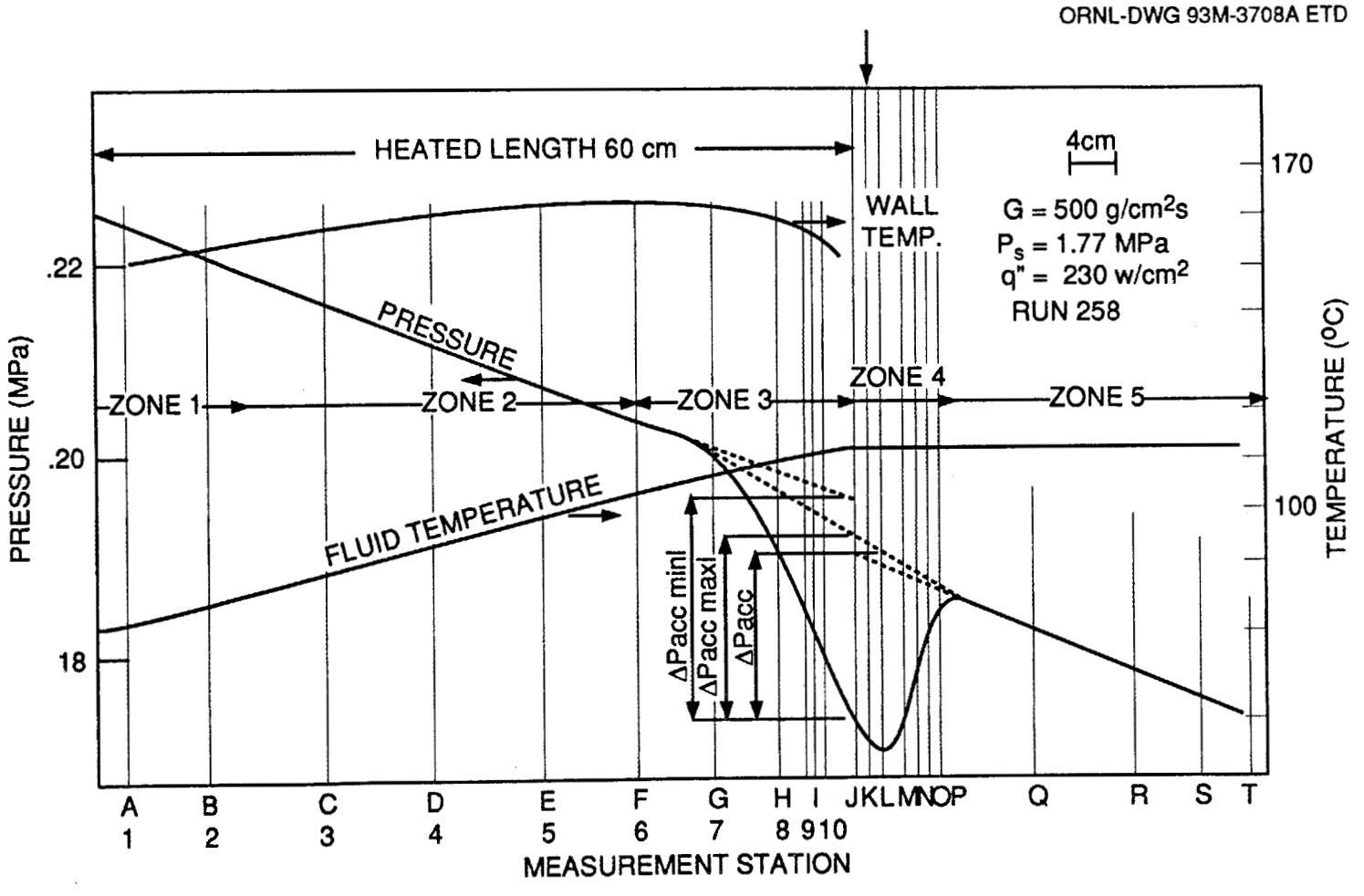

Fig. 6.5. Pressure distribution in subcooled boiling.

This discussion is intended to draw attention to variations between predicted and actual thermal limits likely to result strictly from applying models developed from data taken in uniformly heated channels to heated channels typical of the actual reactor fuel assembly. These variations exist without consideration of manufacturing tolerances, which are normally modest. However, these variations may be more important for the flow situations expected in the ANSR fuel assembly.

Another critical question for the ANSR design is the application of either FE or true CHF to local fuel plate conditions, such as hot spots and hot streaks, that may occur on the fuel plate over a small, limited area as a result of manufacturing imperfections that cause local heat flux peaking. In addition, the effect of the axial and radial power profiles on these thermal limits must be addressed. As discussed earlier, because experimental evidence indicates little mixing across the span,[29,62] FE in the hot streaks can be treated as a narrow, independent subchannel in relation to the rest of the flow in the rectangular channel. Therefore, the heat flux and subcooling in each one of these subchannels can be applied independently, just as in the parallel channel configuration.

Figure 6.6 shows a hot spot, or small region of elevated heat flux, on the surface of a fuel plate. The hot spot could be considered a very short hot stripe. However, evidence indicates that sufficiently small hot spots can withstand higher heat flux values before burnout than uniformly heated channels or hot stripes.[152] There are several reasons why this occurs. First, the hot spot is not sufficiently long to cause a significant change in the local mass flux as a result of additional flow resistance. Therefore, the scenario of a local FE leading to decreased mass flux and DNB does not apply here. Rather, the local mass flux remains at the nominal value and a primary DNB must occur. In this case, the thermal limit is dictated by a CHF phenomenon rather than FE. Several researchers have investigated this kind of flow situation experimentally using water and other fluids. However, the pressures, subcooling levels, and mass flux values in these experiments are all low compared to those in the ANSR during normal operating conditions (see Sect. 3).

The present ANSR T/H design technique applies appropriate uncertainties to each location on the fuel plate and checks the resulting heat flux against various limiting criteria, including FE and CHF. Since it is recognized that very localized boiling will not sufficiently impact the channel pressure drop to cause FE, FE is not used as a limiting criteria when the region of the fuel plate causing the limiting conditions is below a predetermined size (see Sect. 4).

6.1.2 Low Mass Flux Conditions ($G < 2000\ kg \cdot m^{-2} \cdot s^{-1}$)

Low pressure, low mass flux, and CHF will occur at low heat flux values. The likely mechanism for the thermal limit will be a local DNB as predicted using a model developed by Griffith, Schumann, and Neustal[153] for low mass flux situations. This model predicts DNB when the local heat flux exceeds the local liquid volume fraction taken times the pool boiling heat flux as given by Zuber.[154] These localized DNBs will be accompanied by flow oscillations. Therefore, periodic DNBs followed by rewetting are very likely to precede the prolonged DNB that would lead to overheating of the fuel. These phenomena were examined in experiments by Mishima and Ishii[155] (upflow), Mishima and Nishihara[156] (upflow and downflow), and Mishima, Nishihara, and Michiyoshi[159] (upflow and downflow).

The fuel assembly is clad in aluminum and some oxide will form on the cooling surfaces. The oxide has low thermal conductivity and low heat capacity. The rewetting of the surface is very sensitive to the surface conditions. Low conductivity, low heat capacity films are often added to the surface of high conductivity, high heat capacity materials to promote rewetting in quenching

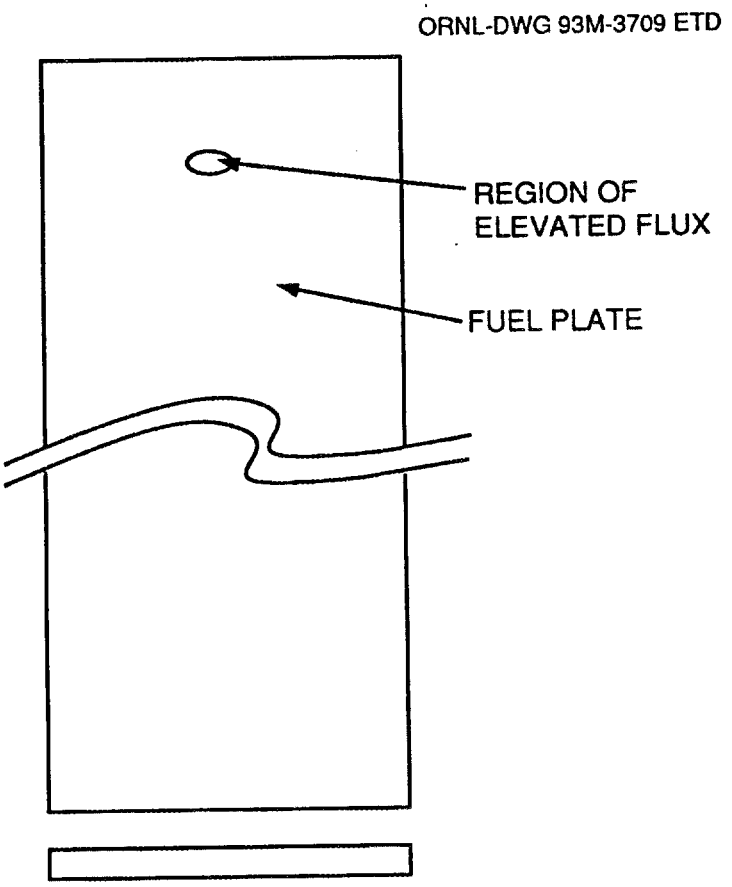

Fig. 6.6. Fuel plate hot spot.

operations.[158] Therefore, it will be important to simulate the effect of the oxide film on the rewetting process. The thermal diffusivity and the heat capacity of the heated wall must also be prototypic in order to obtain the proper wall temperature response in the experiment.

The period and amplitude of the boiling instabilities associated with the low mass flux CHF must be properly simulated in the experiment if the wall temperature response is to be prototypic of the reactor. This implies that the length of the channel should be prototypic since many boiling instabilities have characteristic periods associated with the transport time of a fluid element through the heated section. The heat flux and power-to-volume ratio in the heated section should also be identical to the reactor if the boiling instabilities are to be prototypic of those expected in the reactor.

Significant pressure variations are experienced as a result of the rapid generation of vapor volume in these low flow situations. Experiments to establish thermal limits during natural circulation in a research reactor developed by Interatom revealed that the fuel assembly would incur structural damage as a result of the hydrodynamic loads before the actual CHF.[159] The pressure drop across any single channel in the fuel assembly is imposed by the behavior of the hundreds of other channels positioned in parallel. Clause, Lahey, and Podowski[160] have addressed this situation for two-phase boiling systems and indicate that a constant pressure drop boundary condition is appropriate. In this respect, there is no difference between the low and high mass flux cases.

Mishima, Nishihara, and Michiyoshi[157] measured a dramatic variation in CHF when the pressure drop characteristics imposed on the heated channel were altered. Unfortunately, no low mass flux data are available where constant pressure drop boundary conditions were held on the heated channel. The flow conditions preceding CHF in low mass flux, low pressure systems are very rich in phenomenology involving strong nonlinearities. Therefore, these flows are difficult to model computationally. Prototypic data is needed to establish thermal limits in these situations. The resulting CHF model should be keyed to the imposed channel pressure drop. Local conditions models will be unreliable because of the uncertainty associated with modeling the spatially and temporally varying local conditions in the channel. Time average pressure drop and mass flux information can be coupled with the CHF model to allow a lumped parameter simulation of the fuel assembly performance in these situations.

The heat flux levels are low (i.e., decay heat levels) in these situations. Hot spots are less important because of conduction in the aluminum cladding. Spanwise and axial flux profiles are less important since two-phase turbulence associated with the positive quality flow will promote spanwise mixing.

6.2 OVERVIEW OF EXPERIMENTAL PLAN

Experiments are planned to allow development and validation of models used in the T/H analysis. This plan incorporates experimentation to examine phenomena that are critical to characterizing the T/H behavior of ANS and to evaluate more integral type phenomena, which must ultimately be determined using codes and models. Both fuel element performance and the thermal performance of components external to the core region are targeted by this program. The plan attempts to isolate the important phenomena and to provide specific experimentation in order to correctly define the phenomena as well as, under some circumstances, collect data to support statistical analysis of the reactor performance. These experiments will result in a more complete understanding of the physical phenomena that influence the thermal limits in the fuel assembly and other components. Quantification of the uncertainties associated with code calculations may also be evaluated from the data.

A general description of the test facilities follows, including a list of the associated experiments planned to be performed in each facility. Appendix B provides an overview and summary of all the

experiments and the facilities that are currently being considered and planned, some of which are already operating. In the following sections, each facility and experimental group is discussed individually. Since the status of each experiment is different at this point in the project, some are discussed in greater detail than others. The following text will define and describe the objectives of the experiments themselves and will discuss the facilities in which these experiments are to be implemented.

6.2.1 Corrosion Test Loop

Status: Operating.

Objective: The corrosion test loop (CTL) was designed to provide relevant data on oxide film growth rates and oxide spallation on the aluminum fuel clad at ANS conditions.

Facility Description: Key parameters that affect oxide growth rates have been identified and are being used to develop predictive capability for design models. These models include both temporal and spatial variation of oxide film layers and subsequent effects on fuel temperature and integrity.

The test facility is a forced-flow water loop fabricated entirely of 304-L stainless steel components, capable of pressurized operation to 7 MPa and coolant water flows to 2 L/s. The specimen consists of an aluminum alloy tube forming a rectangular flow channel that is equivalent in gap width to that of the ANS coolant channels. A drawing of the main section of the specimen is presented in Fig. 6.7. The specimen is surrounded by insulation and pressure backing (not shown in the figure), welded to large electrodes, and attached to the main section of the loop so that coolant velocities in the specimen channel up to 35 m/s ($Re > 1 \times 10^5$) can be achieved. A simplified schematic drawing of the test loop system is shown in Fig. 6.8. The heat flux (up to 20 MW/m^2) is produced by self-resistance heating of the specimen, where the irregular cross section concentrates the heat flux to the desired central region. Approximately 80% of the heat is generated in the thick central region of the specimen. The power is furnished by a 30-kA dc power supply, and the heat is removed by a water-cooled heat exchanger downstream of the specimen. System pressure is maintained in the high-pressure circulation loop (up to 4 MPa at the specimen inlet) by allowing a small, continuous water flow through a modulated letdown valve to a low-pressure secondary loop, where instrumentation and equipment for maintaining suitable water chemistry are located. Makeup water flow is provided by a high-head, positive displacement pressurization pump. The coolant circulation system in the loop is similar to that employed in many research reactors.

Test Channel Design: The outer surface of the main section of the specimen (see Fig. 6.7) is instrumented along its central axis with ungrounded, stainless steel sheathed (0.5 mm), type-N thermocouples. Seven thermocouples are arranged axially 25.4 mm apart on one side; three are located on the other side to provide additional measurements and comparisons. Because the coolant temperature increases as the specimen is traversed axially, the severity of the oxidation reaction also increases from the entrance to the exit of the specimen.

For a given level of electrical power supplied to the specimen and a given coolant flow rate, a temperature profile along the specimen is established. If the loop's T/H parameters are then held constant, changes in the measured temperatures along the outer part of the specimen can be related quantitatively to the buildup of oxidation products at the specimen-coolant interface. At the high heat fluxes involved in this work, temperature increases from this source in excess of 100°C are not uncommon.

Fabrication of a test section specimen requires precision electron-beam welding of two carefully prepared specimen halves to form the shape shown in Fig. 6.7, followed by conventional gas-tungsten-arc welding of the completed specimen to the massive electrodes. Documented procedures for accomplishing the welding, instrumentation, and other assembly steps have been developed and improved throughout the program.

The loop operates under computer control of the electrical and coolant flow parameters, including various safety features. The associated data acquisition system records all temperatures, pressures, flow rates, power levels, and water properties at designated time intervals. Although, in principle, the test loop and its support equipment are uncomplicated, integrated operation at the required performance level has entailed continuous attention to the various components. In particular, a significant amount of time and effort has been expended on the measurement and control of the pH and conductivity of the coolant water in the loop.

The ANS corrosion test loop facility provides the means to expose an aluminum surface to rapidly flowing coolant under heat transfer conditions. During a test, the electrical power generated in the specimen and the coolant conditions are generally held constant so that changes in temperatures of the specimen at its outer, insulated side are mostly from increases in the thermal resistance in the heat path resulting from the growth of the corrosion product at the metal-coolant interface. While these changes, per se, are important observations in that they imply similar increases in the fuel temperature in the ANS core, they are also useful in obtaining the oxide thickness and growth kinetics through established heat transfer and T/H calculations. Certain results and implications of these calculations can be checked by observations and measurements on the reacted specimen surface at the completion of the experiment, but the important results are basically all calculated quantities.

6.2.2 Thermal-Hydraulic Test Loop

Status: Operating.

Objective: The Thermal-Hydraulic Test Loop (THTL) was constructed to acquire both critical heat flux and flow instability data over a range of ANSR operating conditions. The facility is also designed to examine other T/H phenomena as well as some off-normal and transient conditions.

Facility Description: The THTL was designed and built to provide known T/H conditions to a simulated full-length coolant subchannel of the ANSR core, allowing experimental determination of the thermal limits (both FE and CHF) under anticipated ANS T/H conditions. A more detailed discussion of FE and CHF is given in Sect. 6.1. An isometric view of the facility is shown in Fig. 6.9 and a schematic diagram of the loop and its major components and instrumentation is presented in Fig. 6.10. A detailed description of the test facility is given by Felde et al.[27]

The THTL was designed to accommodate both CHF and FE experiments, responding to three separate modes of operation as enumerated below.

1. A "soft" system was used to perform actual FE tests with burnout. In this mode, a large bypass around the test section was fully open so that the flow could split between the test section and the bypass to maintain an almost constant common pressure drop across both, thus closely simulating the ANSR configuration.

ORNL-DWG 90-15575

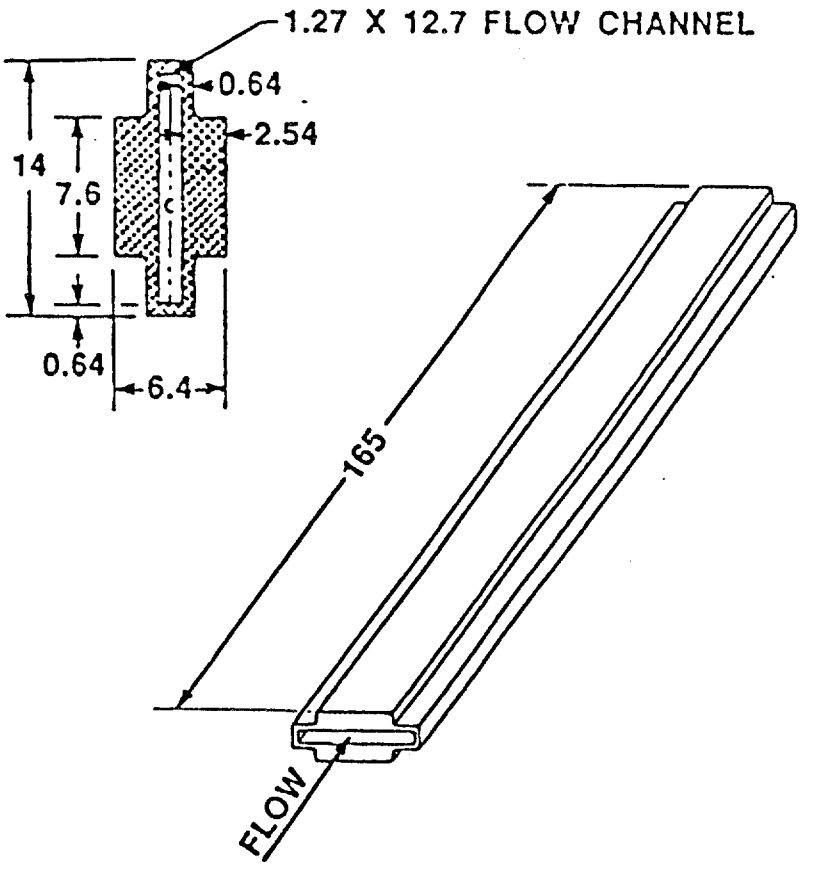

Fig. 6.7. Central section of corrosion test specimen. (Note: All dimensions are in millimeters.)

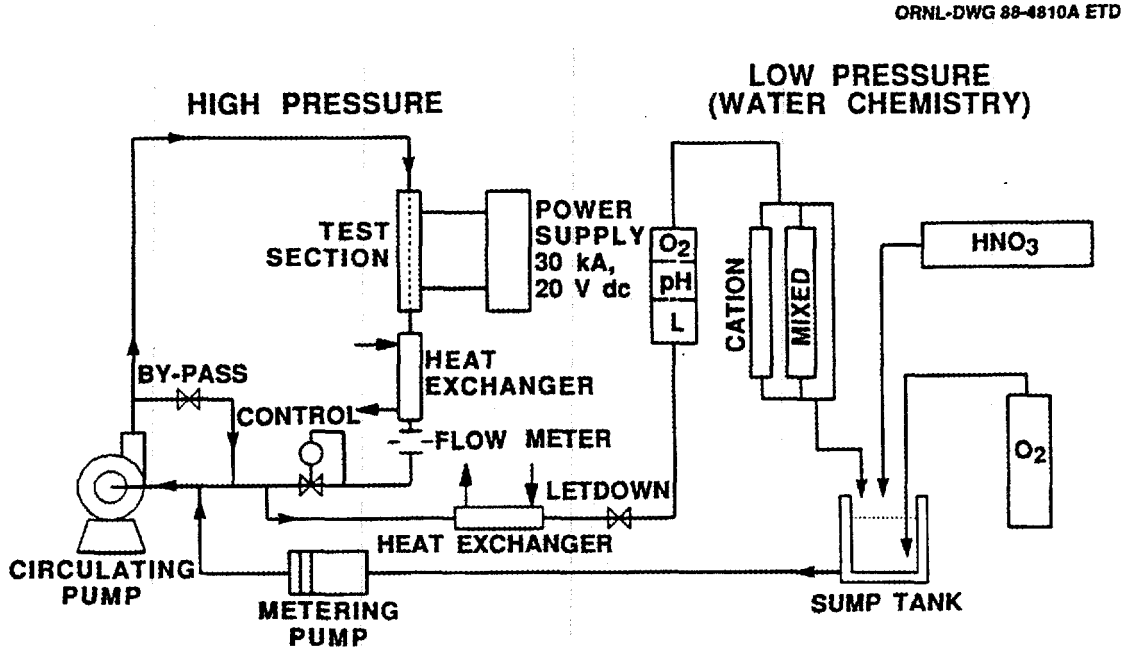

FEATURES:

- 304-L STAINLESS STEEL THROUGHOUT
- 7-MPa (1000-psi) OPERATION
- 35-m/s COOLANT FLOW
- 20-MW/m^2 HEAT FLUX FOR CORROSION TESTS [ESTIMATED 32 MW/m^2 FOR THERMAL-HYDRAULIC (T/H) TESTS]
- 65-kW SPECIMEN POWER (325 kW FOR T/H)
- CONTROL OF WATER CHEMISTRY
- CONTROL OF COOLANT TEMPERATURES
- COMPUTERIZED CONTROL, SAFETY, AND RECORDING

Fig. 6.8. Corrosion test loop flow schematic.

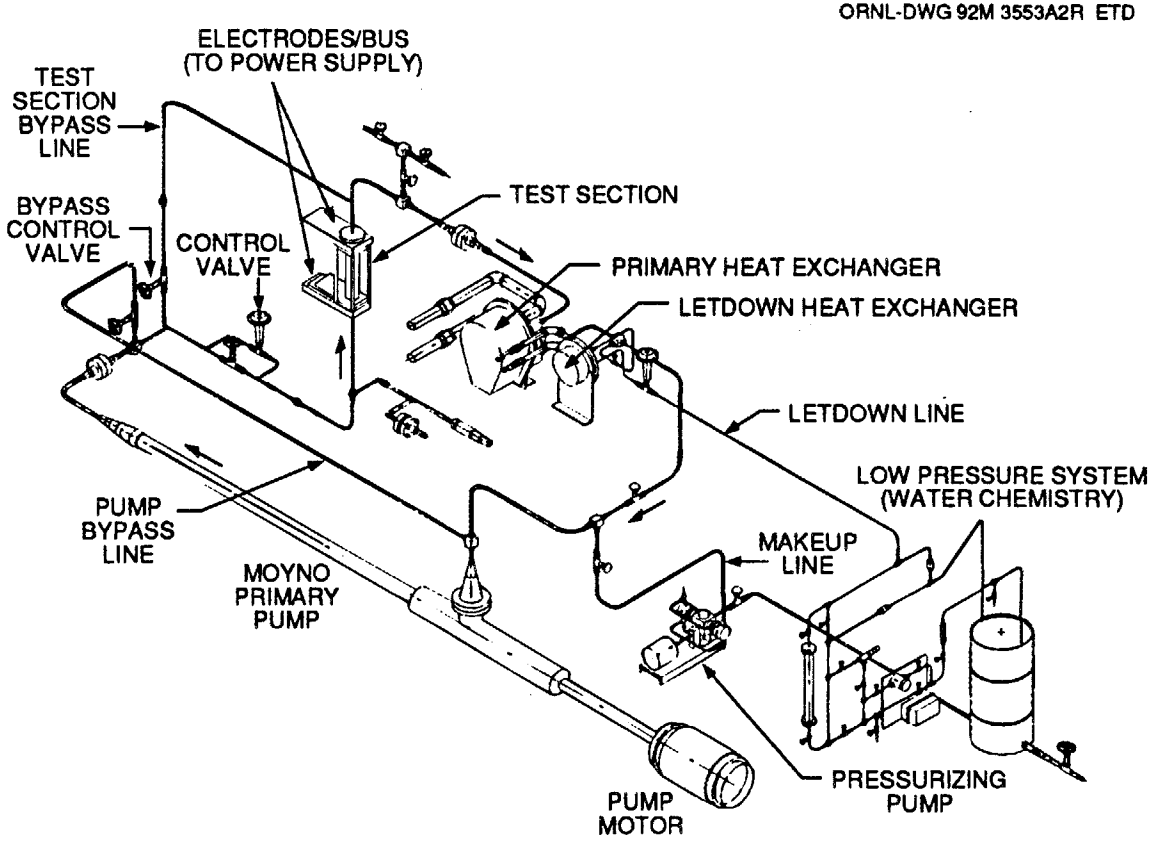

Fig. 6.9. An isometric view of the ANS thermal-hydraulic test loop.

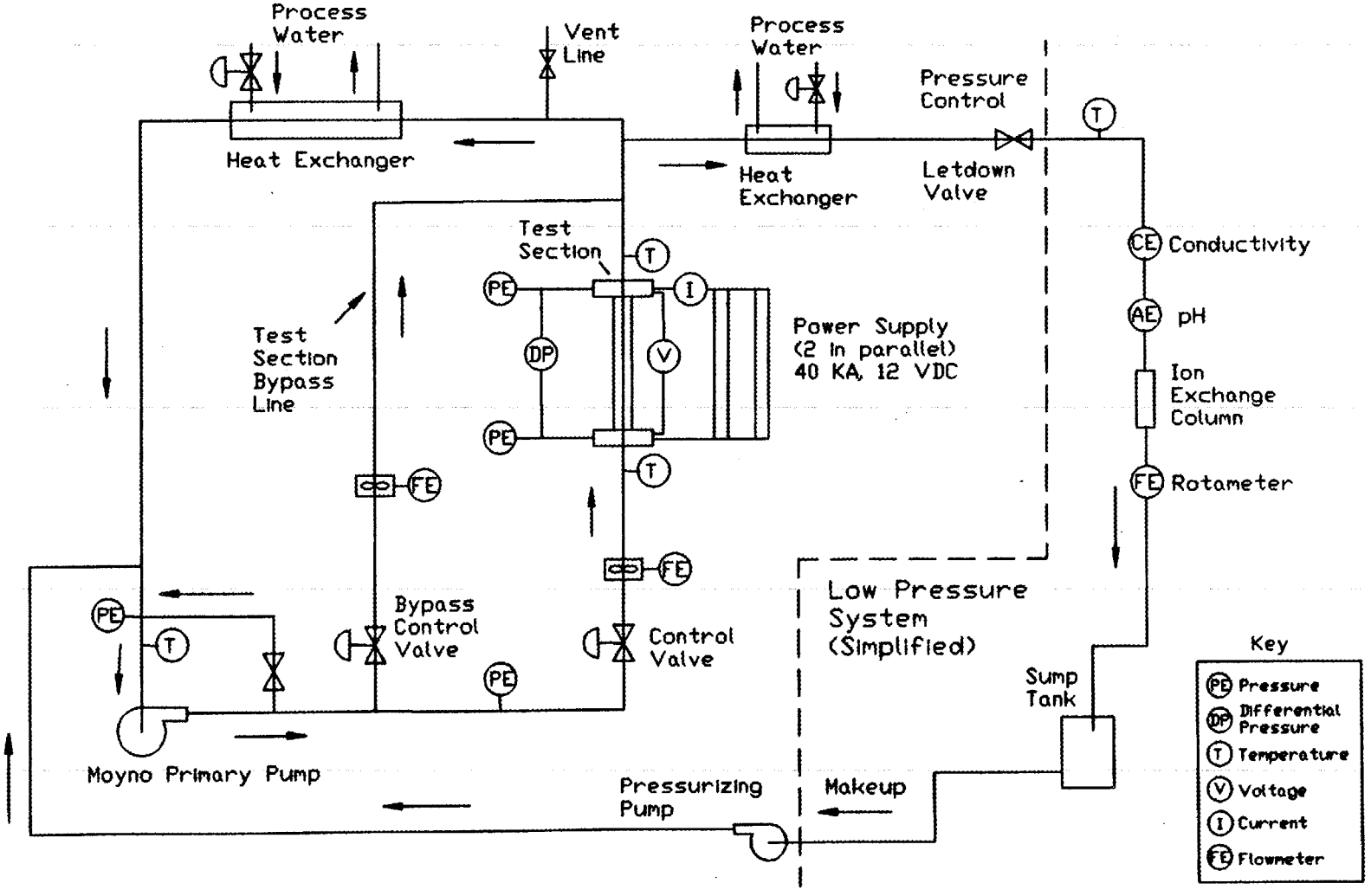

Fig. 6.10. Schematic diagram of the thermal-hydraulic test loop, including major components and instrumentation.

2. A "stiff" system was used to perform true CHF tests with actual burnout at constant and known flow rates. In this mode, the bypass around the test section was completely closed to maintain a constant flow through the test section. In addition, a near positive-displacement pump that provides a nearly constant flow rate was used in the primary loop. This pump is insensitive to the system pressure-drop characteristics. Small diameter piping (to reduce volume) and a throttling valve were also used upstream of the test section inlet to enhance flow stability.

3. A modified "stiff" system was used to perform simulated FE tests without experiencing actual FE. In this mode, a closed or minimal bypass configuration along with a significant pressure drop across the flow control valve upstream of the test section was used to prevent actual FE or other flow instability. In this case, the potential for FE was determined by detecting the minimum pressure drop in a plot of pressure drop vs flow rate (which coincides with the ONVG point) as demonstrated by Maulbetsch and Griffith,[146] Whittle and Forgan,[44] Costa,[29] Johnston,[161] Dougherty,[162] and others. Most of the FE tests were performed using this approach.

Since the ANSR has many channels in parallel, an ideal bypass simulation in the THTL would require a very large bypass flow ratio ("infinite bypass") and, therefore, an unrealistically large pump. In practice, however, a reasonable, but not ideal, flow ratio can provide a very close simulation with no significant error. The lowest bypass flow ratio necessary (which still provides sufficiently constant pressure-drop boundary conditions) was investigated in two independent studies—one transient and one steady-state. Both studies are based on models simulating the THTL as a pressure-drop vs flow network to determine the sensitivity of the bypass pressure drop to changes in test section flow for a variety of bypass-to-test-section flow ratios. The first model showed that bypass ratios ≥ 4 begin to approach the response of an infinite bypass, with absolute flow rates within 3% of the infinite bypass steady-state flow rates.[27] The second model showed in a preliminary way that the slope of the bypass pressure drop with the test section flow rate [supply side $d(\Delta P_{ext})/dV$ in Eq. (6.1)] exceeds the slope of the test section pressure drop vs flow rate curve [demand side $d(\Delta P_{tt})/dV$ in Eq. (6.1)] for a bypass ratio of ≥ 3, satisfying the condition for instability Eq. (6.1). This supply-side slope becomes extremely small (practically horizontal) for bypass ratios above ~ 6, closely simulating the ANSR parallel channel configuration. (See Fig. 6.1 for the supply and demand pressure-drop relationships.)

In order to accommodate the three desired modes of operation, a Moyno primary circulation pump is driven by a variable speed motor through a gear drive. This pump and motor combination is capable of providing a wide range of flow and pressure conditions with near-positive displacement characteristics, which means flow supply is insensitive to the loop pressure drop. Using the variable speed of the motor drive provides capability for operating over most of the flow-pressure diagram up to 2.5 L/s flow and 4.1 MPa differential pressure across the pump at 750 rpm. When this pump is used in combination with the test section bypass line, a very wide range of mass flow conditions at the test section is possible. In the stiff mode with a closed bypass, a near-constant test section mass flux in the range of 7,000–42,000 kg/m^{2}s can be used. (The maximum mass flux is limited by the overall pressure rating for the test loop.) In the soft mode, with a bypass flow ratio of 10 to 1, a maximum mass flux of 12,000 kg/m^{2}s at a near-constant bypass pressure drop can be used. At a 5 to 1 bypass flow ratio, this maximum increases to 23,000 kg/m^{2}s. The approximation of the ideal bypass ratio (infinite) with a practical bypass ratio is in the nonconservative direction for FE, but, as discussed earlier, it is believed that the approximation is sufficient from a practical point of view. Additional parametric studies will be performed to quantify the bypass ratio, and, if necessary, an additional pump will be installed parallel to the existing one to achieve even higher test section flows and bypass ratios.

Test Channel Design: The test section and its boundary conditions were of primary interest in determining the T/H limits. The cross-section design was similar to that used by Gambill and

Bundy[163] but is modified in accordance with the ANS characteristics as shown in Fig. 6.11. The test section simulated a single subchannel in the ANSR core with a cross section that had a full prototypic length (507 mm), the same flow-channel gap (1.27 mm), and the same material (aluminum), with a surface roughness (~ 0.5 μm) reasonably close to that expected in the ANSR fuel plates. The channel span was scaled down to 12.7 mm (vs 87 and 70 mm for the upper and lower core halves in the ANSR) in order to limit total power requirements to the test section. The involute shape of the plates was not simulated in order to simplify the experimental design and operation. Other researchers have demonstrated that there is little lateral fluid mixing in such rectangular channels even under two-phase flow conditions.[29,62] Furthermore, sources also maintain that span width (or span-to-gap ratio) does not have a significant effect on either CHF or FE.[44,161-163] The test section wall thickness was 2.54 mm, dictated by the voltage/current relationship of the power supplies. The reduced wall thickness at the curved ends was designed to reduce the heat flux and prevent the coolant bulk temperature from peaking on the curved ends of the channel, which could have led to premature burnout. The ratio of heat flux on the curved ends to that on the flat ends was 36% for the design shown in Fig. 6.11. Possible effects of lateral and axial heat redistribution by thermal conduction within the test section metal will be considered later through the use of a 3-D conduction model.

The test channel instrumentation was placed on the back of the channel wall with type N thermocouples. The locations of these thermocouples on the test section are shown in Fig. 6.12. The spacing was staggered, as shown, to provide improved definition in the region close to the channel's exit, where FE or CHF was expected. Measurements are made on both sides of the channel for the axial locations shown for redundancy. Pressure and temperature of the water were measured at the test section inlet and outlet with the pressure taps installed in the test section flanges as shown in Fig. 6.11. The taps were located axially 12.7 mm from the "heated" channel at each end, which allowed a closer determination of the pressure drop across the heated region without the effects of possible condensation and dynamic pressure recovery that can occur between the end of the heated channel and the point of pressure measurement.[29]

The test channel is enclosed inside a stainless steel pressure backing and is thermally and electrically isolated from the backing by Mycalex insulation. The test channel was either welded or brazed on both ends into aluminum flanges, each 25.4-mm thick. The test section flanges are sandwiched between two 25.4-mm thick aluminum electrical bus plates. The water connection to the test section was made concentrically inside this bus connection by a 50.8-mm flange and teflon gasket that were fastened through the test section flange. The teflon gasket and micarta bolt sleeves provide electrical isolation for the piping loop. The stainless steel backing, which was in direct contact with the test section flanges at both ends, was split in the center and isolated at this point by Mycalex insulation. This design effectively separated the electrical contact requirements from the water sealing requirements of the loop interface.

6.2.2.1 Destructive and Nondestructive Flow Excursion and Critical Heat Flux Tests

Status: Ongoing.

Objective: Use THTL to determine FE and CHF limits within the ANSR fuel assembly.

Testing and Data Reduction: Before installation of the test channel assembly into the loop, the channel surface undergoes a surface treatment procedure similar to that used for fuel elements in the HFIR at ORNL and expected to be used for the ANSR fuel elements. This procedure involves cleaning and degreasing, followed by an acid treatment and hot water rinse. In addition, the as-fabricated flow-channel gap is measured at locations along the axial length using a capacitance-type

- **1.27 x 12.7 mm coolant channel**
- **Full length = 507 mm**
- **Directly heated using dc current**

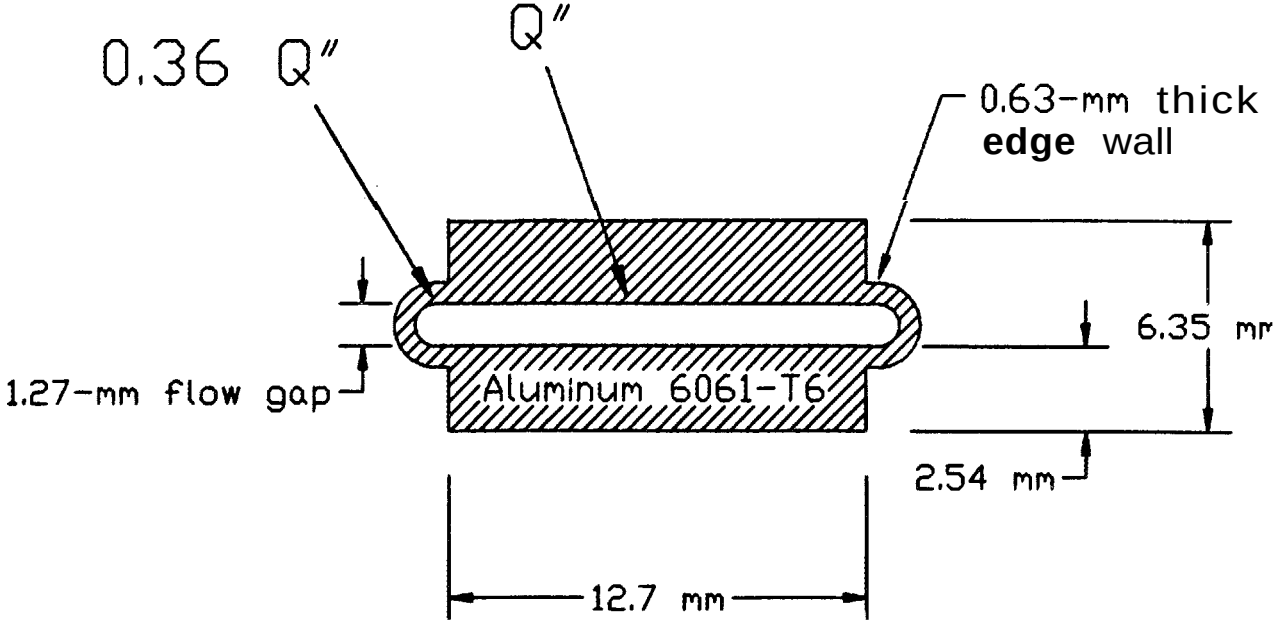

Fig. 6.11. Cross section of the test channel in the thermal-hydraulic test loop.

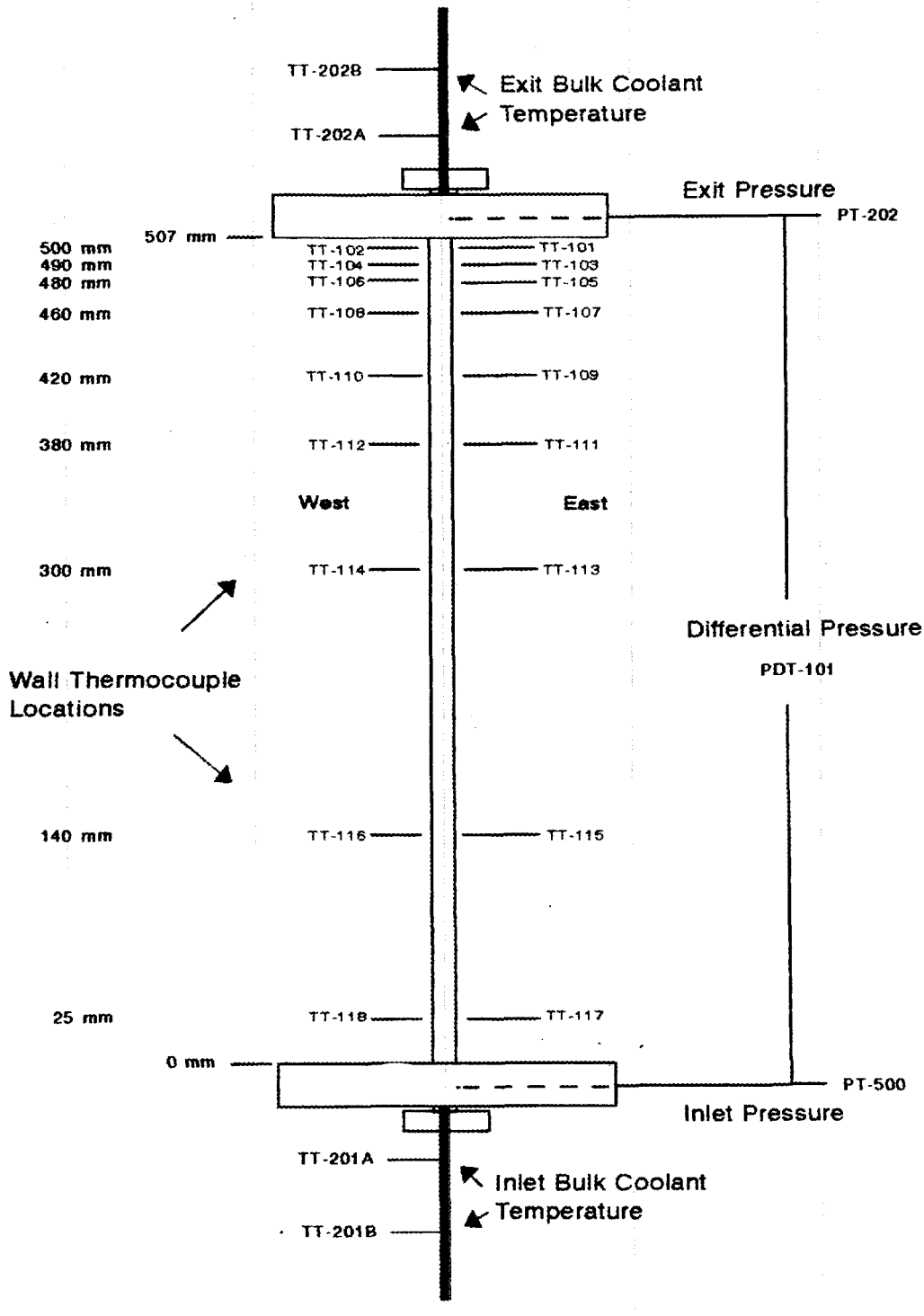

Fig. 6.12. Thermal-hydraulic test section instrumentation.

probe inserted into the channel. These data are used to improve conversion of volumetric flow measurements (made upstream from the test section) to local velocities in the channel.

FE tests (without burnout) are conducted in a stiff mode as described earlier. These tests are initiated by controlling test section flow to a level where no boiling exists at the target heat flux level. The applied power to the test section is then raised to produce the target heat flux level. Exit pressure is automatically controlled at the desired setting (nominally 1.7 MPa) via the system letdown valve and high pressure makeup pump. Process water flow to the secondary side of the heat exchanger is also automatically controlled to maintain the inlet bulk coolant temperature at the desired set point (nominally 45°C).

Data are recorded continuously during these processes by the personal-computer-(PC-) based data acquisition system. Once the system is stabilized and data are obtained under steady-state conditions, the velocity is reduced to a lower level while monitoring the measured differential pressure across the test channel. This reduction is made through either pump speed reduction, flow control valve positioning, bypass flow adjustment, or some combination of the above, depending on the proximity of the conditions to the expected minimum. As the minimum is approached, the loop configuration is adjusted to minimize the amount of bypass flow and to maximize the pressure drop across the control valve in order to prevent an actual FE and channel failure. The system is allowed to stabilize at each of the selected velocity settings. Power supply and velocity adjustments are made concurrently in order to maintain the average heat flux constant. (This concurrent adjustment is necessary because the temperature coefficient of resistivity of the aluminum affects the current-voltage characteristics of the test channel as velocity is reduced and test channel wall temperatures increase.) Once the minimum in pressure drop has been determined (by observation of increasing pressure drop as velocity is further decreased), the velocity is increased once again, and data are taken at some of the velocity points obtained during the earlier sequence for comparison.

An experimental data reduction model was developed for single-phase forced-convection flow, focusing on the flat portion of the test channel. Fundamental variables required to identify heat transfer characteristics in single-phase forced-convection heat transfer were local heat flux (Q''_{loc}), local inside surface temperature ($T_{w,in}$) of test section, local bulk coolant temperature (T_b), and coolant velocity (V) in the flat channel. Local heat flux on the flats (Q''_{loc}) was calculated based on temperature-dependent resistivity of the aluminum test section and the average heat flux on the flats (Q''_{av}). The latter was determined based on the total heat input (Q_{tot}) into the test channel flats, as follows:

$$Q''_{av} = Q_{tot} \cdot \left(1-\frac{Q_{loss}}{Q_{tot}}\right) \cdot th_{Al} / (L \cdot A_{Al}) \quad , \tag{6.2}$$

where

Q_{loss} = heat loss (kW),
th_{Al} = aluminum thickness (m),
L = heated length (m),
A_{Al} = aluminum cross-sectional area (m^2).

Total heat input (Q_{tot}) is given by the product of the current (I) and the voltage (E) applied to the test section. Heat loss (Q_{loss}) is calculated by comparing the heat input (Q_{tot}) with the heat rate (Q_{cool}) transferred to the coolant, as follows:

$$\frac{Q_{loss}}{Q_{tot}} = 1 - \frac{Q_{cool}}{Q_{tot}} = 1 - \frac{\rho V A_{cs} C_p \Delta T_b}{EI} \quad , \tag{6.3}$$

where

ρ = coolant density (kg/m^3),
V = coolant velocity (m/s),
E = voltage (V),
I = current (A),
A_{cs} = cross sectional flow area (m^2),
C_p = mean coolant specific heat (kJ/kg · K),
T_b = bulk coolant temperature (K).

The heat loss range of the tests was calculated to be between 5–12% of Q_{tot} with the higher values being for the lower velocities. Coolant flow velocity (V) in the flat channel was converted from average coolant velocity (V_{av}) so that the pressure drop of the flat channel is equal to that of the curved end channels.

As already described, the temperature of the test section required to identify the heat-transfer characteristics is the surface temperature ($T_{w,in}$) on the flow channel side, but the thermocouples are attached on the surface on the ceramic insulator side ($T_{w,ex}$). Therefore, $T_{w,in}$ is determined based on the local heat flux (Q''_{loc}) in the flats, as follows:

$$T_{w,in} = T_{w,ex} - \frac{Q''_{loc} th_{Al}}{2k_{Al}} - \frac{Q''_{loc} th_{ox}}{k_{ox}} \quad , \tag{6.4}$$

where

$T_{w,in}$ = aluminum conductivity (W/m/°C),
$T_{w,ex}$ = temperature on ceramic insulator (K),
th_{Al} = aluminum thickness (m),
th_{ox} = oxide thickness (m),
k_{Al} = aluminum thermal conductivity (W/m/°C)
k_{ox} = oxide thermal conductivity (W/m/°C).

The experimental data reduction model also includes a single-phase pressure-drop calculation model. As described earlier, the test section inlet and outlet pressures were measured at the taps installed in the test section flanges, which are located axially 12.7 mm from the heated channel at each end. The pressure drop of the heated channel (ΔP_H) was converted from a measured pressure drop by excluding the pressure drops across the nonheated sections. The pressure drop across the nonheated section between the end of the test channel and the pressure tap is calculated with the Darcy friction factor using the Filonenko correlation.[16]

The THTL experimentation for the ANSR T/H correlations is still in its initial stages. The current THTL and test section design are the result of a number of initial shakedown and benchmark tests, which led to successive modifications both in the loop and the test section design. A discussion of early test results from these experiments and future plans are presented by Siman-Tov et al.[164]

6.2.2.2 Two-Sided Heated Core Parametric Tests

Status: Planned.

Objective: This series of tests will use the existing THTL facility and will extend the tests on two-sided heated channels to include measurement of the effects of axial flux profiles, parametric studies on span effects, measurement of axial pressure distribution in the channel, and measurement of thermal limits under off-normal conditions.

Background: This effort may require modification to the facility, including additional pumping capability and power supplies to match characteristics of possible alternate test channel materials and test section span.

The specific tests to be performed in this facility include:

- destructive and nondestructive FE tests and CHF tests for ANSR prototypic local conditions;
- effects of material, surface oxide, and surface characteristics on FE, CHF, friction factor (FF), and heat transfer coefficient (HTC);
- effects of heavy water, water chemistry, and dissolved gas on FE, CHF, FF, and HTC;
- isothermal single-phase FF and pressure-drop tests;
- heated single-phase FF and pressure-drop tests (effects of temperature and viscosity);
- IB tests;
- span scaling validation tests—medium-span two-phase pressure drop and void fraction tests, medium-span two-phase nucleate boiling HTC tests, medium-span FE tests with axial heat flux distribution, and medium-span FE tests with lateral heat flux distribution; and
- THTL transient conditions tests.

6.2.2.3 Low Mass Flux Departure from Nucleate Boiling Tests

Status: Planned.

Objective: Use the THTL to evaluate low mass flux thermal limit behavior in the core.

Background: These tests are planned to examine low mass flux conditions where unsteady, positive quality or near-positive quality flows may be encountered. Data are not available for conditions prototypic of either ANSR or low mass flux CHF under these conditions. A full span and full length heated channel is planned for use in a modified THTL. In order to control the inlet and exit pressure to the channel to obtain the constant pressure drop boundary condition that would be imposed by the reactor, it will most likely be necessary to add large gas pressurizers to the THTL facility. In addition to measuring thermal limits, these tests will relate the time average mass flux through the fuel assembly with the applied power and applied pressure drop. This information will make modeling of boiling natural circulation in the reactor possible. It has been shown that RELAP5 is capable of following the phenomena associated with low pressure, low mass flux, and positive quality flows if care is taken to select a reasonably fine nodalization of the heated channel and if correspondingly

small time steps are used.[165] Unfortunately, this method is a very cumbersome way to analyze these situations, and a very large uncertainty is associated with the predicted results. This experiment will provide a relationship between the time averaged mass flux, the heat flux, and the pressure drop that will allow the details of the flow in the fuel cooling channels to be bypassed during situations where unsteady positive quality flows are expected. See Sect. 6.1.2 for a more detailed discussion.

6.2.2.4 Small Scale RELAP Simulation Tests

Status: Planned.

Objective: To provide small scale transient testing using an existing facility in order to benchmark transient codes.

Background: Some small scale transient tests are also proposed to allow many portions of the RELAP5 code to be exercised simultaneously. These tests can be accomplished by modifying the original loop used to establish thermal limits in the fuel assembly. A control system will be added to allow rapid variations in the applied power to simulate reactor shutdown. A pump will be used or programmed to provide head characteristics similar to those expected in the reactor main cooling pumps. A break simulator (i.e., rupture disks at two or three locations in the loop) and some additional instrumentation will also be needed. A uniformly heated channel with a coolant bypass will simulate the reactor fuel assembly. The basic T/H phenomena associated with a system piping break and reactor shutdown will be present in this facility. A RELAP5 model of this facility will be developed and used to simulate the response of the system to the imposed transients. The RELAP5 simulation results and the measured transient response of the system can then be directly compared.

6.2.3 Prototypic Span Experiments

Status: Planned.

Objective: This facility will further expand the capability for thermal limit testing in full span channels. Present plans call for a facility that can accommodate a full span, full length test channel with testing of CHF and FE thermal limits. It has not yet been determined whether the test sections will be fabricated from aluminum or alternate materials in light of the recent results that show significant spallation of the oxide layer under IB conditions for aluminum. If it is necessary to use aluminum test channels, the low voltage, high current requirements will significantly affect facility cost. In addition to the two-sided heated channel tests, a single-side full span heated test section is planned to examine hot stripe and hot spot conditions.

Background: These tests could be performed in the facility just described or in a modified THTL if full power aluminum channel testing is determined not to be required. The test channel would incorporate a transparent window on the nonheated side to provide observation and measurement of the phenomenon associated with hot stripes and hot spots. The flow field can be observed and measured from the unheated side of the channel. The facility would probably require a different power supply to match voltage-current requirements of a nonaluminum material.

The proper use of subchannel analysis must be well defined and well defended since it is fundamental to both the steady-state and accident thermal limit calculational procedures. The discussion of thermal limits during high mass flux situations shows the need to study the dependence of the thermal limit on flux profile and hot stripe parameters (see Sect. 6.1). A single channel heated

on one side is used in some of these experiments, as shown in Fig. 6.13. Other possible test section configurations were presented in Figs. 6.2, 6.3, and 6.5. Three sets of experiments are planned, one with various flux profiles, one with various types of hot stripes, and a single uniformly heated case for reference.

Both spanwise and axial flux profiles will be considered. The magnitude of the peak-to-average flux will be representative of those expected in the ANSR fuel. Local pressure drop values and spanwise exit bulk temperature profiles will be measured. The tests will be run under constant inlet mass flux conditions (i.e., positive displacement pump, no bypass). Inconel will most likely be used for the heater section to prevent heater damage when local FE conditions are encountered.

Different hot stripes will be tested to determine the influence of stripe width and of the ratio of stripe flux over the channel average flux. It is expected that these heaters will also be made of Inconel. Ratios of stripe flux over average channel flux equal to 1.3 and 1.6 will be investigated for each stripe width. Spanwise exit bulk temperature profiles and local pressure gradients will be measured during these tests.

The wall temperature will be monitored throughout these tests by thermocouples spring-loaded to the back of the heated wall. Local FE within the heated channel will be detected by wall superheat excursions, combined with flow visualization. The point of global FE in the channel will be identified by monitoring the total channel pressure drop as a function of heat flux.

The thermal limit at the hot spot can be investigated using techniques similar to those developed by Simon and Lee.[152] Most experiments to date have concentrated on a single heated spot in an otherwise adiabatic channel. However, experiments performed at SRL did involve a heated spot (i.e., actually a hot stripe located transverse to the flow) of elevated flux in a heated channel. Their experiments confirmed that hot spots require higher flux values to attain a so-called burnout. However, some of the measured burnouts occurred well downstream of the hot region. This would imply that a mechanism is responsible for the burnout quite different from that modeled by those measuring thermal limits at hot spots in otherwise adiabatic channels.

Several experimental methodologies are available to create localized hot spots or transverse hot streaks within a nonadiabatic test section. These methodologies include variation of heating element thickness in a resistance heated test section, separate, independently powered heaters, and heating of the spot by laser irradiation, etc. In these techniques, evaluation of the importance of conduction within the test section at the localized hot spot would be required in order to adequately characterize the local thermal conditions that would be necessary. Temperature measurements could include thermocouple arrays as noted above or the use of more advanced techniques such as phosphor luminescence or thermochromic crystal thermometry.

The experimental determination of the thermal limit in a heated channel with a hot spot can be evaluated by combination of the local heating and surface temperature measurement technique developed by Simon and Lee with direct uniform heating of the flow channel. The channel heated from one side would be used for this purpose.

It is not feasible to obtain a statistically meaningful body of data for nonuniformly heated conditions. The flux profiles in the reactor vary both spatially and temporally, giving a very wide range of possibilities to test. The intention of these experiments is to establish when the application of subchannel analysis techniques is adequate and/or conservative.

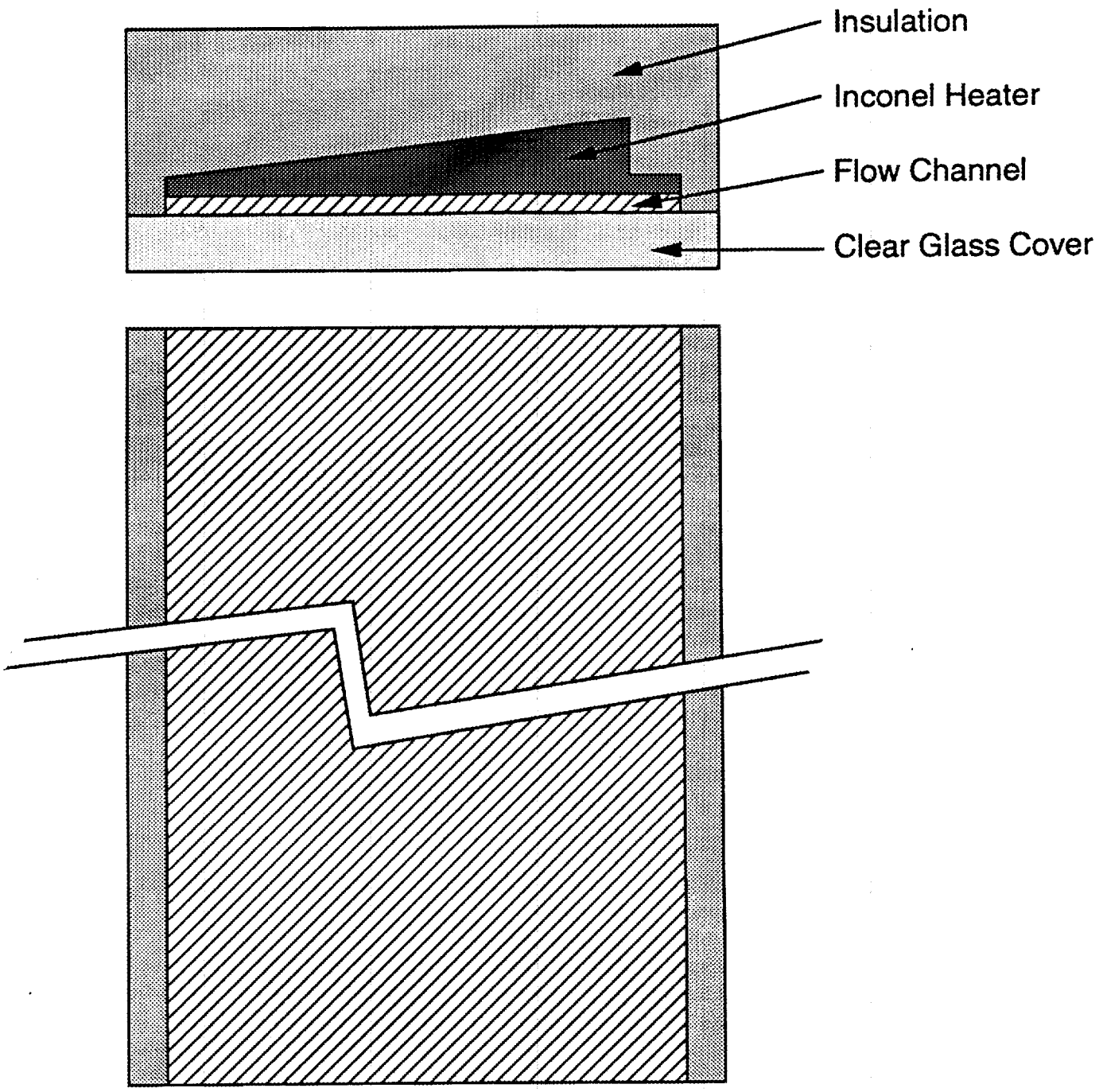

Fig. 6.13. Spanwise flux profile test section (one side heated).

Testing envisioned for this facility includes full-span:

- uniformly heated FE and CHF tests using aluminum test channels (if needed),
- FE tests with lateral heat flux distribution,
- FE tests with combined axial and lateral heat flux distribution,
- FE tests with hot streaks, and
- FE tests with hot spots.

6.2.4 Multichannel Thermal-Hydraulic Testing

Status: Planned.

Objective: To determine the effect of multiple heated channels on the FE phenomenon.

Background: This facility provides a further extension of testing conducted on single-channel full-scale test elements. Because of power supply limitations for multichannels, it is expected that this facility would use nonaluminum materials for the test assembly. This facility would be used to address "hot channel" effects on adjacent channels. The pressure drop flow rate curve discussed in Sect. 6.1 and shown in Fig. 6.1 describes the demand curve of a single heated channel. If all channels except the one of interest (described by this curve) do not experience the same parameter variation (i.e., decrease in flow, increase in power, etc.) as the channel of interest, then the supply curve dictated by these channels is flat (zero slope) as discussed in Sect. 6.1.1. However, if all channels experience the same parameter variation (as would be the case for a decrease in core flow, or an increase in core power), then the supply curve (as dictated by the other channels) has much the same shape as the channel of interest. The channel of interest (here assumed to be perturbed from the others by some small amount, such as higher heat flux) now experiences a supply curve with almost the same pressure drop/flow rate slope as itself. In order properly to characterize this behavior analytically, the code(s) used must be able to predict accurately the correct two-phase channel pressure drop through the event of interest in order to be able to predict the point where the perturbed channel experiences FE. The tests discussed here are designed to verify the predictive capability of the codes and to establish correct multiple heated channel FE behavior.

6.2.5 Flow Blockage Test Facility

Status: Under construction.

Objective: To determine the effect of a partial flow channel blockage on the heat-transfer characteristics downstream of the blockage.

Background: Partial flow blockage of the fuel element by debris in the primary loop is an important event that significantly impacts the likelihood of fuel damage. Experimentation to establish the type of blockage necessary to initiate fuel damage is therefore an important aspect of the overall T/H effort. The results from this experiment will also provide a useful tool in validating or benchmarking a computational fluid dynamics code. If such a code was successfully validated under typical ANS flow conditions, it would be a useful analysis tool for a broad range of T/H parameters.

The test section will have a span and gap of 80 and 1.27 mm, respectively, and a total channel length of ~50 cm, closely mimicking the flow channels within the ANS core region. Blockages ranging from 5–50% of the channel's span and located at both edge and central locations will be

tested. Bulk average temperatures will be measured at the inlet and outlet of the test section, along with fluid flow rates and upstream and downstream pressures.

The flow separation and rotational behavior behind a blockage would be changed by the introduction of any kind of pressure sensing instrumentation. Therefore, indirect methods of measuring the fluid velocity vectors and pressure fields will be used. The first method that will be used is shown in Fig. 6.14. The heater strip covers ~30 mm of the channel's length on one side. The temperature pattern on the back side of the heater will be measured and used to interpret the velocity field within the flow channel. Initially, heater power levels will be constrained to the minimum necessary to produce measurable temperature differences. Later tests will increase the heater power to determine the effect of the heat flux on the shape and size of the recirculation zone. A computer analysis of the heater's temperature-dependent resistivity, the surface heat transfer, and the resulting heat flux will be used to provide necessary corrections to the data analysis.

Other methods of velocity field measurement are also under consideration. They include the use of a laser Doppler anemometer and the introduction of phosphor particles into the circulating water. These phosphor particles can be used with an array of optical equipment to record velocity vectors within the fluid.

6.2.6 Natural Circulation Test Facility

Status: Planned.

Objective: Evaluate the natural circulation performance of the ANS design, including both loop and core behavior.

Background: Natural circulation in plate-fueled research reactors is not well understood and deserves a careful experimental evaluation since decay heat removal after loss of flow is associated with many initiating events. ANS is designed to provide natural convection cooling after shutdown for these initiating event scenarios. Multiloop designs with the possibility of different flow conditions in different loops may cause asymmetries that can affect the stability and behavior of the total system. Experimental validation and/or development of models and correlations that can predict the system response under natural convection conditions are necessary to ensure the capability for cooling under shutdown conditions. In addition, both in-loop and ex-loop core T/H behavior under natural circulation conditions must be characterized. It is expected that two separate facilities will be used to accomplish these tasks. The first will be a small scale facility designed to examine loop-to-loop interactions, while the second will be a facility designed to look at core and system performance under natural circulation conditions.

6.2.6.1 Loop-to-Loop Testing

Status: Planned.

Objective: To evaluate loop-to-loop interactions related to single-phase natural circulation cooling.

Background: This facility will examine issues related to natural circulation within the primary system. The design will encompass phenomena such as loop-to-loop interactions under free convection

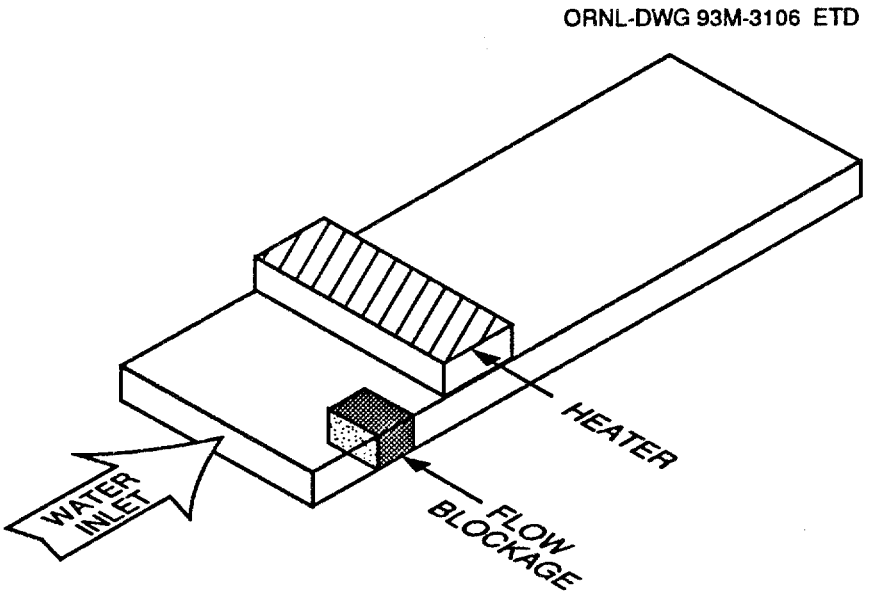

Fig. 6.14. Method for testing core inlet flow blockage.

conditions as well as accumulator-to-accumulator crosstalk. It is expected that this facility will not have to be full scale but will still have to incorporate a heated region to simulate properly the natural circulation conditions within the reactor primary coolant loops. Initial conditions within the flow loops will be varied (e.g, one pump off with the others operating, two pumps off, etc.) in order to determine the worst-case conditions for core and component cooling. Interactions between accumulators will be studied by incorporating scaled accumulators in the facility.

6.2.6.2 Core Region Natural Circulation Testing—Normal and Off-Normal

Status: Planned.

Objective: To evaluate core and overall scaled loop thermal limits under natural circulation conditions.

Background: Natural circulation testing of the core and primary system will require a facility that incorporates scaled elevations, power deposition, frictional resistance, etc. This facility is anticipated to have a heated test section that represents a multiple fuel plate section of the core. The design of the facility will allow both single-phase (within the loop) testing as well as two-phase testing to be performed. The objective of the testing will be to evaluate both the core thermal limit behavior, as well as the primary loop response under natural circulation conditions. The design of the heater simulating the core becomes critical for these tests as a result of the increased importance of properly simulating heat capacity and thermal response for two-phase conditions.

Boiling natural circulation flows are subject to several types of instabilities. The nature of the boiling channel performance is strongly linked to the hydraulic properties of the surrounding flow loop. Therefore, it is important to have an experimental arrangement that accurately simulates the pressure-drop and mass-flux performance of the ANSR during natural circulation decay heat removal. The most prototypic situation would include a bank of parallel heated channels in a natural circulation loop, complete with a riser above the fuel element. Such a loop for a natural circulation experiment will include a heated "fuel assembly simulator," followed by an upper flow annulus, hot leg piping, heat exchanger, cold leg piping, and pump discharging to the simulated "fuel assembly."

Two-phase (in the piping) natural circulation may not occur as a result of any of the design basis accidents. Thus, tests examining the two-phase natural circulation performance of the reactor may not need to be extensive since larger uncertainties and conservatisms are permissible in analysis of events with very low probabilities. Realistic quantification of margins associated with the single-phase natural circulation performance of the reactor will be difficult unless the two-phase natural circulation performance and associated thermal limits are understood. However, a conservative limit may be defined by holding the exit wall surface temperature less than saturation.

6.2.6.3 Thermal-Hydraulic Testing for Refueling

Status: Planned.

Objective: To determine core thermal limits applicable to the fuel element transport process during refueling.

Background: This test series is also expected to use the natural convection test facility instrumentation system, modified to address conditions expected during refueling. A separate pool and

associated hardware may be required to provide simulation of fuel element transport conditions. These experiments will address natural convection cooling capability during movement of the elements.

6.2.7 Hydraulic Tests of Nonfuel Components

Status: Planned.

Objective: Evaluate thermal performance of noncore components.

Background: This facility will provide data on local thermal and hydraulic characteristics of reflector tank components under controlled conditions. The facility will comprise a flow loop, power supplies, and associated instrumentation and controls necessary to provide the T/H conditions of the reflector tank. Modular test assemblies for the different geometries of various components will be installed in the flow loop as necessary. Components that may require testing include the outer shutdown rod assembly, the hydraulic lines to the outer shutdown rods, the tangential thermal beam tubes, the thermal through beam tube, the slant thermal beam tube, the hydraulic rabbit tubes for light isotope and transuranium production, the pneumatic rabbit tubes for analytical chemistry, the isotope production vertical holes, the slant irradiation tubes, the cold source thimbles, and the hot source thimbles. In addition, such items as cooling of the inner control rods, the CPBT, and the irradiation capsules will be experimentally investigated as necessary.

6.2.8 Integral Transient Performance Tests

Status: Planned.

Objective: Provide on integral test platform to perform RELAP benchmarks.

Background: This facility will provide an extension of the small scale RELAP simulation tests discussed in Sect. 6.2.2.4 and will be designed to provide benchmark data for RELAP5 under ANS type transients with loop components similar to the ANS. This scaled feasibility will focus on loop behavior (as opposed to detailed core behavior) and will be used for integral testing to gather pressure and flow response (and other) data. These data will be used to validate codes such as RELAP5 to ensure that it can properly predict transient system behavior. Several issues may need to be addressed in this facility. If transient results indicate that air ingestion (from a closed-volume cell) during a pipe break occurs or that flashing flows or pump cavitation is an issue, then two-phase pump performance must be characterized. Pressure wave propagation around the loop after a pipe break will also be examined to confirm the times predicted between break initiation and trip of the reactor as well as the magnitude of the pressure waves as they traverse the piping and core. Interaction of accumulators with the loop system during a rapid transient could also be examined.

6.2.9 Full-Scale/Full-Flow Hydraulic Test Facility

Status: Planned.

Objective: Evaluate core flow distribution and confirm component vibration behavior.

Background: The present ANS core region design includes ten separate orifices in order to distribute the flow properly. Thermal limits within the core and nonfuel components are dictated by these flows.

This facility will therefore examine issues associated with integrated operation of a complete core assembly under ANS design flow conditions. Included will be measurement and evaluation of flow distribution between fuel elements and other core components, measurement of pressure distributions within the core region, and evaluation of component stability and vibration under full-flow conditions. In addition, measurement of flow patterns established at the core inlet as a result of structural components and evaluation of these effects on fuel channel flow distributions will be made.

7. REFERENCES

1. "Pressure Vessels, Alternative Rules," *ASME Boiler and Pressure Vessel Code*, Sect. VIII, Division 2, American Society Mechanical Engineers, New York, 1989.

2. C. D. Fletcher and L. S. Ghan, *Analysis of Loss of Coolant Accidents in the Advanced Neutron Source Reactor*, EGG-EAST-8700, Idaho National Engineering Laboratory, Idaho Falls, Idaho, May 1990.

3. N. C. J. Chen and C. D. Fletcher, "Modeling Advanced Neutron Source Reactor Station Blackout Accident Using RELAP5," presented at the 1990 Joint RELAP5 and TRAC-BWR International User Seminar, Chicago, September 17-21, 1990.

4. N. C. J. Chen, M. W. Wendel, and G. L. Yoder, Jr., "Loss-of-Coolant Accident Mitigation for the Advanced Neutron Source Reactor," *Proceedings 29th ASME/AIChE/ANS/AIAA, National Heat Transfer Conference*, Atlanta, August 1993.

5. N. C. J. Chen, M. W. Wendel, and G. L. Yoder, Jr., "Conceptual Design Loss-of-Coolant Accident Analysis for the Advanced Neutron Source Reactor," *Nucl. Technol.* **105**, No.1, January 1994.

6. H. A. McLain, *HFIR Fuel Element Steady State Heat Transfer Analysis Revised Version*, ORNL/TM-1904, Union Carbide Corporation, Oak Ridge National Laboratory, December 1967.

7. D. G. Morris and W. R. Nelson, Martin Marietta Energy Systems, Inc., to D. L. Selby, Martin Marietta Energy Systems, Inc., "Documentation of Revisions to ANSR Steady-State Thermal Core Code for Monte Carlo Uncertainty Analysis," November 15, 1990.

8. J. A. Crabtree and M. Siman-Tov, *Thermophysical Properties of Saturated Light and Heavy Water for Advanced Neutron Source Application*, ORNL/TM-12322, Martin Marietta Energy Systems, Inc., Oak Ridge National Laboratory, May 1993.

9. C. Doderlein, "Untersuchungen Zur Kühlbarkeit Eines Kompakten Reaktorkerns Mit Evolventenförmigen Brennstoffplatten," thesis, Fakultät Für Physik E21 Technische Universität München, Garching, p. 41, Eq. 4.25, December 1989.

10. R. S. Smith and W. L. Woodruff, *A Computer Code, NATCON, for the Analysis of Steady-State Thermal-Hydraulics and Safety Margins in Plate-Type Research Reactors Cooled by Natural Convection*, ANL/RERTR/TN-12, Argonne National Laboratory, Chicago, December 1988.

11. Y. Sudo et al., "Experimental Study of Differences in Single-Phase Forced-Convection Heat Transfer Characteristics Between Upflow and Downflow for Narrow Rectangular Channel," *J. Nucl. Sci. and Technol.* 22(3), 202-212 (March 1985).

12. W. M. Kays, *Convection Heat and Mass Transfer*, McGraw Hill Book Co., Inc., New York, 1966.

13. E. R. G. Eckert and T. F. Irvine, Jr., *Incompressible Friction Factor, Transition and Hydrodynamic Entrance Length Studies of Ducts with Triangular and Rectangular Cross Sections*, WADC Tech. Report 58-85, University of Minnesota Heat Transfer Laboratory, Minneapolis, 1957.

14. R. K. Shah and A. L. London, "Laminar Flow Forced Convection in Ducts," *Adv. Heat Transfer, Rectangular Ducts*, 199-201, Academic Press, New York, 1978.

15. C. F. Bonilla, "Fluid Flow in Reactor Systems," in *Nuclear Engineering Handbook*, 9-35, 1st ed., H. Etherington (Ed.), McGraw-Hill, New York, 1958.

16. G. K. Filonenko, "Hydraulic Resistance in Pipes," *Teploenergetika* **1**(4), 40-44 (1954).

17. *TK Solver Plus*, Universal Technical Systems, Inc., Rockford, Illinois, July 1989.

18. *Mathcad*, MathSoft Inc., 201 Broadway, Cambridge, Maryland, 1989.

19. *PATRAN PLUS Reference Manual*, PDA Engineering, Costa Mesa, California, October 1990.

20. *P-THERMAL User Manual*, PDA Engineering, Costa Mesa, California, April 1991.

21. J. M. Ryskamp, Idaho National Engineering Laboratory, Idaho Falls, Idaho, memorandum to D. L. Selby, Martin Marietta Energy Systems, Inc., "Idaho National Engineering Laboratory Monthly Report for October 1990," November 1990.

22. M. El-Wakil, *Nuclear Heat Transport*, The American Nuclear Society, LaGrange Park, Indiana, 1978.

23. R. S. Ondrejcin, *Evaluation of Mark 22 Cladding*, DPST-83-324, Savannah River Laboratory, Aiken, South Carolina, March 1983.

24. *Advanced Continuous Simulation Language (ACSL) Reference Manual*, Mitchell & Gauthier Associates, Concord, Massachusetts, 1986.

25. K. W. Childs, *HEATING 7.2 User's Manual*, ORNL/TM-12262, Martin Marietta Energy Systems, Inc., Oak Ridge National Laboratory, February 1993.

26. M. Siman-Tov et al., "Thermal Hydraulic Correlations for the Advanced Neutron Source Reactor Fuel Element Design and Analysis," *Proceeding 1991 ASME Winter Annual Meeting, Atlanta*, December 1-6, 1991.

27. D. K. Felde et al., "The Advanced Neutron Source Thermal Hydraulic Test Loop," *Proceedings 8th Power Plant Dynamics, Control and Testing Symposium*, Knoxville, Tennessee, May 27-29, 1992.

28. W. R. Gambill, "Generalized Prediction of Burnout Heat Flux for Flowing, Subcooled, Wetting Liquids," *Chem. Eng. Prog. Symp. Series* **59**(41), 71–87 (1963).

29. J. Costa, *Measurement of the Momentum Pressure Drop and Study of the Appearance of Vapor and Change in the Void Fraction in Subcooled Boiling at Low Pressure*, presented at the Meeting of the European Group Double-Phase, Winfrith, England, 1967, translated from French as ORNL/TR-90/21, Martin Marietta Energy Systems, Inc., Oak Ridge National Laboratory, 1990.

30. A. E. Bergles and W. M. Rohsenow, *Forced-Convection Surface Boiling Heat Transfer and Burnout in Tubes of Small Diameter*, DSR Report No. 8767-21, Department of Mechanical Engineering, Massachusetts Institute of Technology, Cambridge, Massachusetts, 1962.

31. B. S. Petukhov, "Heat Transfer and Friction in Turbulent Pipe Flow with Variable Physical Properties," *Adv. Heat Transfer* **6**, 504 (1970).

32. R. J. Weatherhead, *Nucleate Boiling Characteristics and the Critical Heat Flux Occurrence in Subcooled Axial-Flow Water Systems*, ANL-6675, Argonne National Laboratory, Chicago, March 1963.

33. W. R. Gambill and T. Mochizuki, "Advanced Neutron Source Design: Burnout Heat Flux Correlation Development," *Trans. Am. Nucl. Soc.* **57**, 298–300 (October 1988).

34. L. Bernath, "A Theory of Local Boiling Burnout and Its Application to Existing Data," *Chem. Eng. Prog. Symp. Series* **56**(30), 95–116 (1960).

35. C. H. Oh, *Critical Heat Flux and Flow Instability Study for Ultra High Flux Reactor*, EPM-A-016, EG&G Idaho, Inc., Idaho Falls, Idaho, April 1986.

36. E. J. Thorgerson, D. H. Knoebel, and J. H. Gibbons, "A Model to Predict Convective Subcooled Critical Heat Flux," *ASME J. of Heat Trans.*, February 1974.

37. D. A. Labuntsov, "Critical Thermal Loads in Forced Motion of Water which is Heated to a Temperature below the Saturation," translated from *Atomnaya Energiya* **10**(5), 523–525 (May 1961).

38. M. E. Shitsman, "Method of Calculating Critical Heat Flux for a Forced Flow of Water," translated from Russian as AEC-tr 6290, *Teploenergetika* **10**(10), 76–78 (1963).

39. R. W. Bowring, *A Simple but Accurate Round Tube, Uniform Heat Flux, Dryout Correlation over the Pressure Range 100–2500 psia*, Report AEEW-R-789, Atomic Energy Establishment, (UKAEE), Winfrith, England, 1972.

40. Y. Katto, "Prediction of CHF of Subcooled Flow Boiling in Round Tubes," *Intl. J. of Heat and Mass Tran.* **33**(9), 1921–1928 (1990).

41. J. Weisman and S. Ileslamlou, "A Phenomenological Model for Prediction of CHF under Highly Subcooled Conditions," *Fusion Technol.* **13** (May 1988).

42. Y. Komori et al., "Experimental Study on DNB Heat Flux Correlations for JMTR Satety Analysis," presented at the International Meeting on Reduced Enrichment for Research and Test Reactors, Newport, Rhode Island, 1990.

43. R. W. Bowring, *Physical Model, Based on Bubble Detachment, and Calculation of Steam Voidage in the Subcooled Region of Heated Channel*, H.P.R. 10, OECD Halden Reactor Project, Institut for Atomenergi, Halden, Norway, December 1962.

44. R. H. Whittle and R. Forgan, "A Correlation for the Minima in the Pressure Drop vs. Flow-Rate Curves for Subcooled Water Flowing in Narrow Heated Channels," *Nucl. Eng. Design* **6**, 89–99 (1967).

45. P. Saha and N. Zuber, "Point of Net Vapor Generation and Vapor Void Fraction in Subcooled Boiling," *Proceedings 5th International Heat Transfer Conference*, Tokyo, Japan **IV**, 175–179 (1974).

46. U. Moritz, *Governing Law for the Occurrence of Excursive Flow Instability*, Interatom internal report No. 54.07337.2.A, August 2, 1988.

47. U. Moritz, *Absicherung des ETA-Stabilitätskriteriums für hohe Wassergeschwindigkeiten*, Interatom-Notiz no. 54.07747.5, 1989.

48. S. S. Papell, *Subcooled Boiling Heat Transfer under Forced Convection in a Heated Tube*, National Aeronautics and Space Administration, Technical Note D-1583, Lewis Research Center, Cleveland, Ohio, March 1963.

49. E. J. Davis and G. H. Anderson, "The Incipience of Nucleate Boiling in Forced Convection Flow," *AIChE J.* **12**(4), 774–780 (July 1966).

50. W. Frost and G. S. Dzakowic, *An Extension of the Method of Predicting Incipient Boiling on Commercially Finished Surfaces*, ASME Paper No. 67-HT-61, American Society of Mechanical Engineers, 1967.

51. R. Hino and T. Ueda, "Studies of Heat Transfer and Flow Characteristics in Subcooled Flow Boiling—Part 1, Boiling Characteristics," *Int. J. of Multiphase Flow* **11**(3), 260–281 (1985).

52. P. W. Dittus and L. M. K. Boelter, "Heat Transfer in Automobile Radiators of the Tubular Type," *Univ. Calif. Pub. Eng.* 2(13), 443–461 (1930), reprinted in *Int. Comm. Heat Mass Transfer* **12**, 3–22 (1985).

53. E. N. Sieder and G. E. Tate, "Heat Transfer and Pressure Drop of Liquids in Tubes," *Ind. Eng. Chem.* **28**, 1429–1435 (1936).

54. H. Hausen, "Extended Equation for Heat Transfer in Tubes at Turbulent Flow," *Warme-und Stoffubertragung* 7, 222-225 (1974).

55. V. Gnielinski, "New Equations for Heat and Mass Transfer in Turbulent Pipe and Channel Flow," *Int. Chem. Eng.* **16**(2), April 1976.

56. L. Prandtl, *Führrer durch die Stomungslehre, Vieweg, Braunschweig*, p. 359, 1944, English translation, Blackie, London, 1952.

57. T. von Karman, "Turbulence and Skin Friction," *J. Aerosp. Sci.* **33**(9), 1921-1928 (1934).

58. J. Nikuradse, *GesetzmaVigkeiten der turbulenten Stromung in glattern Rohren, Forsch. Arb. Ing.-Wes.*, No. 356, 1932, translated by National Aeronautics and Space Administration, NASA TT F-10, 359, 1966.

59. R. Techno et al., "An Accurate Equation for the Computation of the Friction Factor for Smooth Pipes from the Reynolds Number," *J. of Appl. Mechs.* **32**, 443 (1965).

60. C. F. Colebrook, "Turbulent Flow in Pipes with Particular Reference to the Transition Region between the Smooth and Rough Pipes Laws," *J. of Inst. Civ. Eng.* **11**, 133-156 (1939).

61. N. H. Chen, "An Explicit Equation for Friction Factor in Pipe," *Ind. Eng. Chem.* **11**, 133-156 (1939).

62. E. D. Waters, *Heat Transfer Experiments for Advanced Test Reactor*, BNWL-216, UC-80 (TID-4500), Battelle Northwest Laboratory, Richland, Washington, May 1966.

63. R. D. Boyd, "Subcooled Water Flow Boiling at 1.66 MPa Under Uniform High Heat Flux Conditions," *Fusion Technol.* **16**, 324 (November 1989).

64. G. L. Yoder, Martin Marietta Energy Systems, Inc., memorandum to D. L. Selby, Martin Marietta Energy Systems, Inc., "ANS Reactor Core Analysis Task Monthly Progress Report," August 1991.

65. M. S. Bhatti and R. K. Shah, "Turbulent and Transition Flow Convective Heat Transfer in Ducts," *Handbook of Single-Phase Convective Heat Transfer*, ed. C. S. Kakac, R. K. Shah, and W. Aung, John Wiley & Sons, New York, 1987.

66. W. R. Gambill, Martin Marietta Energy Systems, Inc., memorandum to D. L. Selby, Martin Marietta Energy Systems, Inc., "Hydrodynamic Smoothness of the ANSR Fuel Plates," August 1989.

67. R. E. Pawel et al.,*The Development of a Preliminary Correlation of Data on Oxide Growth on 6061 Aluminum under ANS Thermal-Hydraulic Conditions*, ORNL/TM-11517, Martin Marietta Energy Systems, Inc., Oak Ridge National Laboratory, June 1990.

68. B. H. Montgomery, R. E. Pawel, and G. L. Yoder, "The Advanced Neutron Source Test Loop Facility," *Trans. Am. Nucl. Soc.* **57**, 300 (1988).

69. R. E. Pawel et al., "Fuel Cladding Corrosion Studies for the Advanced Neutron Source," *Trans. Am. Nuc. Soc.* **61**, 388 (1990).

70. R. E. Pawel et al., "The Corrosion of 6061 Aluminum under Heat Transfer Conditions in the ANS Corrosion Test Loop," *Oxid. Metals* **36**(1/2), 175 (1991).

71. J. C. Griess, H. C. Savage, and J. L. English, *Effect of Heat Flux on the Corrosion of Aluminum by Water. Part IV. Tests Relative to the Advanced Test Reactor and Correlation with Previous Results*, ORNL-3541, Union Carbide Corporation, Oak Ridge National Laboratory, February 1964.

72. SAS Institute, Inc., SAS Circle, Cary, North Carolina, 27512-8000.

73. D. H. Knoebel et al., *Forced-Convection Subcooled Critical Heat Flux*, Report DP-1306, E. I. du Pont de Nemours and Co., Savannah River Laboratory, Aiken, South Carolina, 1973.

74. W. R. Gambill, R. D. Bundy, and R. W. Wansbrough, "Heat Transfer, Burnout, and Pressure Drop for Water in Swirl Flow through Tubes with Internal Twisted Tapes," *Chem. Eng. Prog. Symp. Series* 57(32), 127–137 (1961).

75. W. R. Gambill and R. D. Bundy, "Heat Transfer Studies of Water Flow in Thin Rectangular Channels, Part I: Forced Convection," *Nucl. Sci. and Eng.* **18**, 69–79 (1964).

76. S. Mirshak, W. S. Durant, and R. H. Towell, *Heat Flux at Burnout*, Report DP-355, E. I. du Pont de Nemours and Co., Savannah River Laboratory, Aiken, South Carolina, February 1959.

77. D. F. Babcock and R. R. Hood, *Heavy Water Moderated Power Reactors Progress Report of March 1962*, Report DP-725, E. I. du Pont de Nemours and Co., Savannah River Laboratory, Aiken, South Carolina, April 1962.

78. E. Burck and W. Hufschmidt, *Messong der Keitischen Wärmestromdichte von Wasser im Unterkühlten Zustand in Rohren bei Erzwungener Strömung*, Report EUR-2432.d, EURATOM, Ispra, Italy, June 1965.

79. W. H. Jens and P. A. Lottes, *Analysis of Heat Transfer, Burnout, Pressure Drop and Density Data for High-Pressure Water*, ANL-4627, as reported by DeBortoli et al., *Forced Convection Heat Transfer Burnout Studies for Water in Rectangular Channels and Round Tubes at Pressures above 500 psia*, Westinghouse Report WAPD-188, Westinghouse, Pittsburgh, Pennsylvania, October 1958.

80. J. W. Schaefer and J. R. Jack, *Investigation of Forced-Convection Nucleate Boiling of Water for Nozzle Cooling at Very High Heat Fluxes*, National Aeronautics and Space Administration, NASA TN-D-1214, May 1962.

81. J. Mayersak, S. D. Raezer, and E. A. Brent, "Confirmation of Gambill-Greene Straight-Flow Burnout Heat Flux Equation at Higher Flow Velocity," *ASME J. of Heat Trans.* **297** (May 1964).

82. W. R. Gambill and N. D. Greene, "Boiling Burnout with Water in Vortex Flow," *Chem Eng. Prog. Symp. Series* **54**(10)68, October 1958.

83. T. Dormer and R. D. Bergles, *Pressure Drop with Surface Boiling in Small Diameter Tubes,* DSR Report No. 8767-31 (MIT-8767-31), Department of Mechanical Engineering, Massachusetts Institute of Technology, Cambridge, Massachusetts, September 1964.

84. A. E. Bergles, *Subcooled Burnout in Tubes of Small Diameter,* ASME Paper 63-WA-182, American Society of Mechanical Engineers, 1963.

85. B. C. Skinner and C. S. Loosmore, *Subcooled Critical Heat Flux for Water in Round Tubes,* thesis, Massachusettes Institute of Technology, Cambridge, Massachusetts, June 1965.

86. J. M. Reynolds, *Burnout in Forced Convection Nucleate Boiling of Water,* DSR Report No. 7-7673, Massachusetts Institute of Technology, Cambridge, Massachusetts, 1957.

87. H. L. Wessel, *Investigation of Forced-Convection Subcooled Boiling,* Ph.D. thesis, Massachusetts Institute of Technology, Cambridge, Massachusetts, 1964.

88. L. S. Scarola, *Investigation of Additives on the Critical Heat Flux in Nucleate Boiling,* Ph.D. thesis, Massachusetts Institute of Technology, Cambridge, Massachusetts, 1964.

89. A. P. Ornatskii, "The Influence of Length and Tube Diameter on Critical Heat Flux for Water with Forced Convection and Subcooling," *Teploenergetika* **6**, 67 (1960).

90. C. L. Vandervort, "Ultimate Limits of Boiling Heat Fluxes," *Proceedings Eighth Symposium on Energy Engineering Sciences,* CONF-9005183, Micro/Macro Studies of Multiphase Media, Argonne National Laboratory, Chicago, May 1990.

91. A. P. Ornatskii and A. M. Kichigan, "Critical Thermal Loads during the Boiling of Subcooled Water in Small Diameter Tubes," *Teploenergetika* **6**, 75 (1962).

92. R. D. Boyd, "Subcooled Water Flow Boiling Experiments under Uniform High Flux Conditions," *Fusion Technol.* **13**, 131-142 (January 1988).

93. A. P. Ornatskii and L. S. Vinyarskii, "Heat Transfer Crisis in a Forced Flow of Underheated Water in Small Bore Tubes," translated from *Teplofizika Vyskkikh Temperatur (High Temperature)* 3(3), 400 (1964).

94. G. P. Celata et al., "Preliminary Remarks on High Heat Flux CHF, Subcooled, Water Flow Boiling," *Int. J. of Heat and Technol.* 8(1-2), 20-42 (1990).

95. J. Lafay, G. Maisonnier, and F. Girard, *Compte rendu d'essais flux de redistribution de débit—expulsion et caléfaction—à basse pression et qux faibles bitesses en canal rectangulaire*, TT/65-17-B/JL-GM-FG, November 1965.

96. J. Lafay, *Détermination expérimentale du flux de redistribution de débit—à basse pression et en régime permanent—influence du diamétre hydraulique*, Note TT No. 204, 1965.

97. M. Courtaud, G. Coulon, and F. Mazzili, *Compte rendu d'essais, boucle casimir tracé du courbes en S (Canal de 900 MM) Essais de dépressuration*, TT/66-7-B/MC-GC-FM, March 1966.

98. M. Courtaud, G. Coulon, and F. Mazzili, *Compte rendu d'essais boucle casimir tracé de courbes en S lére partie Eau dégazée*, TT/66-2/MC-GC-FM, January 1966.

99. M. Courtaud et al., *Compte rendu d'essais Pertes de charge de redistribution de débit sur des canaux rectangulaires de 1,8 mm d'entrefer*, (Type R. H. F.), TT/67-7-B/MC-KS-GC-FM, June 1967.

100. P. Vernier, *Compte rendu d'essais Osiris—étude de sûreté détermination expérimentale de courbes en s et des conditions de redistribution de débit*, TT/65-19-B/PV, December 1965.

101. M. Courtaud, G. Coulon, and F. Mazzilli, *Compte rendu d'essais, boucle casimir Tracé de courbes en S sur des canaux á flux non uniforme*, TT/66-14-B/MC-GC-FM, June 1966.

102. K. Schleisiek and J. C. Dumaine, *Compte rendu d'essais Essais préliminaires pour RHF détermination expérimental des conditions de redistribution de débit aux pressions entre 4 et 5 kg/cm² abs pour un canal rectangulaire de 2 mm d'épaisseur et de 60 cm de longueur*, TT/66-10-B/KS-JCD,27, April 1966.

103. J. Lafay, G. Maisonnier, and F. Mazzili, *Compte rendu d'essais Influence de la répartition axiale du flux sur les seuils d'apparition de la redistribution de débit*, TT/68-4-B/JL, February 1968.

104. T. Sato and H. Matsumura, "On the Conditions of Incipient Subcooled Boiling," *Bull. of Japan Soc. of Mech. Eng.* 7(26), 392–398 (1964).

105. Y. Sudo et al., "Experimental Study of Incipient Nuclear Boiling in Narrow Vertical Rectangular Channel Simulating Subchannel of Upgraded JRR-3," *J. of Nucl. Sci. and Technol.* **23**(1), 73–82 (1986).

106. W. Hufschmidt and E. Burck, "The Effect of Temperature Dependent Properties of Materials on Heat Transfer in the Turbulent Flow of Liquids in Tubes at High Heat Fluxes and Plandtl Numbers," (in German) *Intl. J. of Heat and Mass Trans.* **11**(7)1041–1048 (July 1986).

107. R. L. Webb, "A Critical Evaluation of Analytical Solutions and Reynolds Analogy Equations for Turbulent Heat and Mass Transfer in Smooth Tubes," *Warme-und Stoffubertragung (Thermo and Fluid Dynamics)* **4**, 197–204 (1971).

108. J. C. Hartnett, Y. Koh, and S. T. McComas, "A Comparison of Predicted and Measured Friction Factors for Turbulent Flow through Rectangular Ducts," *ASME J. of Heat Trans.*, 82–88 (February 1962).

109. O. C. Jones, Jr., "An Improvement in the Calculation of Turbulent Friction in Rectangular Ducts," *J. of Fluids Eng.* **98**, 173–181 (June 1976).

110. O. C. Jones, Jr., unpublished data, 1963. See Jones, ref. 109.

111. L. Schiller, "Uber den Stronumgswiderstand von Rohren verschiedenen Querschnitts und Rauhigkeitsgrades," *Zeitschrift fur Angewandte Mathematik and Mechanik* **3**, 2–13 (1923).

112. E. R. Eckert and T. F. Irvine, Jr., "Incompressible Friction Factor, Transition and Hydrodynamic Entrance Length Studies of Ducts with Triangular and Rectangular Cross Section," *Proceedings of the 5th Midwestern Conference on Fluid Mechanics*, University of Michigan Press, Ann Arbor, Michigan, 122–145, 1957.

113. L. Washington and W. M. Marks, "Heat Transfer and Pressure Drop in Rectangular Air Passages," *Ind. Eng. Chem.* **29**, 337–345 (1937).

114. D. P. Bozarth, Science Applications International Corporation, memorandum to D. L. Selby, Martin Marietta Energy Systems, Inc., "Transmittal of SAMPLE Code and Initial Results for ANS Statistical Thermal-Hydraulic Analysis," July 10, 1991.

115. Y.-T. Wu, *Fast Probability Integration (FPI) Theoretical Manual* (FPI Version 4.2, December 1989), Southwest Research Institute, San Antonio, Texas, December 1989.

116. W. R. Gambill, Martin Marietta Energy Systems, Inc., memorandum to D. L. Selby, Martin Marietta Energy Systems, Inc., "Uncertainty Factors for the ANS Reactor Core Design," March 21, 1988.

117. Technical Program Group, *Quantifying Reactor Safety Margins, Application of Code Scaling, Applicability, and Uncertainty Evaluation Methodology to a Large-Break, Loss-of-Coolant Accident*, NUREG/CR-5249, EG&G Idaho, Idaho Falls, Idaho, December 1989.

118. R. H. Wilson, D. A. Farnsworth, and K. E. Kneidel, *BWC—An Improved Correlation of Critical Heat Flux for Babcock & Wilcox Fuel Assemblies,* presented at 1982 AIAA/ASME Joint Fluids, Plasma, Thermophysics and Heat Tranfer Conference, St. Louis, June 7–11, 1982.

119. L. S. Tong, "Prediction of Departure From Nuclear Boiling for an Axially Non-Uniform Heat Flux Distribution," *J. Nucl. Energy* **6**, 21–27 (1967).

120. J. Weisman and B. S. Pei, "Prediction of Critical Heat Flux in Flow Boiling at Low Qualities," *Intl. J. Heat Mass Transfer* **26**(10), 1463–1477 (1983).

121. Y. Katto, "Prediction of Critical Heat Flux of Subcooled Flow Boiling in Round Tubes," *Intl. J. Heat Mass Transfer* **33**(9), 1921–1928 (1990).

122. D. G. Morris and M. Siman-Tov, Martin Marietta Energy Systems, Inc., memorandum to D. L. Selby, Martin Marietta Energy Systems, Inc., "Preliminary Uncertainty Distributions for Selected ANSR Parameters," November 15, 1990.

123. R. W. Knight, J. Binns, and G. M. Adamson, Jr., *Fabrication Procedures for Manufacturing High Flux Isotope Reactor Fuel Elements*, ORNL-4242, Union Carbide Corp., Oak Ridge National Laboratory, June 19, 1968.

124. I. Miller and J. E. Freund, *Probability and Statistics for Engineers*, 2nd ed., Prentice-Hall, Inc., Englewood, New Jersey, 1977.

125. C. C. Davis, University of Tennessee, *Statistical Uncertainty Analysis Applied to the ANSR*, informal report for the Science and Engineering Research Semester (SERS) Program at Oak Ridge National Laboratory, April 28, 1992.

126. C. C. Davis, University of Tennessee, *Documentation for Steady State Alternating Channel Code*, informal report for the Science and Engineering Research Semester (SERS) Program at Oak Ridge National Laboratory, August 7, 1992.

127. C. R. Luttrell, Martin Marietta Energy Systems, Inc., letter to D. G. Morris, Martin Marietta Energy Systems, Inc., "Temperature Effects on Gap Between ANS Fuel Plates," October 28, 1992.

128. W. K. Sartory, *Nonlinear Analysis of Hydraulic Buckling Instability of ANS Involute Fuel Plates*, ORNL/TM-12319, Martin Marietta Energy Systems, Inc., Oak Ridge National Laboratory, March 1993.

129. W. F. Swinson, R. L. Battiste, C. R. Luttrell, and G. T. Yahr, *Fuel Plate Stability Experiments and Analysis for the Advanced Neutron Source*, ORNL/TM-12353, Martin Marietta Energy Systems, Inc., Oak Ridge National Laboratory, May 1993.

130. J. L. Anderson, Martin Marietta Energy Systems, Inc., letter to M. Siman-Tov, Martin Marietta Energy Systems, Inc., "ANS Acceptance Criteria," March 4, 1992.

131. *Reactor Safety Study*, WASH-1400, NUREG-75/014, U.S. Nuclear Regulatory Commission, October 1975.

132. J. R. Kirkpatrick, Martin Marietta Energy Systems, Inc., memorandum to G. L. Yoder, Martin Marietta Energy Systems, Inc., "Preliminary Results for ANS Fuel Plate Peaking Factors for Non-bonds," September 18, 1989.

133. M. Mazumdar, "Use of Statistical Theory of Extremes in Hot Channel Analysis of a Liquid Metal Fast Breeder Reactor," *Nucl. Sci. and Eng.* **47**, 187–194 (1972).

134. P. L. Arnsberger and M. Mazumdar, "The Hot Channel Factor as Determined by the Permissible Number of Hot Channels in the Core," *Nucl. Sci. and Eng.* **47**, 140–149 (1972).

135. A. Amendola, "Statistical Evaluation of the Maximum Temperatures in Reactor Cores," *Nucl. Sci. and Eng.* **41**, 343-350 (1970).

136. H. J. Reilly, J. D. Hansell, and G. L. Heath, "Treatment of Uncertainties in Reactor Heat Transfer Calculations," *Nucl. Sci. and Eng.* **38**, 135-142 (1969).

137. J. Rest and J. L. Snelgrove, Argonne National Laboratory, Chicago, Illinois, memorandum to G. E. Giles, Martin Marietta Energy Systems, Inc., "An Estimate of Evolution of Dispersion Fuel Thermal Conductivity for Hot Spots with Segregations (50% U_3Si_2, 15% void)," April 8, 1992.

138. J. R. Kirkpatrick, *Calculations for HFIR Fuel Plate Non-bonding and Fuel Segregation Uncertainty Factors*, K/CSD/TM-79, Martin Marietta Energy Systems, Inc., Oak Ridge National Laboratory, October 1990.

139. J. R. Kirkpatrick, Martin Marietta Energy Systems, Inc., memorandum to G. L. Yoder, Martin Marietta Energy Systems, Inc., "Preliminary Worst Case Results for ANS Fuel Plate Peaking Factors and Temperatures for Fuel Segregation," November 1989.

140. G. E. Giles, Martin Marietta Energy Systems, Inc., memorandum to G. L. Yoder, Martin Marietta Energy Systems, Inc., "Thermal Studies of ANS Fuel Plate-Distributed Segregation Assumption and Centered Meat Fuel Design," October 9, 1991.

141. J. R. Kirkpatrick, Martin Marietta Energy Systems, Inc., memorandum to G. L. Yoder, Martin Marietta Energy Systems, Inc., "Preliminary Results for ANS Fuel Plate Peaking Factors for Non-Bonds—Addendum: Peak Temperatures for Low Power Level," September 18, 1989.

142. G. L. Yoder et al., "The Effect of Aluminum Corrosion on the Advanced Neutron Source Reactor Fuel Design," *Nucl. Eng. and Design* **136**, 401-408, 1992.

143. M. Leddineg, "Unstabitit der Stromung bei naturlichen und Zwangumlauf," *die Warme* **61**(48), 891-898 (1938).

144. M. Leddineg, "Flow Distribution in Forced-Circulation Boilers," *Eng. Digest* **10**, 85-89 (1949).

145. J. S. Maulbetsch and P. Griffith, *A Study of System-Induced Instabilities in Forced-Convection Flows with Subcooled Boiling*, Report No. 5382-35, Department of Mechanical Engineering, Massachusetts Institute of Technology, Cambridge, Massachusetts, April 1965.

146. R. T. Lahey, Jr. and F. J. Moody, *The Thermal Hydraulics of a Boiling Water Nuclear Reactor*, American Nuclear Society, LaGrange Park, Illinois, 1977.

147. R. B. Duffey and E. D. Hughes, "Static Flow Instability Onset in Tubes, Channels, Annuli, and Rod Bundles," *Proceedings 1990 ASME Winter Annual Meeting*, Dallas, HTD-Vol. 150, November 25-30, 1990.

148. F. Inasaka, H. Nariai, and T. Shimura, "Pressure Drops in Subcooled Flow Boiling in Narrow Tubes," *Heat Transfer: Japanese Research* **18**(1), 1989.

149. W. M. Rohsenow and J. A. Clark, "Heat Transfer and Pressure Drop Data for High Heat Flux Densities to Water at High Subcritical Pressure," NP-3385, Massachusetts Institute of Technology, Cambridge, Massachusetts, April 1951.

150. F. C. Gunther, "Photographic Study of Surface Boiling Heat Transfer to Water with Forced Convection," *Trans. ASME* **73**, 115–123, February 1951.

151. W. R. Gambill, "Boiling-Burnout Research at the Savannah River Laboratory," memorandum to distribution, Union Carbide Corporation, Oak Ridge National Laboratory, July 16, 1962.

152. T. W. Simon and T. Y. Lee, "High Heat Flux Forced Convection Boiling from Small Regions," 26th National Heat Transfer Conference, HTD Vol. 111, Heat Transfer in Electronics, ASME, Philadelphia, 1989.

153. P. Griffith, W. A. Schumann, and A. D. Neustal, "Flooding and Burn-out in Closed-End Vertical Tubes," Two-Phase Fluid Flow Symposium Paper No. 5, Institute Mechanical Engineers, London, England, 1962.

154. N. Zuber, *Hydrodynamic Aspects of Boiling Heat Transfer*, AECU-4439, University of California at Los Angeles, 1959.

155. K. Mishima and M. Ishii, *Critical Heat Flux Experiments under Low Flow Conditions in a Vertical Annulus*, NUREG/CR-2647 (ANL 82-6), 1982.

156. K. Mishima and H. Nishihara, "Effect of Channel Geometry on Critical Heat Flux for Low Pressure Water," *Intl. J. of Heat and Mass Transfer* **30**(6), 1169–1182 (1987).

157. K. Mishima, H. Nishihara, and I. Michiyoshi, "Boiling Burnout and Flow Instabilities," *Intl. J. of Heat and Mass Transfer* **28**(6), 1115–1129 (1985).

158. G. H. Llewellyn et al., *Experimental and Analytical Studies in Quenching Uranium-0.75% Titanium Alloy Cylinders*, Y-12 Report No. Y-2397, Martin Marietta Energy Systems, Inc., February 1989.

159. Herbert Reutler, Interatom, Bergisch Gladbach, Germany, personal communication to A. E. Ruggles, Martin Marietta Energy Systems, Inc., 1989.

160. A. Clause, R. T. Lahey, Jr., and M. Podowski, "An Analysis of Stability and Oscillation Modes in Boiling Multichannel Loops Using Parameter Perturbation Methods," *Intl. J. of Heat and Mass Transfer* **32**(11), 2055–2064 (1989).

161. B. S. Johnston, *Subcooled Boiling of Downward Flow in a Vertical Annulus*, DPST-88-891, Savannah River Laboratory, Aiken, South Carolina, 1988.

162. T. Dougherty et al., "Flow Instability in Vertical Down-Flow at High Fluxes," *Proceedings 1989 American Society of Mechanical Engineers Winter Annual Meeting* **119**, 17-23 (1989).

163. W. R. Gambill and R. D. Bundy, *Burnout Heat Fluxes for Low-Pressure Water in Natural Circulation*, ORNL-3026, Union Carbide Corporation, Oak Ridge National Laboratory, 1960.

164. M. Siman-Tov et al., "Experimental Investigation of Thermal Limits in Parallel-Plate Configuration for the Advanced Neutron Source Reactor," Symposium Series Vol. 89, *Proceedings 29th ASME/AIChE/ANS/AIAA National Heat Transfer Conference*, Atlanta, August 1993.

165. A. E. Ruggles and P. T. Williams, "RELAP5/MOD2 Benchmarking Study: Critical Heat Flux Under Low Flow Conditions," *Trans. Am. Nucl. Soc.* **61**, 204-5 (June 1990).

Appendix A. ADVANCED NEUTRON SOURCE L7 CORE DESIGN FUEL PLATES

Appendix A. ADVANCED NEUTRON SOURCE L7 CORE DESIGN FUEL PLATES

The following figures present contour plots of the various thermal parameters used in the hot spot studies. The L7 design values were provided by Trent Primm and Bill Nelson. The L7 coarse mesh tables[A-1] include meat thickness, uranium surface density, and fuel burnup reported at 300 points on the lower and 324 points on the upper core fuel plate. The relative power density[A-2] and oxide layer thickness[A-3] are reported on a finer mesh that is used by the VENTURE and steady-state T/H codes. The power density is reported at cell centers on this finer mesh, while the oxide thickness is reported at cell edges. There was a total of 1656 points in the power density mesh for both the upper and lower core.

The meat thickness and original uranium surface density do not change with time. The fuel burnup, power density, and oxide thickness are time dependent and are reported at selected time steps by the VENTURE and ANS steady-state T/H codes.

Each point in the coarse mesh defines the center of a rectangular region or cell that has the same meat thickness and original surface density. The local time-dependent burnup is also assumed to be uniform over this cell. The power density and, therefore, oxide thickness can change within this cell as a result of the neutronics and thermal considerations. The power density and oxide thickness were interpolated on the coarse mesh by taking the maximum relative power density and the minimum local oxide thickness within the cell. The oxide thickness was assumed to be located at the same points as the power density. This procedure will produce conservative peaking factors but not necessarily conservative maximum temperatures.

Figures A.1 and A.2 present the meat thickness and initial surface density variations for both the upper and lower cores. Figure A.3 presents the EOC burnup distribution for both cores. Figures A.4 and A.5 present the normal fuel conductivity and segregated fuel conductivity distributions calculated from the burnup and surface density and tables of conductivity as a function of fission density. Figures A.6 and A.7 present the relative power density, oxide thickness distributions interpolated on the coarse mesh.

REFERENCES

A-1. T. Primm, Martin Marietta Energy Systems, Inc., memorandum to G. E. Giles, Martin Marietta Energy Systems, Inc., "L7 Design Tables for Surface Density, EOC Fuel Depletion, and Meat Thickness," February 6, 1992.

A-2. T. Primm and W. R. Nelson, Martin Marietta Energy Systems, Inc., memorandum to G. E. Giles, Martin Marietta Energy Systems, Inc., "L7 Design Tables for Relative Power Density," February 10, 1992.

A-3. W. R. Nelson, Martin Marietta Energy Systems, Inc., memorandum to G. E. Giles, Martin Marietta Energy Systems, Inc., "ANS Steady State T-H Code Produced Oxide Layer Thickness for L7 Design," June 23, 1992.

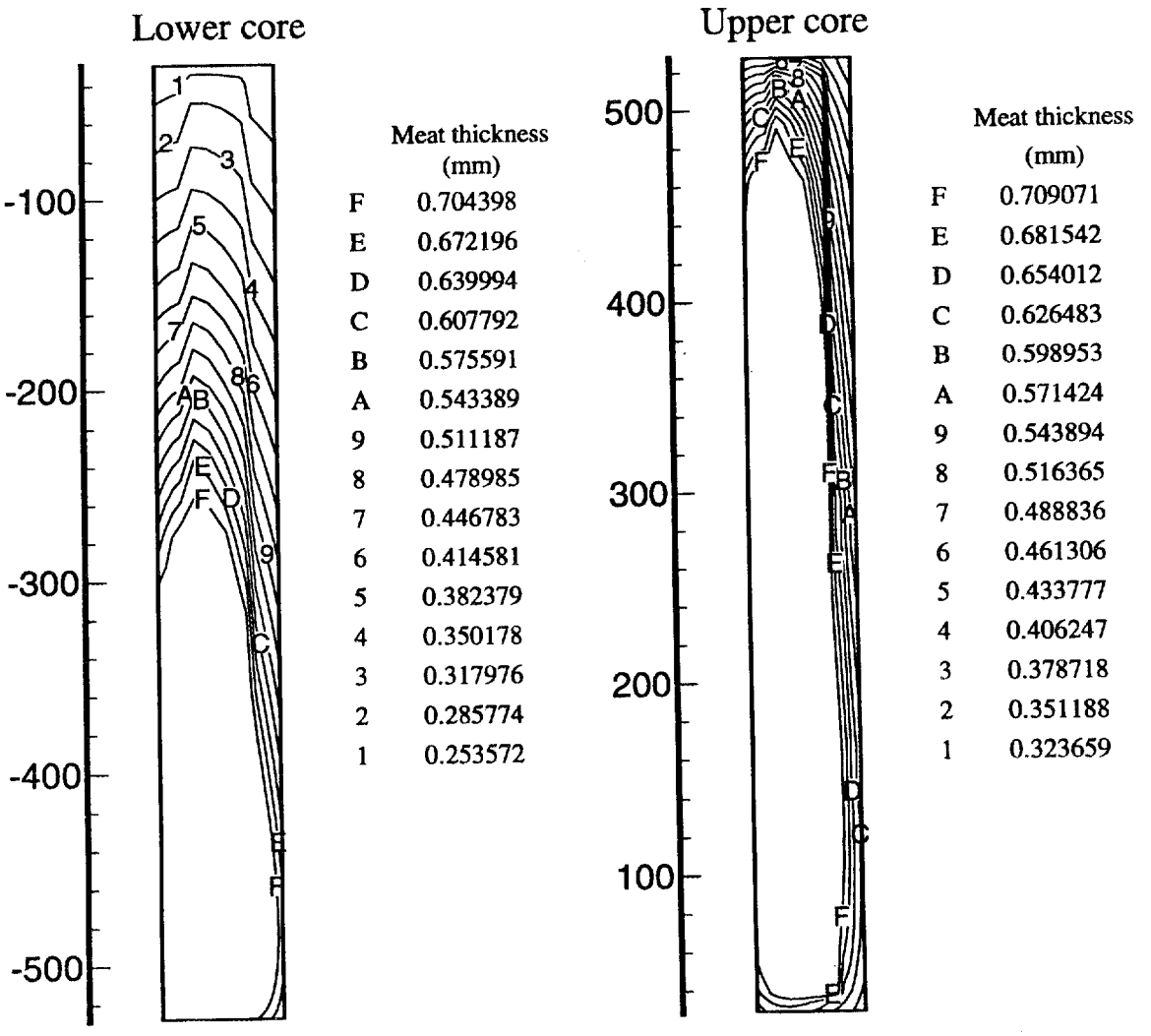

Fig. A.1. L7 design meat thickness distribution.

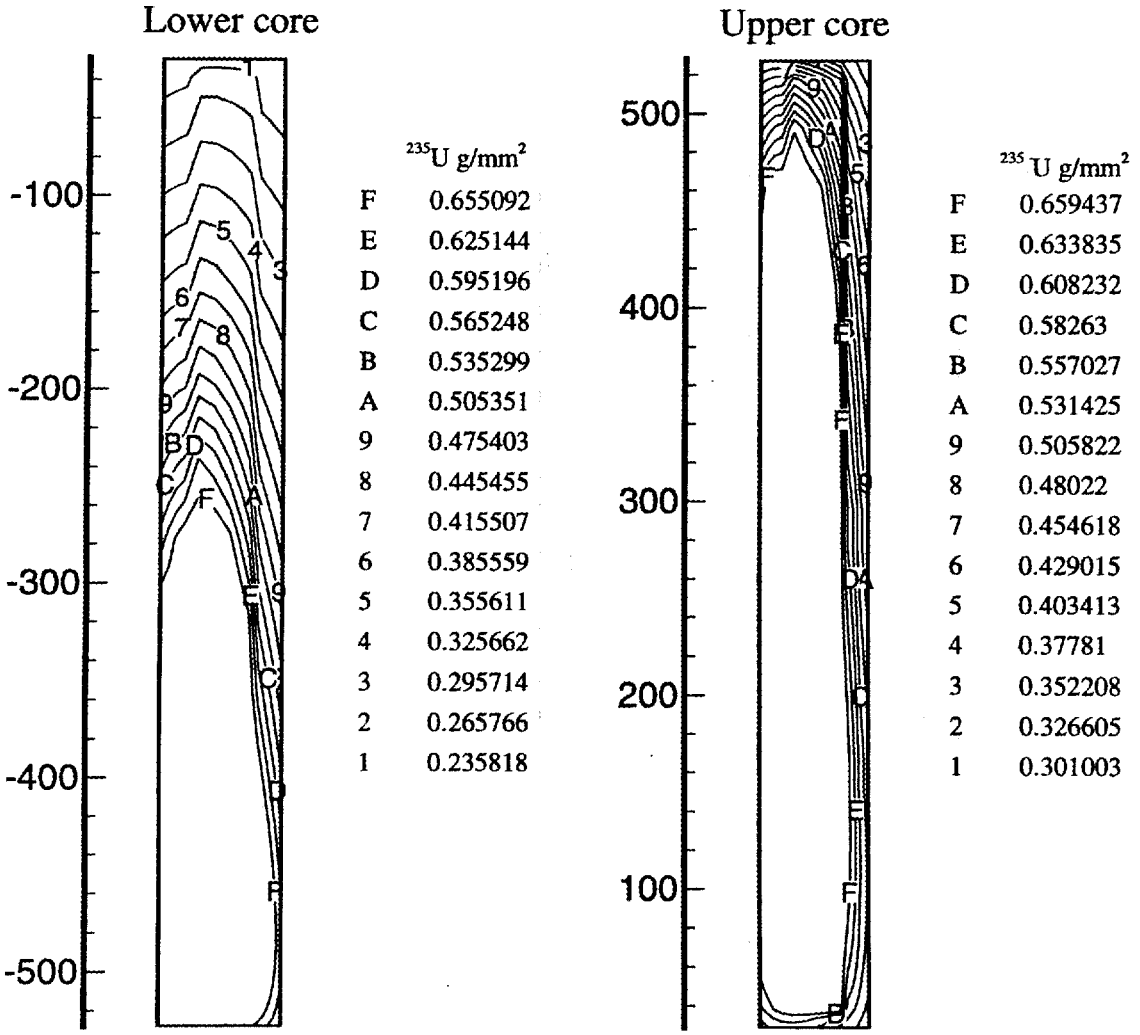

Fig. A.2. L7 design original surface density distribution.

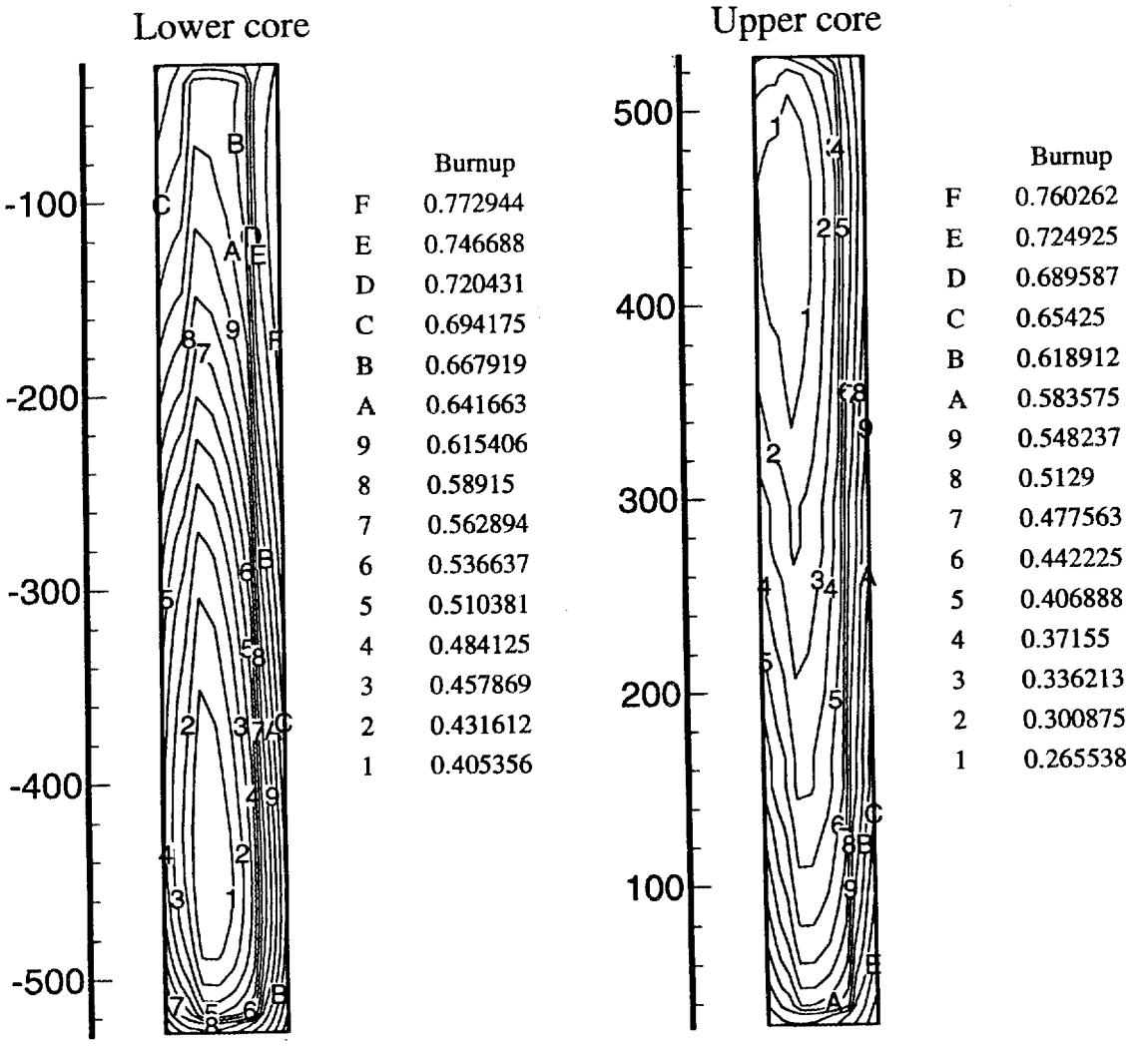

Fig. A.3. L7 design burnup distribution.

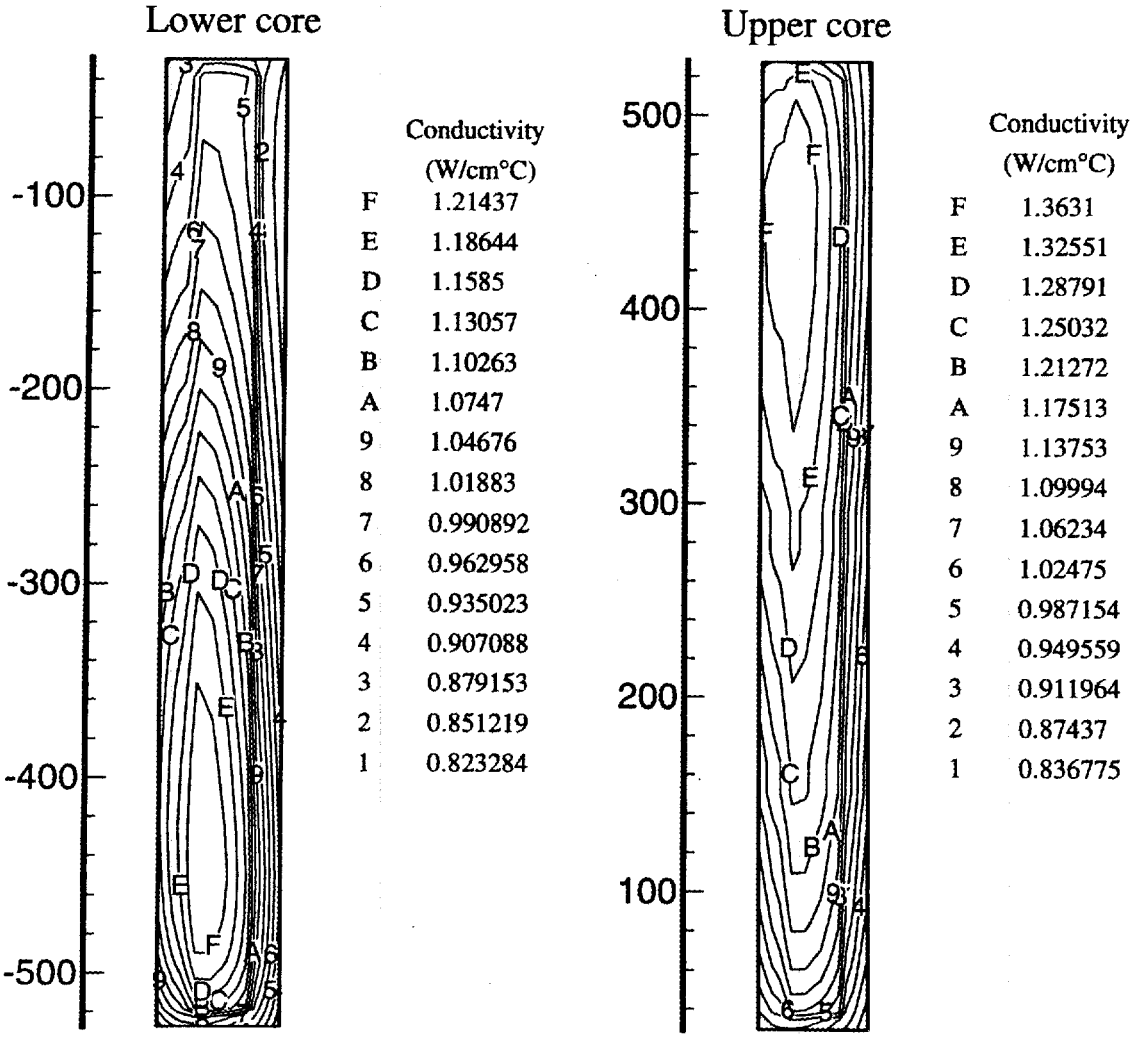

Fig. A.4. L7 design normal fuel conductivity distribution.

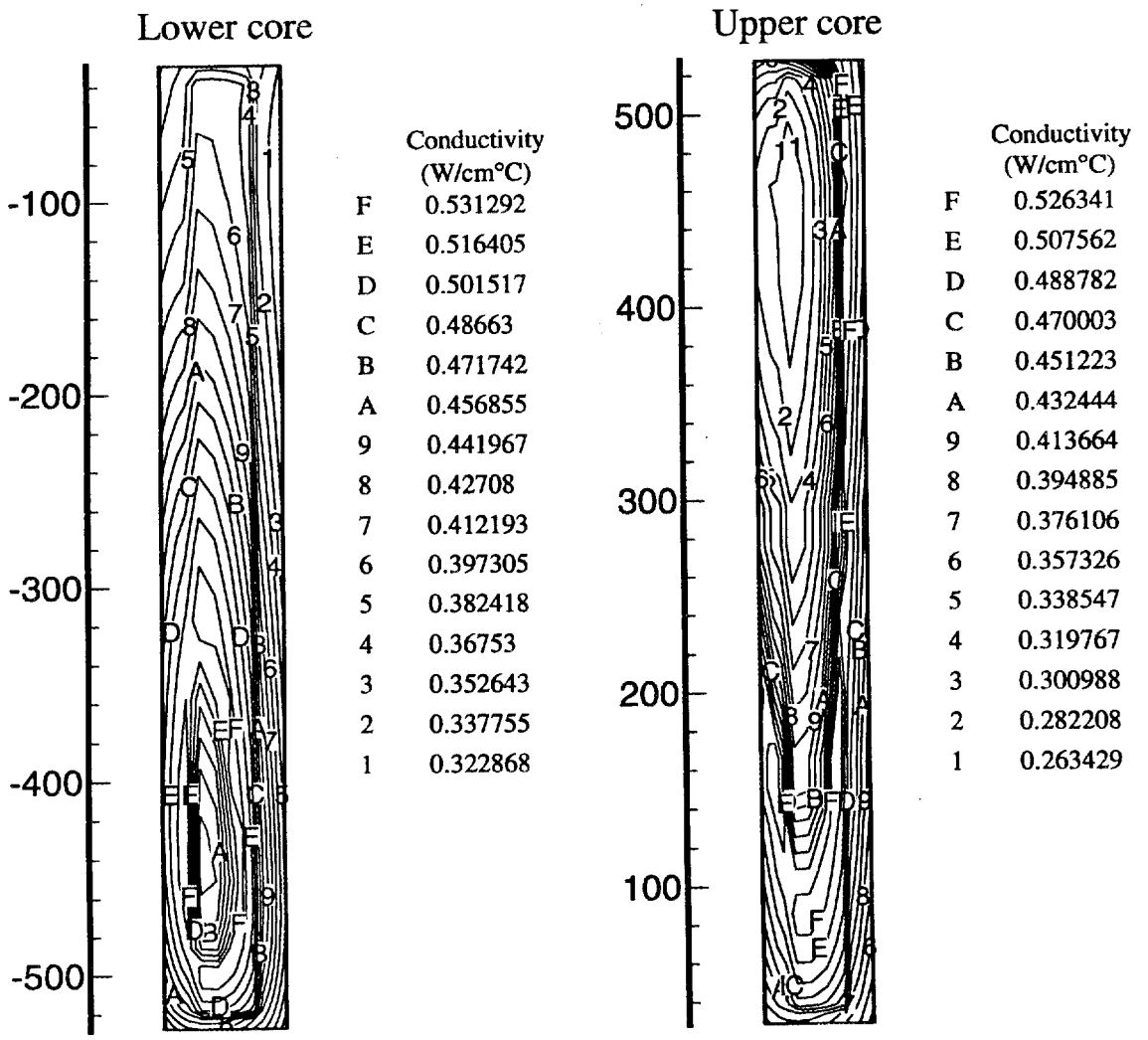

Fig. A.5. L7 design segregated fuel conductivity distribution.

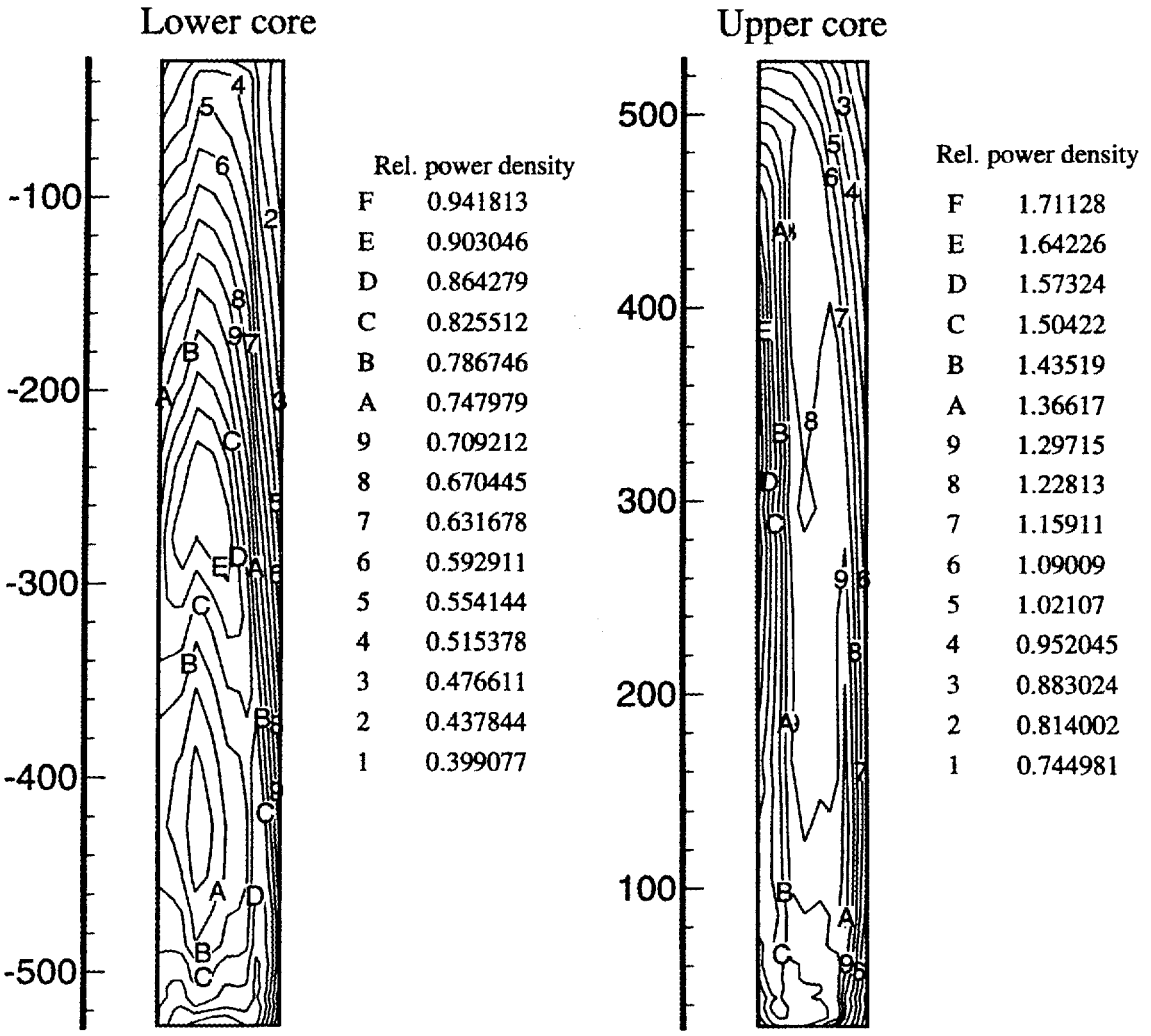

Fig. A.6. L7 design relative power density.

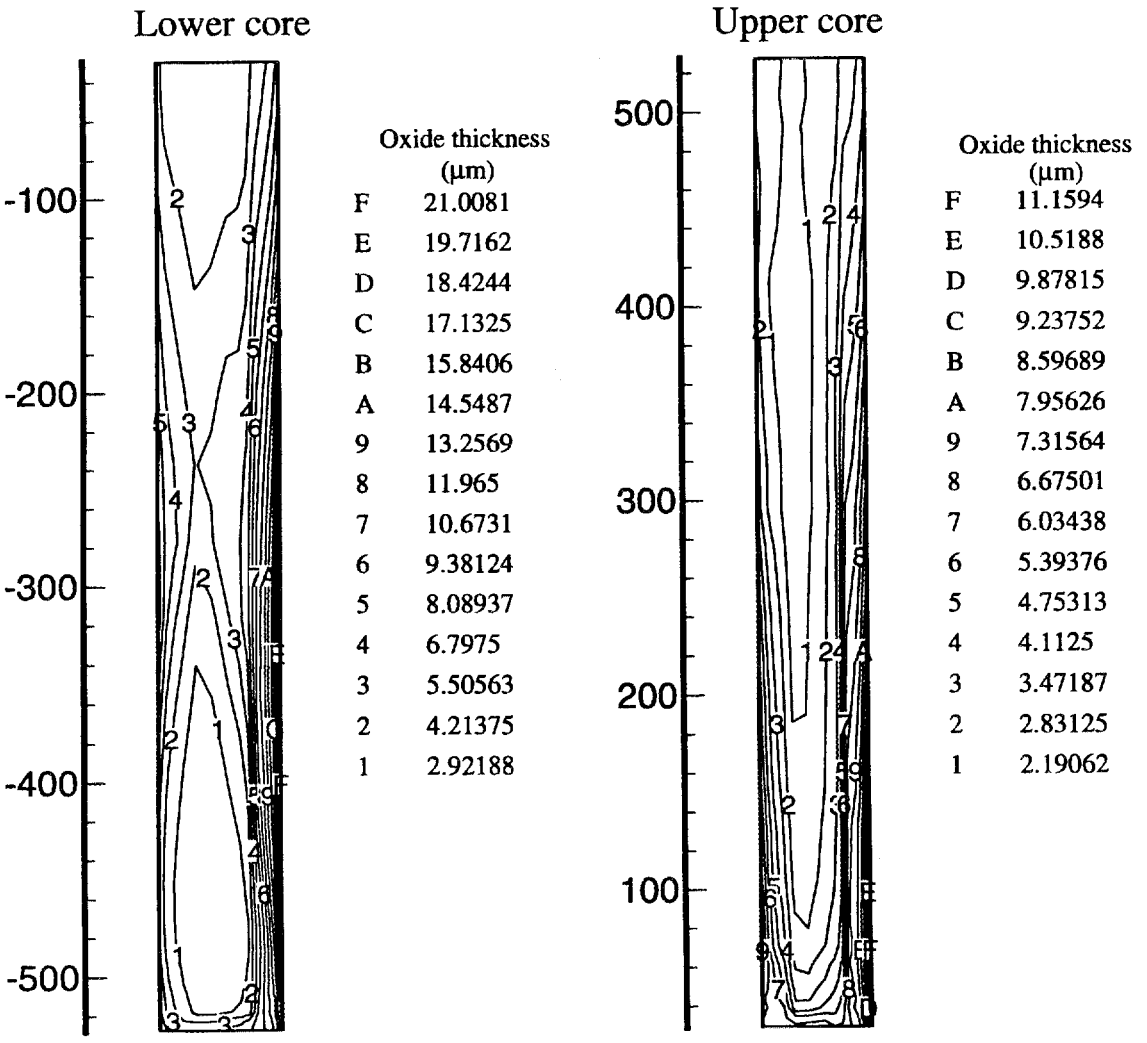

Fig. A.7. L7 design oxide layer thickness distribution.

Appendix B. OVERVIEW OF EXPERIMENTS

Table B.1. Overview of experiments—planned and operating

	A	B	C	D	E	F	G	H	I	J
427										
428										
429		(a) THTL Facilities and Its Modifications (Task 1.1.4 & 1.1.14)								
430										
431		WBS Task # (Budget)	1.1.14.2.2 ($2035K)	1.1.14.2.2 (included)	1.1.14.2.2 (included)	1.1.14.2.2 (included)	1.1.14.2.2 (included)	1.1.14.2.2 (included)	1.1.14.2.2 (included)	1.1.14.2.2 (included)
432		Facility "WBS Name"	THTL 2-S Channel Tests ---THTL/Orig. ---	THTL 2-S Channel Tests ---THTL/Orig. ---	THTL 2-S Channel Tests ---THTL/Orig. ---	THTL 2-S Channel Tests ---THTL/Orig. ---	THTL 2-S Channel Tests ---THTL/Orig. ---	THTL 2-S Channel Tests ---THTL/Orig. ---	THTL 2-S Channel Tests ---THTL/Orig.[2] ---	THTL 2-S Channel Tests ---THTL/Orig.[2] ---
433		**Phen. & Purpose**	**Non-Destr. Flow Exc.Tests**	**Destructive Flow Exc. (Burnout) Tests**	**Destr. CHF (DNB burnout) Tests**	**Protot. ANSR Conds.Tests (CHF & FE)**	**Mat., Oxide & Surf. Effs. on FE, CHF, FF, HTC**	**D2O, W.Chem. & Gas Effs. on FE, CHF, FF, HTC**	**1-P FF & dP (Isothermal) Tests [2]**	**1-P HTC & FF as f(Temp & visc.) Tests [2]**
434		Data prior.(1-5)[sequence]	1(1)	1(1)	1(1)	1(1)	2 (1)	2 (1)	3 (1)	3 (1)
435		Sched. data is needed								
436		Exper. approx. schedule	1994/1995/1996	1994/1995/1996	1994/1995/1996	1994/1995/1996	1994/1995/1996	1994/1995/1996	1994/1995/1996	1994/1995/1996
437		Budget alloc./year	$800K/1132K/104K	(incl. above)	(incl. above)	(incl. above)	(incl. above)	(incl. above)	(incl. above)	(incl. above)
438		Facility type & unique features:	Basic THTL Facility: Prototy. except reduced span and thicker Al. walls	See Col. C	See Col. C	Change TS design to get protot. ANSR local CHF & FE conds (short length, external heating, etc)	Tests var. mat., oxide film, & surf. roughn., etc, in tubes and confirm in rect. chan.	Test var. Water chem., Dis. gas, & D2O in tubes and confirm in rect. chan.	Used as ref. for next test series	Use of low to med. heat flux Prop. resol. of T/Cs and inter. heat redist. is necessary
439		Max. power avail. (or needed), kw	492 kw (25 MW/m2)	See Col. B	See Col. B	See Col. B				
440		Max. pump cap. avail. (or needed), L/s @ ?? MPa	2.36L/s @ 0. MPa 1.95L/s @ 4.1MPa,	See Col. B	See Col. B	See Col. B				
441		Min. pump cap. (avail. (or needed), L/s @ ?? MPa	0.118L/s @0. MPa 0.097L/s @ 4.1MPa	See Col. B	See Col. B	See Col. B				
442		Major loop modifs needed (comp. to present)	See Table 7							
443		TS#	TDS-3 (diff. TS for trans.)	TDS-3 (diff. TS for trans.)	TDS-3 (diff. TS for trans.)	TDS-3 (diff. TS for trans.)	TDS-3 (diff. TS for trans.)	TDS-3 (diff. TS for trans.)	TDS-3 (diff. TS for trans.)	TDS-3 (diff. TS for trans.)
444		TS geom., & size	R: 507x12.7x1.27	R: 507x12.7x1.27	R: 507x12.7x1.27	R: 507???x12.7x1.27	T: 2.54&6.0 ID	T: 2.54&6.0 ID	R: 507x12.7x1.27	R: 507x12.7x1.27
445		TS material	Ziconium-Copper or Bronze	Ziconium-Copper or Bronze	Ziconium-Copper or Bronze	Ziconium-Copper or Bronze ?????	Al-6061	Al-6061	Ziconium-Copper or Bronze	Ziconium-Copper or Bronze
446		Alt. TS for final confirm.	Al-6061	Al-6061	Al-6061	Al-6061	Ziconium-Copper or Bronze	Ziconium-Copper or Bronze	Al-6061	Al-6061
447		Unique instrumentation								
448		Add. TS design and modifs needed	See Table 7			Attempt new TS designs, incl. ext. heating				
449		Bypass posit. (flow ratio)	Closed (min)	Open (>10 : 1)	Closed (zero)	Closed (zero)/Open	Closed (zero)	Closed (zero)	Closed (zero)	Closed (zero)
450		Measure (const.)	Tin, Pex, Qt [1]	Tin, Pex, Qt [1]	Tin, Pex, Qt [1]	Tin, Pex, Qt [1]			Tin, Pex	Tin, Pex, Qt
451		Measure (vary, active)	Vel [1]	Vel [1]	Vel [1]	Vel [1]			Vel	Vel
452		Measure (vary, passive)	Pin,dP,Tex, TCs	Pin,dP,Tex, TCs	Pin,dP,Tex, TCs	Pin,dP,Tex, TCs			Pin, dP	Pin, dP,Tex, Twm
453		Determine	min. dP, Vcr	FE Burnout, Vcr	CHF Burnout, Vcr	CHF Burnout, Vcr			FF, Re	Twz, Tbz, Hz
454		Plot	dP=f(Vel), dP min	dP=f(Vel), FE	dP=f(Vel), CHF	dP=f(Vel), CHF			FF=f(Re)	Hz=f(Re,Pr, T)
455		Inlet T, C (const.)	40-45-50	40-45-50	40-45-50	40-45-50			40-45-50	40-45-50
456		Exit pres., MPa (const.)	0.5 - 2.0	0.5 - 2.0	0.5 - 2.0	0.5 - 2.0			1.5-1.7-1.9	1.5-1.7-1.9
457		Heat flux, MW/m2 (const.)	3 - 17	3 - 17	3 - 17	3 - 17			No Power	3.0-6.0-9.0
458		Inlet velocity, m/s (vary)	2 - 28	2 - 28	2 - 28	2 - 28				

Table B.1 (continued)

	K	L	M	N	O	P	Q	R
427								
426								
429								
430								
431	1.1.14.2.2 (included)	1.1.14.2.2 (included)	1.1.14.2.2 (included)	1.1.14.2.2 (included)	1.1.14.2.2 (included)	1.1.14.2.2 (included)	1.1.14.2.2 (included)	1.1.14.2.4 ($1653K)
432	THTL 2-S Channel Tests ---THTL/Orig.[2]---	THTL 2-S Channel Tests ---THTL/Var. Span---	THTL 2-S Channel Tests ---THTL/M. Span & P.Taps---	THTL 2-S Channel Tests ---THTL/M. Span & P.Taps---	THTL 2-S Channel Tests ---THTL/M. Span & P.Taps---	THTL 2-S Channel Tests ---THTL/M. Span & P.Taps---	THTL 2-S Channel Tests ---THTL/Mod.??---	THTL 2-S Channel Tests ---THTL/Prot. Surf.---
433	**Inciplent Boiling Tests [2]**	**Span scaling Validation Tests**	***2 9* dP & Void Frac. Tests**	**2-P Nucl. Boll. HTC Tests**	**Ax. H. F. Dists. Effects on FE**	**.Lat. H. F. Dists. Effects on FE - Med. Span (??)**	**THTL Quasi-Trans. Conds. Tests**	**Low Mass Flux, Positive Quality DNB Tests**
434	2 (1)	2 (1)	2 (1)	2 (1)	3 (1)	3 (1)	3 (1)	4 (7)
435								
436	1994/1995/1996	1994/1995/1996	1994/1995/1996	1994/1995/1996	1994/1995/1996	1994/1995/1996	1994/1995/1996	1995/1996
437	(incl. above)	(incl. above)	(incl. above)	(incl. above)	(incl. above)	(incl. above)	(incl. above)	$618/1036K
438	Protot. surf. char.'s are very important.	Try 2 &3 times the prev. span and determine span scalibility. Use of full Length?	New TS design with press. taps along channel. Necessary span scale to be deter. earlier.	New TS design with press. taps along channel. Necessary span scale to be deter. earlier.	Two Axial H.F. profiles, Needs high power? New TS design with press. taps along channel. Necessary span scale to be deter. earlier.	Add max. lateral dQ/dy to Ax. distr. New TS design with press. taps along channel. Necessary span scale to be deter. earlier.	Use the basic THTL facil. for testing quasi-steady state conds occur. in safety trans.'s. Specific tasks will be sch. later.	Modified TS to haveprotot. surf. and int. wall chars. for Oscil. & rewet. DNB One sided?, Full span?, Full length?
439								Low H.F.
440								
441								
442		New power Supp.? Add. Pump Cap.?	New power Supp.? Add. Pump Cap.?	New power Supp.? Add. Pump Cap.?	New power Supp.? Add. Pump Cap.?	New power Supp.? Add. Pump Cap.?	Mods for trans.	Needs gas pressurizers to slab. press. bounds?
443	TDS-3 (diff. TS for trans.)	TDS-4(??) (diff.TS lor trans.)	TDS-4(??) (diff.TS for trans.)	TDS-4(??) (diff.TS lor trans.)	TDS-5(??) (diff.TS tor trans.)	TDS-6(??) (diff.TS lor trans.)	TDS-??? (diff. tor diff. trans)	Protot. H.F. & Power/Vol ratio
444	R: 507x12.7x1.27	R: 507x25.4 & 38.1x(1.27-3.8177)	R: 507x25.4x(1.27?) Larger span??	R: 507x25.4x(1.27?) Larger span??	R: 507x25.4x(1.27?) Var. ax thick.	R:507x25.4x1.27, Lat. lin. thick.		Protot. wall length. thick. & material
445	Zlconium-Copper or Bronze	Zlconium-Copper or Bronze or Inconel	Zlconium-Copper or Bronze or Inconel	Zlconium-Copper or Bronze or Inconel	Zlconium-Copper or Bronze or Inconel	Zlconium-Copper or Bronze or Inconel		Oxide surf. impor. tor rewetting involved
446	Al-6061	Al-8081	Al-6061	Al-6061	Al-6061	Al-6061		
447		P. taps f(z)	P. taps f(z)	P. taps f(z)	P. taps f(z)	P. taps f(z)		
448		Add pres. laps along chan. Lat. Tb,ex for mixing??	Add pres. taps alongchan. Lat. Tb,ex for mixing ??	Add pres. laps along chan. Lat. Tb,ex tor mixing 77	Add pres. taps along chan. Lat. Tb,ex for mixing ??	Add pres. laps along chan. Let. Tb,ex lor mixing 77		
449	Clcsed (zero)				Open (>10 : 1)	Cbsed [zero]		
450	Tin, Pex, Vel [1]							
451	at [1]							
452	Pin,dP,Tex, TCs		Pin,dP,Tex, TCs(z), P(z)	Pin,dP,Tex, TCs(z), P(z)	Pin,dP,Tex, TCs(z), P(z)	Pin,dP,Tex, TCs(z), P(z)		
453	TC#3, Qt							
454	Qt=f(Tw-Ts)							
455	40-45-50							
456	0.5 - 2.0							
457	3 : 17							

Table B.1 (continued)

	S	T	U	V	W	X	Y	Z
427								
428								
429							(a) Other T/H Facilities	
430								
431	New	1.1.14.2.3 ($5887K)	1.1.14.2.3 (incl.)	1.1.14.2.3 (incl.)	1.1.14.2.3 (incl.)	1.1.14.2.10 ($5148K)	WBS Task # (Budget)	1.1.14.2.1 ($261K)
432	THTL 2-S Channel Tests --- THTL/Integral ---	Protot. Span Test Loop --- PSTL ---	Protot. Span Test Loop --- PSTL ---	Protot. Span Test Loop --- PSTL ---	Protot. Span Test Loop --- PSTL ---	Multi-Chan. Therm.-Hyd. Tests --- THTL/Multi.Ch. --- or --- PSTL/Multi.Ch. ---	Facility "Code Name"	Flow Blockage Test Fac. --- FBTF ---
433	**Small Scale RELAP Integral Tests**	**Lat. H. F. Dist.s Effects on FE in Full Span**	**Comb. Ax. & Lat. H. F. Dist.s on FE in Full Span**	**Hot Streak Effects on FE - Full Span**	**Hot Spot Effects on CHF - Full Span**	**Multi-Chan. Ass. T/H Tests**	**Phen. & Purpose**	**Flow Blockage Tests**
434	????	2 (3)	2 (3)	1 (3)	1 (3)	4 (6)	Data priority (1-5)	1 (2)
435							Sched. data is needed	
436		1994/1995/1996/1997/1998	1994/1995/1996/1997/1998	1994/1995/1996/1997/1998	1994/1995/1996/1997/1998	1995/1996/1997/1998/	Exper. approx. schedule	1994 (being built in 1993)
437		$370/2092/1352/1342/732	(incl. above)	(incl. above)	(incl. above)	$1064K/1549/1512/1024	Budget alloc./yr	$261K
438	RELAP simul. of full integration in small scale comp.'s of one loop: Pump, Acc., Rupture Disks, etc	Full Span Two Axial H.F. profiles, Needs high power? Use half or full length?	Full Span. Two comb. of H.F. profiles, Needs high power? Use half or full length?.	Streaks 1.5, 5.0 & 10.0 mm, Ax. H.F. ratios: 1.3 & 1.6 Needs high power? Protot. span. Half length.	Attempt an "array of hot spots"?? Needs high power? Protot. span. Half length.	Test cond. & FE mutual effects between adjusant channels. Could FE occur before Min. dP?	Facility type & unique features:	One sided, full span, turbulance & eddies.
439							Max. power avail. (or needed), kw	
440							Max. pump cap. avail. (or needed), L/s @ ?? MPa	
441							Min. pump cap. (avail. (or needed), L/s @ ?? MPa	
442		New Power Supply (H.V.). Add. Pump Cap.	New Power Supply (H.V.). Add. Pump Cap.	New Power Supply (H.V.). Add. Pump Cap.	New Power Supply (H.V.). Add. Pump Cap.		Major loop modifs. needed (compared to present)	
443		1-Side heated, other transparent	1-Side heated, other transparent	1-Side heated, other transparent	1-Side heated, other transparent	TDS-???	TS#	
444		R:254?x87x1.27, Lat. var. thick	R:254?x87x1.27, Lat. var. thick	R:254?x87x1.27 with Hot Strks	R:254?x87x1.27 with Hot Strks	Semi-scale 3-Chan. "fuel ass." ??	TS geom., & size	
445		Ziconium-Copper or Bronze or Inconel	Ziconium-Copper or Bronze or Inconel	Ziconium-Copper or Bronze or Inconel	Ziconium-Copper or Bronze or Inconel		TS material	
446		Al-6061	Al-6061	Al-6061	Al-6061		Alt. TS for final confirm.	
447		P. taps f(z)	P. taps f(z)	P. taps f(z)	P. taps f(z)		Unique instrumentation	
448		Add pres. taps along chan. Lat. Tb,ex for mixing	Add pres. taps along chan. Lat. Tb,ex for mixing	Add pres. taps along chan. Lat. Tb,ex for mixing	Add pres. taps along chan. Lat. Tb,ex for mixing		Add. TS design and modifs. needed (compared to present)	
449		Open (>10 : 1)	Open (>10 : 1)	Open (>10 : 1)	Closed (zero)		Bypass posit. (flow ratio)	
450							Measure (const.)	
451							Measure (vary, active)	
452							Measure (vary, passive)	
453							Determine	
454							Plot	
455							Inlet T, C (const.)	
456							Exit pressure, MPa (const.)	
457							Heat flux, MW/m2 (const.)	
458								

Table B.1 (continued)

	AA	AB	AC	AD	AE	AF	AG
427							
428							
429							
430							
431	1.1.4 ($3275K)	1.1.14.2.6 ($1679K)	1.1.14.2.9 ($1819K)	1.1.14.2.7 ($3100K)	1.1.14.2.8 ($891K)	1.1.14.2.5 ($4910K)	1.1.14.2.11 ($7005K)
432	Natural Circ. Test Facility {Core Flow (1.1.4)} --- NCTF ---	Natural Circ. Test Facility {Mod. Core Flow (1.1.4)} --- NCTF ---	Natural Circ. Test Facility {Mod. Core Flow (1.1.4)} --- NCTF ---	Non-Fuel Comp.s Test Fac. --- NFCTF ---	Pipe Break Expers Fac. --- PBEF ---	Integral Trans. Perf. Test Fac. ---- ITPTF ---	Full Scale/Full Flow Integ. Fac. --- FSFFITF ---
433	**Natural Circ. Tests (Decay Heat)**	**Natural Circul. Off-Nom. Tests**	**Thermal-Hyd. Refueling Testing**	**Hydraulic Tests of Non-Fuel Comp.s**	**Pipe Break Experiments (was for NPR)**	**Scaled Trans. Pump Perf. Tests (B.D., Cavit.& Flash)**	**Full Scale & Full Flow Trans. Integral Tests**
434	2	3 (5)	5 (9)	5 (8)	5 (10)	3 (4)	5 (11)
435							
436	1994/1995/1996/1997	1997/1998/1999	1997/1998/1999	1995/1996/1997/1998	1994/1995	1995/1996/1997/1998	1995/1996/1997/1998/1999
437	$397K/1458/1062/358	$559K/1012/109	$674K/1037/109	$881K/1050/1061/109	$454K/437K	$1790K/1162/1053/905	$351K/3733/1387/1323/212
438	Basic nat. circ. system loop for testing at nominal conds.	Modified loop of 1.1.4 Possible oscil. & instabs. May not need to be extensive and sophist.	Nat. Conv. in a pool Is it poss. to use mod. 1.1.4 loop?	Control rods, Beam tubes, CPBT, Reflector tank walls, etc.	Inst. vs limited time Doub.-ended guill. vs leak-bef. break Earthquake,	Hot leg depres. blowd. conds. pump exit break. Pump cavit. & flash. Also test crit. vel. and press. Wave. Red. scale integr. RELAP simul.	RELAP simul. of full integration of reduced scale (semi??) comps. of one loop: pump, acc., rupture disks, etc
439							
440						One semiscale pump	One semiscale pump
441						One semiscale pump	One semiscale pump
442		Fuel Ass. simul. Riser above heat source				One semiscale accum., Rupture disks	One semiscale accum., Rupture disks
443							
444		Protot. wall length, thick. & material					Semiscale 3-Chan. "fuel ass." ??
445		Oxide surf. impor. for phen. involved					
446							
447							
448							
449							
450							
451							
452							
453							
454							
455							
456							

INTERNAL DISTRIBUTION

1. C. W. Alexander
2. D. J. Alexander
3. R. R. Allen
4. E. E. Alston
5. J. L. Anderson
6. B. R. Appleton
7. J. G. Arterburn
8. R. E. Battle
9. R. S. Booth
10. W. W. Bowman
11. R. A. Brown
12. G. J. Bunick
13. J. J. Carbajo
14–18. J. H. Campbell
19. P. F. Cento
20. N. C. J. Chen
21. K. K. Chipley
22. J. E. Cleaves
23. J. T. Cleveland
24. G. L. Copeland
25. J. A. Crabtree
26. W. G. Craddick
27. J. R. Dixon
28. F. F. Dyer
29. K. Farrell
30. G. Farquharson
31. D. K. Felde
32. J. Freels
33. R. E. Fenstermaker
34. M. L. Gildner
35. G. E. Giles
36. H. A. Glovier
37. D. C. Haberkost
38. R. M. Harrington
39. J. B. Hayter
40. S. E. Holliman
41. M. M. Houser
42. R. O. Hussung
43. D. T. Ingersoll
44–47. R. L. Johnson
48. R. A. Lillie
49. M. A. Linn
50. A. T. Lucas
51. J. A. March-Leuba
52. B. S. Maxon
53. G. T. Mays
54. J. L. McDuffee
55. M. T. McFee
56. S. V. McGrath
57. T. J. McManamy
58. G. R. McNutt
59. J. T. Mihalczo
60. R. M. Moon
61. D. G. Morris
62. D. L. Moses
63. Y. Murayama
64. W. R. Nelson
65. R. E. Pawel
66. H. R. Payne
67. F. J. Peretz
68. G. M. Powers
69. C. C. Queen
70. S. Raman
71. C. T. Ramsey
72. J. S. Rayside
73. W. R. Reed
74. J. P. Renier
75. J. B. Roberto
76. R. E. Rothrock
77. T. L. Ryan
78. D. L. Selby
79. H. B. Shapira
80. C. D. Sulfredge
81. M. Siman-Tov
82. B. R. Smith
83. T. K. Stovall
84. R. P. Taleyarkhan
85. D. W. Thiesen
86. P. B. Thompson
87. K. R. Thoms
88. S. R. Tompkins
89. B. D. Warnick
90. M. W. Wendel
91. C. D. West
92. J. L. Westbrook
93. D. M. Williams
94. B. A. Worley
95. G. T. Yahr
96–105. G. L. Yoder
106. ORNL Patent Office
107–108. Document Research Library
109. Y-12 Technical Library
110–111. Laboratory Records
112. Laboratory Records (RC)

EXTERNAL DISTRIBUTION

113. R. Awan, U.S. Department of Energy, NE-473, Washington, DC 20585.
114. K. K. Conway, Laboratory Facilities Branch, U.S. Department of Energy, Oak Ridge Operations Office, CE-523, P.O. Box 2001, Oak Ridge TN 37831-2001.
115. R. R. Fullwood, Brookhaven National Laboratory, Upton, NY 11973.
116. Y. Elkassabgi, Texas A&I University, Department of Mechanical Engineering, Campus Box 191, Kingsville, TX 78363
117. C. D. Fletcher, MS 3885, EG&G Idaho Inc., P.O. Box 1625, Idaho Falls, ID 83415-3885
118. W. R. Gambill, Route 5, Box 220, Clinton, TN 37716.
119. P. Griffith, Professor, Massachusetts Institute of Technology, Department of Mechanical Engineering, 77 Massachusetts Avenue, Room 7-044, Cambridge, Massachusetts 02139.
120. A. F. Henry, Professor, Department of Nuclear Engineering, Massachusetts Institute of Technology, 77 Massachusetts Avenue, Cambridge, MA 02139.
121. R. A. Hunter, Director, Office of Facilities, Fuel Cycle, and Test Programs, Nuclear Energy Division, U.S. Department of Energy, NE-47, Washington, DC 20585.
122. T. L. Kerlin, University of Tennessee, College of Engineering, 315 Pasqua Engineering Building, Knoxville, TN 37996-2300.
123. M. Kaminaga, Japan Atomic Energy Research Institute, 2-4 Shirakata-Shirane, Tokai-mura, Naka-gun, Ibarakiken, 319-11, Japan.
124. J. A. Lake, manager, Nuclear Engineering and Reactor Design, Idaho National Engineering Laboratory, P.O. Box 1625, Idaho Falls, ID 83415.
125. J. E. Mays, Research and Test Reactor Fuel Elements, Babcock and Wilcox Co., P.O. Box 785, Lynchburg, VA 24505.
126. J. P. Mulkey, U.S. Department of Energy, NE-473, Washington, DC 20585.
127. W. T. Oosterhuis, Materials Sciences Division, Office of Basic Energy Sciences, Office of Energy Research, U.S. Department of Energy, ER-132, Washington, DC 20585.
128. A. E. Ruggles, Pasqua Nuclear Engineering Building, University of Tennessee, Knoxville, TN 37996-2300.
129. J. Reyes, Oregon State University, 1566 N.W. Jonquil Place, Corvallis, OR 97330.
130. J. M. Ryskamp, Idaho National Engineering Laboratory, P.O. Box 1625, Idaho Falls, ID 83415-3885.
131. J. L. Snelgrove, Coordinator, Engineering Applications, RERTR Program, Argonne National Laboratory, 9700 South Cass Avenue, Argonne, IL 60439.
132. T. Theofanous, Theofanous & Company, 857 Sea Ranch Drive, Santa Barbara, CA 93109
133. I. Thomas, Director, Materials Science Division, Office of Energy Research, U.S. Department of Energy, ER-13, Washington, DC 20585.
134. U. S. Department of Energy, ANS Project Office, Oak Ridge Operations Office, FEDC, MS-8218, P.O. Box 2009, Oak Ridge, TN 37831-8218.
135. G. E. Wilson, EG&G Idaho Inc., P.O. Box 1625 (m/s 3895), Idaho Falls, ID 83415-3895.
136. H. G. Wood, III, Associate Professor, Department of Mechanical and Aerospace Engineering, Thornton Hall, University of Virginia, Charlottesville, VA 22901.
137. Office of Assistant Manager for Energy Research and Development, U.S. Department of Energy, Oak Ridge Operations Office, P.O. Box 5001, Oak Ridge, TN 37831-2001.
138–139. Office of Scientific and Technical Information, P.O. Box 62, Oak Ridge, TN 37831.